Novel quantum-based interatomic potentials applied to magnesium and its alloys

Skinner, Guy Christopher Goodrich

Awarding institution:
King's College London

Novel Quantum-Based Interatomic Potentials Applied to Magnesium and its Alloys

Guy Christopher Goodrich Skinner

Department of Physics

King's College London

A thesis submitted in partial fulfilment of the requirements for the degree of Doctor of Philosophy at the King's College London.

August 2019

Acknowledgements

Firstly, I'd like to thank Jemma, Mum, Dad, Bertie (the miniature poodle) and Inca (the labrador). Your love has been without condition and I am very proud to have such wonderful people (and dogs) close to me.

I'd like to thank my supervisor Prof. Tony Paxton who has inspired my passion for physics and its applications. Tony has made the last 3.5 years very enjoyable and has given me the confidence to succeed in the next phase of my life. I would also like to thank Dr. John Moriarty. I spent a memorable summer visiting him at LLNL where I learnt invaluable lessons on how to conduct research.

I'd also like to thank Luke, Lefteri, Tigany, Bartek, Dimitar, Jarvist, Ivo and everyone else who has been a part of Tony's research group over the last few years. It has been a pleasure to work with all of you. I would also like to thank Evan, Rob and Max for always being willing to discuss science even with a pint in hand. And of course Gerard whose general discomfort whilst being in Los Angeles was a great form of relief.

And to the rest of my friends, notably Mills and Ish who have lived with me during this PhD. Although Mills should be thanking me. A special mention goes to Henry, whose own career in physics was inspirational. To everyone at Dulwich, particularly Stewart, Q, Lester and AJ, who prove that cricket is not just about a rig and pipes.

Publications

The following publications are mentioned in this thesis

- Guy C. G. Skinner, John A. Moriarty and Anthony T. Paxton. 'Local Volume Effects in the Generalised Pseudopotential Theory,' *Submitted to Phys. Rev. B.*
- Guy C. G. Skinner, John A. Moriarty and Anthony T. Paxton. 'Stability of the BCC Structure in the Mg-Ca Alloy System,' *In Preparation.*

Abstract

Metals have many desirable properties for industrial applications including strength, ductility and hardness. These and other mechanical properties are determined by the behaviour and interaction of crystal defects at the microscale. In order to make top-down predictions for novel alloy design with optimised mechanical properties, the energetics of crystal defects must be calculated with quantum-mechanical accuracy. Quantum-mechanical simulation takes many forms, as highlighted in Chapters 1 and 2, owing to the fact that a solution to the Schrödinger equation is computationally intractable for most systems. Density functional theory (DFT) is one such method which combines accuracy with efficient scaling. However, for the application of extended defects in metals, it is often unable to simulate the requisite number of atoms. This has led to the development of methods which combine the quantum-mechanical insight of DFT with the linear scaling of interatomic potentials. These methods are known as quantum-based interatomic potentials (QBIPs) and the focus of this thesis is the development of QBIPs for Magnesium and its alloys. In particular, we present work on the extension and application of the generalised pseudopotential theory (GPT). We develop the so-called adaptive GPT (aGPT) which resolves a discrepancy in the simple-metal limit of the GPT when applied to free surfaces and free volumes. The GPT formalism has also been applied to alloys, and this was used to generate interatomic potentials for the Magnesium-Calcium alloy system. These potentials were used to study phase stability in order to move towards a ductile Magnesium alloy.

List of Abbreviations

AHS	Austin, Heine and Sham
aGPT	adaptive Generalised Pseudopotential Theory
APW	Augmented-Plane Wave
BCC	Body-Centred Cubic
BO	Born-Oppenheimer
BOP	Bond-Order Potential
CPA	Coherent Potential Approximation
CRSS	Critically Resolved Shear Stress
DFT	Density Functional Theory
EXX	Exact Exchange
FCC	Face-Centred Cubic
FP-LMTO	Full Potential Linear Muffin-Tin Orbital
GGA	Generalised Gradient Approximation
GPT	Generalised Pseudopotential Theory
HCP	Hexagonal Close-Packed
HK	Hohenberg-Kohn
KS	Kohn and Sham
KKR	Korringa-Kohn-Rostoker
LAPW	Linear Augmented Plane-Wave
LCAO	Linear Combination of Atomic Orbitals
LMTO	Linear Muffin-Tin Orbital
LDA	Local Density Approximation

MGPT	Model Generalised Pseudopotential Theory
MP	Model Pseudopotentials
NRG	Numerical Renormalisation-Group
OF-DFT	Orbital-Free Density Functional Theory
OPW	Orthogonalised Plane Waves
PAW	Projector Augmented Wave
PBE	Perdew, Burke and Ernzerhof
PKA	Phillips, Kleinman and Antoncik
PP	Pseudopotential
PZ	Perdew-Zunger
QMC	Quantum Monte Carlo
QBIPs	Quantum-Based Interatomic Potentials
RPA	Random Phase Approximation
SCF	Self-Consistent Field
SQS	Special Quasi-random Structures
VCA	Virtual Crystal Approximation
VWN	Vosko-Wilk-Nusair

Table of contents

List of figures

List of tables

Chapter 1

Introduction

"All models are wrong, but some are useful"

George E. P. Box

The processing and manufacturing of metals for components is one of the largest industrial sectors, worth €1.3 trillion to the European Economic Area [1]. The importance of this industry to the global economy arose following the industrial revolution in the 18th and 19th century where metals where utilised for their strength, ductility and hardness. However, an understanding of the fundamental atomic processes that give a metal its mechanical properties did not come until the early 20th century [2–4]. Most of the subsequent advances in metallurgy have occurred from the bottom-up and have been explained theoretically *post hoc*.

The challenge for theoretical metallurgy is how to make predictions given the lack of universality; each metal has a completely different metallurgy owing to the different chemistry, defect mechanics and crystal structure. An exceptional example, which is the focus of this thesis, is Magnesium (Mg) which forms in the hexagonally-close packed (hcp) phase. Like all hcp metals, Mg suffers from a plastic anisotropy [5]. However, the anisotropy is particularly pronounced in Mg and the defect mechanics

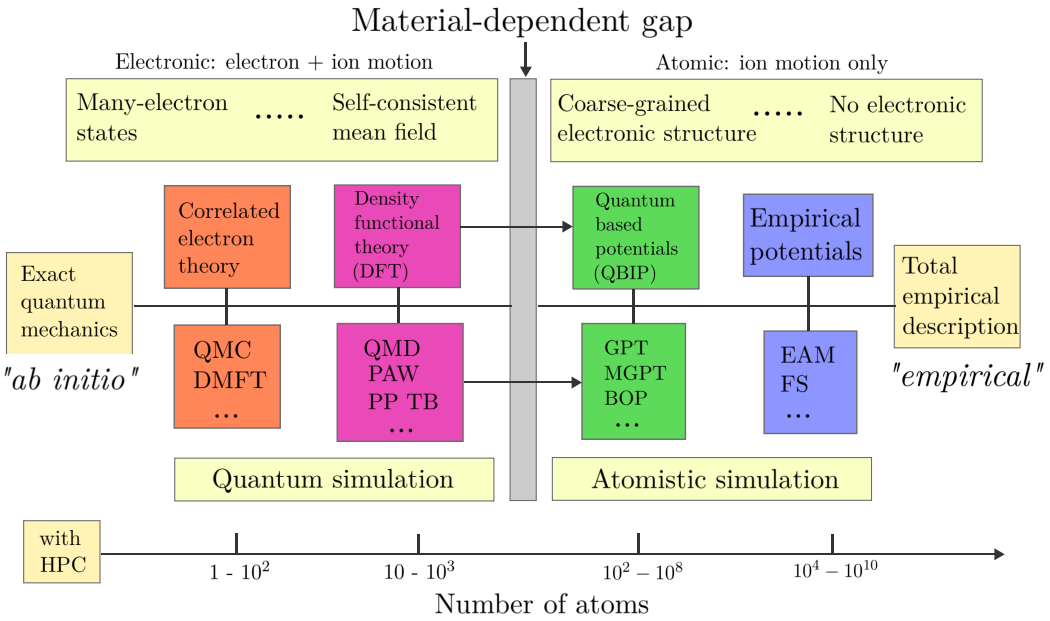

Fig. 1.1: The hierarchy of electronic structure methods across the length-scales is plotted from high-accuracy inefficient-scaling strongly-correlated electron methods to low-accuracy computationally-efficient empirical interatomic potentials. The accuracy and scaling depend on the material being modelled; this is the 'Material-dependent Gap'. This plot is a reproduction of one given by Moriarty [10].

are extremely complex [6–8]. Contrast this to the fact that Mg is an archetypal simple metal [9] whose physics is very well understood. How does such complex metallurgy in Mg emerge from such simple chemical bonding? The answer is related to the roughly four orders of magnitude difference in length scale between the atomic scale and the microscale. To understand and predict the metallurgy at the microscale, we need to develop quantum-mechanical methods that are able to be applied to the microscale. In this thesis, we further develop a method called the generalised pseudopotential theory (GPT); a linear-scaling electronic structure method for metals.

1.1 Overview of Electronic Structure Theory

Uncovering and predicting the fundamental quantum processes which lead to macroscopic physical properties in real materials is the motivation behind electronic struc-

ture theory. Uniquely, the quantum-mechanical governing equations are known [10–14] but an analytic solution is only possible for the simplest quantum mechanical systems [15–17] or systems with a large number of exploitable symmetries [18]. Numerical solution generally requires approximation too, owing to the extremely large dimension of the many-body Hilbert space for molecules [19] and solids [20]. In certain physical situations, the full quantum-mechanical formalism can be approximated to remove unnecessary features. As an example, in techniques based on the numerical renormalisation-group procedure of Wilson [21], only many-electron quantum states belonging to a variational submanifold are considered [22, 23]. These methods provide an extremely accurate solution to the quantum many-body ground state but, as a result, are typically restricted to either low-dimensional lattice models [24, 25] or embedded within molecules [26].

At a similar level of accuracy are the quantum Monte Carlo (QMC) methods (see Fig.(1.1)) which stochastically integrate expectation values given some wavefunction [20, 27]. There are many flavours of QMC, of particular importance are diffusion Monte Carlo [28–30] and variational Monte Carlo [31, 32] as they have been applied to the cohesive energy of real solid-state systems such as the semiconductors Si [33] and Ge [34], and also solid H [35–39]. QMC has also been used to study the homogenous electron gas [32, 40]; these results play a central role in more approximate methods. There are computational advantages to QMC; its computational scaling is $\mathcal{O}\left(N^3\right)$ in time and certain flavours are embarrassingly parallel [27]. However, just like classical Monte Carlo [41], the stochastic error scales with $M^{-1/2}$ where M is the number of simulation steps. The cubic scaling of QMC (with the number of electrons N) combined with a huge prefactor puts accurate QMC out of reach for most real materials at present.

The next set of electronic structure methods down in accuracy are the mean- or

self-consistent field (SCF) methods (see Fig.(1.1)). These methods take the single electron approximation and thus are conceptually different to the NRG and QMC methods. Broadly speaking the coupled N-electron Schrödinger equation is replaced by N mean-field single-electron Schrödinger equations. In SCF methods, the effective mean-field potential seen by each electron is a non-linear function of the one-electron wavefunctions. Historical SCF methods such as the Hartree [42, 43] and Hartree-Fock [44] approximations, suffered from qualitative and quantitative disagreement compared with experiment in real metals [45]. Theoretical justification for the SCF approximation came from the two Hohenberg-Kohn (HK) theorems [46] which proved that the total energy of a many-electron system was a functional of the electron density $n(\mathbf{r})$ alone and that this functional is variational with $n(\mathbf{r})$. The HK theorems are the foundational result of modern density functional theory (DFT). A year after the publication of the HK theorems, two important concepts were introduced by Kohn and Sham [47] that made DFT practical. Kohn and Sham (KS) made the ansatz that the fully-interacting, many-electron system could be replaced with an auxiliary non-interacting system. This requires the introduction of a so-called exchange correlation functional which captures the many-body character of the fully-interacting system. An approximate form of the exchange-correlation functional, known as the local density approximation (LDA), was given and has proved surprisingly robust in the calculation of physical properties of real materials and molecules [14, 48–50].

DFT is easily the most popular simulation method in electronic structure theory and materials science; it is considered the industry standard [50] as its accuracy and computational scaling are sufficient for many systems. However, KS-DFT in the LDA is known to give spurious results for the strongly-correlated electron materials, such as certain transition-metal oxides [51, 52] and certain f-band actinide metals [53]. This has led to the development of methods that use KS-DFT as a reference for a

more refined treatment of exchange and correlation. Examples include methods based on many-body perturbation theory, like the *GW* approximation [54–56], and methods which embed a higher accuracy method within KS-DFT, such as LDA+DMFT [57, 58]. This improved treatment of exchange and correlation comes at the price of increased computational scaling [20] and difficulties arising in the computation of total energies [59] and forces [60–62]. These methods present a different approach to exchange and correlation than in the LDA. Specifically, these methods are material-specific tailor-made approaches to exchange and correlation whereas the LDA treats the electron density as belonging to a homogenous electron gas. There is a plethora of exchange-correlation functionals which are more aligned with the LDA and which offer an improved treatment of exchange and correlation. These functionals include the generalised gradient approximation (GGA) [63–65], meta-GGA [66–68], exact exchange (EXX) [69–71] and hybrid functionals [72–74]. These functionals do give better quantitative agreement with experiment than the LDA and, for some properties, similar accuracy to the many-body theoretic approaches to exchange and correlation. However, the empiricism of these functionals results in a loss of explanatory power relative to the many-body theoretic approaches to exchange and correlation.

For the purposes of this thesis, the main problem with KS-DFT is the computational scaling of its implementations. There are a number of different ways to formulate KS-DFT in extended systems. These differences amount to whether the inner-core electrons are included explicitly and the basis-set that is to be used. There are a handful of all-electron methods including the linear muffin-tin orbital (LMTO) and linear augmented plane-wave (LAPW) [75], linearisations of the Korringa-Kohn-Rostoker (KKR) method [76, 77] and Slater's augmented-plane wave (APW) method [78, 79] respectively, and also the projector augmented wave (PAW) method [80] which is a frozen-core approximation. In addition, there are plane-wave KS-DFT methods

that use a pseudopotential (PP); an ionic potential where the inner-core electrons have been projected out [81, 82].

All of these methods are formulated in terms of an ordinary or generalised eigenvalue problem whose numerical solution scales as $\mathcal{O}(N^3)$, where N is the dimension of the Hamiltonian [83]. This limits KS-DFT to roughly 250-500 atoms over 1-10 ps of molecular dynamics simulation time [10]. Tight binding (TB) methods based on KS-DFT simplify the Hamiltonian construction leading to a more computationally efficient representation of the electronic structure [84]. However, TB is difficult to apply to the simple metals and retains the $\mathcal{O}(N^3)$ Hamiltonian diagonalisation albeit with a minimal linear combination of atomic orbitals (LCAO) basis set. Other methods have been developed in recent years, including PEXSI which avoids diagonalisation of the KS Hamiltonian through a finite-temperature pole-expansion of the Fermi-Dirac distribution [85, 86]. Whilst the computational scaling is $\mathcal{O}(N^2)$, a large number of atoms are required to achieve this. Linear scaling KS-DFT methods [87] have been developed using the principle of 'near-sightedness' [88, 89] which allows for the truncation of (far) off-diagonal density matrix elements. The major challenge for $\mathcal{O}(N)$ KS-DFT methods are metals at low temperatures; this is due to the presence of a sharp Fermi surface and resulting Friedel oscillations [14, 90]. As a result, some authors have developed an alternative $\mathcal{O}(N)$ DFT method which is not based on the KS ansatz [91]. This method known as orbital-free DFT (OF-DFT) works with the electron density alone through the introduction of an approximate kinetic energy functional. OF-DFT suffers from convergence issues and requires the introduction of a local pseudopotential, but has produced reasonable results in the simple metals [92].

An alternative approach, which we take and develop throughout this thesis, is to coarse-grain the DFT electronic structure and derive a set of quantum-based interatomic potentials (QBIPs) (see Fig.(1.1)). The earliest approaches, using pseudopo-

tential perturbation theory, focused primarily on the *sp*-valent simple metals since the valence electron pseudowavefunctions in these metals can be reasonably described as a perturbation from a plane-wave [93, 94]. Pseudopotential perturbation theory was later rigorously formulated entirely within first-principles KS-DFT based pseudopotential perturbation theory [95–97]. This led to a derived total-energy functional including a self-consistently screened pair potential.

Metallic elements with empty or filled *d*-bands pose problems for ordinary pseudopotential perturbation theory as these *d*-band wavefunctions are qualitatively different to those for the *sp*-valence electrons. Inclusion of *d*-state tight binding matrix elements and their hybridisation with the *sp*-valence states leads to an accurate account of the angular bonding in transition metals. QBIPs which achieve this include the generalised pseudopotential theory (GPT) [98, 99], the model GPT (MGPT) [100–103] and the tight-binding based bond-order potential (BOP) [12, 104–109]. The formalism applied to tight-binding *d* states can be extended to the *f*-bonded early actinide metals, where strong electron correlation is not present. This has been done specifically in the case of MGPT potentials [103]. The computational scaling of these QBIP methods is $\mathcal{O}(N)$. In particular, the GPT is linear-scaling at roughly 1000 atoms, comparable to empirical potentials, due to its long-ranged and oscillatory nature. Thanks to advances in computer processing power and memory, QBIPs have been used to study solidification using supercells containing 30 million atoms [110]. Supercells of this size are at the microscale where a metal's mechanical properties are determined [111]; this is usually the domain of continuum crystal plasticity models [112]. In the next section, we will review the motivation for QBIPs and their relationship to empirical interatomic potentials.

1.2 Interatomic Potentials in Metals

The dynamics of the ions in a metal are conventionally assumed to be classical [113] whereas a quantum mechanical description is necessary for the electrons [15–17]. In a QBIP representation, we make the assumption that the electrons move rigidly with the ions and, as a result, we only need to perform a single quantum mechanical calculation for the electrons. In this picture, the ions experience an effective screened Coulomb interaction, due to the quantum-mechanical electrons, which is not rescreened during ionic motion. This is the approximation of neutral pseudoatoms [114]. Pseudoatoms behave rather differently to normal atoms with the main distinction being that they cannot be polarised [13]. The central quantity in DFT quantum mechanics is the electron density $n(\mathbf{r})$ [46] and, without approximation, the DFT total energy can be written as

$$E_{\mathrm{tot}}\left(\{\mathbf{R}\}\right) = \frac{1}{2}{\sum_{ij}}' \frac{Z_i Z_j e^2}{R_{ij}} + E_{\mathrm{ion-el}}\left[n\left(\mathbf{r}\right), \{\mathbf{R}\}\right] \tag{1.1}$$

where $\{\mathbf{R}\}$ denotes the set of all ionic positions, Z_i is the atomic number of the atom i, R_{ij} is the interatomic separation (where the prime over the summation refers to the exclusion of the $i = j$ term) and $E_{\mathrm{ion-el}}$ is an unknown energy functional describing the ion-electron and electron-electron interaction, dependent on both the electron density and ionic positions. The ion-electron energy functional is an extremely complex many-body function of which only a small contribution will be pairwise. This contribution will act so as to screen the bare ionic Coulomb interaction. We may consider a general cluster expansion of $E_{\mathrm{ion-el}}$, in which case we get triplet v_3, quadruplet v_4 and higher order interaction terms, in addition to a many-body embedding contribution and pairwise term. These interaction terms can either be derived as in the GPT [10, 99, 115, 116], or they can be assumed in a parameterised form as in empirical

interatomic potentials [117–122].

The simplest representation of Eq.(1.1) is that of a pure pair potential v_2, which was a viewpoint advocated in metals by early practitioners of empirical interatomic potentials [112, 123–126]. The cohesive energy in such a representation is taken with respect to the individual atomic total energies

$$E_{\mathrm{coh}}\left(\{\mathbf{R}\}\right) = \frac{1}{N} E_{\mathrm{tot}}\left(\{\mathbf{R}\}\right) - E_{\mathrm{tot}}^{\mathrm{atom}} = \frac{1}{2N} {\sum_{ij}}' v_2\left(R_{ij}\right). \tag{1.2}$$

This representation assumes that the residual many-body on-site term (in this sense many-ion not many-electron) is negligible and that the multi-ion terms are effectively averaged over. It is only physically applicable to the insulating rare-gas solids, which are effectively weakly interacting free-atoms with tightly-bound s and p valence electrons. There are a number of constraints on the functional forms of these parameterised empirical pair-potentials.

Firstly, they are generally required to exhibit 'hard-core' repulsion which means that they are large and positive at short distances to prevent one atom penetrating the inner-core of another. Furthermore, it is usually assumed that these empirical pair potentials are short-ranged [112, 123–126]. The short-range, typically over the first couple of neighbour shells, is usually justified for reasons of computational efficiency. However it corresponds to a (very) high electron temperature ($\sim 10^3$-10^4 K) since the long-ranged Friedel oscillations are damped exponentially with temperature [90]. For most physical properties, this is usually not a major concern, in fact most DFT implementations feature a smearing corresponding to a similarly high electron temperature. However, it is important for properties which depend on the structure of the Fermi surface including Kohn anomalies and phase transitions driven by Fermi surface nesting [127]. Another consequence of the short-range of empirical pure pair potential models is that they need to have a deep negative minima in the vicinity

of the nearest-neighbour distance. The earliest parametric interatomic potential that satisfied these constraints was due to Lennard-Jones [117]

$$v_2^{\mathrm{LJ}}(r) = v_0 \left[\left(\frac{r_0}{r} \right)^{12} - 2 \left(\frac{r_0}{r} \right)^{6} \right] \tag{1.3}$$

where v_0 and r_0 are free parameters. Physically the Lennard-Jones potential applies to insulators such as the rare-gas solids with the $1/r^6$ term arising from the van der Waals interaction. Fitting of these free parameters depends on the application, and in general these parametric models are not sufficiently flexible to be transferable to any ion configuration. In general, they are designed to ensure a correct description of cohesion in which case we can find the free parameters by constraining the cohesive energy E_{coh}, equilibrium pressure P^0_{tot} and bulk modulus B^0_{tot}. It is possible to dispense with the parameterisation, as it is unable to give a full account of metallic cohesion which requires full control over the shape and range of the pair potential. A parameter-free approach was given by Carlsson *et al.* [128] where an interatomic potential was derived directly through the inversion of KS-DFT calculations.

There are a number of fundamental problems associated with the assumption of a pure pair potential. Firstly, the energy differences between crystal structures are known experimentally to be three orders of magnitude less than cohesive energies [10, 12]. As a result, the pure pair potential model is necessarily dependent on structure at least on the energy scale of structural energy differences $\sim$ 0.1-10 mRy. Secondly, the cubic elastic constants C_{12} and C_{44} in a pure pair potential model are constrained to be equal. This is sometimes phrased as having a Cauchy ratio σ_C [10, 13]

$$\sigma_C \equiv C_{12}/C_{44} = 1. \tag{1.4}$$

This is generally not satisfied in any metal, whether a simple metal like face-centred cubic (fcc) Al ($\sigma_C = 2.2$) or a transition metal like fcc Cu ($\sigma_C = 1.6$) [10, 13]. As a

result, we may conclude that neither elastic constants nor lattice vibrations may be accurately described by a pure pair potential model. Another problem is associated with the vacancy formation energy. In a pure pair potential model, the unrelaxed vacancy formation energy at zero pressure is simply $E^{\mathrm{u}}_{\mathrm{vac}} = -E_{\mathrm{coh}}$. The effect of relaxation is generally small and so can be ignored for our discussion. As measured experimentally, the cohesive energy is roughly 3 times larger than the vacancy formation energy for metals [10, 13].

Rather than including the necessary many-body terms, the solution in the 1960s and 1970s was to fit the pair potential to elastic constants, lattice vibrations or crystal defect data [125, 129]. Such a pair potential is quantitatively different to that which results from fitting to cohesive energy data. The formalism of empirical pair potentials was extended from the simple models of Lennard-Jones or Morse [117, 118] to the more general spline representation of Johnson [125, 129]. These pair potentials remain, like all pure potentials, unable to span both the energy scale of the cohesive energy and structural energy differences. Furthermore, such pair potentials show significant non-uniqueness and variance when fit to essentially the same experimental data [126].

The primary conclusion is that, even in the simple metals, a many-body contribution is necessary for a generalisable and transferable model. This many-body contribution occurs in the form of a directional multi-ion contribution and/or a collective, non-directional many-body contribution which is essential in the simple metals whose forces are essentially central. The collective, non-directional many-body contribution arises from embedding the ions in a compensating uniform electron density $n_{\mathrm{unif}} = Z/\Omega$ where Z is the effective *sp* valence occupation. In the GPT, the embedding term E_{vol} is volume-dependent and so is the pair potential term v_2

$$E_{\mathrm{coh}}\left(\{\mathbf{R}\},\Omega\right) = E_{\mathrm{vol}}\left(\Omega\right) + \frac{1}{2N}{\sum_{ij}}' v_2\left(R_{ij},\Omega\right). \tag{1.5}$$

These functions have been calculated from self-consistently screened pseudopotential perturbation theory by a variety of different authors beginning with Harrison [93]. Formulations based on DFT quantum mechanics emerged in the 1970s and 1980s by Rasolt and Taylor [130], Dagens *et al* [95], Hafner [97] and as the simple-metal limit of the GPT [115, 116] which is discussed in Chapter 2. Both of these terms are fully transferable to any bulk ion configuration and can accurately describe structural, thermodynamic and mechanical properties [10]. Addressing the failings of the pure pair potential models, the GPT is able to describe both cohesion and structural energy differences accurately because the volume term $E_{\rm vol}$ is of the same order of magnitude as the cohesive energy (see Fig.(3.1)) and the interatomic pair potential is of the same of magnitude as structural energy differences (see Fig.(2.4)). Since the virial pressure is no longer required to vanish at equilibrium, as it is balanced by an equal and opposite volume term contribution, the Cauchy ratio is no longer unity. It is replaced by the positive Cauchy pressure condition [10, 13]

$$P_C = C_{12} - C_{44} = \frac{1}{2} P^0_{\rm vir} > 0 \tag{1.6}$$

which is observed in simple metals. The unrelaxed vacancy formation energy gets a correction from the non-zero virial pressure [100]

$$E^{\rm u}_{\rm vac} = -\left(E^0_{\rm coh} - E^0_{\rm vol}\right) + \Omega_0 P^0_{\rm vir}. \tag{1.7}$$

This correction can be thought of as the pressure required to compress the cell uniformly by Ω_0 to retain constant volume after an atom has been removed and replaced on the surface. This improves the unrelaxed vacancy formation energy to roughly the same order of magnitude as experimental values. However, as we shall see in Chapter 3, there remains a large quantitative discrepancy between the GPT vacancy formation energy and the experimental value. In hcp Mg at the observed equilibrium atomic

volume, the GPT vacancy formation energy is approximately half the experimental value.

The extension of Eq.(1.5) to empty d-band, filled d-band and transition series metals was achieved by Moriarty [98, 99] following on the work of Harrison [131]. The empty and filled d-band are still adequately described at the pair potential level whilst the transition metals require additional multi-ion potentials due to the localised d-state tight-binding matrix elements [99]. In the full GPT, we have for the cohesive energy

$$E_{\rm coh}\left(\{\mathbf{R}\},\Omega\right) = E_{\rm vol}\left(\Omega\right) + \frac{1}{2N}\sum_{ij}{}' v_2\left(ij,\Omega\right) + \frac{1}{6N}\sum_{ijk}{}' v_3\left(ijk,\Omega\right) + \frac{1}{24N}\sum_{ijkl}{}' v_4\left(ijkl,\Omega\right) + \cdots \tag{1.8}$$

In the GPT, the multi-ion potentials v_2, v_3 and v_4 do not posess closed-form mathematical expressions. Whilst this is fine for v_2, there are challenges in tabulation of the higher order potentials. This led to the development of the MGPT [100, 101] where v_3 and v_4 are replaced by analytic forms derived using canonical d bands which retain the dominant physics of the theory. Moreover, the GPT/MGPT formalism has been very successful in a wide range of applications including the structural, thermodynamic and mechanical properties of the bulk metal. One weakness of the formalism is in the applications of Eq.(1.8) to simple metal free surfaces such as voids, cracks and cleaved surfaces or, as we shall see in Chapter 3, certain crystal defects such as vacancies. It is not even clear which value of the atomic volume to use in the presence of a free surface since the near-neighbour environment is inhomogeneous. This led some authors in the 1980s to dispense with the volume dependence and suppose that the embedding function was a non-linear function of interatomic separation. This gives us the following

cohesive energy

$$E_{\text{coh}}\left(\{\mathbf{R}\},\Omega\right)=\frac{1}{N}\sum_{i}F\left[\sum_{j}{}'\,g\left(R_{ij}\right)\right]+\frac{1}{2N}\sum_{ij}{}'\,v_{2}\left(R_{ij}\right) \tag{1.9}$$

where F is a non-linear embedding function and $g(r)$ is an unspecified short-ranged function of the interatomic separation. The unknown quantities may vary in their definition, particularly since the pair potential v_2 can be redefined to include the linear part of the embedding function.

Important examples of potentials which have the functional form of the cohesive energy in Eq.(1.9) include the embedded atom potential (EAM) potential [119], the effective medium theory (EMT) [132] and the many-body Finnis-Sinclair (FS) potential [133]. In the EAM and EMT approach, the function $g(R_{ij})$ represents a background contribution from the site j to the electron density at site i and the function F represents the energy required to embed the atom in the metal. Potentials of this kind are most relevant to the simple metals where the bonding has a non-directional character. As a result, empirical potentials of this form have been most successfully applied to the fcc simple and late-series transition metals such as Al and Cu. These short ranged potentials are unable to capture subtle features in the phonon spectra known as Kohn anomalies [10, 134, 135], which arise due to the logarithmic singularity in the dielectric function. Therefore, both an accurate description of screening and a sharp Fermi surface, absent in EAM/EMT potentials, are required to describe Kohn anomalies. Further extensions to the EAM and EMT models were given in the 1990s. One particular model, which added an angular component to the background electron density, is the modified EAM (MEAM) developed by Baskes and co-workers [122]. The angular components reflect the angular bonding encountered in the mid-series transition metals. The MEAM has been reasonably successful in capturing the physics of these metals, owing more to the increased number of fitting parameters than being justified

by quantum mechanics.

The major problem with empirical potentials is the question of their predictive power. Since their functional forms are arbitrary and without a rigorous basis in quantum mechanics, we have already lost the explanatory power of DFT and the GPT. For instance, the GPT has been used to highlight the importance of *sp*-*d* hybridisation in Ca which stabilises the fcc ground state [136]. The predictive power of a method like the EAM or MEAM is a function of the quality of their many-body co-ordinates and functional forms. Fitting for these potentials is generally done through the matching of forces to DFT data [137]. Ercolessi and Adams used this procedure to fit an EAM potential with 40 parameters to Al. The residual root-mean-square force was roughly 20% of the root-mean-square force in the DFT data. The EAM model was then used to calculate the melt temperature and did so within 1% of experiment. An EAM model for Mg was fitted using the same force-matching scheme and similar data [138]. The residual force was also around 20% yet the melt temperature was only within 20% of experiment. Both of these potentials used a larger cut-off radius than is typically used, roughly half that of the GPT. Contrast this to the agreement to within 4% of experiment for the GPT [139]. There are a number of factors at work in this discrepancy between the EAMs for Al and Mg. Both are simple metals so if the EAM description is sufficient for Al then it should also be sufficient for Mg. This discrepancy speaks to the challenge of fitting empirical interatomic potentials. It is important to stress, however, that the residual fitting error is not the only contribution to the total prediction error [140] and cross-validation might be advised to minimise this quantity.

Recent developments in empirical potentials based on machine learning regression have achieved quantum accuracy and predictive power [141]. Amongst the most famous of these is the Gaussian Approximation Potential (GAP) of Bartók, Csányi and co-workers [142–145]. In the GAP, the cohesive energy functional is given the rather

general form

$$E_{\text{coh}} = \frac{1}{N} \sum_i \varepsilon_i \left(\{ \hat{\mathbf{q}}_i \} \right) \tag{1.10}$$

where ε_i are localised atomic energies whose form depends on the atomic environment within a finite cut-off radius and $\hat{\mathbf{q}}$ is a normalised 'descriptor' that represents the local environment in a manner which respects the translational, rotational and permutation symmetries of ε_i. A typical descriptor is formed by using the expansion coefficients of the local atomic density in a basis of spherical harmonics [146]. The localised atomic energies are fitted to a database of DFT calculations using Gaussian process regression

$$\varepsilon_i \left(\hat{\mathbf{q}}_i \right) = \sum_j \alpha_j K \left(\hat{\mathbf{q}}_j, \hat{\mathbf{q}}_i \right) \tag{1.11}$$

where K is the covariance kernel which measures the similarity between two atomic environments, $\{\alpha_j\}$ are the expansion co-efficients and the sum runs over the database. The covariance kernel is arbitrary but a default choice is the smooth overlap of atomic positions (SOAP) [146]. A number of high-precision GAPs have been developed for various transition metals including W and ferromagnetic Fe. The GAPs have proved tremendously successful in reproducing DFT calculations of properties such as elastic moduli, phonons, vacancies and surface energies within 1-2%. Transferability in the GAP is achieved through the inclusion of all relevant atomic configurations. The major practical challenge with the GAP is in the construction of the DFT database. In particular, how to balance the competing interests of computational efficiency and transferability. At present, the GAP is too expensive to perform multi-million atom calculations or nanosecond time scale molecular dynamics.

We have introduced the state-of-the-art interatomic potentials: on the empirical side machine-learning potentials such as GAP, and on the first-principles side the GPT/MGPT. Whilst it is natural to see these methods as competitors, the reality is

that they each offer something different to the researcher. Machine learning potentials are dependent on the quality of the data that makes up the database and their predictive power originates from their ability to describe any atomic configuration that can be interpolated from the database. On the other hand, first-principles interatomic potentials derive their predictive power from their coarse-grained electronic structure, such that the important physics is retained. There are advantages to both methods and perhaps the best approach would be to combine these methods. Machine learning potentials are not limited to DFT quantum mechanics and their computational cost is not a function of a how accurate the underlying total energy calculation was. On the other hand, quantum-based interatomic potentials are, at present, limited to DFT quantum mechanics. The main advantage of QBIPs is their explanatory power in terms of electronic structure; something that is lost in empirical potential models. Progress in QBIPs has occurred at a slower rate than other parts of electronic structure theory and empirical potentials. Given their explanatory power, scaling and accuracy, this will hopefully change in the future.

1.3 Structure of this Thesis

In this thesis, we first introduce the background electronic structure theory in Chapter 2. This chapter is a presentation of known results. Starting with the Born-Oppenheimer approximation and ending with a derivation of the simple-metal limit of the GPT in its modern self-consistent KS-DFT formalism. We derive self-consistently screened interatomic potentials for Mg using the GPT formalism. Using these potentials, we develop the so-called adaptive GPT (aGPT) in Chapter 3. In a bulk elemental metal, the aGPT and GPT are guaranteed to be equivalent representations. However, the aGPT adds a many-body correction when free surfaces or volumes are encountered. We derive expressions for the forces and stress tensor, and apply these

expressions to a range of properties including the relaxed vacancy formation energy. In Chapter 4, we use the GPT alloy theory to derive self-consistent interatomic potentials for the Mg-Ca alloy system. The central problem for industrial applications of wrought Mg is the plastic anisotropy. This is not unique to Mg and is found across hcp metals (although the plastic anisotropy in Mg is particularly severe). We explore the thermodynamic and mechanical stability of the body-centred cubic (bcc) phase in this alloy system, as the bcc phase is inherently more isotropic. We conclude in Chapter 5, outlining future research directions in the GPT and aGPT.

1.4 Innovations & Codes

There are a number of novel developments detailed in this thesis. The work in Chapter 3 is a follow up on the work by Moriarty and Phillips [147] who first introduced the electron density representation that we describe in the next subsection. This representation was used to calculate total energies alone and was not able to calculate forces. The novelty and my contribution in this chapter was the development of derivatives of the aGPT total energy, and the minor adjustments to the formalism that this requires.

Chapter 4 presents a number of new results including new Mg-Ca GPT potentials that were derived in collaboration with John Moriarty. These potentials were used to calculate the thermodynamic and mechanical stability of Mg-Ca at different concentrations. These calculations were done by myself, using several codes that I developed and are currently used by Prof. Paxton's research group.

The first of these codes `ph.gpt` is a phonon code written in Fortran for the GPT/aGPT that calculates band structures, density of states and thermodynamic properties (using tetrahedron integration [80]). The second of these codes `md.gpt` is a molecular statics/dynamics code for the GPT and aGPT. The molecular statics por-

tion of the code is an implementation of the FIRE algorithm [148] using forces derived from the GPT/aGPT potentials. The molecular dynamics portion of the code implements a number of thermostats including the stochastic velocity rescaling thermostat [149] and Langevin thermostat [150]. In addition, there is also a barostat optimised for use with these thermostats [151]. Finally, for the special quasirandom structure calculations, I wrote a C++ code called `mc.sqs` which was designed for larger systems with looser constraints on the matching of the figures to the perfectly random alloy.

Chapter 2

Electrons in Simple Metals

"Much too complicated to be soluble."

Paul A. M. Dirac FRS

The physics of metals crosses many length and time scales: from the atomic scale where the nature of the metallic bond is determined [12, 13], to the microscale where the interaction of defects governs the mechanical properties [111]. In this chapter, we seek to build a quantum mechanical description of the fundamental electronic and ionic processes. Such a description will need to be both scalable and accurate. Our starting point is the total many-body Schrödinger equation. This equation governs the dynamics of non-relativistic electrons and nuclei. Whilst even the total (electrons plus nuclei) many-body Schrödinger equation is an approximate version of reality, there is no reason to go beyond this in the metals of interest to this thesis. Furthermore, we will see that there is a need to form a hierarchy of approximations to render a model which is computationally tractable for studying the mechanical properties of metals. There is debate as to whether all of the approximations detailed in this section are systematically improvable. However, all of the approximations are justifiable *a posteriori* for our applications [10, 99, 115, 116].

In this chapter, we shall begin our discussion with the total many-body Schrödinger equation and apply the Born-Oppenheimer approximation [152] to it in Section 2.1. The resulting many-electron Schrödinger equation is not a great deal easier to solve, hence we explore the approximations which lead to density functional theory (DFT) in Section 2.2. We are left with an equation for the total energy of a simple metal for which the only unknowns are the eigenvalues of the DFT Hamiltonian. We find these via perturbation theory which requires the introduction of pseudopotentials in Section 2.3. In Section 2.4, we use all of the approximations introduced to construct the real-space total energy in terms of a volume term E_{vol} and a volume-dependent pair potential v_2. This chapter contains no new innovations and is simply a literature review.

2.1 The Born-Oppenheimer Approximation

A foundational approximation upon which electronic structure theory is built is the Born-Oppenheimer (BO) approximation [152]. This approximation makes it possible to separate nuclear and electron motion and is the basis for all the subsequent discussion. The justification given for this approximation relies upon the roughly 4 orders of magnitude difference between electronic and nuclear masses. Thus, the characteristic time scales for electronic and nuclear motion are rather different. In fact, the electrons are moving at speeds roughly 50-100 times that of the nuclei, the nuclei appear approximately stationary. This allows the electrons to relax into their ground state with respect to the configuration of the nuclei. From the perspective of the nuclei, the fast motion of the electrons creates an effective mean-field potential for the nuclei to move in. However, not all electrons behave in the same way but, for now, we will not distinguish between bound inner-core and itinerant valence electrons. More quantitatively, we begin with a total many-body Hamiltonian of an elemental metal. This

metal consists of N nuclei with $Z_a N$ electrons where Z_a is the atomic number. Hence, the metal is constrained to be charge-neutral. The total many-body Hamiltonian $\mathcal{H}_{\text{tot}}$ can be factorised into an electronic part $\mathcal{H}_{\text{e}}$ and a nuclear part $\mathcal{H}_{\text{n}}$

$$\mathcal{H}_{\text{tot}} = \mathcal{H}_{\text{e}} + \mathcal{H}_{\text{n}}. \tag{2.1}$$

The electronic Hamiltonian $\mathcal{H}_{\text{e}}$ is given by

$$\mathcal{H}_e = T_{\text{e}} + V_{\text{ee}} + V_{\text{en}}. \tag{2.2}$$

The first term is the electron kinetic energy operator and the final two terms are the electron-electron and electron-nuclei Coulomb interaction. It is generally assumed that any quantum corrections to the electromagnetic interaction are negligible. The nuclear Hamiltonian $\mathcal{H}_{\text{n}}$ is given by

$$\mathcal{H}_{\text{n}} = T_{\text{n}} + V_{\text{nn}} \tag{2.3}$$

where the first term is the nuclear kinetic energy and the second term is the Coulomb potential energy operator of the nuclei. Whilst it is possible to separate the Hamiltonian into a nuclear part and an electronic part, these operators continue to act on the entire many-body Hilbert space. In general, this leads to eigenstates which are entangled. Therefore, it is not possible to separate the electrons and nuclei into a product of pure states describing the electrons and the nuclei unless an approximation is made[i]. This is the BO approximation

$$|\psi_{\text{tot}}\rangle = |\psi_{\text{e}}\rangle \otimes |\psi_{\text{n}}\rangle = |\psi_{\text{e}}\psi_{\text{n}}\rangle \tag{2.4}$$

[i]One can write down a quantum state describing the electrons or nuclei without approximation. However, this state will be a mixed state. First, we would have to solve for the total density operator and marginalise over the electron co-ordinates for the nuclei density operator and vice-versa.

i.e. that the many-body electronic and nuclear wavevectors form a product state. In other words, there is no entanglement between the electrons and nuclei, and all statistical correlation between electrons and nuclei is purely classical. The BO approximation restricts the wavefunction to lie within a subspace of the total Hilbert space. Furthermore, this subspace has a lower dimension than the total Hilbert space. The electronic wavevector $|\psi_\mathrm{e}\rangle$ is an eigenfunction of the electronic Hamiltonian $\mathcal{H}_\mathrm{e}$

$$\mathcal{H}_\mathrm{e}|\psi_\mathrm{e}\rangle = E_\mathrm{e}|\psi_\mathrm{e}\rangle \tag{2.5}$$

where E_e is the energy eigenvalue. This leaves us with the following equation to solve

$$\mathcal{H}_\mathrm{tot}|\psi_\mathrm{tot}\rangle = (\mathcal{H}_\mathrm{e} + \mathcal{H}_\mathrm{n})\,|\psi_\mathrm{e}\psi_\mathrm{n}\rangle = E_\mathrm{n}|\psi_\mathrm{e}\psi_\mathrm{n}\rangle. \tag{2.6}$$

In position representation, the electronic Hamiltonian $\mathcal{H}_\mathrm{e}$ depends on both the electronic and nuclear co-ordinates whereas the nuclear Hamiltonian $\mathcal{H}_\mathrm{n}$ only depends on the nuclear co-ordinates. In order to satisfy Eq.(2.5), the action of the electronic Hamiltonian on the nuclear wavefunction must be the identity operator

$$(\mathcal{H}_\mathrm{e} \otimes \mathbf{1}_\mathrm{n})\,|\psi_\mathrm{e}\rangle \otimes |\psi_\mathrm{n}\rangle = E_e|\psi_\mathrm{e}\rangle \otimes |\psi_\mathrm{n}\rangle. \tag{2.7}$$

Unfortunately, the nuclear Hamiltonian does not admit a similar decomposition since the electron wavefunction depends on the nuclear co-ordinates. The second part of the BO approximation is to assume that such a decomposition can be made. By marginalising over the electron wavefunctions, we have (in position representation)

$$\left[-\frac{\hbar^2}{2M}\sum_\mathrm{n}\nabla_\mathrm{n}^2 + E_\mathrm{tot}\left(\mathbf{R}_1,\ldots,\mathbf{R}_N\right)\right]\psi_n\left(\{\mathbf{R}\}\right) = E_n\psi_n\left(\{\mathbf{R}\}\right) \tag{2.8}$$

where M is the nuclear mass (taken to be constant for simplicity, as in an elemental metal), the first term is the nuclear kinetic energy T_n and $E_\mathrm{tot} = E_\mathrm{e} + V_\mathrm{nn}$ is the

effective mean-field potential energy operator. The pair of BO approximations have resulted in a single Schrödinger equation for the nuclei. Born and Oppenheimer showed that the leading corrections to these approximations are of order $(m/M)^{1/4}$ [152]. These contributions constitute the electron-phonon interaction in solids and we shall assume that they are insignificant. In addition to the BO approximation, we will typically make the assumption that the nuclei are classical. This approximation holds at ambient temperatures and for nuclei heavier than H and He. The decoherence timescale [153] of heavier nuclei is believed to be extremely rapid. This assumption is the basis for molecular dynamics [41, 154] in which we replace the Schrödinger equation in Eq.(2.8) by the corresponding classical Hamilton's equations.

2.2 Density Functional Theory

Whilst the BO approximation simplifies the problem considerably, the resulting many-electron Schrödinger equation in Eq.(2.5) is intractable for all but the simplest of atomic and molecular systems. The difficulty arises due to the dimension of the many-electron Hilbert space. This is in direct analogy to the situation in the case of the total many-body Schrödinger equation. Like in the BO approximation, we first make the product-state ansatz

$$\psi_{\mathrm{e}}\left(\{\mathbf{r}\}\right) = \bigotimes_{\alpha=1}^{N_{\mathrm{e}}} \psi_{\alpha}\left(\sigma_{\alpha}, \mathbf{r}_{\alpha}\right) \tag{2.9}$$

where $N_{\mathrm{e}} = Z_a N$ is the number of electrons, ψ_{α} are one-electron wavefunctions and σ_{α} is the electron spin. In terms of the one-electron orbitals, we may write the wavefunctions as

$$\psi_{\alpha}\left(\sigma_{\alpha}, \mathbf{r}_{\alpha}\right) = \tilde{\psi}_{\alpha}\left(\mathbf{r}_{\alpha}\right) \chi_{\alpha}\left(\sigma_{\alpha}\right) \tag{2.10}$$

where χ are the one-electron spinors and $\tilde{\psi}$ are the one-electron orbitals. We will ignore this distinction between the one-electron orbitals and the one electron wavefunctions. Furthermore, we shall implicitly include the spin within $\mathbf{r}$. We have essentially restricted the solution to an unentangled subspace within the many-electron Hilbert space. This approximation is referred to as the Hartree approximation [42, 43]. We recognise that E_e can be written as a functional of the one-electron orbitals

$$E_e\left[\{\psi_\alpha\}\right] = \int \left[\prod_{\alpha=1}^{N_\mathrm{e}} \mathrm{d}\mathbf{r}_\alpha\right] \; \psi_1^*\left(\mathbf{r}_1\right) \cdots \psi_{N_\mathrm{e}}^*\left(\mathbf{r}_{N_\mathrm{e}}\right) \mathcal{H}_\mathrm{e} \psi_1\left(\mathbf{r}_1\right) \cdots \psi_{N_\mathrm{e}}\left(\mathbf{r}_{N_\mathrm{e}}\right) \tag{2.11}$$

subject to the orthonormality constraint

$$\int \mathrm{d}\mathbf{r} \; \psi_\alpha^*\left(\mathbf{r}\right) \psi_\beta\left(\mathbf{r}\right) = \delta_{\alpha\beta} \tag{2.12}$$

where δ is the Kronecker delta. Taking the functional derivative of the above $\delta E_\mathrm{e}/\delta\psi_\alpha^*$, and introducing the orthonormality constraint through the Lagrange multiplier E_α, yields the following equation for the one-electron orbitals

$$\left[-\frac{\hbar^2}{2m}\nabla^2 + V_\mathrm{eff}\left(\mathbf{r}\right)\right] \psi_\alpha\left(\mathbf{r}\right) = E_\alpha \psi_\alpha\left(\mathbf{r}\right) \tag{2.13}$$

which is equivalent to the Rayleigh-Ritz principle. Interpreting this equation is rather simple; it is the Schrödinger equation for a non-interacting electron moving in an effective potential V_eff. The effective potential V_eff depends on all of the occupied one-electron orbitals being calculated through the electron density $n(\mathbf{r})$. This means that this partial differential equation is non-linear and must be solved self-consistently. In the Hartree approximation, the effective potential is given by

$$V_\mathrm{eff} = V_\mathrm{en} + V_\mathrm{H} \tag{2.14}$$

where V_{en} is the external potential due to the nuclei configuration and V_{H} is the Hartree potential. The Hartree potential $V_H(\mathbf{r}_0)$ is the classical Coulomb potential arising at the point $\mathbf{r}_0$ from the mean charge density $-en(\mathbf{r})$ of all the other electrons in the system. The electron density $n(\mathbf{r})$ can be written as

$$n\left(\mathbf{r}\right) = 2\sum_{\alpha} \psi_{\alpha}^{*}\left(\mathbf{r}\right)\psi_{\alpha}\left(\mathbf{r}\right). \tag{2.15}$$

where the factor of 2 accounts for the spin degeneracy. In real materials, the Hartree approximation fails to be quantitatively accurate. This is due to the neglect of the anti-symmetry of the many-electron wavefunction [155, 156] and many-electron correlation. The total electron wavefunction (including spin) is required to be antisymmetric under exchange i.e.

$$\psi_{\text{e}}\left(\mathbf{r}_1, \mathbf{r}_2\right) = -\psi_{\text{e}}\left(\mathbf{r}_2, \mathbf{r}_1\right) \tag{2.16}$$

for a two-electron system. This condition is clearly not satisfied by the product state ansatz (Eq.(2.9)) in the Hartree approximation. In terms of the one-electron orbitals, the simplest ansatz wavefunction which has the full exchange symmetry is the Slater determinant [157]

$$\psi_{\text{e}} = \frac{1}{\sqrt{N!}} \sum_{\{i\}=1}^{N} \mathcal{A}_{i_1 \cdots i_N} \psi_1\left(\mathbf{r}_{i_1}\right) \cdots \psi_N\left(\mathbf{r}_{i_N}\right) \tag{2.17}$$

where $\mathcal{A}$ is the Levi-Civita alternating tensor. The resulting self-consistent field method with the Slater determinant ansatz is known as the Hartree-Fock approximation [44]. The ansatz adds a complicated non-local potential to the effective potential in Eq.(2.18). The Hartree-Fock effective potential is given by

$$V_{\text{eff}} = V_{\text{nn}} + V_{\text{H}} + V_{\text{x}}, \tag{2.18}$$

where V_{x} is the exchange potential. The Hartree-Fock equations are in general much more challenging to solve than the Hartree equations with integrals whose evaluation scales as $\mathcal{O}(N^4)$ in time [158][ii]. However, the computational cost is not the reason that the Hartree-Fock approximation is not used in the study of metals. In the homogenous electron gas, which is the limiting case of a simple metal, the density of states vanishes at the Fermi level [159]. This can be shown analytically. The eigenstates of the Hartree-Fock Hamiltonian in the homogenous electron gas can be shown to be plane-waves [127], as they are for the non-interacting case. The energy eigenvalues are given by

$$\varepsilon_{\mathbf{k}} = \frac{\hbar^2 k^2}{2m} - \frac{2e^2 k_F}{\pi} \mathcal{F}\left(k/k_F\right), \tag{2.19}$$

where m is the electron mass, k_F the Fermi wave-vector and $\mathcal{F}(x)$ is the Lindhard function

$$\mathcal{F}\left(x\right) = \frac{1}{2} + \frac{(1-x^2)}{4x} \log\left|\frac{1+x}{1-x}\right|. \tag{2.20}$$

The density of states $g(E)$ is proportional to the inverse of the absolute magnitude of the gradient of Eq.(2.19) with respect to the wavevector $\mathbf{k}$. The derivative of the Lindhard function diverges logarithmically at the Fermi level. Hence, the density of states vanishes identically. In other words, Hartree-Fock predicts that the homogenous electron gas is a semi-metal; an absurd result. Furthermore, the logarithmic divergence means that the electrons at the Fermi level should have infinite velocity. Fortunately, we note that this divergence does not occur in general for a non-Coulombic interaction and can be traced back to the ultraviolet divergence as $k \to 0$ in the Fourier transform of the Coulomb interaction i.e. $4\pi e^2/k^2$. In real metals, the Coulomb interaction is screened at long range and the $4\pi e^2/k^2$ divergence disappears, but it is always

[ii]Most of these integrals can be ignored which reduces the computational cost to $\mathcal{O}\left(N^2\right)$.

present in Hartree-Fock theory and affects the results deleteriously. The inclusion of additional entanglement beyond Hartree-Fock, so-called 'correlation', screens the bare Coulomb interaction. This transforms the interacting electron gas into a gas of weakly interacting Landau quasiparticles i.e. a Fermi liquid [160]. The inclusion of correlation is vital to a quantitatively accurate model of a metal.

There are multiple ways to include correlation in our calculations. One way would be to modify the ansatz in Eq.(2.17) to include additional Slater determinants containing excited single electron orbitals [19]. However, wavefunction methods are challenging to apply to the solid state not least because of the computational cost. Another approach would be to use many-body perturbation theory from a non-interacting reference state [54]. Whilst highly successful in predicting the band-gaps of semiconductors [161], total energies and interatomic forces remain an open research question [62]. This is because these perturbative approaches are non-variational. An alternative approach, density functional theory treats the electron density $n(\mathbf{r})$ as the central quantity of interest. This is fully justified by the Hohenberg-Kohn theorems [46]. Practical approaches to DFT trade some empiricism for quantitative accuracy and computational efficiency. As a result, DFT has become the industry standard method for calculating the mechanical properties of metals. However, DFT is not without fault. In the following subsections, we shall review the formalism of DFT.

2.2.1 The Hohenberg-Kohn Theorems

Hohenberg and Kohn [46] proved a pair of theorems which built upon the previous work of Thomas, Fermi and Dirac [162–164]. The first theorem shows that there exists a unique mapping from the ground state density $n_0(\mathbf{r})$ to the external potential $V_{\text{en}}(\mathbf{r})$ (up to a constant). As a consequence, the Hamiltonian is also determined (up to a constant energy shift) and so too are the eigenfunctions including excited states.

Hence, all physical properties are determined by the ground state density [14].

The second theorem defines a universal functional for the total energy $E_{\text{tot}}[n]$ in terms of the electron density

$$E_{\text{tot}}[n] = T_{\text{e}}[n] + \int \mathrm{d}\mathbf{r}\; V_{\text{en}}(\mathbf{r})\, n(\mathbf{r}) + E_{\text{ee}}[n] + E_{\text{nn}}, \tag{2.21}$$

$$= F_{\text{HK}}[n] + \int \mathrm{d}\mathbf{r}\; V_{\text{en}}(\mathbf{r})\, n(\mathbf{r}) + E_{\text{nn}} \tag{2.22}$$

where F_{HK} is the universal electron functional which is the same for all electron systems subject to the minimal assumptions of Hohenberg and Kohn. The theorem states that the global minimum of this functional is the exact ground state electron density $n_0(\mathbf{r})$ i.e.

$$\left.\frac{\delta E_{\text{tot}}\left[n(\mathbf{r})\right]}{\delta n(\mathbf{r})}\right|_{n_0(\mathbf{r})} = 0. \tag{2.23}$$

This means that the functional E_{tot} is sufficient to determine the exact ground state electron density [46]. There are two unknown terms in the total energy functional, both of which are contained within the universal electron functional F_{HK}. Firstly, we do not know the precise form for the electron-electron energy functional E_{ee}. However, we know how to write the classical portion as a functional of the density. This is the familiar energy due to the Hartree potential V_{H}. The portion of E_{ee} that we do not know will have terms arising from exchange and correlation. Unsurprisingly, we call it the exchange-correlation functional E_{xc}. Hence,

$$E_{\text{ee}}[n] = \frac{1}{2}\int \mathrm{d}\mathbf{r}\mathrm{d}\mathbf{r}'\; \frac{n(\mathbf{r})\, n(\mathbf{r}')}{|\mathbf{r}-\mathbf{r}'|} + E_{\text{xc}}[n] = E_{\text{H}}[n] + E_{\text{xc}}[n]. \tag{2.24}$$

The other unknown functional is the electron kinetic energy functional $T_{\text{e}}[n]$. In practical DFT calculations, both of these functionals are approximated.

2.2.2 The Kohn-Sham Ansatz

A crucial step towards a practical DFT scheme was given by Kohn and Sham [47] where the interacting electron system is replaced with a soluble non-interacting auxiliary system. It is assumed that the auxiliary system's ground state density is equal to that of the interacting electron system. There is no general proof that it is always possible to find an auxiliary non-interacting system with the same ground state density as the interacting system. However, it is true for the homogenous electron gas and Kohn and Sham [47] proved that it remains true for small deviations from the homogenous electron gas. In addition, there seem to be no significant practical difficulties arising from the lack of a general proof of this statement. The Kohn-Sham ansatz transforms the kinetic energy functional T_{e} to

$$T_{\mathrm{e}}\left[n\left(\mathbf{r}\right)\right] \rightarrow T_{\mathrm{e}}^{\mathrm{s}}\left[n\left(\mathbf{r}\right)\right]. \tag{2.25}$$

where T_e^s is the kinetic energy of the non-interacting auxiliary system and the difference is absorbed into a redefined exchange-correlation energy functional E_{xc}

$$E_{\mathrm{xc}}\left[n\left(\mathbf{r}\right)\right] \rightarrow E_{\mathrm{xc}}\left[n\left(\mathbf{r}\right)\right] + \left(T_{\mathrm{e}}\left[n\left(\mathbf{r}\right)\right] - T_{\mathrm{e}}^{\mathrm{s}}\left[n\left(\mathbf{r}\right)\right]\right). \tag{2.26}$$

Gunnarsson [165] showed that the kinetic energy difference is automatically included in the exchange-correlation function when it is given by the adiabatic variation of the electron-electron interaction (minus the Hartree energy). Furthermore, one can write the exchange-correlation function in terms of the radius of the exchange-correlation hole. That is the small volume of space, carrying an effective positive charge, where electrons are excluded due to exchange and correlation. The auxiliary system can be described by one-electron orbitals, of the kind introduced in Eq.(2.9), whose electron density is given by Eq.(2.15). An effective Schrödinger equation can be found by

variationally minimizing the electron energy functional $E_{\mathrm{e}}[n] = E_{\mathrm{tot}}[n] - E_{\mathrm{nn}}$ with respect to the auxiliary orbitals

$$\frac{\delta E_{\mathrm{e}}}{\delta \psi_{\alpha}^{*}(\mathbf{r})} = \frac{\delta T_{\mathrm{e}}^{\mathrm{s}}}{\delta \psi_{\alpha}^{*}(\mathbf{r})} + \left(\frac{\delta E_{\mathrm{en}}}{\delta n(\mathbf{r})} + \frac{\delta E_{\mathrm{H}}}{\delta n(\mathbf{r})} + \frac{\delta E_{\mathrm{xc}}}{\delta n(\mathbf{r})} - E_{\alpha} \right) \frac{\delta n(\mathbf{r})}{\delta \psi_{\alpha}^{*}(\mathbf{r})} = 0 \tag{2.27}$$

where E_{α} is a Lagrange multiplier that guarantees orthonormality. This leads to a Schrödinger equation of the same form as Eq.(2.13) albeit with a different effective potential

$$V_{\mathrm{eff}}^{\mathrm{KS}}(\mathbf{r}) = V_{\mathrm{en}}(\mathbf{r}) + V_{\mathrm{H}}(\mathbf{r}) + V_{\mathrm{xc}}(\mathbf{r}). \tag{2.28}$$

2.2.3 The Local Density Approximation

Until now, we haven't given a precise form for the exchange-correlation functional. If $n(\mathbf{r})$ is sufficiently slowly varying, the exchange-correlation contribution can be written as

$$E_{\mathrm{xc}}^{\mathrm{LDA}}[n(\mathbf{r})] = \int \mathrm{d}\mathbf{r}\ \varepsilon_{\mathrm{xc}}(n(\mathbf{r}))\, n(\mathbf{r}), \tag{2.29}$$

where $\varepsilon_{\mathrm{xc}}(n)$ is the total exchange-correlation energy per electron of a homogenous electron gas with uniform density n. This is known as the Local Density Approximation (LDA) [47]. As we saw in the in the Hartree-Fock approximation, the true exchange-correlation potential will be non-local. Thus, it is perhaps surprising that the LDA gives a quantitatively accurate picture of a metal.

There are many different parameterisations of the LDA exchange-correlation energy. In general, we split it up into an explicit exchange part and an explicit correlation

part

$$\varepsilon_{\mathrm{xc}}(n) = \varepsilon_{\mathrm{x}}(n) + \varepsilon_{\mathrm{c}}(n). \tag{2.30}$$

Since Hartree-Fock is exactly solvable for the homogenous electron gas, the exchange energy is known analytically

$$\varepsilon_{\mathrm{x}}(n) = -\frac{3}{2}e^2\left(\frac{3n}{8\pi}\right)^{1/3}. \tag{2.31}$$

On the other hand, the correlation energy is not known analytically. Ceperley and Alder [32] calculated the correlation energy numerically for the homogenous electron gas using accurate QMC over a wide range of electron densities (including electron densities that correspond to a metal at ambient pressures and temperatures). A wide variety of functional forms have been fit to the Ceperley-Alder data [166–168]. A couple of these LDA correlation functions are plotted in Fig.(2.1) alongside the earlier LDA correlation function of Hedin and Lundqvist [169] that was fitted to data from many-body perturbation theory. In general, we will use the Vosko-Wilk-Nusair (VWN) [167] form in the development of interatomic potentials. Note that, at metallic densities, the exchange energy is much larger than the correlation energy.

In the LDA, the Kohn-Sham effective potential $V_{\mathrm{eff}}^{\mathrm{KS}}$ is explicitly given by

$$V_{\mathrm{KS}}(\mathbf{r}) = -\sum_i \frac{Z_a e^2}{|\mathbf{r}-\mathbf{R}_i|} + e^2\int \mathrm{d}\mathbf{r}'\,\frac{n(\mathbf{r}')}{|\mathbf{r}-\mathbf{r}'|} + \mu_{\mathrm{xc}}(n(\mathbf{r})) \tag{2.32}$$

where $\mu_{\mathrm{xc}} = \mathrm{d}(n\varepsilon_{\mathrm{xc}})/\mathrm{d}n$ is the exchange-correlation potential. Once the Schrödinger equation is solved, the total energy E_{tot} may be constructed as

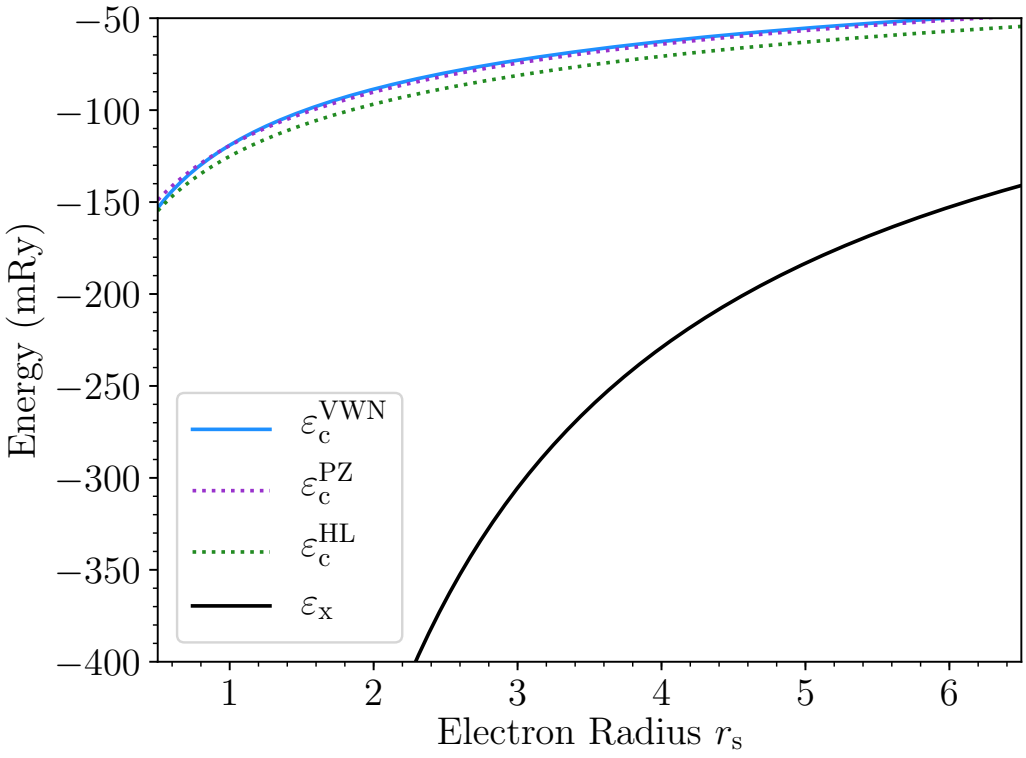

Fig. 2.1: Different parameterisations of the correlation energy ε_c. The Hedin-Lundqvist (HL) parameterisation is the oldest and was fit to data calculated from many-body perturbation theory [169]. The other parameterisations, Perdew-Zunger (PZ) [166] and Vosko-Wilk-Nusair (VWN) [167], are fitted to the accurate, Quantum Monte Carlo calculations of Ceperley and Alder [32]. These parameterisations largely agree and are considered to be a closer representation of the true correlation energy of the homogenous electron gas. For comparison, these correlation energies are plotted along side the analytic exchange energy of the homogenous electron gas ε_x.

$$E_{\text{tot}} = \frac{1}{2}{\sum_{ij}}' \frac{(Z_a e)^2}{|\mathbf{R}_i - \mathbf{R}_j|} + \sum_\alpha E_\alpha - \frac{e^2}{2}\int \mathrm{d}\mathbf{r}\mathrm{d}\mathbf{r}' \, \frac{n(\mathbf{r})\, n(\mathbf{r}')}{|\mathbf{r} - \mathbf{r}'|} + \int \mathrm{d}\mathbf{r} \; \left[\varepsilon_{\text{xc}}(n(\mathbf{r})) - \mu_{\text{xc}}(n(\mathbf{r}))\right] n(\mathbf{r}) \,. \tag{2.33}$$

The first term is the Coulomb interaction between charged nuclei while the second term is a sum over occupied one-electron orbital energies for the auxiliary system. The third

term removes the classical electron-electron interaction which is doubly counted in the second term. Likewise the final term guarantees that the exchange-correlation energy is correct. Furthermore, if we make a small error in the exact ground state electron density Δn then, since the functional derivative of E_{tot} with respect to the electron density is zero, the error in E_{tot} is proportional to $(\Delta n)^2$.

2.2.4 Exchange & Correlation Beyond the LDA

Whilst the LDA is a reasonable approximation, it does systematically underestimate the equilibrium lattice parameters in metals [170]. This is one of the primary reasons for the roughly 10% discrepancy between LDA elastic constants and experiment. One method to go beyond the LDA is to add derivatives of the density into the exchange-correlation function [64, 65]

$$E_{\text{xc}}^{\text{GGA}}\left[n\left(\mathbf{r}\right)\right] = \int \mathrm{d}\mathbf{r}\; n\left(\mathbf{r}\right) f_{\text{xc}}\left(\mathbf{r}\right) \tag{2.34}$$

where f_{xc} is some unknown function of $n\left(\mathbf{r}\right)$ and $\nabla n\left(\mathbf{r}\right)$, analogous to ε_{xc}. There have been a number of different proposals for f_{xc} [64, 170]. A ubiquitous parameterisations of f_{xc} was given by Perdew, Burke and Ernzerhof (PBE) [65, 170] whereby

$$f_{\text{xc}}^{\text{PBE}}\left[n, \nabla n\right] = \varepsilon_{\text{x}} F_{\text{xc}}\left(r_s, s\right) \tag{2.35}$$

with $r_s = (3/4\pi n)^{1/3}$ as the electron radius and $s = |\nabla n|/2k_F n$. The use of the GGA within the context of the Generalised Pseudopotential Theory (GPT) [99, 115, 116] is restricted to transition and actinide metals, thanks to the presence of localised d- and f-states.

For the valence s- and p-states, the GPT uses many-body perturbation theory of the interacting electron gas to go beyond the LDA. Consider a perturbation in the

electron density $\delta n(q)$, the resulting change in the potential [160] is given by

$$\delta V\left(q\right)=\frac{4\pi e^{2}}{q^{2}}\left[1-G\left(q\right)\right]\delta n\left(q\right), \tag{2.36}$$

where $G(q)$ is a static local-field correction which captures the effect of exchange and correlation on the potential. If there is no exchange and correlation $G(q) = 0$ and Eq.(2.36) is just the Fourier transform of the Coulomb interaction. The earliest and simplest representation of the local field correction was given by Hubbard [171], $G(q) = q^2/(q^2+k_F^2)$ which is zero in the $q \to 0$ limit but leads to negative values of the electron-electron pair correlation function [172]. A representation for the local-field correction can be written in terms of the LDA exchange-correlation potential [173]

$$G\left(q\right)=-\left(\frac{q^{2}}{4\pi e^{2}}\right)\frac{\mathrm{d}\mu_{\mathrm{xc}}\left(n\right)}{\mathrm{d}n}. \tag{2.37}$$

The LDA local field correction does not generally obey the limits composed by the compressibility sum rule, which relates the curvature of $G(q)$ to the bulk modulus of the homogenous electron gas in the $q \to 0$ limit [13]. More troublesome for the LDA, is the divergent behaviour in the short wavelength limit $q \to \infty$ (as seen in Fig.(2.2)). This limit has been shown to be exactly

$$\lim_{q\to\infty}G\left(q\right)=1-g\left(r=0\right) \tag{2.38}$$

where g is the electron-electron pair correlation function [172, 174, 175]. Several effective representations of the local-field correction $G(q)$ have been proposed which do obey the correct limits [173, 176, 177]. We will use exclusively the local-field correction proposed by Ichimaru and Utsumi referenced to the correlation energy of Vosko, Wilk and Nusair [167] which itself is a fit to highly-accurate QMC data.

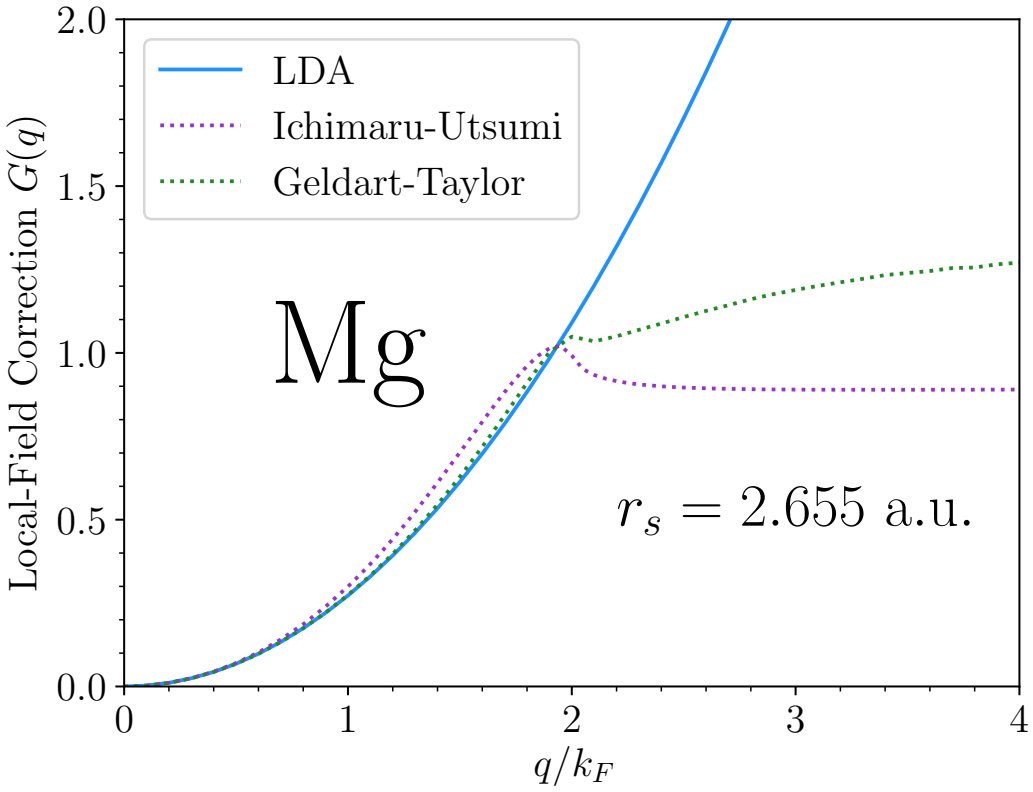

Fig. 2.2: The LDA local-field correction $G(q)$ is plotted for Mg at the equilibrium atomic volume $\Omega = 156.8$ a.u. in the Vosko-Wilk-Nusair representation [167]. It is plotted next to the local-field corrections given by Geldart and Taylor [176], referenced to the correlation energy of Hedin and Lundqvist [169], and Ichimaru and Utsumi, [177] referenced to the correlation energy of Vosko-Wilk-Nusair [167]. The LDA local-field correction diverges as $q \to \infty$.

2.3 Pseudopotentials

The only quantities left to calculate in Eq.(2.33) are the Kohn-Sham eigenvalues $\{E_\alpha\}$ and there are number of ways to do this calculation [75, 80]. There is a considerable amount of freedom in our choice of method. Fortunately, we have the competing interests of transferability and scalability to narrow the search. Following Harrison [178–180], we will use perturbation theory. Naïvely we might take the Kohn-Sham potential V_{KS} to be a perturbation from the free electron gas. The eigenstates of the free-electron gas are known; they are plane waves. However, we immediately run into

pathological problems. Firstly, the perturbative expansion is divergent [94] due to the large discrepancy between the Fermi energy and the energy of the bound states of V_{KS}. This problem is resolved through the introduction of a pseudopotential. Secondly, an expansion of the wavefunctions in terms of plane waves is only reasonable for the valence electrons outside of the inner core regions. We partition the valence and core electrons using the small core approximation [93].

2.3.1 Small Core Approximation

The electrons in DFT can be separated into two broad groups. Firstly, there are localized electrons confined to a relatively small inner-core region whose one-electron eigenfunctions $\psi_\alpha = \phi_c$ are approximately equal to those of an isolated atom. These electrons move rigidly with the nuclei. Secondly, there are valence electrons whose eigenfunctions $\psi_\alpha = \psi_{\mathbf{k}}$ are concentrated in the interstitial regions. Under the small core approximation [93], we treat these two classes of electrons separately. This separation is not always easy or possible. For the simple metals of primary interest in this thesis, this distinction is sharp and the small-core approximation gives rise to negligible errors. The simple metal core is defined to be the last complete noble gas configuration. The valence electrons are the remaining Z electrons which can be read off from their periodic table group. On the other hand, the small-core approximation yields non-negligible errors for the noble or transition metals. The filled or partially-filled d bands overlap significantly with neighbouring cores and cannot be simply incorporated into the valence. The core eigenfunctions obey the following Schrödinger equation

$$\left[-\frac{\hbar^2}{2m}\nabla^2 + V_{\mathrm{KS}}\left(\mathbf{r}\right)\right]\phi_c\left(\mathbf{r}\right) = E_c\phi_c\left(\mathbf{r}\right) \tag{2.39}$$

where E_c is the eigenvalue of the core state c. Whilst the core eigenfunctions ϕ_c resemble those of the free atom very closely, the eigenvalues E_c are shifted. The

valence eigenstates $\psi_{\mathbf{k}}$ obey the following Schrödinger equation

$$\left[-\frac{\hbar^2}{2m}\nabla^2 + V_{\mathrm{KS}}(\mathbf{r})\right]\psi_{\mathbf{k}}(\mathbf{r}) = E_{\mathbf{k}}\psi_{\mathbf{k}}(\mathbf{r}) \tag{2.40}$$

where $\mathbf{k}$ is a wavevector and $\{\psi_{\mathbf{k}}\}$ are orthogonal to the core electrons $\{\phi_c\}$. The valence orbitals $\psi_{\mathbf{k}}$ are Bloch wavefunctions and thus can be written as

$$\psi_{\mathbf{k}}(\mathbf{r}) = e^{i\mathbf{k}\cdot\mathbf{r}}u_{\mathbf{k}}(\mathbf{r}) \tag{2.41}$$

where u is a function with the same periodicity as the crystal. Whilst we have written down two separate Schrödinger equations in Eq.(2.39) and Eq.(2.40), they are just different solutions to the same equation. The Kohn-Sham potential V_{KS} depends on the total electron density $n(\mathbf{r})$. We split the total electron density into an inner core density and a valence density

$$n(\mathbf{r}) = n_{\mathrm{val}}(\mathbf{r}) + \sum_i n_{\mathrm{core}}(\mathbf{r} - \mathbf{R}_i) \tag{2.42}$$

where n_{val} is the valence electron density and n_{core} is the core electron density centred on a site i. In terms of the one-electron valence orbitals, n_{val} is given by

$$n_{\mathrm{val}}(\mathbf{r}) = 2\sum_{\mathbf{k}} f_{\mathbf{k}}\psi^*_{\mathbf{k}}(\mathbf{r})\,\psi_{\mathbf{k}}(\mathbf{r}) \tag{2.43}$$

where $f_{\mathbf{k}}$ is the Fermi-Dirac distribution, ensuring that the sum is over the occupied orbitals only. The core density can be written as

$$n_{\mathrm{core}}(\mathbf{r} - \mathbf{R}_i) \equiv n_i = 2\sum_c \phi^*_c(\mathbf{r} - \mathbf{R}_i)\,\phi_c(\mathbf{r} - \mathbf{R}_i). \tag{2.44}$$

We then factorise the Kohn-Sham potential V_{KS} along the following lines

$$V_{\mathrm{KS}}(\mathbf{r}) = V_{\mathrm{ion}}(\mathbf{r}) + V_{\mathrm{val}}(\mathbf{r}) + \mu_{\mathrm{xc}}(n_{\mathrm{val}}). \tag{2.45}$$

The valence potential V_{val} is simply the Hartree potential for the valence electron density

$$V_{\mathrm{val}}(\mathbf{r}) = e^2 \int \mathrm{d}\mathbf{r}' \, \frac{n_{\mathrm{val}}(\mathbf{r}')}{|\mathbf{r} - \mathbf{r}'|} \tag{2.46}$$

and V_{ion} is the ionic contribution to the Kohn-Sham potential

$$V_{\mathrm{ion}}(\mathbf{r}) = \sum_i \left[-\frac{Z_a e^2}{|\mathbf{r} - \mathbf{R}_i|} + \mu^*_{\mathrm{xc}}(n_i) + v_{\mathrm{core}}(\mathbf{r} - \mathbf{R}_i) \right]. \tag{2.47}$$

The first term of the ionic potential V_{ion} is the external potential due to the ions and the final term is the Hartree potential due to the core electron density about the site i. In addition, we have also defined a new potential μ^*_{xc} localised about the site i which is the finite difference

$$\mu^*_{\mathrm{xc}}(n_i) = \mu_{\mathrm{xc}}(n_i + n_{\mathrm{val}}) - \mu_{\mathrm{xc}}(n_{\mathrm{val}}). \tag{2.48}$$

This finite difference appears as the contribution of atom i in the first term of a cluster expansion which is given in general by

$$\begin{aligned} \mu_{\mathrm{xc}}(n) = \mu_{\mathrm{xc}}(n_{\mathrm{val}}) &+ \sum_i \mu^*_{\mathrm{xc}}(n_i) \\ &+ \frac{1}{2} {\sum_{ij}}' \left[\mu^*_{\mathrm{xc}}(n_i + n_j) - \mu^*_{\mathrm{xc}}(n_i) - \mu^*_{\mathrm{xc}}(n_j) \right] + \cdots \end{aligned} \tag{2.49}$$

This was introduced so as to avoid the need for derivatives to express the total exchange-correlation potential in terms of contributions from the valence and inner-

core. If the cores do not overlap, which they don't under the small-core approximation (Sec. 2.3.1), then the right hand side can be truncated at linear order in the core densities n_i. In practice, it is usually sufficient to replace n_{val} with the uniform valence electron density n_{unif} [115, 181]. The total energy in Eq.(2.33) may be partitioned into an energy E_{core} from the $(Z_a - Z)$ core electrons and a binding energy from the valence electrons E_{bind}. In addition, there is further valence-core overlap energy $E_{\text{val-core}}$ which arises from the residual dependence on the valence and core electron density due to the nonlinear nature of μ_{xc}. Thus, we may write the energy per atom as

$$\frac{E_{\text{tot}}}{N} = E_{\text{bind}} + E_{\text{core}} + E_{\text{val-core}} \tag{2.50}$$

where the total valence binding energy can be written as

$$\begin{aligned} NE_{\text{bind}} = \frac{1}{2}{\sum_{ij}}' \frac{(Ze)^2}{|\mathbf{R}_i - \mathbf{R}_j|} + 2\sum_{\mathbf{k}} E_{\mathbf{k}} - \frac{1}{2}\int \mathrm{d}\mathbf{r}\; n_{\text{val}}(\mathbf{r})\, V_{\text{val}}(\mathbf{r}) \\ + \int \mathrm{d}\mathbf{r}\; n_{\text{val}}(\mathbf{r}) \left[\varepsilon_{\text{xc}}(n_{\text{val}}) - \mu_{\text{xc}}(n_{\text{val}})\right]. \end{aligned} \tag{2.51}$$

Within the small-core approximation, the core energy E_{core} and valence-core overlap energy $E_{\text{val-core}}$ are the same in the metal and in the free atom. Hence, it is sensible to work with the cohesive energy E_{coh}

$$E_{\text{coh}} = \frac{1}{N}E_{\text{tot}} - E_{\text{tot}}^{\text{atom}} = E_{\text{bind}} - E_{\text{bind}}^{\text{atom}} \tag{2.52}$$

where $E_{\text{bind}}^{\text{atom}}$ is the valence electron binding energy in the free atom and can be calculated within LDA Kohn-Sham DFT [99]. In any case, for a fixed valence occupation Z, as in the simple metal, this quantity will be a constant.

2.3.2 The Pseudopotential Transformation

To evaluate the binding energy in Eq.(2.51), and hence the cohesive energy E_{coh} up to a constant, two unknowns need to be calculated: the band-energy $E_{\mathbf{k}}$ and the valence electron density n_{val}. The following Schrödinger equation needs to be solved

$$(T + V)\,|\psi_{\mathbf{k}}\rangle = E_{\mathbf{k}}\,|\psi_{\mathbf{k}}\rangle \tag{2.53}$$

where T is the one-electron kinetic energy operator and V is the Kohn-Sham potential defined in Eq.(2.45). The one-electron kinetic energy operator T has plane wave eigenvectors with energy $\varepsilon_{\mathbf{k}}$. We can replace V by a weaker pseudopotential W with no bound core states. The condition on the pseudopotential transformation $V \to W$ is that the eigenvalue $E_{\mathbf{k}}$ must be unchanged. This condition does not lead to a unique pseudopotential transformation. Whilst the eigenvalues are invariant, the true valence wavefunctions $\psi_{\mathbf{k}}$ are replaced by pseudowavefunctions $\phi_{\mathbf{k}}$. This gives us a new Schrödinger equation

$$(T + W)\,|\phi_{\mathbf{k}}\rangle = E_{\mathbf{k}}\,|\phi_{\mathbf{k}}\rangle\,. \tag{2.54}$$

The weakness of the pseudopotential W results from the valence s and p electrons being excluded from the inner-core region where V is strong (provided the the pseudopotential does not conserve the norm of the wavefunction). The non-uniqueness of the pseudopotential transformation allows us to choose a transformation which yields smooth and nodeless pseudowavefunctions (see Fig.(2.3)).

The first pseudopotential transformation was discovered by Phillips, Kleinman [182] and Antoncik [183, 184] (PKA). A more general transformation was subsequently

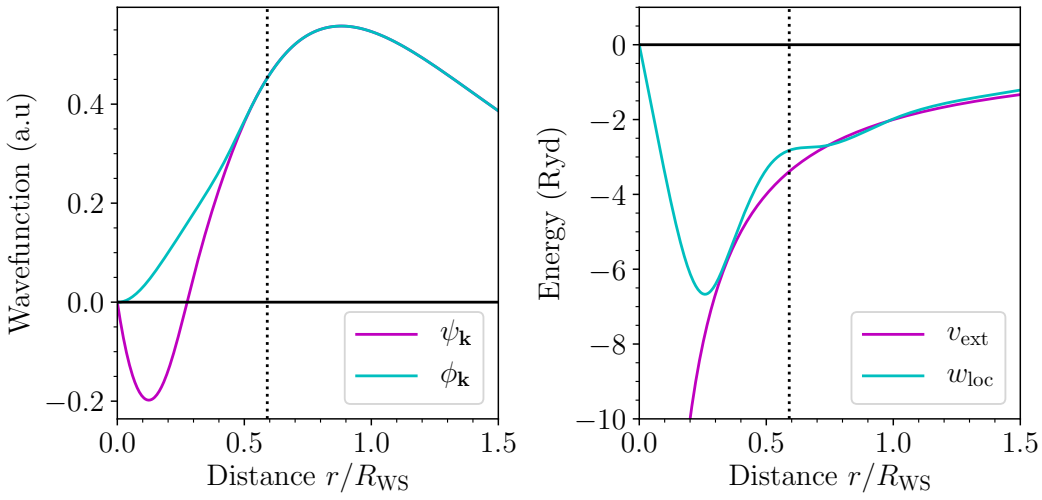

Fig. 2.3: The pseudopotential transformation can be chosen such that the pseudowavefunction is smooth and nodeless. The pseudowavefunction $\phi_{\mathbf{k}}$ (left) is plotted for a valence aluminium $3p$ state relative to the 'true' wavefunction $\psi_{\mathbf{k}}$ from Kohn-Sham DFT. The pseudopotential w_{loc} (right) is weaker than the bare-ion Coulomb potential v_{ext}. Specifically, w_{loc} is the local part of the total atomic pseudopotential i.e. $w = \sum_{lm} w_{\mathrm{loc}}(r) |Y_{lm}\rangle\langle Y_{lm}|$.

given by Austin, Heine and Sham (AHS) [185]. Explicitly this takes the form

$$W = V + \sum_{i,c} \left|\phi_c^i\right\rangle \left\langle\phi_c^i\right| O_{\mathbf{k}} \tag{2.55}$$

where $|\phi_c^i\rangle$ is the core state c centred on site i and $O_{\mathbf{k}}$ is an arbitrary operator which may or may not depend on the state $\mathbf{k}$. The operator $O_{\mathbf{k}}$ can be chosen to produce the smoothest possible pseudowavefunctions. For our purposes, this operator is taken to be close to the PKA choice $O_{\mathbf{k}} = -V_{\mathbf{k}}$. This can be neatly summarised as

$$W = (\mathbf{1} - P_c)\, V, \tag{2.56}$$

where P_c is the inner-core projection operator

$$P_c = \sum_{i,c} \left|\phi_c^i\right\rangle \left\langle\phi_c^i\right|. \tag{2.57}$$

In the core regions, where the core orbitals form an almost complete basis set $P_c \approx \mathbf{1}$, there is near total cancellation of the true potential V. Outside the inner-core, the projection operator is the null operator and $W = V$. The AHS pseudopotential is generally non-Hermitian

$$\langle \phi_{\mathbf{k}'} | W | \phi_{\mathbf{k}} \rangle \neq \langle \phi_{\mathbf{k}} | W | \phi_{\mathbf{k}'} \rangle^* \tag{2.58}$$

for non-trivial $O_{\mathbf{k}}$. The plane wave matrix elements of W are given by

$$\langle \mathbf{k}' | W | \mathbf{k} \rangle = \langle \mathbf{k}' | V | \mathbf{k} \rangle + \sum_{i,c} (\varepsilon_{\mathbf{k}} - E_c) \langle \mathbf{k}' | \phi_c^i \rangle \langle \phi_c^i | \mathbf{k} \rangle \tag{2.59}$$

which we find by inserting $V = H - T$ into the expression for the AHS pseudopotential. The total pseudopotential can then be formed analogously to Eq.(2.45) by adding in the valence and exchange-correlation potentials

$$W(\mathbf{r}) = W_{\text{ion}}(\mathbf{r}) + V_{\text{val}}(\mathbf{r}) + \mu_{\text{xc}}(n_{\text{val}}(\mathbf{r})) \tag{2.60}$$

with W_{ion} being a sum of weak ionic pseudopotentials from each site

$$W_{\text{ion}} = \sum_i w_{\text{ion}}^i. \tag{2.61}$$

The arbitrariness of the operator $O_{\mathbf{k}}$ means that the core orbitals do not need to explicitly appear in the pseudopotential formulation provided that the scattering properties are preserved. These are the so-called model pseudopotentials (MP) introduced by Heine and Abarenkov [186]. Explicitly, we expand in an angular momentum basis

$$w_{\text{ion}} = \sum_l w_l |Y_{lm}\rangle \langle Y_{lm}| \tag{2.62}$$

with the position matrix elements of $\langle \mathbf{r}'|w_l|\mathbf{r}\rangle = w_l(r,E)\delta(\mathbf{r}-\mathbf{r}')$. The quantity $w_l(r,E)$ contains a couple of parameters to be determined through optimisation. In general, it is given by

$$w_l(r,E) = \begin{cases} -A_l(r,E) & r < R_l \\ -\frac{Ze^2}{r} & r \geq R_l \end{cases} . \tag{2.63}$$

In the limit that $A_l \to 0$ and $R_l \to R_c$, we recover the Ashcroft empty-core pseudopotential [45]. MPs are widely used in modern day electronic structure calculations [187, 188]. The GPT, however, uses a non-local energy-dependent AHS pseudopotential. In the derivation of the GPT potential in the next section, we shall take the pseudopotential to be local for simplicity and add the corrections in retroactively.

2.3.3 Charge Density Considerations

The major benefit of AHS pseudopotentials for developing quantum-based interatomic potentials, such as the GPT, is that there exists a unique transformation between the pseudowavefunctions $\{\phi_{\mathbf{k}}\}$ and the 'true' wavefunctions $\{\psi_{\mathbf{k}}\}$ [93]

$$|\psi_{\mathbf{k}}\rangle = C_{\mathbf{k}}(\mathbf{1} - P_c)|\phi_{\mathbf{k}}\rangle \tag{2.64}$$

This is effectively a Gram-Schmidt orthogonalisation procedure multiplied by a normalisation constant $C_{\mathbf{k}}$. A pseudopotential for which $C_{\mathbf{k}} = 1$ is said to be norm-conserving [187]. A norm-conserving pseudopotential produces pseudowavefunctions with the property that the integrated charge, inside the core radius R_c, matches that of the 'true' wavefunction

$$Q_{\mathbf{k}} = \int_0^{R_c} \int r^2 \mathrm{d}r\mathrm{d}\Omega \ |\phi_{\mathbf{k}}(\mathbf{r})|^2 = \int_0^{R_c} \int r^2 \mathrm{d}r\mathrm{d}\Omega \ |\psi_{\mathbf{k}}(\mathbf{r})|^2 . \tag{2.65}$$

where Ω is the solid angle. Whilst norm-conservation is a useful property for DFT practitioners, where norm-conservation means that the diagonalisation of $\mathcal{H}$ is an ordinary eigenvalue problem, it is non-essential for our purposes. Norm-conserving pseudopotentials tend to be MPs which means that there is no longer an exact transformation from the pseudowavefunctions to the 'true' wavefunctions. This will mean that the valence electron density n_{val} will have a missing term called the orthogonalisation hole density n_{oh}. To see this explicitly, we write the valence pseudodensity $n_{\text{val}}^{\text{ps}}$ as

$$n_{\text{val}}^{\text{ps}}(\mathbf{r}) = 2\sum_{\mathbf{k}} f_{\mathbf{k}}\phi_{\mathbf{k}}^{*}(\mathbf{r})\,\phi_{\mathbf{k}}(\mathbf{r})\,. \tag{2.66}$$

If the pseudopotential is norm-conserving, the valence pseudodensity $n_{\text{val}}^{\text{ps}}$ will be precisely the same as the 'true' valence electron density n_{val} outside of the inner core region. However, inside the inner core region, there is no way of determining the 'true' valence electron n_{val} density from the valence pseudodensity $n_{\text{val}}^{\text{ps}}$. For an AHS potential, we can use Eq.(2.64) to find

$$n_{\text{val}}(\mathbf{r}) = n_{\text{val}}^{\text{ps}}(\mathbf{r}) + \delta n_{\text{oh}}(\mathbf{r}) \tag{2.67}$$

where δn_{oh} is the orthogonalisation hole correction. In second-order pseudopotential perturbation theory, the correction has the form [99]

$$\delta n_{\text{oh}}^{c}(\mathbf{r}) = \left(\frac{Z^{*}}{Z} - 1\right) n_{\text{unif}} + \sum_{i} n_{\text{oh}}(\mathbf{r} - \mathbf{R}_{i}) \tag{2.68}$$

where Z^{*} is an effective valence occupation ($Z^{*} \geq Z$) and n_{oh} is a localized hole density centred on a particular atom. For a simple metal, n_{oh} is confined to the inner core region of the atom at site i. Both Z^{*} and n_{oh} depend on the properties of the

pseudopotential. For an non-local, energy-dependent AHS pseudopotential, we have

$$Z^* = Z + \int \mathrm{d}\mathbf{k}\ f_{\mathbf{k}} \langle \mathbf{k}|P_c|\mathbf{k}\rangle \tag{2.69}$$

and

$$n_{\mathrm{oh}}(\mathbf{r}) = \frac{2\Omega}{(2\pi)^3} \int \mathrm{d}\mathbf{k}\ f_{\mathbf{k}} \left[\langle \mathbf{r}|P_c|\mathbf{k}\rangle\langle \mathbf{k}|P_c|\mathbf{r}\rangle - (\langle \mathbf{r}|P_c|\mathbf{k}\rangle\langle \mathbf{k}|\mathbf{r}\rangle + \text{c.c.})\right]. \tag{2.70}$$

The orthogonalisation hole density represents a depletion of the charge in the inner-core region whilst adds charge to the valence. Integrating over the entirety of space yields

$$\int \mathrm{d}\mathbf{r}\ \delta n_{\mathrm{oh}}(\mathbf{r}) = 0. \tag{2.71}$$

2.3.4 Perturbation Theory

The pseudo-Schrödinger equation in Eq.(2.54) can be solved by matrix diagonalisation which is the conventional approach to DFT. However, due to the computational cost being $\mathcal{O}(N^3)$ there is a computational bottleneck. An alternative approach would be to approximate the pseudo-wavefunctions using second-order perturbation theory in the pseudopotential W. As we shall see in the next section, an approach based on second-order pseudopotential perturbation theory leads to a pairwise interaction for a simple metal [189, 190]. Furthermore, we assume that the pseudopotential W is sufficiently weak to expect good physical convergence at second-order. The nodeless pseudo-wavefunction $\phi_{\mathbf{k}}$ can be thought of as a small perturbation away from a plane wave with wavevector $\mathbf{k}$. With a non-local AHS pseudopotential, it is clear from Eq.(2.64) that this is equivalent to expanding the 'true' valence wavefunction in orthogonalised

plane waves (OPW) [191]. For a particular **k**-point, we expand the energy eigenvalue $E_{\mathbf{k}}$ to second order

$$E_{\mathbf{k}} = \varepsilon_{\mathbf{k}} + \langle \mathbf{k}|W|\mathbf{k}\rangle + {\sum_{\mathbf{q}}}' \frac{\langle \mathbf{k}|W|\mathbf{k}+\mathbf{q}\rangle\langle \mathbf{k}+\mathbf{q}|W|\mathbf{k}\rangle}{\varepsilon_{\mathbf{k}} - \varepsilon_{\mathbf{k}+\mathbf{q}}} \tag{2.72}$$

where the checked sum refers to the omission of the $\mathbf{q} = 0$ plane wave. This expression can be simplified by assuming that the total pseudopotential W can be written as a sum of non-local atomic pseudopotentials. As a result, we may write

$$W(\mathbf{r}, \mathbf{r}') = \sum_i w(\mathbf{r} - \mathbf{R}_i, \mathbf{r}' - \mathbf{R}_i) \tag{2.73}$$

in position representation. The plane-wave matrix elements in Eq.(2.72) can be factorised into structural and atomic components. For a general plane wave matrix element of W, we have

$$\langle \mathbf{k}+\mathbf{q}|W|\mathbf{k}\rangle = \frac{1}{N\Omega}\int \mathrm{d}\mathbf{r}\mathrm{d}\mathbf{r}'\; e^{-i(\mathbf{k}+\mathbf{q})\cdot\mathbf{r}} \sum_i w(\mathbf{r} - \mathbf{R}_i, \mathbf{r}' - \mathbf{R}_i)\, e^{i\mathbf{k}\cdot\mathbf{r}'}, \tag{2.74}$$

by inserting the completeness relation twice. Next, we translate the co-ordinates by $\mathbf{r} \to \mathbf{r} + \mathbf{R}_i$ and $\mathbf{r} \to \mathbf{r} + \mathbf{R}'_i$. This yields

$$\begin{aligned}\langle \mathbf{k}+\mathbf{q}|W|\mathbf{k}\rangle &= \left(\frac{1}{N}\sum_i e^{-i\mathbf{q}\cdot\mathbf{R}_i}\right)\left(\frac{1}{\Omega}\int \mathrm{d}\mathbf{r}\mathrm{d}\mathbf{r}'\; e^{-i(\mathbf{k}+\mathbf{q})\cdot\mathbf{r}} w(\mathbf{r}, \mathbf{r}')\, e^{i\mathbf{k}\cdot\mathbf{r}'}\right), \\ &= S(\mathbf{q})\,\langle \mathbf{k}+\mathbf{q}|w|\mathbf{k}\rangle \end{aligned} \tag{2.75}$$

where $S(\mathbf{q})$ is the structure factor that encodes all the structural information. This expression is general and can be applied to both perfect and defective crystals. Inserting

this result into the perturbative expansion in Eq.(2.72) yields

$$E_{\mathbf{k}} = \varepsilon_{\mathbf{k}} + \langle \mathbf{k}|w|\mathbf{k}\rangle + \sum_{\mathbf{q}}{}' \left|S\left(\mathbf{q}\right)\right|^2 \frac{\langle \mathbf{k}|w|\mathbf{k}+\mathbf{q}\rangle\langle \mathbf{k}+\mathbf{q}|w|\mathbf{k}\rangle}{\varepsilon_{\mathbf{k}} - \varepsilon_{\mathbf{k}+\mathbf{q}}} \tag{2.76}$$

which is the familiar expression first given by Harrison [178, 179]. The pseudowavefunctions can be written as

$$|\phi_{\mathbf{k}}\rangle = |\mathbf{k}\rangle + \sum_{\mathbf{q}}{}' a_{\mathbf{k}+\mathbf{q}} \left|\mathbf{k}+\mathbf{q}\right\rangle . \tag{2.77}$$

The set of co-efficients $a_{\mathbf{k}+\mathbf{q}}$ can be found via first-order perturbation theory [93]. These co-efficients are given by

$$a_{\mathbf{k}+\mathbf{q}} = \frac{\langle \mathbf{k}+\mathbf{q}|W|\mathbf{k}\rangle}{\varepsilon_{\mathbf{k}} - \varepsilon_{\mathbf{k}+\mathbf{q}}} = S\left(\mathbf{q}\right) \frac{\langle \mathbf{k}+\mathbf{q}|w|\mathbf{k}\rangle}{\varepsilon_{\mathbf{k}} - \varepsilon_{\mathbf{k}+\mathbf{q}}}. \tag{2.78}$$

The density operator for the pseudo-wavefunctions can be written as

$$\hat{n}^{\mathrm{ps}}_{\mathrm{val}} = 2\sum_{\mathbf{k}} \left[\left|\mathbf{k}\right\rangle \left\langle \mathbf{k}\right| + \sum_{\mathbf{q}}{}' \left(a_{\mathbf{k}+\mathbf{q}} \left|\mathbf{k}+\mathbf{q}\right\rangle \left\langle \mathbf{k}\right| + a^*_{\mathbf{k}+\mathbf{q}} \left|\mathbf{k}\right\rangle \left\langle \mathbf{k}+\mathbf{q}\right| \right) \right], \tag{2.79}$$

where we have retained only terms linear in the co-efficients $a_{\mathbf{k}+\mathbf{q}}$. The valence electron density n_{val} is the diagonal part of the density operator in position representation

$$n^{\mathrm{ps}}_{\mathrm{val}}\left(\mathbf{r}\right) = \frac{2}{N\Omega} \sum_{\mathbf{k}} \left[1 + \sum_{\mathbf{q}}{}' \left(a_{\mathbf{k}+\mathbf{q}} e^{i\mathbf{q}\cdot\mathbf{r}} + a^*_{\mathbf{k}+\mathbf{q}} e^{-i\mathbf{q}\cdot\mathbf{r}} \right) \right]. \tag{2.80}$$

The first term in the sum can be replaced by $n_{\mathrm{unif}} = Z/\Omega$ since there are ZN states (including spin). Observing the form of Eq.(2.74), we conclude that $a^*_{\mathbf{k}+\mathbf{q}} = a_{-\mathbf{k}-\mathbf{q}}$. This is to be expected from time-reversal symmetry. Since the sum is over the complete set of $\mathbf{q}$- and $\mathbf{k}$-points i.e. it includes the points $\{\mathbf{k}, \mathbf{q}\}$ as well as $\{-\mathbf{k}, -\mathbf{q}\}$, these two

sums are equal. Putting all of these terms together gives us the result

$$n_{\mathrm{val}}^{\mathrm{ps}}(\mathbf{r}) = \frac{Z}{\Omega} + \frac{4}{N\Omega}\sum_{\mathbf{k}}\sum_{\mathbf{q}}{}' S(\mathbf{q})\frac{\langle \mathbf{k}+\mathbf{q}|\, w\, |\mathbf{k}\rangle}{\varepsilon_{\mathbf{k}} - \varepsilon_{\mathbf{k}+\mathbf{q}}} e^{i\mathbf{q}\cdot\mathbf{r}},$$
$$= n_{\mathrm{unif}} + \delta n_{\mathrm{scr}}(\mathbf{r}). \tag{2.81}$$

We have introduced the screening density δn_{scr} as the first-order correction to the uniform electron density. The screening density is oscillatory and charge-neutral like the orthogonalisation hole density.

There are a couple of things to note about the procedure that we have described above. Firstly, the use of perturbation theory does not restrict us to systems with translational invariance where Bloch's theorem holds. Both the expressions for the valence electron density and band energy are equally applicable to ordered and disordered systems. This is particularly useful for our purposes, namely the mechanical properties of metals. Unfortunately, we may be required to go beyond the simplifying features of second order perturbation theory. This is discussed in Chapter 3. Secondly, we have derived these expressions using non-degenerate perturbation theory. This leads to divergences at Bragg planes in the calculation of the electronic band structure. These divergences are easily removed through the use of degenerate perturbation theory. For calculations of the valence electron density and valence binding energy, these divergences were shown by Harrison [93] to contribute negligible higher order corrections.

2.4 Interatomic Potentials for Simple Metals

In Eq.(2.52), we introduced the cohesive energy E_{coh}. The goal of this section is to prove that E_{coh} for an *sp*-valent metal can be written as the sum of a term dependent

on the atomic volume Ω plus a long-ranged pair potential v_2 [189, 190]

$$E_{\text{coh}}\left(\{\mathbf{R}\},\Omega\right) = E_{\text{vol}}\left(\Omega\right) + \frac{1}{2N}\sum_{ij}{}' v_2\left(R_{ij},\Omega\right). \tag{2.82}$$

The volume term E_{vol} is the largest contribution to the cohesive energy and v_2 is responsible for structural energy differences. In this section, we shall prove that the cohesive energy takes this form and derive analytic expressions for E_{vol} and v_2 using results from the previous sections. All terms in the binding energy are now known in terms of the pseudopotential. There are certain terms that can be seen to be equal and opposite. To proceed, we need to partition all structural and volume components. We will first do this in reciprocal-space and then in real-space. In addition, we will temporarily assume that the pseudopotential is local and then generalise our expressions to the non-local case.

2.4.1 Reciprocal Space Representation

For simplicity, we set the orthogonalisation hole density $\delta n_{\text{oh}} \to 0$. This is equivalent to setting the effective valence occupation to $Z^* = Z$ and $n_{\text{oh}} = 0$ in Eqs.(2.69) and (2.70). Using the perturbative results of the previous section, we can fully evaluate E_{bind} in Eq.(2.51). Recall that the band-structure energy E_{band} is given by

$$E_{\text{band}} = \frac{2}{N}\sum_{\mathbf{k}} f_{\mathbf{k}}\left[\varepsilon_{\mathbf{k}} + \langle\mathbf{k}|w|\mathbf{k}\rangle + \sum_{\mathbf{q}}{}' \left|S\left(\mathbf{q}\right)\right|^2 \frac{\langle\mathbf{k}|w|\mathbf{k}+\mathbf{q}\rangle\langle\mathbf{k}+\mathbf{q}|w|\mathbf{k}\rangle}{\varepsilon_{\mathbf{k}} - \varepsilon_{\mathbf{k}+\mathbf{q}}}\right], \tag{2.83}$$

where $f_{\mathbf{k}}$ is the Fermi-Dirac distribution. Given that we restrict our analysis to zero temperature, the Fermi-Dirac distribution is a step function. The first term in our expansion can be evaluated by replacing the summation over $\mathbf{k}$ with an integral

$$\frac{2}{N}\sum_{\mathbf{k}} f_{\mathbf{k}}\varepsilon_{\mathbf{k}} \to \frac{2\Omega}{(2\pi)^3}\int \mathrm{d}\mathbf{k}\ f_{\mathbf{k}}\varepsilon_{\mathbf{k}} = \frac{3}{5}Z\varepsilon_F \tag{2.84}$$

where $\varepsilon_F = (\hbar^2 k_F^2/2m)$ is the Fermi energy and the Fermi wavevector can be written in terms of the valence occupation $k_F = (3\pi^2 Z/\Omega)^{1/3}$ [127]. Under the assumption of $\delta n_{\mathrm{oh}} \to 0$, the total crystal pseudopotential may be written as

$$W = V_{\mathrm{val}} + \mu_{\mathrm{xc}} + W_{\mathrm{ion}} = V_{\mathrm{unif}} + \delta V_{\mathrm{scr}} + \mu_{\mathrm{xc}} + W_{\mathrm{ion}}. \tag{2.85}$$

The second term in the perturbative expansion can be reshuffled into terms which partly cancel other terms in E_{bind}. We can rewrite the matrix element as

$$\frac{2}{N}\sum_{\mathbf{k}} f_{\mathbf{k}}\langle\mathbf{k}|w|\mathbf{k}\rangle = \frac{1}{N}\mathrm{Tr}\left[\hat{n}_{\mathrm{unif}}w\right] = \frac{1}{N}\int \mathrm{d}\mathbf{r}\ n_{\mathrm{unif}}w\left(\mathbf{r}\right). \tag{2.86}$$

where we have introduced the uniform density operator $\hat{n}_{\mathrm{unif}}$ that has been used implicitly in the derivation of the pseudo-density in Eq.(2.81). Before expanding this term, we note that the integral of the product of the uniform density and screening potential vanishes

$$\int \mathrm{d}\mathbf{r}\ \delta V_{\mathrm{scr}}\left(\mathbf{r}\right) n_{\mathrm{unif}} = \int \mathrm{d}\mathbf{r}\ V_{\mathrm{unif}}\left(\mathbf{r}\right)\delta n_{\mathrm{scr}}\left(\mathbf{r}\right) = 0 \tag{2.87}$$

due to the screening density δn_{scr} being charge-neutral. We can now write the second term in the perturbative expansion as

$$\begin{aligned}\frac{2}{N}\sum_{\mathbf{k}} f_{\mathbf{k}}\langle\mathbf{k}|w|\mathbf{k}\rangle = \frac{1}{N}\int \mathrm{d}\mathbf{r}\ n_{\mathrm{unif}}\left[V_{\mathrm{unif}} - \sum_i{}' \frac{Ze^2}{|\mathbf{r}-\mathbf{R}_i|} + \mu_{\mathrm{xc}}\left(n_{\mathrm{val}}\right)\right] \\ + \frac{2\Omega}{(2\pi)^3}\int \mathrm{d}\mathbf{k}\ f_{\mathbf{k}}\langle\mathbf{k}|w_{\mathrm{core}}|\mathbf{k}\rangle\end{aligned} \tag{2.88}$$

where we have defined

$$w_{\text{core}} = w_{\text{ion}} + \frac{Ze^2}{r} \tag{2.89}$$

i.e. the core component of the ionic pseudopotential. The electrostatic terms in Eq.(2.88) can be combined with similar terms from the binding energy E_{bind}. Using Eq.(2.87), we can evaluate the classical electrostatic contribution of valence electron density to the valence binding energy as

$$-\frac{1}{2N}\int \mathrm{d}\mathbf{r}\; n_{\text{val}}(\mathbf{r})\, V_{\text{val}}(\mathbf{r}) = -\frac{1}{2N}\int \mathrm{d}\mathbf{r}\;\left[n_{\text{unif}} V_{\text{unif}}(\mathbf{r}) + \delta n_{\text{scr}}(\mathbf{r})\,\delta V_{\text{scr}}(\mathbf{r})\right]. \tag{2.90}$$

Adding the first term in Eq.(2.90) to the first two terms in Eq.(2.88) and the first term in Eq.(2.51), leaves us with the electrostatic energy per ion of N point ions of charge $+Ze$ in a compensating uniform electron gas

$$E_{\text{es}}(Z,\Omega) = \frac{1}{N}\left[\frac{1}{2}{\sum_{ij}}' \frac{(Ze)^2}{|\mathbf{R}_i - \mathbf{R}_j|} - \int \mathrm{d}\mathbf{r}\; n_{\text{unif}}\left({\sum_{i}}' \frac{Ze^2}{|\mathbf{r}-\mathbf{R}_i|} + \frac{1}{2}V_{\text{unif}}\right)\right]. \tag{2.91}$$

The electrostatic energy can be evaluated numerically using Ewald summations [192–194]. The Ewald summation technique combines real- and reciprocal-space expansions of the Coulomb interaction. The result is

$$E_{\text{es}}(Z,\Omega) = \frac{(Ze)^2}{2}\left[\frac{1}{N}{\sum_{ij}}' \frac{\operatorname{erfc}(\eta R_{ij})}{R_{ij}} + \frac{4\pi}{\Omega}{\sum_{\mathbf{q}}}' |S(\mathbf{q})|^2 \frac{e^{-q^2/4\eta^2}}{q^2} - \left(\frac{2\eta}{\sqrt{\pi}} + \frac{\pi}{\eta^2\Omega}\right)\right]. \tag{2.92}$$

The convergence parameter η can be chosen such that the expansion converges rapidly. This parameter is usually taken to be $\eta = 2/R_{\text{WS}}$ where $R_{\text{WS}} = (3\Omega/4\pi)^{1/3}$ is the

Wigner-Seitz radius. Recall that the electrostatic energy of a single point charge surrounded by a sphere of compensating charge density is $-(9/10)(Ze)^2/R_{\mathrm{WS}}$ where the factor of $-9/10$ arises from the electrostatic energy of the interaction between the ion and the charge density ($-(3/2)(Ze)^2/R_{\mathrm{WS}}$) plus the self-interaction energy of the charge density ($+(3/5)(Ze)^2/R_{\mathrm{WS}}$). This term can be separated from the total electrostatic energy

$$E_{\mathrm{es}}(Z,\Omega) = -\frac{9}{10}\left(Ze^2\right)/R_{\mathrm{WS}} + \delta E_{\mathrm{es}}(Z,\Omega) \tag{2.93}$$

where δE_{es} is the small structure dependent contribution to the electrostatic energy. This term can be expressed in terms of the structure-dependent Madelung constant α_{es}

$$\delta E_{\mathrm{es}}(Z,\Omega) = \frac{1}{2}(1.8-\alpha_{\mathrm{es}})\frac{(Ze)^2}{R_{\mathrm{WS}}}. \tag{2.94}$$

The exchange correlation terms in the cohesive energy $E_{\mathrm{coh}}^{\mathrm{xc}}$ can be grouped together by first adding in the contributions from Eq.(2.88). We have

$$E_{\mathrm{coh}}^{\mathrm{xc}} = \frac{1}{N}\int \mathrm{d}\mathbf{r}\ \left[n_{\mathrm{val}}(\mathbf{r})\,\varepsilon_{\mathrm{xc}}(n_{\mathrm{val}}) - (n_{\mathrm{val}}(\mathbf{r}) - n_{\mathrm{unif}})\,\mu_{\mathrm{xc}}(n_{\mathrm{val}})\right]. \tag{2.95}$$

Expanding both $(n_{\mathrm{val}}\varepsilon_{\mathrm{xc}})$ and μ_{xc} about $\delta n_{\mathrm{scr}} = 0$ gives us with the following expressions. For $(n_{\mathrm{val}}\varepsilon_{\mathrm{xc}})$ we have

$$n_{\mathrm{val}}\varepsilon_{\mathrm{xc}}(n_{\mathrm{val}}) = n_{\mathrm{unif}}\varepsilon_{\mathrm{xc}}(n_{\mathrm{unif}}) + \delta n_{\mathrm{scr}}\mu_{\mathrm{xc}}(n_{\mathrm{unif}}) + \frac{1}{2}(\delta n_{\mathrm{scr}})^2\frac{\mathrm{d}\mu_{\mathrm{xc}}(n_{\mathrm{unif}})}{\mathrm{d}n} \tag{2.96}$$

where we have used the relation $\mu_{\mathrm{xc}} = \mathrm{d}(n\varepsilon_{\mathrm{xc}})/\mathrm{d}n$. The expansion of μ_{xc} need only be

to linear order since it is multiplied by the screening density

$$\mu_{\mathrm{xc}}\left(n_{\mathrm{val}}\right)=\mu_{\mathrm{xc}}\left(n_{\mathrm{unif}}\right)+\frac{\mathrm{d}\mu_{\mathrm{xc}}\left(n_{\mathrm{unif}}\right)}{\mathrm{d}n}\left(\delta n_{\mathrm{scr}}\right). \tag{2.97}$$

Adding all of these terms in the expansion together leaves us with

$$E_{\mathrm{coh}}^{\mathrm{xc}}=\frac{1}{N}\int\mathrm{d}\mathbf{r}\ \left[n_{\mathrm{unif}}\varepsilon_{\mathrm{xc}}\left(n_{\mathrm{unif}}\right)-\frac{1}{2}\left(\delta n_{\mathrm{scr}}\right)^{2}\frac{\mathrm{d}\mu_{\mathrm{xc}}\left(n_{\mathrm{unif}}\right)}{\mathrm{d}n}\right]. \tag{2.98}$$

The first term in this expansion is simply the exchange-correlation energy of a homogenous electron gas and the second term can be interpreted as a second-order contribution from the oscillatory screening field.

There are some additional terms that can be matched in our expansion. First, we rewrite the screening density defined by Eq.(2.81) in the following way

$$\delta n_{\mathrm{scr}}\left(\mathbf{r}\right)=\sum_{\mathbf{q}}{}'\,S\left(\mathbf{q}\right)n_{\mathrm{scr}}\left(q\right)e^{i\mathbf{q}\cdot\mathbf{r}} \tag{2.99}$$

where

$$n_{\mathrm{scr}}\left(q\right)=\frac{4}{N\Omega}\sum_{\mathbf{k}}f_{\mathbf{k}}\frac{\langle\mathbf{k}+\mathbf{q}|w|\mathbf{k}\rangle}{\varepsilon_{\mathbf{k}}-\varepsilon_{\mathbf{k}+\mathbf{q}}}=\frac{4}{\left(2\pi\right)^{3}}\int\mathrm{d}\mathbf{k}\ f_{\mathbf{k}}\frac{\langle\mathbf{k}+\mathbf{q}|w|\mathbf{k}\rangle}{\varepsilon_{\mathbf{k}}-\varepsilon_{\mathbf{k}+\mathbf{q}}}. \tag{2.100}$$

We interpret $n_{\mathrm{scr}}(q)$ as the Fourier transform of the screening density arising from a single site. It only depends on the magnitude of $\mathbf{q}$ by symmetry. The potential due to the screening density can be written as

$$\delta V_{\mathrm{scr}}\left(\mathbf{r}\right)=e^{2}\int\mathrm{d}\mathbf{r}'\ \frac{\delta n_{\mathrm{scr}}\left(\mathbf{r}'\right)}{\left|\mathbf{r}-\mathbf{r}'\right|}=\sum_{\mathbf{q}}{}'\,S\left(\mathbf{q}\right)\left(\frac{4\pi e^{2}}{q^{2}}\right)n_{\mathrm{scr}}\left(q\right)e^{i\mathbf{q}\cdot\mathbf{r}}. \tag{2.101}$$

Therefore, the integral of the screening density with its corresponding screening po-

tential is simply

$$-\frac{1}{2N}\int \mathrm{d}\mathbf{r}\ \delta n_{\mathrm{scr}}\left(\mathbf{r}\right)\delta V_{\mathrm{scr}}\left(\mathbf{r}\right) = -\sum_{\mathbf{q}}{}' \left|S\left(\mathbf{q}\right)\right|^2 \left(\frac{2\pi e^2\Omega}{q^2}\right)\left[n_{\mathrm{scr}}\left(q\right)\right]^2 . \tag{2.102}$$

Along the same lines, the second term in the exchange-correlation expansion is given by

$$-\frac{1}{2N}\int \mathrm{d}\mathbf{r}\ \left(\delta n_{\mathrm{scr}}\left(\mathbf{r}\right)\right)^2 \frac{\mathrm{d}\mu_{\mathrm{xc}}\left(n_{\mathrm{unif}}\right)}{\mathrm{d}n} = \sum_{\mathbf{q}}{}' \left|S\left(\mathbf{q}\right)\right|^2 \left(\frac{2\pi e^2\Omega}{q^2}\right) G\left(q\right)\left[n_{\mathrm{scr}}\left(q\right)\right]^2 , \tag{2.103}$$

where $G(q)$ is the LDA local-field correction (from Eq.(2.37)) evaluated at n_{unif}

$$G\left(q\right) = -\frac{q^2}{4\pi e^2}\frac{\mathrm{d}\mu_{\mathrm{xc}}\left(n_{\mathrm{unif}}\right)}{\mathrm{d}n}. \tag{2.104}$$

In practice, we will replace the LDA local-field correction with the more realistic Ichimaru and Utsumi local-field correction [177]. Combining these two equations with the second order term in the perturbative expansion produces the structural component of the band energy which can be written as

$$E_{\mathrm{bs}} = \sum_{\mathbf{q}}{}' \left|S\left(\mathbf{q}\right)\right|^2 F\left(q,\Omega\right), \tag{2.105}$$

where F is the energy-wavenumber characteristic introduced by Harrison [93]. The energy-wavenumber characteristic F is volume dependent but not structure independent, and is given by

$$F\left(q,\Omega\right) \equiv \frac{2\Omega}{\left(2\pi\right)^3}\int \mathrm{d}\mathbf{k}\ f_{\mathbf{k}}\frac{\left|\langle\mathbf{k}+\mathbf{q}|w|\mathbf{k}\rangle\right|^2}{\varepsilon_{\mathbf{k}}-\varepsilon_{\mathbf{k}+\mathbf{q}}} - \frac{2\pi e^2\Omega}{q^2}\left(1-G\left(q\right)\right)\left[n_{\mathrm{scr}}\left(q\right)\right]^2 , \tag{2.106}$$

where we have assumed the hermiticity of the local pseudopotential w. The volume term $E^q_{\rm vol}$ is distinct from $E_{\rm vol}$ as it is in the reciprocal-space representation.

Using all of the results derived in this subsection, we can write

$$E^q_{\rm vol}(\Omega) = \frac{3}{5} Z\varepsilon_F + Z\varepsilon_{\rm xc}(n_{\rm unif}) - \frac{9}{10}(Ze)^2/R_{\rm WS} + \frac{2\Omega}{(2\pi)^3}\int {\rm d}\mathbf{k}\; f_{\mathbf{k}}\langle\mathbf{k}|w_{\rm core}|\mathbf{k}\rangle - E^{\rm atom}_{\rm bind}. \tag{2.107}$$

The GPT defines a pseudopotential using the zeroth-order pseudoatom method [181]

$$w_{\rm pa} \equiv v_{\rm unif} + w_{\rm ion} - V_0' = v_{\rm unif} - \frac{Ze^2}{r} + w_{\rm core} - V_0' \tag{2.108}$$

where $v_{\rm unif}$ is the Coulomb potential due to a uniform electron gas that is contained within a sphere of radius $R_{\rm WS}$, and V_0' is a zero-of-energy constant chosen to ensure that $\langle 0|w_{\rm pa}|0\rangle = 0$. This constant was given explicitly by Moriarty [99]. The plane wave matrix elements of the pseudoatom can be written as

$$\langle\mathbf{k}|w_{\rm pa}|\mathbf{k}\rangle = -\frac{3}{10}\frac{(Ze)^2}{R_{\rm WS}} + \langle\mathbf{k}|w_{\rm core}|\mathbf{k}\rangle + V_0'. \tag{2.109}$$

Using this representation for the pseudopotential, we may express $E^q_{\rm vol}$ as

$$E^q_{\rm vol}(\Omega) = E^0_{\rm fe}(\Omega) + \frac{2\Omega}{(2\pi)^3}\int {\rm d}\mathbf{k}\; f_{\mathbf{k}}\langle\mathbf{k}|w_{\rm pa}|\mathbf{k}\rangle - E^{\rm atom}_{\rm bind}, \tag{2.110}$$

where $E^0_{\rm fe}$ is the zeroth order free-electron energy

$$E^0_{\rm fe}(\Omega) = \frac{3}{5} Z\varepsilon_F + Z\varepsilon_{\rm xc}(n_{\rm unif}) - \frac{3}{5}\frac{(Ze)^2}{R_{\rm WS}} + ZV_0' \tag{2.111}$$

that represents the free-electron binding energy in the limit $w_{\rm pa} \to 0$. The reciprocal space representation is sufficient to produce quantitatively accurate descriptions of the

mechanical properties of metals. It is often the case that the calculation converges faster in reciprocal space than in real-space. Putting all of these terms together yields the compact result

$$E_{\text{coh}} = E^{q}_{\text{vol}}(\Omega) + \sum_{\mathbf{q}}{}' |S(\mathbf{q})|^2 F(q,\Omega) + \delta E_{\text{es}}(Z,\Omega). \tag{2.112}$$

2.4.2 Real-Space Representation

Our goal is to transform the reciprocal space approach of the previous subsection into a real space interatomic potential plus a volume term. This transformation, and subsequent reseparation of volume- and structure-dependent terms, has to be carefully considered. We follow the approach of Moriarty [99, 115, 116]. We will continue to work in the limit of a local pseudopotential and add in non-locality in the next subsection. First, we add the energy of an ion surrounded by a compensating sphere of radius R_{WS} to recover the full electrostatic energy in Eq.(2.112)

$$E_{\text{coh}} = E^{q}_{\text{vol}} + E_{\text{bs}} + \delta E_{\text{es}} = E^{q}_{\text{vol}} + \frac{9}{10}\frac{(Ze)^2}{R_{\text{WS}}} + E_{\text{bs}} + E_{\text{es}}. \tag{2.113}$$

The sum of the band structure and electrostatic energy can be written as sum of a term multiplied by the structure factor $S(\mathbf{q})$ and a constant

$$E_{\text{bs}} + E_{\text{es}} = \sum_{\mathbf{q}}{}' |S(\mathbf{q})|^2 \left[\frac{2\pi (Ze^2)^2}{q^2\Omega} e^{-q^2/(4\eta^2)} + F(q,\Omega)\right] - \frac{(Ze)^2 \eta}{\sqrt{\pi}}. \tag{2.114}$$

Some of these terms will turn out to be equivalent. To see this,we add and subtract the $\mathbf{q} = 0$ terms to the summation

$$E_{\rm bs}+E_{\rm es}=\sum_{\mathbf{q}}\left|S\left(\mathbf{q}\right)\right|^{2}\left[\frac{2\pi\left(Ze^{2}\right)^{2}}{q^{2}\Omega}e^{-q^{2}/(4\eta^{2})}+F\left(q,\Omega\right)\right]-\frac{\left(Ze\right)^{2}\eta}{\sqrt{\pi}}$$
$$-\lim_{q\rightarrow0}\left[\frac{2\pi\left(Ze^{2}\right)^{2}}{q^{2}\Omega}+F\left(q,\Omega\right)\right]. \tag{2.115}$$

We don't evaluate the limit $q\rightarrow0$ since the first term in the brackets on the final line blows up. We will show that there is an equivalent term in the energy-wavenumber characteristic which cancels this exactly, leaving a finite result. The square structure factor $|S(\mathbf{q})|^2$ can be evaluated as

$$\left|S\left(\mathbf{q}\right)\right|^{2}=\frac{1}{N^{2}}\sum_{ij}e^{-i\mathbf{q}\cdot\left(\mathbf{R}_{i}-\mathbf{R}_{j}\right)}=\frac{1}{N^{2}}\sum_{ij}{}'e^{-i\mathbf{q}\cdot\left(\mathbf{R}_{i}-\mathbf{R}_{j}\right)}+\frac{1}{N} \tag{2.116}$$

where we have explicitly separated the $i=j$ and $i\neq j$ terms. Next, we insert this expression and take the limit $\eta\rightarrow\infty$. Thus

$$E_{\rm bs}+E_{\rm es}=\frac{1}{2N}\sum_{ij}{}'\left[\frac{1}{N}\sum_{\mathbf{q}}\left[\frac{4\pi\left(Ze^{2}\right)^{2}}{q^{2}\Omega}+2F\left(q,\Omega\right)\right]e^{-i\mathbf{q}\cdot\left(\mathbf{R}_{i}-\mathbf{R}_{j}\right)}\right]$$
$$-\lim_{q\rightarrow0}\left[\frac{2\pi\left(Ze^{2}\right)^{2}}{q^{2}\Omega}+F\left(q,\Omega\right)\right]$$
$$+\lim_{\eta\rightarrow\infty}\left[\frac{1}{N}\sum_{\mathbf{q}}\left[\frac{2\pi\left(Ze\right)^{2}}{q^{2}\Omega}e^{-q^{2}/(4\eta^{2})}+F\left(q,\Omega\right)\right]-\frac{\left(Ze\right)^{2}\eta}{\sqrt{\pi}}\right]. \tag{2.117}$$

The two terms involving η cancel exactly since

$$\frac{2\pi\left(Ze\right)^{2}}{N\Omega}\sum_{\mathbf{q}}\left[\frac{1}{q^{2}}e^{-q^{2}/(4\eta^{2})}\right]=\frac{\left(Ze\right)^{2}}{\pi}\int_{0}^{\infty}{\rm d}q\;e^{-q^{2}/4\eta^{2}}=\frac{\left(Ze\right)^{2}\eta}{\sqrt{\pi}}. \tag{2.118}$$

The remaining pure volume terms can be added to the first two terms in Eq.(2.113)

to yield the volume term E_{vol}

$$E_{\text{vol}}(\Omega) = E^{q}_{\text{vol}}(\Omega) + \frac{9}{10}\frac{(Ze)^2}{R_{\text{WS}}} - \lim_{q\to 0}\left[\frac{2\pi(Ze)^2}{q^2\Omega} + F(q,\Omega)\right] + \frac{1}{N}\sum_{\mathbf{q}} F(q,\Omega). \quad (2.119)$$

Therefore, from Eq.(2.117), we can infer the form of the pair potential from the terms remaining

$$v_2(r,\Omega) = \frac{1}{N}\sum_{\mathbf{q}}\left[\frac{4\pi(Ze)^2}{q^2\Omega} + 2F(q,\Omega)\right]e^{-i\mathbf{q}\cdot\mathbf{r}}. \quad (2.120)$$

The expressions in Eqs.(2.119) and (2.120) can be further developed and simplified. In particular, we still need to properly evaluate the limit as $q \to 0$ of F. We first define a normalised energy-wavenumber characteristic

$$\begin{aligned} F_N(q,\Omega) &= -\frac{q^2\Omega}{2\pi(Ze)^2}F(q,\Omega), \\ &= -\frac{q^2\Omega}{4\pi(Ze)^2}\left[-\frac{4}{(2\pi)^3}\int \mathrm{d}\mathbf{k}\; f_{\mathbf{k}}\frac{|\langle\mathbf{k}+\mathbf{q}|w|\mathbf{k}\rangle|^2}{\varepsilon_{\mathbf{k}}-\varepsilon_{\mathbf{k}+\mathbf{q}}} + \frac{4\pi e^2}{q^2}(1-G(q))\left[n_{\text{scr}}(q)\right]^2\right] \end{aligned} \quad (2.121)$$

using $F(q,\Omega)$ from Eq.(2.106). The normalized energy-wavenumber characteristic is so-called since $F(0,\Omega) = 1$. Expanding in terms of small q, the leading term is $(\Omega/Z)^2[n_{\text{scr}}(q)]^2$ and we assume for now that $\lim_{q\to 0} n_{\text{scr}}(q) = Z/\Omega$. The next correction can be shown to be $\mathcal{O}(q^2)$ which yields the Taylor expansion

$$F_N(q,\Omega) = 1 + \frac{1}{2}q^2\left(\frac{\partial^2 F_N(0,\Omega)}{\partial q^2}\right) + \mathcal{O}\left(q^3\right). \quad (2.122)$$

We can now remove the limit from our definition of the volume term E_{vol}. Using Eqs.(2.109) and (2.111), this leaves

$$E_{\text{vol}}(\Omega) = \frac{3}{5} Z\varepsilon_F + Z\varepsilon_{\text{xc}}(n_{\text{unif}}) + \frac{2\Omega}{(2\pi)^3} \int \mathrm{d}\mathbf{k}\ f_{\mathbf{k}} \langle \mathbf{k}|w_{\text{core}}|\mathbf{k}\rangle + \frac{\pi (Ze)^2}{\Omega} \frac{\partial^2 F_N(0,\Omega)}{\partial q^2} - \frac{(Ze)^2}{\pi} \int_0^\infty \mathrm{d}q\ F_N(q,\Omega) - E_{\text{bind}}^{\text{atom}}. \tag{2.123}$$

The equation for the pairwise interaction in Eq.(2.120) can be simplified further. We first note that we can write the Coulomb interaction in reciprocal space as

$$\frac{(Ze)^2}{r} = \frac{1}{N\Omega} \sum_{\mathbf{q}} \frac{4\pi (Ze)^2}{q^2} e^{i\mathbf{q}\cdot\mathbf{r}}. \tag{2.124}$$

For a spherically symmetric function $g(q)$ one has

$$\frac{1}{N\Omega} \sum_{\mathbf{q}} g(q)\, e^{i\mathbf{q}\cdot\mathbf{r}} = \frac{1}{(2\pi)^3} \int \mathrm{d}\mathbf{q}\ g(q)\, e^{i\mathbf{q}\cdot\mathbf{r}} = \frac{1}{2\pi^2} \int_0^\infty \mathrm{d}q\ q^2 g(q) \frac{\sin(qr)}{qr}. \tag{2.125}$$

This results in a simple form for the pair potential v_2

$$v_2(r,\Omega) = \frac{(Ze)^2}{r} \left[1 - \frac{2}{\pi} \int_0^\infty \mathrm{d}q\ F_N(q,\Omega) \frac{\sin(qr)}{q} \right]. \tag{2.126}$$

This expression can be viewed as a screened Coulomb interaction; a sum of the direct interaction between ions and an indirect ion-electron-ion screening interaction. The result can be seen for Mg in Fig.(2.4) at the observed equilibrium volume $\Omega = 156.8$ a.u.. In the limit that $r \to 0$, the Coulomb interaction is dominant which is to be expected, whereas in the long-ranged limit the interaction is oscillatory and converges to the well-known Friedel oscillations [93]

$$v_2(r,\Omega) \sim \frac{9\pi Z^2 [w(2k_F)]^2}{\varepsilon_F} \frac{\cos(2k_F r)}{(2k_F r)^3}, \tag{2.127}$$

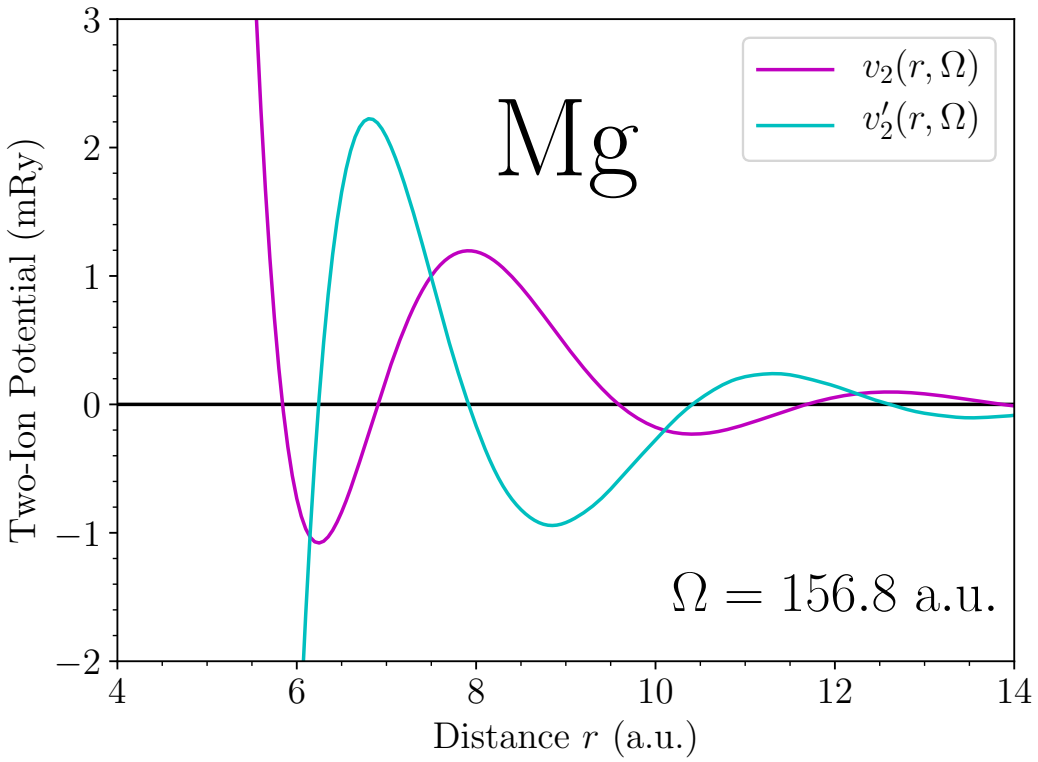

Fig. 2.4: The pairwise interaction for Mg at the observed equilibrium volume with a non-local AHS pseudopotential. The first radial derivative is also plotted.

where $w(2k_F)$ is the pseudopotential form factor at twice the Fermi wavevector. The logarithmic singularity in the Lindhard function is deemed to be responsible for the Friedel oscillations. Pettifor and Ward [195] replaced the Lindhard function $\mathcal{F}$ by a rational function $\mathcal{F}_{\mathrm{PW}}$. This function matches $\mathcal{F}$ very closely but removes the logarithmic singularity. Using a local pseudopotential, Pettifor and Ward were able to compute v_2 analytically via contour integration; exploiting the pole structure of $\mathcal{F}_{\mathrm{PW}}$. The result was an exponentially-damped oscillatory pairwise interaction that vanished in the $r \to 0$ limit.

2.4.3 Extension to Non-Local Pseudopotentials

We have assumed so far in our derivation of a pair potential for simple metals that the pseudopotential was local i.e. $w(\mathbf{r},\mathbf{r}') = w(\mathbf{r})\,\delta(\mathbf{r}-\mathbf{r}')$. The GPT uses a non-local pseudopotential in the AHS form for multiple reasons. Firstly, it has been shown by Chelikowsky [196] that there is a considerable contribution from non-locality to the cohesive energy. Moriarty [10] has shown that a non-local pseudopotential removes the positive energy nearest-neighbour minimum in Al. This finding is in agreement with earlier work by Walker and Taylor [197]. Another argument for pseudopotential non-locality was given by Dharma-wardana and Aers [198] who developed a technique for determining the interatomic potential from experiment and molecular dynamics. Their results indicated that the nearest-neighbour interaction is necessarily positive. The non-locality of the pseudopotential appears through the inclusion of several additional terms. Firstly, a non-local pseudopotential is non-Hermitian and for our pseudopotential form factor, we have

$$\langle \mathbf{k}|w|\mathbf{k}+\mathbf{q}\rangle = \langle \mathbf{k}+\mathbf{q}|w|\mathbf{k}\rangle - (\varepsilon_{\mathbf{k}} - \varepsilon_{\mathbf{k}+\mathbf{q}})\,\langle \mathbf{k}|P_c|\mathbf{k}+\mathbf{q}\rangle. \tag{2.128}$$

Secondly, a non-local pseudopotential has a non-zero orthogonalisation hole density and an effective valence Z^*. For instance, a non-local pseudopotential has the effect that the structural part of the electrostatic energy becomes

$$\delta E_{\mathrm{es}}(Z,\Omega) \rightarrow \delta E_{\mathrm{es}}(Z^*,\Omega) = \frac{1}{2}(1.8-\alpha_{\mathrm{es}})\,\frac{(Z^*e)^2}{R_{\mathrm{WS}}}. \tag{2.129}$$

The energy-wavenumber characteristic F gets an additional contribution from the orthogonalisation hole density due to the exchange-correlation part of E_{coh} [99]

$$F(q,\Omega) \rightarrow F(q,\Omega) - \frac{2\pi e^2\Omega}{q^2} G(q)\,[n_{\mathrm{oh}}(q)]^2\,. \tag{2.130}$$

In analogy with $n_{\rm scr}(q)$, the quantity $n_{\rm oh}(q)$ is the Fourier transform of the orthogonalisation hole density. The non-locality of w gives rise to two further alterations to the volume-term in reciprocal space $E^q_{\rm vol}$. The first is a small self-energy correction due to the finite size of the orthogonalisation hole [99]

$$\delta E_{\rm oh}\left(\Omega\right) = -\frac{9}{10}\left(\frac{\left(Z^* - Z\right)^2 e^2}{R_{\rm WS}}\right) + \frac{1}{2}\int_0^\infty {\rm d}r\; u_{\rm oh}\left(r\right)\left[v_{\rm oh}\left(r\right) - \frac{\left(Z^* - Z\right) e^2 r^2}{R^3_{\rm WS}}\right] \quad (2.131)$$

where $u_{\rm oh} = 4\pi r^2 n_{\rm oh}(r)$ is the radial orthogonalisation hole density and $v_{\rm oh}$ is the Coulomb potential due to $n_{\rm oh}$. The reciprocal-space volume term becomes

$$E^q_{\rm vol}\left(\Omega\right) \rightarrow E^q_{\rm vol}\left(\Omega\right) + \frac{2\Omega}{\left(2\pi\right)^3}\int {\rm d}\mathbf{k}\; f_{\mathbf{k}}\left[\langle\mathbf{k}|w_{\rm pa}|\mathbf{k}\rangle\langle\mathbf{k}|p_c|\mathbf{k}\rangle\right] + \delta E_{\rm oh}\left(\Omega\right), \quad (2.132)$$

where the second term is due to the fact that a non-local pseudopotential is non-Hermitian and/or energy-dependent. The precise form depends specifically on the form of the AHS pseudopotential. In our case, we use the form first suggested by Pick and Sarma [199], which gives rise to the additional volume-dependent contribution to the reciprocal-space volume term $E^q_{\rm vol}$. This can be demonstrated by using Eq.(2.128) in Eq.(2.105) for the structural part of the band-structure energy. With a non-local pseudopotential, the normalised energy-wavenumber characteristic is defined slightly differently to Eq.(2.121). We note that the $q \rightarrow 0$ limit of the screening density is Z^*/Ω with a non-local pseudopotential. This gives

$$F_N\left(q,\Omega\right) \rightarrow -\frac{q^2\Omega}{2\pi\left(Z^* e\right)^2} F\left(q,\Omega\right). \quad (2.133)$$

Thus, the pairwise interaction v_2 becomes

$$v_2(r,\Omega) = \frac{(Z^*e)^2}{r}\left[1 - \frac{2}{\pi}\int_0^\infty \mathrm{d}q\ F_N(q,\Omega)\,\frac{\sin(qr)}{q}\right] \tag{2.134}$$

and the real-space volume term

$$E_{\mathrm{vol}}(\Omega) = E_{\mathrm{fe}}(\Omega) + \frac{2\Omega}{(2\pi)^3}\int \mathrm{d}\mathbf{k}\ f_{\mathbf{k}}\langle\mathbf{k}|w_{\mathrm{pa}}|\mathbf{k}\rangle\left[1 + \langle\mathbf{k}|P_c|\mathbf{k}\rangle\right] + \frac{9}{10}\frac{(Z^*e)^2}{R_{\mathrm{WS}}} + \frac{\pi(Z^*e)^2}{\Omega}\frac{\partial^2 F_N(0,\Omega)}{\partial q^2} - \frac{(Z^*e)^2}{\pi}\int_0^\infty \mathrm{d}q\ F_N(q,\Omega) + \delta E_{\mathrm{oh}}(\Omega) - E_{\mathrm{bind}}^{\mathrm{atom}} \tag{2.135}$$

with $E_{\mathrm{fe}}^0(\Omega)$ given by Eq.(2.111).

2.4.4 Self-Consistent Electron Screening

Even though we have a functional form for the pair potential and the volume term, there are still a few concepts which have been hitherto glossed over. The normalised energy-wavenumber characteristic F_N (shown in Fig.(2.5)) is the essential ingredient to producing accurate calculations of v_2 and E_{vol}. Determination of the energy-wavenumber characteristic requires a self-consistent calculation of the screening density δn_{scr} and the form factor $\langle\mathbf{k}+\mathbf{q}|w|\mathbf{k}\rangle$. These quantities have been introduced through first-order perturbation theory and are one-ion quantities. In this sense, it is typically referred to as linear screening. For a general nonlocal pseudopotential, we have $W = V_{\mathrm{val}} + \mu_{\mathrm{xc}} + W_{\mathrm{ion}}$ and the Coulomb potential $V_{\mathrm{val}} = V_{\mathrm{unif}} + \delta V_{\mathrm{scr}} + \delta V_{\mathrm{oh}}$. For the one ion form factor, we have

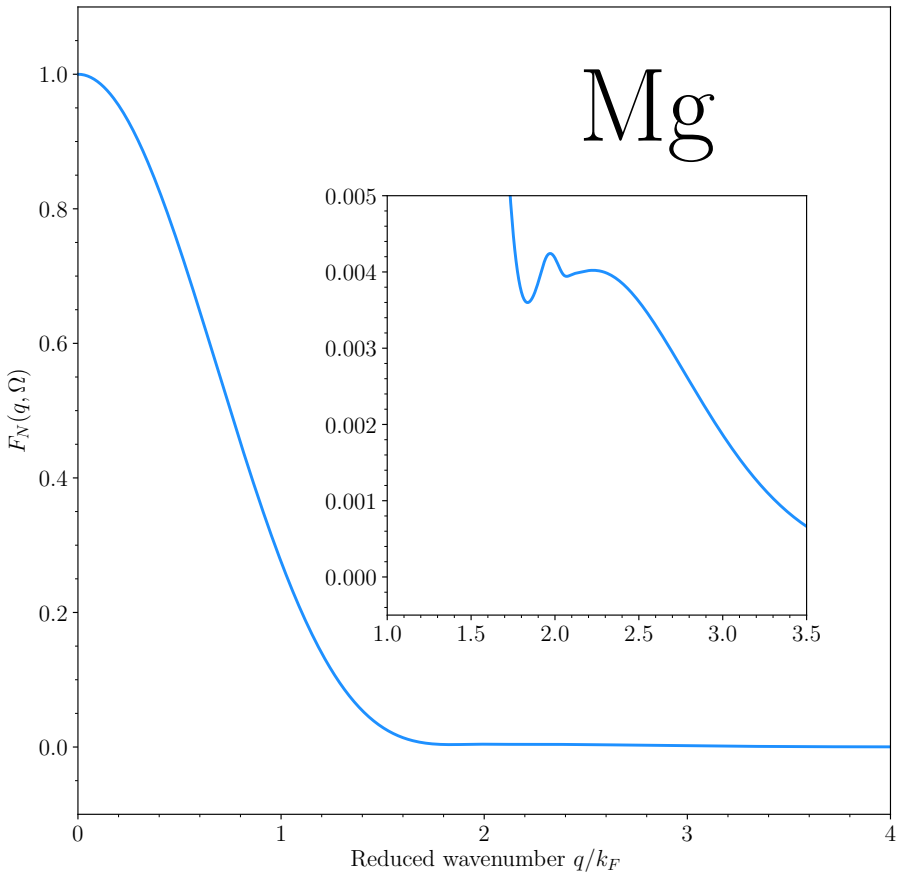

Fig. 2.5: The normalised energy-wavenumber characteristic is plotted Mg at the observed equilibrium atomic volume $\Omega = 156.8$ a.u. We have zoomed in on the logarithmic singularity at $q = 2k_F$ responsible for the Friedel oscillations in the pairwise interaction. The logarithmic singularity is present due to the implicit dependence on the Lindhard function $f_l(q/2k_F)$.

$$\begin{aligned}\langle \mathbf{k}+\mathbf{q}|w|\mathbf{k}\rangle &= v_{\text{scr}}(q) + v_{\text{oh}}(q) + \langle \mathbf{k}+\mathbf{q}|w_{\text{ion}}|\mathbf{k}\rangle, \\ &= \frac{4\pi e^2}{q^2}\left(1 - G(q)\right)\left(n_{\text{scr}}(q) + n_{\text{oh}}(q)\right) + \langle \mathbf{k}+\mathbf{q}|w_{\text{ion}}|\mathbf{k}\rangle \end{aligned} \tag{2.136}$$

where the contribution of the uniform electron density is included through the $q = 0$ component of $n_{\text{scr}}(q)$ and the exchange-correlation contributions to $v_{\text{scr}}(q)$ and $v_{\text{oh}}(q)$

are included through $G(q)$. We insert this expression into Eq.(2.100) to find

$$n_{\mathrm{scr}}(q) = -\left[\frac{4\pi e^2}{q^2}\left(1 - G(q)\right)\left(n_{\mathrm{scr}}(q) + n_{\mathrm{oh}}(q)\right) + \bar{w}_{\mathrm{ion}}(q)\right]\Pi_0(q), \tag{2.137}$$

where $\Pi_0(q)$ is the polarisability of the uniform electron gas in the Hartree or (static) random phase approximation (RPA) [127]

$$\Pi_0(q) = -\frac{4}{(2\pi)^3}\int \mathrm{d}\mathbf{k}\; f_{\mathbf{k}}\frac{1}{\varepsilon_{\mathbf{k}} - \varepsilon_{\mathbf{k}+\mathbf{q}}}. \tag{2.138}$$

We have also defined $\bar{w}_{\mathrm{ion}}$ which is an average of the quantity $\langle \mathbf{k}+\mathbf{q}|w_{\mathrm{ion}}|\mathbf{k}\rangle$ over reciprocal space

$$\bar{w}_{\mathrm{ion}}(q) \equiv -\frac{4}{(2\pi)^3}\frac{1}{\Pi_0(q)}\int \mathrm{d}\mathbf{k}\; f_{\mathbf{k}}\frac{\langle \mathbf{k}+\mathbf{q}|w_{\mathrm{ion}}|\mathbf{k}\rangle}{\varepsilon_{\mathbf{k}} - \varepsilon_{\mathbf{k}+\mathbf{q}}}. \tag{2.139}$$

The self-consistent screening density can be found by rearranging Eq.(2.137)

$$n_{\mathrm{scr}}(q) = -\left[\bar{w}_{\mathrm{ion}}(q) + \frac{4\pi e^2}{q^2}\left(1 - G(q)\right)n_{\mathrm{oh}}(q)\right]\frac{\Pi_0(q)}{\varepsilon(q)}, \tag{2.140}$$

$$= -\left[\bar{w}_{\mathrm{ion}}(q) + v_{\mathrm{oh}}(q)\right]\frac{\Pi_0(q)}{\epsilon(q)} \tag{2.141}$$

with ϵ the dielectric function for the interacting electron gas

$$\epsilon(q) \equiv 1 + \frac{4\pi e^2}{q^2}\left(1 - G(q)\right)\Pi_0(q). \tag{2.142}$$

When the exchange-correlation vanishes, we recover the familiar Hartree dielectric

function. Inserting our expressions back into the form factor yields

$$\langle \mathbf{k}+\mathbf{q}|w|\mathbf{k}\rangle = \frac{1}{\epsilon\left(q\right)}\left[\bar{w}_{\mathrm{ion}}\left(q\right)+v_{\mathrm{oh}}\left(q\right)\right]+\langle \mathbf{k}+\mathbf{q}|w_{\mathrm{ion}}|\mathbf{k}\rangle-\bar{w}_{\mathrm{ion}}\left(q\right). \tag{2.143}$$

Both $n_{\mathrm{scr}}\left(q\right)$ and the form factor $\langle \mathbf{k}+\mathbf{q}|w|\mathbf{k}\rangle$ depend on only the bare-ion pseudopotential w_{ion}, orthogonalisation hole density n_{oh} and properties of the free-electron gas. We can use these quantities to evaluate the normalized energy-wavenumber characteristic F_N. Further work is needed to prove the $q\rightarrow 0$ limit of $n_{\mathrm{scr}}\left(q\right)$, $\langle \mathbf{k}+\mathbf{q}|w|\mathbf{k}\rangle$ and $F_N\left(q,\Omega\right)$. We will once again work in the limit of a local pseudopotential and add in non-locality retroactively. For a local pseudopotential, we have a few simplifications: $n_{\mathrm{oh}}=v_{\mathrm{oh}}=0$, the matrix elements of the bare-ion pseudopotential are independent of $\mathbf{k}$ i.e. $\langle \mathbf{k}+\mathbf{q}|w_{\mathrm{ion}}|\mathbf{k}\rangle = w_{\mathrm{ion}}(q)$, and $\bar{w}_{\mathrm{ion}}(q)=w_{\mathrm{ion}}(q)$. The screening density n_{scr} is given by the simple expression

$$n_{\mathrm{scr}}\left(q\right)=-\frac{w_{\mathrm{ion}}\left(q\right)\Pi_0\left(q\right)}{\epsilon\left(q\right)}. \tag{2.144}$$

The plane-wave matrix elements are also given by a simple expression

$$\langle \mathbf{k}+\mathbf{q}|w|\mathbf{k}\rangle \rightarrow w\left(q\right)=\frac{w_{\mathrm{ion}}\left(q\right)}{\epsilon\left(q\right)}. \tag{2.145}$$

Combining these results leads to a simple expression for the energy-wavenumber characteristic

$$F_N\left(q,\Omega\right)=\left[-\frac{q^2}{4\pi e^2}\frac{\Omega}{Z}w_{\mathrm{ion}}\left(q\right)\right]^2\chi\left(q\right) \tag{2.146}$$

where $\chi(q)$ is the susceptibility for the interacting electron gas given by

$$\chi\left(q\right) \equiv \frac{4\pi e^2}{q^2}\frac{\Pi_0\left(q\right)}{\varepsilon\left(q\right)}. \tag{2.147}$$

The susceptibility of the non-interacting electron gas is found by replacing the dielectric function $\epsilon(q)$ with $\epsilon_0(q)$. The polarisability of the free-electron gas can be written as

$$\Pi_0\left(q\right) = -\frac{4}{\left(2\pi\right)^3}\int \mathrm{d}\mathbf{k}\ \frac{f_{\mathbf{k}}}{\varepsilon_{\mathbf{k}} - \varepsilon_{\mathbf{k}+\mathbf{q}}} = \frac{k_F}{2\pi^2}\mathcal{F}\left(q/2k_F\right) = \frac{k_{TF}^2}{4\pi e^2}\mathcal{F}\left(q/2k_F\right) \tag{2.148}$$

where we have introduced the Thomas-Fermi wavevector $k_{\mathrm{TF}}^2 \equiv 4k_F me^2/(\pi\hbar)^2$ in the final line. The Lindhard function $\mathcal{F}$ has the following behaviour at small and large x [10]

$$\mathcal{F}\left(x\right) = \begin{cases} 1 - \frac{1}{3}x^2, & x \to 0 \\ \left(3x^2\right)^{-1}, & x \to \infty \end{cases}. \tag{2.149}$$

In the limit of small q, where $\mathcal{F} \to 1$, the Hartree dielectric function tends to the Thomas-Fermi value

$$\epsilon_0\left(q\right) \to 1 + \frac{k_{\mathrm{TF}}^2}{q^2} \equiv \epsilon_{\mathrm{TF}}\left(q\right), \tag{2.150}$$

and the corresponding susceptibility $\chi_0(q)$ approaches the Thomas-Fermi susceptibility $\chi_{\mathrm{TF}} \equiv (k_{\mathrm{TF}}^2/q^2)/\epsilon_{\mathrm{TF}}(q)$. In the limit of small q, the full susceptibility $\chi(q)$ has the limiting form [10]

$$\chi\left(q\right) \to 1 - q^2/k_{\mathrm{TF}}^2 + G\left(q\right) = 1 - \frac{q^2}{4\pi e^2}\left[\frac{\left(2/3\right)\varepsilon_F}{Z/\Omega} + \frac{\mathrm{d}\mu_{\mathrm{xc}}\left(n_{\mathrm{unif}}\right)}{\mathrm{d}n}\right]. \tag{2.151}$$

The screening functions $\epsilon_0(q)$ and $\chi_0(q)$ depend on the atomic volume Ω through the uniform electron density $n_{\text{unif}} = Z/\Omega$. This remains true when exchange and correlation are included in $\epsilon(q)$ and $\chi(q)$. This is also the case with a non-local pseudopotential. We are now in a position to evaluate the $q \to 0$ limit of the screening electron density n_{scr}. Firstly, we expose the ionic Coulomb potential contained in w_{ion} by writing

$$w_{\text{ion}}(q) = -\frac{4\pi e^2}{q^2}\frac{Z}{\Omega} + w_{\text{core}}(q). \tag{2.152}$$

Recall that $\lim_{q\to 0}\chi(q) = 1$ and $\lim_{q\to 0} G(q) = 0$, and we assume that the core component of the pseudopotential remains bounded in the $q \to 0$ limit i.e.

$$\lim_{q\to 0} |w_{\text{core}}(q)| < \infty. \tag{2.153}$$

Leaving us with the expected result

$$\lim_{q\to 0} n_{\text{scr}}(q) = n_{\text{unif}} \tag{2.154}$$

as we have previously assumed. For a non-local AHS pseudopotential, this result is replaced by letting $Z \to Z^*$ to account for the fact that the orthogonalisation hole n_{oh} is screened by the additional uniform electron density $(Z^*/Z - 1)n_{\text{unif}}$. Similarly, we find that the local pseudopotential form factor $w(q) \to -(2/3)\varepsilon_F$ as $q \to 0$. This can be generalised for a non-local AHS pseudopotential [200] to

$$\lim_{q\to 0}\langle \mathbf{k}_F + \mathbf{q}|w|\mathbf{k}_F\rangle = -\frac{2}{3}\varepsilon_F, \tag{2.155}$$

where the form factor is confined to the free electron Fermi surface. This result is used to check the accuracy of the numerical calculation of the form factor. Next, we turn to the final evaluation of the energy-wavenumber characteristic and volume term.

For a non-local norm-conserving pseudopotential with $n_{\rm oh}$, we can write the screening density $n_{\rm scr}$ in terms of the susceptibility $\chi(q)$ as

$$n_{\rm scr}\left(q\right) = -\frac{q^2}{4\pi e^2}\bar{w}_{\rm ion}\left(q\right)\chi\left(q\right). \tag{2.156}$$

Substituting this result into the expression for the normalised energy-wavenumber characteristic $F_N(q,\Omega)$ gives

$$F_N\left(q,\Omega\right) = \left[-\frac{q^2}{4\pi e^2}\frac{\Omega}{Z}\bar{w}_{\rm ion}\left(q\right)\right]^2\chi\left(q\right) + \frac{q^2}{4\pi e^2}\left(\frac{\Omega}{Z}\right)^2\left[\overline{w^2_{\rm ion}}\left(q\right) - \left(\bar{w}_{\rm ion}\left(q\right)\right)^2\right]\Pi_0\left(q\right), \tag{2.157}$$

where we have defined the additional average of $\langle\mathbf{k}+\mathbf{q}|w_{\rm ion}|\mathbf{k}\rangle$

$$\overline{w^2_{\rm ion}}\left(q\right) \equiv -\frac{4}{\left(2\pi\right)^3}\frac{1}{\Pi_0\left(q\right)}\int{\rm d}\mathbf{k}\;|\langle\mathbf{k}+\mathbf{q}|w_{\rm ion}|\mathbf{k}\rangle|^2\frac{f_{\mathbf{k}}}{\varepsilon_{\mathbf{k}}-\varepsilon_{\mathbf{k}+\mathbf{q}}}. \tag{2.158}$$

We can use this expression to evaluate the second order derivative $\partial^2 F_N(0,\Omega)/\partial q^2$ analytically in the volume term $E_{\rm vol}(\Omega)$. In analogy with Eq.(2.152) for a local pseudopotential, we write

$$\bar{w}_{\rm ion}\left(q\right) = -\frac{4\pi e^2}{q^2}\frac{Z}{\Omega} + \bar{w}_{\rm core}\left(q\right). \tag{2.159}$$

Hence, we may write

$$F_N\left(q,\Omega\right) = \left[1 - \frac{q^2}{4\pi e^2}\frac{\Omega}{Z}\bar{w}_{\rm core}\left(q\right)\right]^2\chi\left(q\right) + \frac{q^2}{4\pi e^2}\left(\frac{\Omega}{Z}\right)^2\delta\overline{w^2_{\rm core}}\left(q\right)\Pi_0\left(q\right) \tag{2.160}$$

with the definition

$$\delta\overline{w^2_{\rm core}}\left(q\right) = \overline{w^2_{\rm core}}\left(q\right) - \left(\bar{w}_{\rm core}\left(q\right)\right)^2. \tag{2.161}$$

Using the small-q representation of $\chi(q)$ and assuming only that $\bar{w}_{\rm core}(0)$ and $\delta\overline{w^2_{\rm core}}(0)$ are finite, we arrive at the limiting form for $F_N(q,\Omega)$ as $q \to 0$

$$F_N\left(q,\Omega\right) \to 1 - \frac{q^2}{4\pi e^2}\left[\frac{2\Omega}{Z}\left[\frac{1}{3}\varepsilon_F + \bar{w}_{\rm core}\left(0\right)\right] + \frac{{\rm d}\mu_{\rm xc}\left(n_{\rm unif}\right)}{{\rm d}n}\right] + \frac{3q^2}{8\pi e^2\varepsilon_F}\frac{\Omega}{Z}\delta\overline{w^2_{\rm core}}\left(0\right). \tag{2.162}$$

Differentiating the above with respect to q twice, and inserting into the expression for $E_{\rm vol}$ leaves

$$\begin{aligned} E_{\rm vol}\left(\Omega\right) = E_{\rm eg}\left(\Omega\right) - \frac{1}{2}\Omega B_{\rm eg}\left(\Omega\right) + \frac{2\Omega}{\left(2\pi\right)^3}\int {\rm d}\mathbf{k}\ f_{\mathbf{k}}\left[\langle\mathbf{k}|w_{\rm core}|\mathbf{k}\rangle - \bar{w}_{\rm core}\left(0\right)\right] \\ + \frac{3}{4}\frac{Z}{\varepsilon_F}\delta\overline{w^2_{\rm core}}\left(0\right) - \frac{\left(Ze\right)^2}{\pi}\int_0^\infty {\rm d}q\ F_N\left(q,\Omega\right) - E^{\rm atom}_{\rm bind}. \end{aligned} \tag{2.163}$$

for a non-local norm-conserving pseudopotential. The interacting electron-gas energy $E_{\rm eg}$ is given by

$$E_{\rm eg}\left(\Omega\right) \equiv \frac{3}{5}Z\varepsilon_F + Z\varepsilon_{\rm xc}\left(n_{\rm unif}\right) \tag{2.164}$$

and $B_{\rm eg} \equiv \Omega\partial^2 E_{\rm eg}/\partial\Omega^2$ is the bulk modulus of the interacting electron-gas with

$$\Omega B_{\rm eg}\left(\Omega\right) = \frac{2}{3}Z\varepsilon_F + Zn_{\rm unif}\frac{{\rm d}\mu_{\rm xc}\left(n_{\rm unif}\right)}{{\rm d}n}. \tag{2.165}$$

It is possible to express $F_N(q,\Omega)$ in terms of $n_{\rm scr}(q)$ and $n_{\rm unif}$,

$$F_N\left(q,\Omega\right) = \left[\frac{n_{\rm scr}\left(q\right)}{n_{\rm unif}}\right]^2 \chi^{-1}\left(q\right) + \frac{q^2}{4\pi e^2}\delta\overline{w^2_{\rm core}}\left(q\right)\frac{\Pi_0\left(q\right)}{n^2_{\rm unif}}. \tag{2.166}$$

The above results for a non-local norm-conserving pseudopotential can be generalised to a non-local AHS pseudopotential with non-zero orthogonalisation hole density. The

screening density $n_{\rm scr}$ can be written with a non-zero $n_{\rm oh}$ contribution

$$n_{\rm scr}\left(q\right)=\left[n_{\rm unif}-\frac{q^2}{4\pi e^2}\bar{w}_{\rm core}\left(q\right)-\left[1-G\left(q\right)\right]n_{\rm oh}\left(q\right)\right]\chi\left(q\right). \tag{2.167}$$

The normalised energy-wavenumber characteristic F_N generalises to

$$F_N\left(q,\Omega\right)=\left[\frac{n_{\rm scr}\left(q\right)}{n_{\rm unif}}\right]^2\chi^{-1}\left(q\right)+\frac{q^2}{4\pi e^2}\delta\overline{w^2_{\rm core}}\left(q\right)\frac{\Pi_0\left(q\right)}{\left(n^*_{\rm unif}\right)^2}+G\left(q\right)\left[\frac{n_{\rm oh}\left(q\right)}{n^*_{\rm unif}}\right]^2, \tag{2.168}$$

where we have defined $n^*_{\rm unif}\equiv(Z^*/Z)n_{\rm unif}=Z^*/\Omega$. Determination of the small-$\mathbf{q}$ limit of $F_N(q,\Omega)$ is the same as before. The small-$\mathbf{q}$ behaviour of $n_{\rm oh}(q)$ which can be expressed in the form

$$n_{\rm oh}\left(q\right)\rightarrow-\frac{\left(Z^*-Z\right)}{\Omega}\left[1-\gamma^2_{\rm oh}\left(\frac{q}{k_F}\right)\right]. \tag{2.169}$$

The calculation of the constant $\gamma_{\rm oh}$ is given by Moriarty [99]. For the AHS pseudopotential used in the GPT, the volume term is generalized to

$$\begin{aligned}E_{\rm vol}\left(\Omega\right)=E^0_{\rm fe}\left(\Omega\right)-\frac{1}{2}\Omega B_{\rm eg}\left(\Omega\right)+\frac{2\Omega}{\left(2\pi\right)^3}\int{\rm d}\mathbf{k}\ f_{\mathbf{k}}\langle\mathbf{k}|w_{\rm pa}|\mathbf{k}\rangle\left[1+\langle\mathbf{k}|P_c|\mathbf{k}\rangle\right]-Z^*\bar{w}_{\rm core}\left(0\right)\\+\frac{3}{4}\frac{Z}{\varepsilon_F}\delta\overline{w^2_{\rm core}}\left(0\right)+\frac{9}{10}\frac{\left(Z^*e\right)^2}{R_{\rm WS}}-\frac{\left(Z^*e\right)^2}{\pi}\int_0^\infty{\rm d}q\ F_N\left(q,\Omega\right)+\delta E^*_{\rm oh}\left(\Omega\right)-E^{\rm atom}_{\rm bind}\end{aligned} \tag{2.170}$$

with the definition

$$\delta E^*_{\rm oh}\left(\Omega\right)\equiv\delta E_{\rm oh}\left(\Omega\right)+\left[\left(Z^*\right)^2-Z^2\right]\frac{\varepsilon_F}{3Z}-4\pi Z^*e^2\frac{\left(Z^*-Z\right)}{\Omega k^2_F}\gamma_{\rm oh}. \tag{2.171}$$

2.5 Summary of the GPT Formalism

Much of the apparent complexity of the simple-metal GPT is the result of bookkeeping, particularly with regard to the non-local AHS pseudopotential. However, the steps required to derive a simple-metal GPT potential are quite simple in reality. Having said that, a full account of all terms that arise from a non-local pseudopotential combined with self-consistent electron screening is required for close agreement with DFT and experiment.

The first step in a GPT calculation, simple-metal or otherwise, is to calculate the pseudopotential. This is done in the GPT by first defining a zeroth-order pseudoatom [181]. The next step is to perform a self-consistent DFT calculation, typically in the LDA, for the core eigenvalues and core eigenvectors with the pseudoatom potential. The advantage of defining a pseudoatom is that these quantities should be close to the 'true' values in the bulk metal. The core eigenvalues and core eigenvectors are used to construct the non-local AHS pseudopotential in Eq.(2.56). In addition, the effective valence Z^* and orthogonalisation-hole density $n_{\rm oh}$ are calculated at this stage, as too are the plane wave matrix elements of the pseudopotential.

There are only two unknown quantities in the total valence binding energy in Eq.(2.51): the valence eigenvalues $E_{\mathbf{k}}$ and the valence electron density $n_{\rm val}$. These quantities can both be calculated using pseudopotential perturbation theory. This calculation results in a reciprocal space theory which was used in the past to calculate a variety of bulk properties. Nowadays the simple-metal GPT is more useful as a real-space interatomic potential. After some term reshuffling involving $|S(\mathbf{q})|^2$, it can be shown that this entire procedure leads to a real-space volume-dependent pair potential plus a collective many-body volume term.

In a practical calculation, the central quantities of interest are the screening density $n_{\rm scr}$ and normalised energy-wavenumber characteristic F_N. Using linear screening,

these quantities can be written in terms of input pseudopotential and electron gas quantities. The final steps are to calculate the volume term E_{vol} using Eq.(2.163) and the pair potential v_2 is calculated from the integral over $\mathbf{q}$ in Eq.(2.134).

Chapter 3

The Adaptive Generalised Pseudopotential Theory

"Adapt or perish, now as ever, is Nature's inexorable imperative."

H. G. Wells

In the previous chapter, we have introduced electronic structure theory and the generalised pseudopotential theory (GPT) applied to simple metals. The central departure from conventional density functional theory (DFT), is through the calculation of the band energy E_{band} in Eq.(2.83). In the GPT, we expand the band energy E_{band} as a perturbation series truncated at second-order in the total crystal pseudopotential W. The final term in the perturbative expansion in Eq.(2.72) contains a sum over $\mathbf{q}$-vectors. It is important to note that there is no restriction on the $\mathbf{q}$-vectors that can be summed over. For instance, if we restrict the sum to be over the set of $\mathbf{q}$-vectors which are integer multiples of reciprocal lattice vectors $\{\mathbf{G}\}$, then the pseudowavefunctions obey Bloch's theorem [201]. This is evident by rewriting Eq.(2.77) as a sum

over **G**-vectors in position representation

$$\phi_{\mathbf{k}}(\mathbf{r}) = \frac{1}{\sqrt{N\Omega}} \sum_{\mathbf{G}} a_{\mathbf{k}+\mathbf{G}} e^{i(\mathbf{k}+\mathbf{G})\cdot\mathbf{r}} = e^{i\mathbf{k}\cdot\mathbf{r}} u_{\mathbf{k}}(\mathbf{r}) \tag{3.1}$$

where $u_{\mathbf{k}}(\mathbf{r})$ is a function which contains the periodicity of the lattice. This is the standard statement of Bloch's theorem [127], and the function $u_{\mathbf{k}}$ is given by

$$u_{\mathbf{k}}(\mathbf{r}) = \frac{1}{\sqrt{N\Omega}} \sum_{\mathbf{G}} a_{\mathbf{k}+\mathbf{G}} e^{i\mathbf{G}\cdot\mathbf{r}}. \tag{3.2}$$

Bloch's theorem is an exact statement about the electron wavefunctions in the presence of a periodic potential. In order to describe defective crystals where there is no translation symmetry, we would need to lift the restriction on the **q**-vectors and allow them to take any value. This is precisely what is done in Eq.(2.77) and it ensures that the GPT can be applied in the absence of translational symmetry. In real space, the GPT only depends on the volume Ω and the interatomic separation R_{ij}. Therefore, the GPT is transferable to all ion configurations in the bulk ordered and disordered metal, including all structural phases of both the solid and the liquid, as well as the deformed solid and imperfect bulk solid with either point or extended defects present. In particular, the GPT has been successful in the simulation of dislocations [103, 202, 203].

The explicit volume dependence of the volume term E_{vol} and the pair potential v_2 in Eq.(2.82) is global and not local. For instance, if we were to remove an atom and create a vacancy in the centre of a supercell, the effect on the form of the interaction is the same for the nearest neighbours of the vacancy as for the atoms at the edge of the supercell. More generally, the creation of a free surface, or even a bulk defect that comes with significant free volume, such as a vacancy, receives no contribution to its formation energy from E_{vol}. In general, formation energies of such defects or surfaces are severely underestimated as the volume term contains the major contribution to the

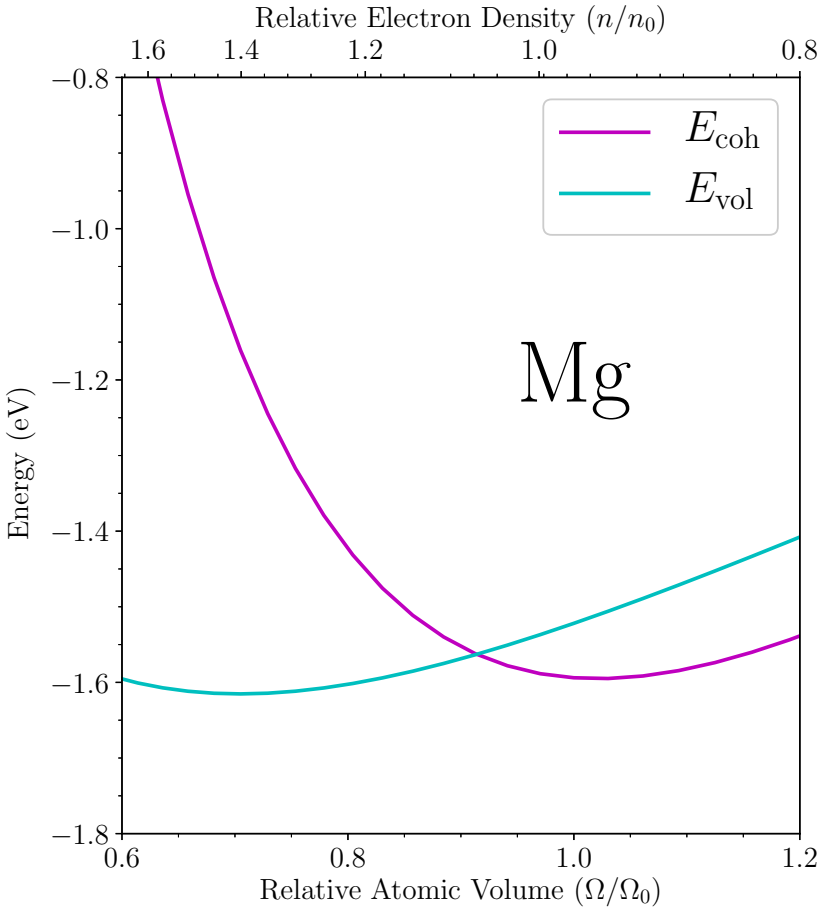

Fig. 3.1: The cohesive energy E_{coh} (magenta) calculated for hcp Mg at fixed $c/a = 1.62$. This is plotted against the volume term E_{vol} where it is evident that it is a considerable proportion of E_{coh}. Here $\Omega_0 = 156.8$ a.u. and $n_0 = Z/\Omega_0$ is the corresponding bulk average valence electron density, with $Z = 2$.

cohesive energy. In Fig.(3.1), we see that the cohesive energy E_{coh} and volume term E_{vol} are of the same order of magnitude. In Mg specifically, there is a discrepancy of around 50% in the predicted vacancy formation energy from the GPT (as we will see later in this chapter). This is an example of a well-known issue with second-order pseudopotential perturbation theory [13].

A related issue is associated with the calculation of the bulk modulus B, sometimes called the inverse compressibility, with second-order pseudopotential perturbation theory. There are multiple methods to calculate the bulk modulus with the GPT. The

first method exploits the fact that B can be defined in terms of the second derivative of the total energy. On the other hand, the second method uses the fact that B can be written as a sum of elastic moduli. For instance, in a cubic crystal we have $B = (C_{11} + 2C_{12})/3$ [204]. The elements of the elastic moduli tensor can, in turn, be related to the phonon group velocities. Therefore, the bulk modulus can also be derived by considering the long wavelength $\mathbf{q} \to 0$ phonon dispersion.

We can derive an expression for the bulk modulus using the simple metal GPT with both methods. We can rewrite the GPT total energy, which is the cohesive energy in Eq.(2.82) multiplied by the number of atoms N, in terms of the average electron density $\bar{n} = n_{\text{unif}}$

$$E_{\text{tot}}\left(\mathbf{R}, \bar{n}\right) = N E_{\text{vol}}\left(\bar{n}\right) + \frac{1}{2}{\sum_{ij}}' v_2\left(R_{ij}, \bar{n}\right). \tag{3.3}$$

This is entirely equivalent to working with the atomic volume Ω. The first method of calculating the bulk modulus B is equivalent to evaluating the following formula

$$B_s = \Omega\left(\frac{\mathrm{d}^2 E_{\text{tot}}}{\mathrm{d}\Omega^2}\right). \tag{3.4}$$

This can be found by numerically fitting an equation of state and calculating the curvature at the volume of interest. Note that we have given B_s a subscript to distinguish as the *static* bulk modulus. Alternatively, we may proceed by calculating the analytic derivatives of Eq.(3.3) directly. First, we expand the operator $\mathrm{d}/\mathrm{d}\Omega$ as a total derivative and using the chain rule

$$\frac{\mathrm{d}}{\mathrm{d}\Omega} = \frac{\partial}{\partial\Omega} + \frac{1}{3\Omega} R_{ij\alpha}\frac{\partial}{\partial R_{ij\alpha}} - \frac{\bar{n}}{\Omega}\frac{\partial}{\partial\bar{n}}. \tag{3.5}$$

Applying this operator twice to Eq.(3.3) and multiplying by the atomic volume Ω yields the static bulk modulus B_s

$$B_s = \frac{\bar{n}^2}{\Omega}\frac{\partial^2 E_{\mathrm{vol}}(\bar{n})}{\partial \bar{n}^2} + \frac{2\bar{n}}{\Omega}\frac{\partial E_{\mathrm{vol}}(\bar{n})}{\partial \bar{n}} + \frac{1}{18\Omega}\sum_{i\neq 0}\left[-2R_{0i}\frac{\partial}{\partial R_{0i}} + R_{0i}^2\frac{\partial^2}{\partial R_{0i}^2}\right] v_2(R_{0i},\bar{n}) + \frac{1}{\Omega}\sum_{i\neq 0}\left[\left(1-\frac{1}{3}R_{0i}\frac{\partial}{\partial R_{0i}}\right)\bar{n}\frac{\partial v_2(R_{0i},\bar{n})}{\partial \bar{n}} + \frac{1}{2}\bar{n}^2\frac{\partial^2 v_2(R_{0i},\bar{n})}{\partial \bar{n}^2}\right]. \quad (3.6)$$

In the above expression, we have assumed that the crystal structure has equivalent ion sites. The density derivatives enter the bulk modulus to account for the change in interaction under homogenous deformation. Contrast this with the second method for calculating the bulk modulus using the inhomogeneous deformations created by a lattice wave. We shall denote this *dynamical* bulk modulus as B_d. Importantly, the propagation of a phonon does not affect the total volume (outside of the $\mathbf{q}\to 0$ limit). Therefore, the density dependence does not enter the expression for B_d. To see this, we first write down the harmonic correction to the internal energy due to an inhomogeneous deformation of the crystal from its equilibrium ion sites $\{\mathbf{R}^0\}$

$$E_{\mathrm{tot}}(\{\mathbf{R}\},\bar{n}) = E_{\mathrm{tot}}(\{\mathbf{R}^0\},\bar{n}) + \frac{1}{2}\sum_{ij\mu\nu} A_{\mu\nu}(R_{ij},\bar{n})\,u_{i\mu}u_{j\nu} \quad (3.7)$$

where $u_i = \mathbf{R}_i - \mathbf{R}_i^0$ is a displacement vector. The second term is the phonon potential in the harmonic approximation and $A_{\mu\nu}$ is the force-constant matrix [204]

$$A_{\mu\nu}(R_{ij},\bar{n}) = -\left(\frac{\partial^2}{\partial R_{ij}^2} - \frac{1}{R_{ij}}\frac{\partial}{\partial R_{ij}}\right) v_2(R_{ij},\bar{n})\,\frac{R_{ij\mu}R_{ij\nu}}{R_{ij}^2} - \frac{1}{R_{ij}}\frac{\partial v_2(R_{ij},\bar{n})}{\partial R_{ij}}\delta_{\mu\nu}. \quad (3.8)$$

The eigensolution of the harmonic phonon Hamiltonian requires the diagonalisation of the dynamical matrix D. For simplicity, we shall assume that the crystal structure is a Bravais lattice and the metal is elemental. In this case, the dynamical matrix will be a real matrix of rank 3. Taking into account the translational symmetry, we may

write the dynamical matrix as

$$D_{\mu\nu}\left(\mathbf{q}\right) = \frac{1}{M}\sum_{i\neq 0} A_{\mu\nu}\left(R_{0i},\bar{n}\right)\left[\cos\left(\mathbf{q}\cdot\mathbf{R}_{0i}\right)-1\right]. \tag{3.9}$$

This form of the dynamical matrix D makes it simple to derive a limiting form for the dynamical matrix D in the $\mathbf{q}\to 0$ limit. We have

$$D_{\alpha\beta}\left(\mathbf{q}\right) \sim \frac{1}{2M}\sum_{j\neq 0}\sum_{\mu\nu} A_{\alpha\beta}\left(R_{0j},\bar{n}\right) q_\mu q_\nu R_{0j\mu}R_{0j\nu} = \Omega\sum_{\mu\nu}\left[\alpha\beta,\mu\nu\right]\tilde{q}_\mu\tilde{q}_\nu, \tag{3.10}$$

where we have introduced the mass-reduced wavevectors $\tilde{q} = q/\sqrt{M}$ and

$$\left[\alpha\beta,\mu\nu\right] = \frac{1}{2\Omega}\sum_{j\neq 0} A_{\alpha\beta}\left(R_{0j},\bar{n}\right) R_{0j\mu}R_{0j\nu}. \tag{3.11}$$

The elastic moduli tensor $C_{\mu\alpha\nu\beta}$ can be written in terms of this new tensor [205]

$$C_{\mu\alpha\nu\beta} = \left[\alpha\beta,\mu\nu\right] + \left[\beta\mu,\alpha\nu\right] - \left[\beta\nu,\alpha\mu\right]. \tag{3.12}$$

The elastic moduli tensor can be used to construct the dynamic bulk modulus B_d using the cubic relation $B_d = (C_{11}+2C_{12})/3$ for instance. This yields

$$B_d = \frac{1}{18\Omega}\sum_{i\neq 0}\left[-2R_{0i}\frac{\partial}{\partial r} + R_{0i}^2\frac{\partial^2}{\partial r^2}\right] v_2\left(R_{0i},\bar{n}\right). \tag{3.13}$$

This can be compared with Eq.(3.6) and clearly $B_s \neq B_d$. Removing the volume dependence from the GPT total energy, i.e. a pure pair potential, brings the static and dynamic bulk modulus back into co-incidence. We know that these two methods should agree since the experimental elastic constants are typically inferred through the phonon group velocities [206]. This problem is known as the bulk modulus discrepancy [207] that affects all interatomic potentials derived using second-order pseudopotential

perturbation theory. The goal of this chapter is to extend the GPT formalism so that these volume derivatives arise naturally and at the same time, correct the discrepancy found in the formation energies of free surfaces and defects associated with free volumes.

3.1 Local Volume Corrections

One conclusion to draw from the previous discussion is that the problem with surface and vacancy formation energies, and the bulk modulus discrepancy can be resolved at higher orders in perturbation theory. Wallace argued that the additional volume derivatives in the static bulk modulus B_s would arise as a result of the inclusion of higher order terms in the pseudopotential [208]. Simultaneously, Brovman and Kagan [209] showed that the discrepancy is formally resolved, albeit in a non-transparent manner, at fourth order perturbation theory where there is an additional second-order correction to the dynamical matrix. Despite this success, we will briefly show why proceeding along these lines is not a good idea. Inclusion of higher-order terms is conceptually straightforward using the pseudo Green's function formalism of Moriarty [210]. The pseudo Green's function can be found to infinite order in perturbation theory via Dyson's equation

$$G_{\mathbf{k}\mathbf{k}'} = G^0_{\mathbf{k}\mathbf{k}'} + \sum_{\mathbf{k}''\mathbf{k}'''} G^0_{\mathbf{k}\mathbf{k}''}\Sigma_{\mathbf{k}''\mathbf{k}'''}G_{\mathbf{k}'''\mathbf{k}'} \tag{3.14}$$

with G^0 being the free-electron pseudo Green's function

$$G^0_{\mathbf{k}\mathbf{k}'} = \frac{\delta_{\mathbf{k}\mathbf{k}'}}{(E + i\eta - \varepsilon_{\mathbf{k}})} \tag{3.15}$$

where η is an infinitesimal parameter which lifts the pole of the Green's function off the real line and $\varepsilon_{\mathbf{k}}$ is the energy of a plane-wave with wavevector $\mathbf{k}$. We will implicitly

work in the limit that $\eta \to 0^+$. The self-energy $\Sigma_{\mathbf{k}\mathbf{k}'}$ is an infinite sum of plane-wave pseudopotential matrix elements

$$\Sigma_{\mathbf{k}\mathbf{k}'} = W_{\mathbf{k}\mathbf{k}'} + \sum_{\mathbf{k}''} \frac{W_{\mathbf{k}\mathbf{k}''}W_{\mathbf{k}''\mathbf{k}'}}{(E+i\eta-\varepsilon''_{\mathbf{k}})} + \sum_{\mathbf{k}''\mathbf{k}'''} \frac{W_{\mathbf{k}\mathbf{k}''}W_{\mathbf{k}''\mathbf{k}'''}W_{\mathbf{k}'''\mathbf{k}'}}{(E+i\eta-\varepsilon''_{\mathbf{k}})\,(E+i\eta-\varepsilon'''_{\mathbf{k}})} + \cdots \tag{3.16}$$

where $W_{\mathbf{k}\mathbf{k}'}$ is shorthand for the plane-wave matrix element of the crystal pseudopotential. The density of states $\rho(E)$ may be written in terms of the pseudo Green's function

$$\rho\,(E) = -\frac{2}{\pi}\mathrm{Im}\sum_{\mathbf{k}} G_{\mathbf{k}\mathbf{k}} = \rho_0\,(E) - \frac{2}{\pi}\mathrm{Im}\sum_{\mathbf{k}} \frac{\Sigma_{\mathbf{k}\mathbf{k}}\,(E)}{(E+i\eta-\varepsilon_{\mathbf{k}})^2} \tag{3.17}$$

and ρ_0 is the free-electron density of states

$$\rho_0\,(E) = -\frac{2}{\pi}\mathrm{Im}\sum_{\mathbf{k}} \frac{1}{E+i\eta-\varepsilon_{\mathbf{k}}} = \left(\frac{2m}{\hbar^2}\right)^{3/2}\frac{\Omega E^{1/2}}{\pi^2}. \tag{3.18}$$

The (valence) band energy E_{band} can be written in terms of the integrated density of states $\mathcal{D}(E) = \mathcal{D}_0(E) + \delta\mathcal{D}_{\mathrm{sp}}(E)$

$$E_{\mathrm{band}} = \frac{3}{5}\,(ZN)\,\varepsilon_F - \int_0^{\varepsilon_F} \mathrm{d}E\;\delta\mathcal{D}_{\mathrm{sp}}\,(E) + \delta E_{\mathrm{band}} \tag{3.19}$$

where ε_F is the free electron Fermi energy and $\delta\mathcal{D}_{\mathrm{sp}}(E)$ is the perturbative correction, summed to all orders, to the integrated density of states

$$\begin{aligned}\delta\mathcal{D}_{\mathrm{sp}}\,(E) = \frac{2}{\pi}\mathrm{Im}\Bigg[&\sum_{\mathbf{k}} \frac{W_{\mathbf{k}\mathbf{k}}}{E+i\eta-\varepsilon_{\mathbf{k}}} + \frac{1}{2}\sum_{\mathbf{k}\mathbf{k}'} \frac{W_{\mathbf{k}\mathbf{k}'}W_{\mathbf{k}'\mathbf{k}}}{(E+i\eta-\varepsilon_{\mathbf{k}})\,(E+i\eta-\varepsilon_{\mathbf{k}'})} \\ &+ \frac{1}{3}\sum_{\mathbf{k}\mathbf{k}'\mathbf{k}''} \frac{W_{\mathbf{k}\mathbf{k}'}W_{\mathbf{k}'\mathbf{k}''}W_{\mathbf{k}''\mathbf{k}}}{(E+i\eta-\varepsilon_{\mathbf{k}})\,(E+i\eta-\varepsilon_{\mathbf{k}'})\,(E+i\eta-\varepsilon_{\mathbf{k}''})} + \cdots\Bigg].\end{aligned} \tag{3.20}$$

The small δE_{band} term is to account for the change in the Fermi energy $\varepsilon_F \to E_F$ once the perturbation is switched on

$$\delta E_{\text{band}} = NZ\left(E_F - \varepsilon_F\right) - \int_{\varepsilon_F}^{E_F} \mathrm{d}E\ \mathcal{D}\left(E\right). \tag{3.21}$$

There are a number of additional complications that have arisen as a result of the inclusion of higher order terms in the pseudopotential W. The Fermi energy E_F can be found by using the constraint at 0 K that

$$ZN = \int_0^{E_F} \mathrm{d}E\ \rho(E). \tag{3.22}$$

Furthermore, the summations in Eq.(3.20) give rise to coupled three-dimensional reciprocal space integrations if W a non-local pseudopotential is used. This renders a reciprocal space total energy formalism effectively intractable. In addition, the self-consistent screening implicit in W should in principle be carried out beyond linear order. Generally for an order-N total energy, the screening should be carried out to order-$(N-1)$.

There has been a number of practical attempts to go beyond second-order pseudopotential perturbation theory. In all of these attempts, the simplifying approximation of a local pseudopotential was made. Specifically, Lloyd and Sholl [211] were able to derive closed form expressions for the third-order band energy and second-order screening (neglecting exchange and correlation) in reciprocal space. Independently, Brovman *et al.* [212] developed a local pseudopotential third-order total energy formalism with first-order screening with corrections for exchange and correlation. This was then applied to Mg where the phonon spectrum, elastic moduli, equations of state and structural energy differences were calculated. The accuracy of these results is comparable to those obtained using a non-local pseudopotential and second-order pseudopotential perturbation theory. Hasegawa [213] was able to transform the third-

order total energy expression with linear screening into real-space. Importantly, however, a fourth-order total energy expression has not been developed. Recall that it is at fourth-order that the bulk modulus discrepancy is formally resolved thanks to the additional second-order contributions to the dynamical matrix.

The inclusion of higher-order terms in the perturbation expansion leads to additional multi-ion potentials in the total energy, whose limiting form was derived by Harrison [214]. These multi-ion potentials do lead to corrections that must resolve both the bulk modulus discrepancy and the problems associated with free surfaces and free volumes. However, there remains a conceptual problem as to how and why these corrections arise. Finnis [190] noted that the bulk modulus discrepancy arises because the pseudoatom cannot adjust its shape or size in the presence of a phonon. Contrast this to the reality that the local electron density will adjust in the presence of a shift in the positions of the ions. An alternative approach allows the pseudoatoms to adjust according to the local electron density environment. Along these lines and following Moriarty and Phillips [147], we can rewrite Eq.(3.3) as

$$E_{\text{tot}}\left(\{\mathbf{R}\}, n_{\text{val}}\right) = \sum_i \left[E_{\text{vol}}\left(\bar{n}_i\right) + \frac{1}{2} \sum_{j \neq i} v_2\left(R_{ij}, \bar{n}_{ij}\right) \right] \tag{3.23}$$

where $\bar{n}_i$ is the average local electron density about the site i and $\bar{n}_{ij} = (\bar{n}_i + \bar{n}_j)/2$ is the arithmetic average. Rosenfeld and Stott [207] used an empirical sum of Gaussians representation of the local electron density, where the width was chosen such that $\bar{n}_i \approx n_{\text{unif}}$ in the bulk perfect crystal. They showed that the bulk modulus discrepancy was resolved in this local electron density approach. The force between ions i and j no longer solely depends on the relative position R_{ij}, but also the relative positions of all the other atoms in the local neighbourhood since these atoms contribute to the shape and size of the pseudoatoms. Subsequently, Moriarty and Phillips [147] derived a first-principles analytic form for the local electron density. This proved

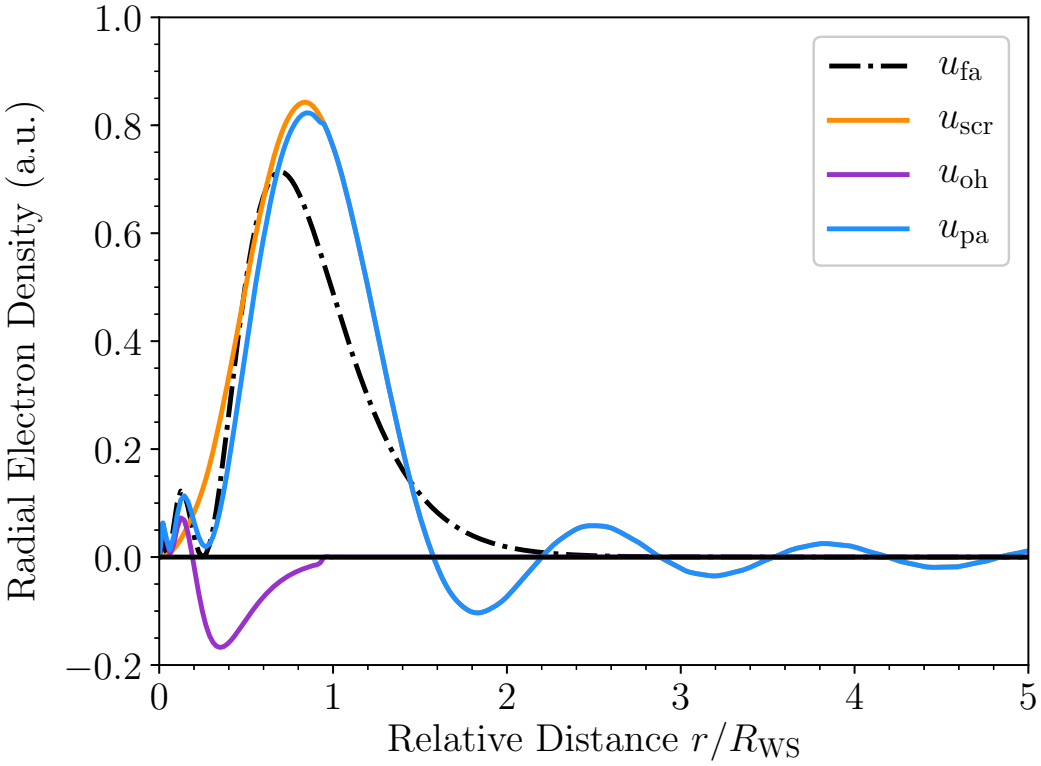

Fig. 3.2: The radial valence electron density $u(r) = 4\pi r^2 n(r)$ for the $3s$ and $3p$ bands in Mg for the pseudoatom $n = n_{\mathrm{pa}}$ (blue) in the bulk metal at $\Omega = 156.8$ a.u.^{3} and also for the free-atom $n = n_{\mathrm{fa}}$ (checked). The pseudoatom density is pushed outward relative to the free-atom, and has the familiar Friedel long-range screening oscillations. Also shown are the real-space screening density n_{scr} (orange) and orthogonalization-hole density (purple).

successful for application to unrelaxed surfaces and vacancy formation energies in Mo and Cu. It is this approach that we further develop and rename the adaptive generalised pseudopotential theory (aGPT).

3.1.1 Representing the Local Electron Density

The total energy in Eq.(3.23) is precisely equivalent to Eq.(3.3) in the perfect crystal with equivalent ion positions. In this case, the aGPT description amounts only to a redefinition of variables. Using the arguments of Finnis [190], we apply Eq.(3.23) as

an ansatz to all ion configurations including free surfaces and defects. From Fig.(3.1), we expect there will be a positive contribution to the formation energy of surfaces and vacancies due to $\bar{n}_i$ being lower near a surface or vacancy site than at a bulk ion site. Moriarty and Phillips were able to show that, for the central transition metal Mo and late transition metal Cu, this ansatz can be used to obtain good unrelaxed surface and vacancy formation energies. In the case of Cu, the local density corrections were found to be very large, roughly 70% for both the surface and vacancy formation energies. In the case of Mo, however, the corrections were found to be considerably smaller roughly 30-40% for the surface energies and just 5% for the vacancy formation energy. The smaller contribution to the vacancy formation energy in Mo suggests that the local character needed in the global-volume representation of the total energy is already present to a large degree through the d bonding contributions to $E_{\rm tot}$ in the central transition metals. In the simple metals, the unrelaxed GPT vacancy formation energy can be written as [10]

$$\begin{aligned} E^{\rm u}_{\rm vac} &= -\left(E^0_{\rm coh} - E^0_{\rm vol}\right) + \Omega_0 P^0_{\rm vir}, \\ &= -\frac{1}{2}\sum_{i\neq 0} v_2\left(R_{0i},\Omega_0\right) - \frac{1}{6}\sum_{i\neq 0} R_{0i}\frac{\partial v_2\left(R_{0i},\Omega_0\right)}{\partial R_{0i}}, \end{aligned} \tag{3.24}$$

where $E^0_{\rm coh} \equiv E_{\rm tot}\left(\{\mathbf{R}^0\},\Omega_0\right)/N$ and $E^0_{\rm vol} \equiv E_{\rm vol}(\Omega_0)$. The virial pressure $P^0_{\rm vir} \equiv P_{\rm vir}(\Omega_0)$ arises in connection with the energy needed to compress the lattice uniformly and maintain constant volume $\Omega = \Omega_0$ once the vacancy is created. It is worth noting that this is the unrelaxed vacancy formation energy and force relaxation works to reduce the vacancy formation energy by a small amount typically 0.01 eV. Of the two terms on the second line of Eq.(3.24), the virial pressure term is largest for Mg at its equilibrium lattice parameters but the total is only $E^u_{\rm coh} = 0.44$ eV some 45% below the experimental value [215] as discussed in Sec.(3.3.1). Due to the fact that Mg is a

simple metal and there is this large discrepancy between the calculated GPT vacancy formation energy, we shall use Mg as a prototype test metal for the aGPT.

We shall proceed in deriving a representation of the local electron density from the GPT formalism and applying it to Mg. Recall that the valence electron density $n_{\rm val}$ in the GPT can be written as

$$n_{\rm val}\left(\mathbf{r}\right) = n_{\rm unif} + \delta n_{\rm scr}\left(\mathbf{r}\right) + \delta n_{\rm oh}\left(\mathbf{r}\right) \tag{3.25}$$

where $n_{\rm unif} = Z/\Omega$, $\delta n_{\rm scr}$ is the screening electron density given by Eq.(2.99) and $\delta n_{\rm oh}$ is the orthogonalisation-hole density given by Eq.(2.68). Alternatively, we can write the valence electron density $n_{\rm val}$ as a sum of self-consistently screened pseudoatom densities $n_{\rm pa}$

$$n_{\rm val}\left(\mathbf{r}\right) = \sum_i n_{\rm pa}\left(\mathbf{r} - \mathbf{R}_i\right). \tag{3.26}$$

The precise form of the pseudoatom density $n_{\rm pa}$ can be easily derived from Eqs.(3.25), (2.99) and (2.68). We do this by first inserting the full form of the structure factor into Eq.(2.99) and adding in the $\mathbf{q} = 0$ term to the sum over $\mathbf{q}$ to account for the nett uniform density $Z^* n_{\rm unif}/Z$. Finally, we convert the sum to an integral and infer that the single-site pseudoatom density must be given by

$$\begin{aligned} n_{\rm pa}\left(\mathbf{r}, \Omega\right) &= \frac{\Omega}{\left(2\pi\right)^3} \int \mathrm{d}\mathbf{q}\; n_{\rm scr}\left(q\right) e^{i\mathbf{q}\cdot\mathbf{r}} + n_{\rm oh}\left(\mathbf{r}\right), \\ &= \frac{\Omega}{2\pi^2 r} \int_0^\infty \mathrm{d}q\; q n_{\rm scr}\left(q\right) \sin\left(qr\right) + n_{\rm oh}\left(\mathbf{r}\right) \end{aligned} \tag{3.27}$$

as the screening density is spherically symmetric. The calculated GPT radial pseudoatom density $u_{\rm pa}(\mathbf{r}) = 4\pi r^2 n_{\rm pa}(\mathbf{r})$ for Mg at the observed equilibrium volume

$\Omega = 156.8$ a.u. is shown in Fig.(3.2) and compared with the corresponding free-atom density for the valence $3s$ and $3p$ electrons. In this calculation, the local field correction was taken to be of the Ichimaru-Utsumi form [177] referenced to the correlation energy function of Vosko-Wilk-Nusair [167].

To connect the GPT valence electron density with the aGPT total energy in Eq.(3.23), we spatially average the GPT valence electron density about the site i using an arbitrary normalized distribution function f_w. For a bulk crystal with equivalent ion sites, the spatially averaged electron density $\bar{n}_i$ about a site i is constrained to be the uniform valence electron density n_{unif}. Combining the two equivalent expressions for the valence electron densities in Eq.(3.25) and Eq.(3.26) yields the *bulk constraining equation*

$$\bar{n}_i \equiv n_{\text{unif}} = \sum_j \bar{n}_{\text{pa}}\left(R_{ij}, \Omega\right) - \delta\bar{n}^i_{\text{oh}} - \delta\bar{n}^i_{\text{scr}}. \tag{3.28}$$

Here the bar over the densities refer to an averaging with respect to some distribution function f_w i.e.

$$\bar{n}_{\text{pa}}\left(R_{ij}, \Omega\right) = \int \mathrm{d}\mathbf{r}\ f_w\left(\mathbf{r} - \mathbf{R}_i\right) n_{\text{pa}}\left(\mathbf{r} - \mathbf{R}_j, \Omega\right) \tag{3.29}$$

with $\delta\bar{n}^i_{\text{scr}}$ and $\delta\bar{n}^i_{\text{oh}}$ having similar forms. Typically, this averaging smooths out the long-range screening oscillations. As a result of the bulk constraining equation, the aGPT preserves the bulk total energy for any given crystal structure with equivalent ion sites. The first step towards developing a practical aGPT scheme for describing defects or surfaces is to make the approximation that

$$\bar{n}_i = \sum_j \bar{n}_{\text{pa}}\left(R_{ij}, \Omega\right) - \delta\bar{n}^i_{\text{oh}} - \delta\bar{n}^i_{\text{scr}} \tag{3.30}$$

can be applied generally. Furthermore, the spatially-averaged local electron density $\bar{n}_i$

can be broken down into an effective on-site contribution $\bar{n}_a^i = \bar{n}_{\mathrm{pa}}(R_{ii}, \Omega) - \delta\bar{n}_{\mathrm{oh}}^i - \delta\bar{n}_{\mathrm{scr}}^i$ and an off-site or background component $\bar{n}_b^i$ where

$$\bar{n}_b^i = \sum_{j \neq i} \bar{n}_{\mathrm{pa}}\left(R_{ij}, \Omega\right). \tag{3.31}$$

We make an additional assumption that the on-site density is constant $\bar{n}_a^i \equiv \bar{n}_a$ and as a result only the background density n_b^i is site-dependent. Under these assumptions, we may calculate the on-site density $\bar{n}_a$ using the bulk-constraining equation in Eq.(3.28). In practice this amounts to first calculating $\bar{n}_a$ for an ideal bulk crystal prior to calculating the total energy for the surface or defective crystal. As a result, there is a small structure dependence in $\bar{n}_a$. For certain d-band metals e.g. Cu, there may be s-d transfer between the surface and the bulk [147]. In which case, all of the densities must be scaled by a factor Z_i/Z to account for this, where Z_i is a self-consistently determined effective sp occupation on the site i.

The next step towards a practical implementation of the aGPT is to specify the form of the distribution function f_w in Eq.(3.29). We choose f_w to correspond to a sigmoid function

$$f_w(r) = \begin{cases} \mathcal{N}^{-1} & r < R_a \\ \mathcal{N}^{-1}\left(1 + \alpha\left(\frac{r}{R_0} - 1\right)^2\right)\exp\left[-\alpha\left(\frac{r}{R_0} - 1\right)^2\right] & r \geq R_a \end{cases} \tag{3.32}$$

which is the sigmoid function that is typically used in the GPT to truncate the pairwise interaction [202] albeit with a different value of the parameter α. For large values of α this corresponds to an average over a sphere of radius R_a. The normalisation $\mathcal{N}$ of the distribution function f_w is given by

$$\mathcal{N} = V_w + \left[\frac{8\pi}{\alpha} + \frac{5\pi^{3/2}}{2\alpha^{3/2}} + \frac{3\pi^{3/2}}{\sqrt{\alpha}}\right] R_a^3 \tag{3.33}$$

which in the limit $\alpha \to \infty$ is the volume of a sphere of radius R_a. The two parameters α and R_a represent the only parameters in this form of the aGPT. The first parameter α, which adjusts the width of the Gaussian, is chosen such that the radial derivatives of the spatially averaged pseudoatom density are 'smooth'. If the radial derivatives were not 'smooth' then there would be an unphysically large change in the forces as the interatomic separation changes from less than R_a to greater than R_a and vice-versa. We usually take $\alpha = 25$ which produces a spatially averaged pseudoatom density with smooth derivatives over a wide range of averaging sphere radii. We have a certain amount of freedom in choosing a value for R_a since physical properties do not seem strongly dependent on R_a (as we shall see in the upcoming sections). We choose the optimum R_a to be that which reproduces the GPT volume-conserving elastic constants most closely. Whilst other normalized distribution functions have been trialled, including distributions with fatter tails, none represented an improvement on the sigmoid function.

The resulting spatially-averaged pseudoatom density was calculated numerically using a composite Simpson's rule and is plotted in Fig.(3.3). For values of R_a in the range $R_a/R_{\mathrm{WS}} \in [1, 2]$, the spatially averaged pseudoatom density looks like a Gaussian. A function of this type was proposed in the empirical approach taken previously [207]. For larger values of R_a in the range $R_a/R_{\mathrm{WS}} \in [3, 4]$, the resulting spatially-averaged pseudoatom density is almost flat over the first two neighbour shells.

The spatially-averaged pseudoatom density is smoothly truncated to ensure force continuity during molecular dynamics. If we denote R_0 and R_c as the cut-off onset and final termination respectively, then our approach is to replace $\bar{n}_{\mathrm{pa}}$ by a polynomial whose value and derivatives exactly match $\bar{n}_{\mathrm{pa}}$ at R_0 and whose derivatives are precisely zero at R_c. This polynomial can be found using Hermite interpolation which finds an $(nm - 1)$ interpolating polynomial given knowledge of the function

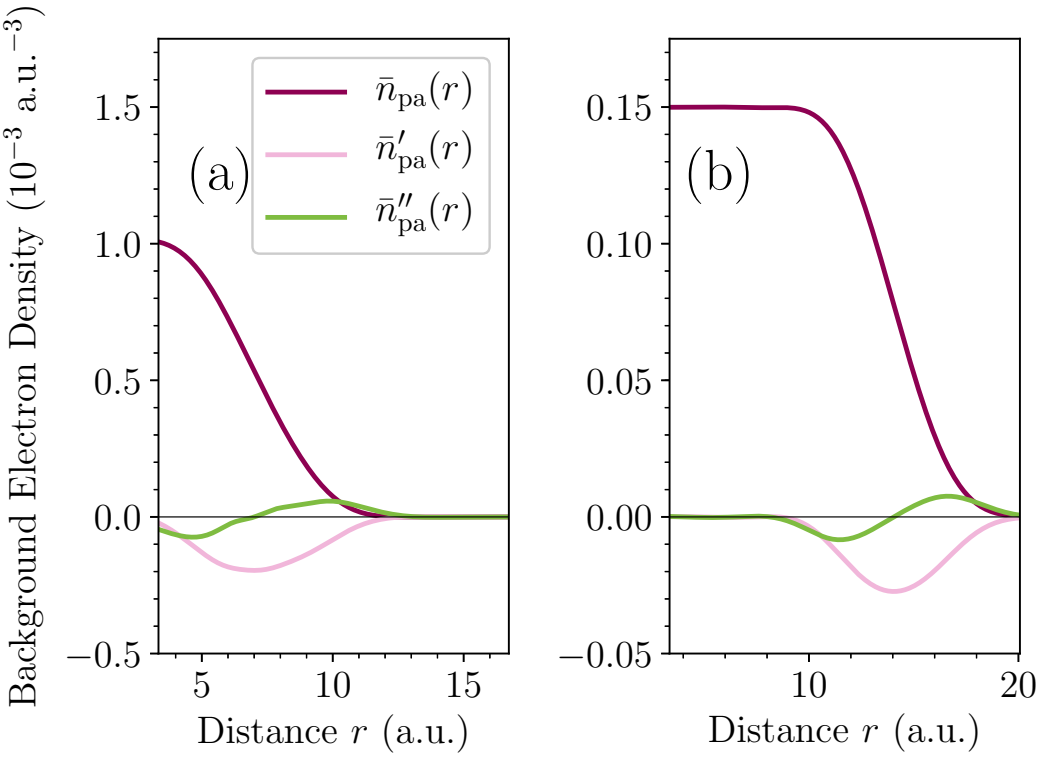

Fig. 3.3: The spatially-averaged pseudoatom density $\bar{n}_{\mathrm{pa}}$ (magenta) is calculated for Mg at the observed equilibrium volume $\Omega = 156.8$ a.u.. The radial derivatives (green and pink) of the spatially-averaged pseudoatom density were calculated using a Lagrange interpolating polynomial. All of these quantities are calculated at $\alpha = 25$ and for two values of the averaging sphere radius $R_a = 1.8R_{\mathrm{WS}}$ in (a) and $R_a = 3.4R_{\mathrm{WS}}$ in (b).

and $(m-1)$ derivatives at n points. For our purposes, we choose $m = 3$, $n = 2$ and $(R_c - R_0) = 0.5R_{\mathrm{WS}}$.

3.1.2 Summary and Algorithm

The central quantity is the spherically-averaged pseudoatom density $\bar{n}_{\mathrm{pa}}$ within the aGPT. This is usually tabulated ahead of time and is an input quantity to a molecular statics or dynamics code. The average local electron density is made up of an off-site or background contribution directly from $\bar{n}_{\mathrm{pa}}$ plus an on-site term $\bar{n}_a$. This on-site term is calculated indirectly using the bulk constraining equation. This means that

alongside the supercell that we intend to calculate forces for, we must also provide a reference bulk structure (with equivalent ion sites, typically the equivalent primitive cell). This allows us to infer the on-site density using the uniform electron density and the background component. This is done prior to the initial relaxation or molecular dynamics loop. Within the loop and using the on-site density, we calculate the local electron density for each site as a loop over neighbours (just like for a pure pair potential). The local electron density is then converted into a local atomic volume using the formula $\bar{n}_i = Z/\Omega_i$ (akin to the definition of a uniform density). The volume term E_{vol} and pair potential v_2 are then interpolated to their respective local atomic volumes and the contribution to the total energy, force and/or stress tensor is calculated. In summary:

1. Read in tabulated pair potentials v_2, volume terms E_{vol}, spherically-averaged pseudoatom density $\bar{n}_{\text{pa}}$ and reference structure e.g. the primitive cell.

2. Calculate on-site density $\bar{n}_a$ using the background density of the reference structure and also the uniform density

$$\bar{n}_a = \bar{n}_a^i = n_{\text{unif}} - \sum_{j \neq i} \bar{n}_{\text{pa}} \left(R_{ij}, \Omega_0 \right) \tag{3.34}$$

   where the sum is over the neighbours in the reference structure.

3. Enter the relaxation or molecular dynamics loop. Calculate the local average electron density using $\bar{n}_{\text{pa}}$ and $\bar{n}_a$

$$\bar{n}_i = \bar{n}_a + \sum_{j \neq i} \bar{n}_{\text{pa}} \left(R_{ij}, \Omega_0 \right). \tag{3.35}$$

4. Convert the local electron densities into a local atomic volume using the formula $\bar{n}_i = Z/\Omega_i$. Interpolate the pair potential and volume terms accordingly, and

calculate total energies, forces and/or stress tensor.

3.2 Derivatives of the Total Energy

The total energy can be used to calculate unrelaxed physical properties at zero temperature. Comparing these values to experiment is slightly artificial since all experimental values are at finite temperature and implicitly include the effects of atomic relaxation. These effects can be included in the aGPT formalism through the explicit calculation of derivatives of the total energy. In this section, we will derive explicit forms for both the forces and stress tensor.

3.2.1 Forces and Force Constants

The force $F_{i\alpha}$ on the atom i describes how the total energy changes with respect to an infinitesimal shift in its position $R_{i\alpha}$. As the ion-ion potential is self-consistently screened [216, 217], we can ignore variations in the wavefunctions and write the force as

$$F_{i\alpha} = -\frac{\partial E_{\text{tot}}}{\partial R_{i\alpha}} \left(\{\mathbf{R}\}, \Omega\right). \tag{3.36}$$

The force in the GPT involves only radial derivatives of the screened ion-ion interaction whereas the aGPT force will involve contributions from density derivatives of both E_{vol} and v_2. It is instructive to decompose the force into three parts

$$F_{i\alpha} = F_{i\alpha}^{[\text{I}]} + F_{i\alpha}^{[\text{II}]} + F_{i\alpha}^{[\text{III}]} \tag{3.37}$$

where the second term is the force due to the radial derivatives of v_2, the first and third components are the forces due to the density derivatives of E_{vol} and v_2 respectively.

The first component can be written

$$F_{i\alpha}^{[\mathrm{I}]} = -\frac{\partial E_{\mathrm{vol}}}{\partial \bar{n}_i}\frac{\partial \bar{n}_i}{\partial R_{i\alpha}} - \sum_{j\neq i}\frac{\partial E_{\mathrm{vol}}}{\partial \bar{n}_j}\frac{\partial \bar{n}_j}{\partial R_{i\alpha}} \tag{3.38}$$

where $\partial E_{\mathrm{vol}}/\partial \bar{n}_i$ is shorthand for the density derivative evaluated at $\bar{n}_i$. We can write the derivatives of the spatially-averaged local electron density, noting that the on-site density $\bar{n}_a$ does not contribute, as

$$\frac{\partial \bar{n}_i}{\partial R_{i\alpha}} = \sum_{j\neq i}\frac{\partial \bar{n}_{\mathrm{pa}}}{\partial R_{ij}}\frac{R_{ji\alpha}}{R_{ij}} \tag{3.39}$$

and

$$\frac{\partial \bar{n}_j}{\partial R_{i\alpha}} = \frac{\partial \bar{n}_{\mathrm{pa}}}{\partial R_{ij}}\frac{R_{ji\alpha}}{R_{ij}} \tag{3.40}$$

where $R_{ji\alpha}$ is the α component of the difference between position vectors $(\mathbf{R}_i - \mathbf{R}_j)$ and $R_{ji\alpha}/R_{ij}$ are the direction cosines. Eq.(3.38) can be cast into a more symmetric form

$$F_{i\alpha}^{[\mathrm{I}]} = \sum_{j\neq i}\left(\frac{\partial E_{\mathrm{vol}}}{\partial \bar{n}_i} + \frac{\partial E_{\mathrm{vol}}}{\partial \bar{n}_j}\right)\frac{\partial \bar{n}_{\mathrm{pa}}}{\partial R_{ij}}\frac{R_{ij\alpha}}{R_{ij}}. \tag{3.41}$$

The second component of the force looks similar to the GPT force. However, it is only equal to the GPT force in the bulk. It is given by

$$F_{i\alpha}^{[\mathrm{II}]} = \sum_{j\neq i}\frac{\partial v_2}{\partial R_{ij}}\left(R_{ij}, \bar{n}_{ij}\right)\frac{R_{ij\alpha}}{R_{ij}}. \tag{3.42}$$

The final component, which contains an additional neighbour sum, is given by

$$F_{i\alpha}^{[\mathrm{III}]} = \frac{1}{2}\sum_{j\neq i}\frac{\partial v_2}{\partial \bar{n}_{ij}}\left(\frac{\partial \bar{n}_i}{\partial R_{i\alpha}} + \frac{\partial \bar{n}_j}{\partial R_{i\alpha}}\right) + \frac{1}{4}\sum_{j\neq i}\sum_{k\neq j\neq i}\frac{\partial v_2}{\partial \bar{n}_{jk}}\left(\frac{\partial \bar{n}_j}{\partial R_{i\alpha}} + \frac{\partial \bar{n}_k}{\partial R_{i\alpha}}\right). \tag{3.43}$$

The bulk force constant matrix $A_{ij\alpha\beta}$ will largely be the same as for the GPT. However, there will be small contributions from the density derivatives of E_{vol} and v_2. We will derive them analytically by separating the contributions from the volume term and pairwise interaction

$$A_{ij\alpha\beta} = A^{(\text{vol})}_{ij\alpha\beta} + A^{(\text{pair})}_{ij\alpha\beta}. \tag{3.44}$$

Next, we expand the volume term in Eq.(3.23) as

$$\sum_k E_{\text{vol}}\left(\bar{n}_k\right) = E_{\text{vol}}\left(\bar{n}_i\right) + E_{\text{vol}}\left(\bar{n}_j\right) + \sum_{k\neq j\neq i} E_{\text{vol}}\left(\bar{n}_k\right) \tag{3.45}$$

which allows us to explicitly write the volume-term contribution to the force-constant matrix

$$\begin{aligned} A^{(\text{vol})}_{ij\alpha\beta} = &\frac{\partial^2 E_{\text{vol}}}{\partial \bar{n}_i^2}\frac{\partial \bar{n}_i}{\partial R_{i\alpha}}\frac{\partial \bar{n}_i}{\partial R_{j\beta}} + \frac{\partial^2 E_{\text{vol}}}{\partial \bar{n}_j^2}\frac{\partial \bar{n}_j}{\partial R_{i\alpha}}\frac{\partial \bar{n}_j}{\partial R_{j\beta}} + \frac{\partial E_{\text{vol}}}{\partial \bar{n}_i}\frac{\partial^2 \bar{n}_i}{\partial R_{i\alpha}\partial R_{j\beta}} + \frac{\partial E_{\text{vol}}}{\partial \bar{n}_j}\frac{\partial^2 \bar{n}_j}{\partial R_{i\alpha}\partial R_{j\beta}} \\ &+ \sum_{k\neq j\neq i}\left[\frac{\partial^2 E_{\text{vol}}}{\partial \bar{n}_k^2}\frac{\partial \bar{n}_k}{\partial R_{i\alpha}}\frac{\partial \bar{n}_k}{\partial R_{j\beta}} + \frac{\partial E_{\text{vol}}}{\partial \bar{n}_k}\frac{\partial^2 \bar{n}_k}{\partial R_{i\alpha}\partial R_{j\beta}}\right] \end{aligned} \tag{3.46}$$

where the derivatives of the spatially-averaged pseudoatom density are given by

$$\frac{\partial \bar{n}_i}{\partial R_{i\alpha}} = \sum_{k\neq i} \frac{\partial \bar{n}_{\mathrm{pa}}}{\partial R_{ik}} \frac{\partial R_{ik}}{\partial R_{i\alpha}} = -\sum_{k\neq i} \frac{\partial \bar{n}_{\mathrm{pa}}}{\partial R_{ik}} \frac{R_{ik\alpha}}{R_{ik}} \tag{3.47}$$

$$\frac{\partial \bar{n}_i}{\partial R_{j\beta}} = \frac{\partial \bar{n}_{\mathrm{pa}}}{\partial R_{ij}} \frac{\partial R_{ij}}{\partial R_{j\beta}} = \frac{\partial \bar{n}_{\mathrm{pa}}}{\partial R_{ij}} \frac{R_{ij\beta}}{R_{ij}} \tag{3.48}$$

$$\frac{\partial^2 \bar{n}_i}{\partial R_{i\alpha} \partial R_{j\beta}} = -\left(\frac{\partial^2 \bar{n}_{\mathrm{pa}}}{\partial R_{ij}^2} - \frac{1}{R_{ij}} \frac{\partial \bar{n}_{\mathrm{pa}}}{\partial R_{ij}} \right) \frac{R_{ij\alpha} R_{ij\beta}}{R_{ij}^2} - \frac{\partial \bar{n}_{\mathrm{pa}}}{\partial R_{ij}} \frac{\delta_{\alpha\beta}}{R_{ij}} \tag{3.49}$$

$$\frac{\partial \bar{n}_j}{\partial R_{i\alpha}} = -\frac{\partial \bar{n}_{\mathrm{pa}}}{\partial R_{ij}} \frac{R_{ij\alpha}}{R_{ij}} \tag{3.50}$$

$$\frac{\partial \bar{n}_j}{\partial R_{j\beta}} = -\sum_{k\neq j} \frac{\partial \bar{n}_{\mathrm{pa}}}{\partial R_{jk}} \frac{R_{jk\beta}}{R_{jk}} \tag{3.51}$$

$$\frac{\partial^2 \bar{n}_j}{\partial R_{i\alpha} \partial R_{j\beta}} = -\left(\frac{\partial^2 \bar{n}_{\mathrm{pa}}}{\partial R_{ij}^2} - \frac{1}{R_{ij}} \frac{\partial \bar{n}_{\mathrm{pa}}}{\partial R_{ij}} \right) \frac{R_{ij\alpha} R_{ij\beta}}{R_{ij}^2} - \frac{\partial \bar{n}_{\mathrm{pa}}}{\partial R_{ij}} \frac{\delta_{\alpha\beta}}{R_{ij}} \tag{3.52}$$

$$\frac{\partial \bar{n}_k}{\partial R_{i\alpha}} = \frac{\partial \bar{n}_{\mathrm{pa}}}{\partial R_{ki}} \frac{\partial R_{ki}}{\partial R_{i\alpha}} = \frac{\partial \bar{n}_{\mathrm{pa}}}{\partial R_{ki}} \frac{R_{ki\alpha}}{R_{ki}} \tag{3.53}$$

$$\frac{\partial \bar{n}_k}{\partial R_{j\beta}} = \frac{\partial \bar{n}_{\mathrm{pa}}}{\partial R_{kj}} \frac{\partial R_{kj}}{\partial R_{j\beta}} = \frac{\partial \bar{n}_{\mathrm{pa}}}{\partial R_{kj}} \frac{R_{kj\beta}}{R_{kj}} \tag{3.54}$$

$$\frac{\partial^2 \bar{n}_k}{\partial R_{i\alpha} \partial R_{j\beta}} = 0. \tag{3.55}$$

The force constant matrix due to the volume term can then be written as

$$\begin{aligned} A_{ij\alpha\beta}^{(\mathrm{vol})} = & \left(\frac{\partial E_{\mathrm{vol}}}{\partial \bar{n}_i} + \frac{\partial E_{\mathrm{vol}}}{\partial \bar{n}_j} \right) \mathcal{K}_{ij\alpha\beta} + \sum_{k\neq j\neq i} \frac{\partial^2 E_{\mathrm{vol}}}{\partial \bar{n}_k^2} \frac{\partial \bar{n}_{\mathrm{pa}}}{\partial R_{ki}} \frac{\partial \bar{n}_{\mathrm{pa}}}{\partial R_{kj}} \frac{R_{ki\alpha} R_{kj\beta}}{R_{ki} R_{kj}} \\ & - \frac{\partial^2 E_{\mathrm{vol}}}{\partial \bar{n}_i^2} \frac{\partial \bar{n}_{\mathrm{pa}}}{\partial R_{ij}} \frac{R_{ij\beta}}{R_{ij}} \sum_{k\neq i} \frac{\partial \bar{n}_{\mathrm{pa}}}{\partial R_{ik}} \frac{R_{ik\alpha}}{R_{ik}} - \frac{\partial^2 E_{\mathrm{vol}}}{\partial \bar{n}_j^2} \frac{\partial \bar{n}_{\mathrm{pa}}}{\partial R_{ji}} \frac{R_{ji\beta}}{R_{ji}} \sum_{k\neq j} \frac{\partial \bar{n}_{\mathrm{pa}}}{\partial R_{jk}} \frac{R_{jk\alpha}}{R_{jk}} \end{aligned} \tag{3.56}$$

where $\mathcal{K}_{ij\alpha\beta} = \partial^2 \bar{n}_i / \partial R_{i\alpha} \partial R_{j\beta}$. We can expand the pairwise interaction in a similar way to the volume term

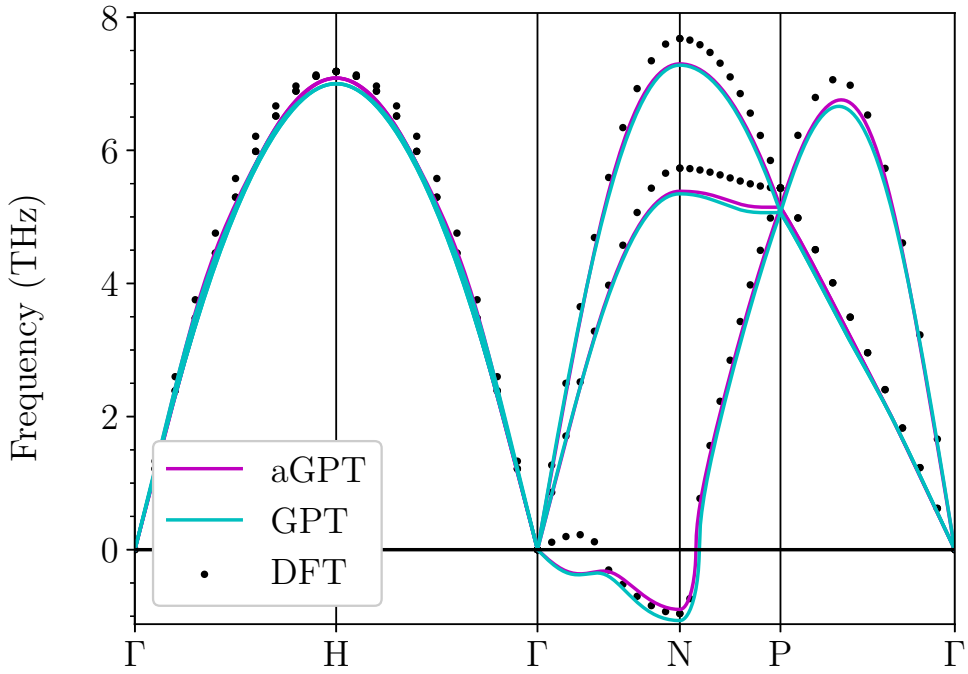

Fig. 3.4: Phonon dispersion relation for mechanically unstable bcc Mg at the equilibrium volume. The averaging sphere radius was taken to be $R_a = 1.8R_{\mathrm{WS}}$. The aGPT phonon band structure (magenta) is quantitatively similar to the GPT (cyan) deviating only in the imaginary sector between high-symmetry points Γ to N. The DFT data (black points) is in good agreement with the aGPT/GPT results. The small qualitative difference in the imaginary sector along Γ-N is associated with subtle differences in pressure.

$$\frac{1}{2}\sum_{kl}{}' v_2\left(R_{kl},\bar{n}_{kl}\right) = v_2\left(R_{ij},\bar{n}_{ij}\right) + \sum_{k\neq j\neq i}\left[v_2\left(R_{ik},\bar{n}_{ik}\right) + v_2\left(R_{jk},\bar{n}_{jk}\right)\right] + \frac{1}{2}\sum_{k\neq j\neq i}\sum_{l\neq k\neq j\neq i} v_2\left(R_{kl},\bar{n}_{kl}\right). \tag{3.57}$$

The pairwise interaction term can be evaluated using Eq.(3.57) and the density derivatives that we wrote down previously. This becomes

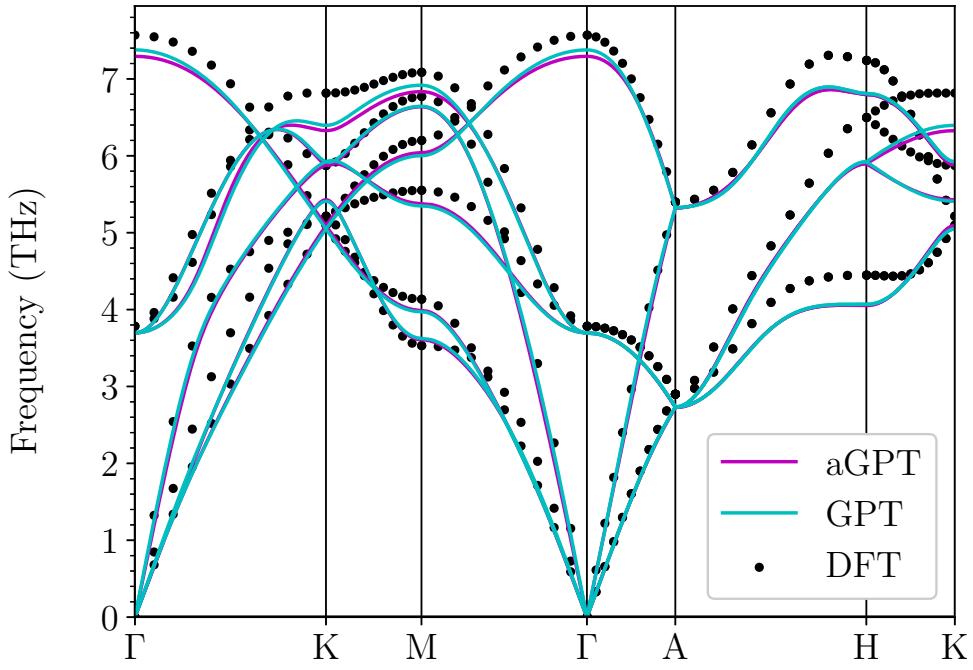

Fig. 3.5: Phonon dispersion relation for hcp Mg at the equilibrium volume and c/a ratio. The averaging radius was taken to be $R_a = 1.8R_{\mathrm{WS}}$. The aGPT phonon band-structure (magenta) is quantitatively similar to the GPT (cyan). Both the aGPT and GPT are in good qualitative agreement with the DFT data (black dots).

$$
\begin{aligned}
A^{(\mathrm{pair})}_{ij\alpha\beta} = {} & \frac{\partial^2 v_2}{\partial R_{ij}^2}\frac{\partial R_{ij}}{\partial R_{i\alpha}}\frac{\partial R_{ij}}{\partial R_{j\beta}} + \frac{\partial v_2}{\partial R_{ij}}\frac{\partial^2 R_{ij}}{\partial R_{i\alpha} R_{j\beta}} + \frac{\partial v_2}{\partial \bar{n}_{ij}}\frac{\partial \bar{n}_{ij}}{\partial R_{i\alpha}}\frac{\partial \bar{n}_{ij}}{\partial R_{j\beta}} + \frac{\partial^2 v_2}{\partial \bar{n}_{ij}^2}\frac{\partial^2 \bar{n}_{ij}}{\partial R_{i\alpha} R_{j\beta}} \\
& + \frac{\partial v_2}{\partial \bar{n}_{ij}}\frac{\partial \bar{n}_{ij}}{\partial R_{i\alpha}}\frac{\partial \bar{n}_{ij}}{\partial R_{j\beta}} + \frac{1}{2}\frac{\partial^2 v_2}{\partial R_{ij}\partial \bar{n}_{ij}}\left(\frac{\partial \bar{n}_{ij}}{\partial R_{i\alpha}}\frac{\partial R_{ij}}{\partial R_{j\beta}} + \frac{\partial \bar{n}_{ij}}{\partial R_{j\beta}}\frac{\partial R_{ij}}{\partial R_{i\alpha}}\right) \\
& + \sum_{k\neq j\neq i}\left[\frac{\partial^2 v_2}{\partial \bar{n}_{ik}\partial R_{ik}}\frac{\partial R_{ik}}{\partial R_{i\alpha}}\frac{\partial \bar{n}_{ik}}{\partial R_{j\beta}} + \frac{\partial^2 v_2}{\partial \bar{n}_{ik}^2}\frac{\partial \bar{n}_{ik}}{\partial R_{i\alpha}}\frac{\partial \bar{n}_{ik}}{\partial R_{j\beta}} + \frac{\partial v_2}{\partial \bar{n}_{ik}}\frac{\partial^2 \bar{n}_{ik}}{\partial R_{i\alpha}\partial R_{j\beta}}\right] \\
& + \sum_{k\neq j\neq i}\left[\frac{\partial^2 v_2}{\partial \bar{n}_{jk}\partial R_{jk}}\frac{\partial R_{jk}}{\partial R_{j\beta}}\frac{\partial \bar{n}_{jk}}{\partial R_{i\alpha}} + \frac{\partial^2 v_2}{\partial \bar{n}_{jk}^2}\frac{\partial \bar{n}_{jk}}{\partial R_{i\alpha}}\frac{\partial \bar{n}_{jk}}{\partial R_{j\beta}} + \frac{\partial v_2}{\partial \bar{n}_{jk}}\frac{\partial^2 \bar{n}_{jk}}{\partial R_{i\alpha}\partial R_{j\beta}}\right] \\
& + \frac{1}{2}\sum_{k\neq j\neq i}\sum_{l\neq k\neq j\neq i}\left[\frac{\partial^2 v_2}{\partial \bar{n}_{kl}^2}\frac{\partial \bar{n}_{kl}}{\partial R_{i\alpha}}\frac{\partial \bar{n}_{kl}}{\partial R_{j\beta}} + \frac{\partial v_2}{\partial \bar{n}_{kl}}\frac{\partial^2 \bar{n}_{kl}}{\partial R_{i\alpha}\partial R_{j\beta}}\right].
\end{aligned}
\tag{3.58}
$$

This equation can be tidied up somewhat by removing all terms equal to zero and recognising that the first terms correspond to the GPT force-constant matrix in the bulk crystal with ions in their equilibrium configuration

$$
\begin{aligned}
A^{(\mathrm{pair})}_{ij\alpha\beta} = A^{\mathrm{GPT}}_{ij\alpha\beta} &+ \frac{\partial^2 v_2}{\partial R_{ij}\partial \bar{n}_{ij}}\left(\frac{\partial \bar{n}_{ij}}{\partial R_{i\alpha}}\frac{R_{ij\beta}}{R_{ij}} + \frac{\partial \bar{n}_{ij}}{\partial R_{j\beta}}\frac{-R_{ij\alpha}}{R_{ij}}\right) + \frac{\partial v_2}{\partial \bar{n}_{ij}}\mathcal{K}_{ij\alpha\beta} \\
&+ \sum_{k\neq j\neq i}\left[\frac{\partial^2 v_2}{\partial \bar{n}_{ik}\partial R_{ik}}\frac{-R_{ik\alpha}}{R_{ik}}\frac{\partial \bar{n}_{ik}}{\partial R_{j\beta}} + \frac{\partial^2 v_2}{\partial \bar{n}^2_{ik}}\frac{\partial \bar{n}_{ik}}{\partial R_{i\alpha}}\frac{\partial \bar{n}_{ik}}{\partial R_{j\beta}} + \frac{\partial v_2}{\partial \bar{n}_{ik}}\mathcal{K}_{ij\alpha\beta}\right] \\
&+ \sum_{k\neq j\neq i}\left[\frac{\partial^2 v_2}{\partial \bar{n}_{jk}\partial R_{jk}}\frac{-R_{jk\beta}}{R_{jk}}\frac{\partial \bar{n}_{jk}}{\partial R_{i\alpha}} + \frac{\partial^2 v_2}{\partial \bar{n}^2_{jk}}\frac{\partial \bar{n}_{jk}}{\partial R_{i\alpha}}\frac{\partial \bar{n}_{jk}}{\partial R_{j\beta}} + \frac{\partial v_2}{\partial \bar{n}_{jk}}\mathcal{K}_{ij\alpha\beta}\right] \\
&+ \frac{1}{2}\sum_{k\neq j\neq i}\sum_{l\neq k\neq j\neq i}\frac{\partial^2 v_2}{\partial \bar{n}^2_{kl}}\frac{\partial \bar{n}_{kl}}{\partial R_{i\alpha}}\frac{\partial \bar{n}_{kl}}{\partial R_{j\beta}}.
\end{aligned}
\tag{3.59}
$$

The additional neighbour sums that arise as a result of the local electron density can be seen as the third- and fourth-order terms that are necessary to capture features of the phonon dispersion in certain metals, particularly Be [218]. Despite this, the phonon dispersion is generally dominated by the bulk GPT force constant matrix. Deviations in the band structure in the low $\mathbf{q}$ limit are expected and correspond to changes in the elastic constants.

The phonon dispersion was calculated for mechanically unstable bcc Mg at the equilibrium volume in Fig.(3.4). This crystal structure was chosen as a representative example die to the presence of imaginary phonon frequencies along the $\mathbf{q}$-point path from Γ to N. The bcc phase will be discussed further in Chapter 4. In addition, the phonon dispersion relation for thermodynamically stable hcp Mg as the equilibrium atomic volume and c/a ratio is shown in Fig.(3.5). The dispersion relations for the aGPT and GPT were calculated using the analytic formulae and the DFT data was calculated numerically with the code ALAMODE [219] using supercells that were extended by $3\times3\times3$. The DFT results were calculating using the FP-LMTO method

of van Schilfgaarde and co-workers [220] as implemented in the Questaal suite. The Brillouin zone integrations were performed with Methfessel-Paxton sampling [221] and $30 \times 30 \times 30$ **q**-point subdivisions. The exchange-correlation functional was taken in the local-density approximation using the correlation function of Perdew and Wang [168]. The local density approximation was used since it is closest to the treatment of exchange and correlation within the GPT. There is good agreement with the DFT data and the aGPT/GPT.

3.2.2 Stress Tensor and Elastic Constants

Molecular dynamics simulations that sample an isobaric ensemble require a barostat to match the external pressure to the internal pressure $P^{\text{int}} = \sum_\alpha \sigma_{\alpha\alpha}/d$ [204] where σ is the internal stress tensor and d is the dimension of the cell. This matching is essentially the equilibrium condition; the time average of the internal pressure is the external pressure. In such simulations, only the lattice parameter a is dynamic. This constraint is slightly artificial if the crystal has multiple lattice parameters as in the case of hexagonal crystals. Relaxing this constraint requires that we now sample an isostress ensemble [222, 223] where the internal stress tensor is matched to an external stress tensor. The stress tensor is defined as the infinitesimal change in total energy as a result of an infinitesimal strain [204]

$$\sigma_{\alpha\beta} = \frac{1}{V}\left(\frac{\partial E_{\text{tot}}}{\partial \varepsilon_{\alpha\beta}}\right)\bigg|_{\varepsilon_{\alpha\beta}=0} \tag{3.60}$$

where the prefactor of the inverse volume V^{-1} is required by dimensional analysis, and $\varepsilon_{\alpha\beta}$ is a first-order strain. The application of a strain changes the lattice vectors

h in the following way

$$h_{\alpha\beta} \rightarrow \tilde{h}_{\alpha\beta} = \sum_{\gamma} \left(\delta_{\alpha\gamma} + \varepsilon_{\alpha\gamma}\right) h_{\gamma\beta} \tag{3.61}$$

where δ is the Kronecker delta. Since the lattice vectors act as basis vectors for the position vectors of the atoms, a strain transforms the ion at site i to a new position $\tilde{R}_{i\alpha}$ i.e.

$$R_{i\alpha} \rightarrow \tilde{R}_{i\alpha} = \sum_{\beta} \tilde{h}_{\alpha\beta} S_{i\beta} = R_{i\alpha} + \sum_{\beta\gamma} \varepsilon_{\alpha\beta} h_{\beta\gamma} S_{i\gamma} \tag{3.62}$$

where $S_{i\alpha}$ is the position of site i in a fractional co-ordinate system. After application of the strain, the Cartesian distance between sites i and j is given by

$$\tilde{R}_{ij} = \sqrt{\sum_{\alpha\beta} \tilde{G}_{\alpha\beta}\left(\varepsilon\right) S_{ij\alpha} S_{ij\beta}} \tag{3.63}$$

where $\tilde{G}_{\alpha\beta}\left(\varepsilon\right) = \sum_{\gamma} \tilde{h}_{\gamma\alpha} \tilde{h}_{\gamma\beta}$ is the strained metric tensor. If the strain is sufficiently small so as to vanish at quadratic order $\varepsilon_{\alpha\beta} = \delta\varepsilon_{\alpha\beta}$, we may write

$$\tilde{G}_{\alpha\beta}\left(\varepsilon\right) = G_{\alpha\beta} + 2\sum_{\mu\nu} \delta\varepsilon_{\mu\nu} h_{\mu\alpha} h_{\nu\beta} \tag{3.64}$$

where $G_{\alpha\beta}$ is the metric tensor of the unstrained crystal. By denoting the second term as $\delta G_{\alpha\beta}$ and expanding Eq.(3.62) about $\delta G = 0$, we find

$$\tilde{R}_{ij} = R_{ij} + \frac{1}{2R_{ij}} \sum_{\alpha\beta} \delta G_{\alpha\beta} S_{ij\alpha} S_{ij\beta}. \tag{3.65}$$

This Taylor expansion allows us to explicitly evaluate the derivative of the interatomic separation R_{ij} with respect to strain

$$\frac{\partial R_{ij}}{\partial \varepsilon_{\alpha\beta}} = \lim_{\delta\varepsilon_{\alpha\beta} \rightarrow 0} \left[\frac{\tilde{R}_{ij} - R_{ij}}{\delta\varepsilon_{\alpha\beta}}\right] = \frac{R_{ij\alpha} R_{ij\beta}}{R_{ij}}. \tag{3.66}$$

Turning to the aGPT stress tensor, we make a decomposition of the stress tensor along the same lines of the force

$$\sigma_{\alpha\beta} = \sigma_{\alpha\beta}^{[\mathrm{I}]} + \sigma_{\alpha\beta}^{[\mathrm{II}]} + \sigma_{\alpha\beta}^{[\mathrm{III}]}. \tag{3.67}$$

The second term in the decomposition takes the form of a virial stress tensor

$$\sigma_{\alpha\beta}^{[\mathrm{II}]} = \frac{1}{2V} \sum_{ij}{}' F_{ij\alpha}^{[\mathrm{II}]} R_{ij\beta} \tag{3.68}$$

where the prime over the summation refers to the exclusion of the $i = j$ and $F_{ij\alpha}^{[\mathrm{II}]}$ is defined as the force on ion i due to ion j

$$F_{i\alpha}^{[\mathrm{II}]} = \sum_{j \neq i} F_{ij\alpha}^{[\mathrm{II}]}. \tag{3.69}$$

Including volume dependence of the spatially-averaged pseudoatom density will mean that first contribution to the total stress tensor cannot be written as a virial

$$\sigma_{\alpha\beta}^{[\mathrm{I}]} = \frac{1}{V} \sum_{i} \frac{\partial E_{\mathrm{vol}}}{\partial \bar{n}_i} \frac{\partial \bar{n}_i}{\partial \varepsilon_{\alpha\beta}} \tag{3.70}$$

where, using the identity $\partial\Omega/\partial\varepsilon_{\alpha\beta} = \Omega\delta_{\alpha\beta}$, we have

$$\frac{1}{V}\frac{\partial \bar{n}_i}{\partial \varepsilon_{\alpha\beta}} = \frac{1}{N}\left(\frac{\partial \bar{n}_a}{\partial \Omega} + \sum_{j \neq i} \frac{\partial \bar{n}_{\mathrm{pa}}}{\partial \Omega}\left(R_{ij}, \Omega\right)\right)\delta_{\alpha\beta} + \frac{1}{V}\sum_{j \neq i} \frac{\partial \bar{n}_{\mathrm{pa}}}{\partial R_{ij}} \frac{R_{ij\alpha} R_{ij\beta}}{R_{ij}}. \tag{3.71}$$

This form can be inserted into Eq.(3.70) and made more explicitly symmetric in i and j

$$\sigma_{\alpha\beta}^{[\mathrm{I}]} = \frac{1}{N}\frac{\partial \bar{n}_a}{\partial \Omega}\sum_i \frac{\partial E_{\mathrm{vol}}}{\partial \bar{n}_i}\delta_{\alpha\beta} + \frac{1}{2N}\sum_{ij}{}' \left(\frac{\partial E_{\mathrm{vol}}}{\partial \bar{n}_i} + \frac{\partial E_{\mathrm{vol}}}{\partial \bar{n}_j}\right)\frac{\partial \bar{n}_{\mathrm{pa}}}{\partial \Omega}\delta_{\alpha\beta} + \frac{1}{2V}\sum_{ij}{}' \left(\frac{\partial E_{\mathrm{vol}}}{\partial \bar{n}_i} + \frac{\partial E_{\mathrm{vol}}}{\partial \bar{n}_j}\right)\frac{\partial \bar{n}_{\mathrm{pa}}}{\partial R_{ij}}\frac{R_{ij\alpha}R_{ij\beta}}{R_{ij}}. \tag{3.72}$$

The final contribution to the total stress tensor is given by

$$\sigma_{\alpha\beta}^{[\mathrm{III}]} = \frac{1}{4V}\sum_{ij}{}' \frac{\partial v_2}{\partial \bar{n}_{ij}}\left(\frac{\partial \bar{n}_i}{\partial \varepsilon_{\alpha\beta}} + \frac{\partial \bar{n}_j}{\partial \varepsilon_{\alpha\beta}}\right). \tag{3.73}$$

We calculate the elastic moduli numerically by approximating the derivative

$$C_{\alpha\beta\gamma\delta} = \left(\frac{\partial \sigma_{\alpha\beta}}{\partial \varepsilon_{\gamma\delta}}\right)\Bigg|_{\varepsilon_{\alpha\beta}=0}. \tag{3.74}$$

Note that this assumes that we start from an initially unstressed state. Therefore, this tensor is precisely the elastic moduli tensor at the equilibrium lattice parameters. At finite stress, this tensor is the Wallace tensor [204] which does not obey the Voigt symmetry. In Chapter 4, we will elaborate on this difference further.

Since the elastic moduli are extremely sensitive to minor changes in the potential, we choose to approximate the derivative in Eq.(3.74) using a central difference method whose error is of quartic order in the strain parameter. These results are shown alongside GPT and experimental values in Table 3.1. The dynamic bulk modulus B_d is calculated by using combinations of volume-dependent elastic moduli. The aGPT values ($B_d = 35.9$ GPa in Table 3.1) are in excellent agreement with the static bulk modulus $B_s = 35.8$ GPa that was calculated from derivatives of the equation of state.

The elastic moduli can be used to find an optimum value of the averaging sphere radius R_a. In particular, the volume-conserving elastic moduli should be equivalent in the GPT and aGPT. The difference arises as a result of the approximations and

Table 3.1: Elastic constants calculated for hcp Mg with the experimentally observed values for $\Omega = 156.8$ a.u. and $c/a = 1.62$. The GPT elastic constants were calculated in two ways, using only the virial stress tensor without basal plane relaxation (labelled 'Virial' in the table) and using the virial stress tensor with volume derivatives and basal plane relaxation. The aGPT elastic constants were calculated at two physically reasonable values of the averaging-sphere radius. The experimental values were measured at 4 K [206] and we are comparing against the DFT values of Yin *et al.* [224].

[GPa]	C_{11}	C_{12}	C_{13}	C_{33}	C_{44}	C_{66}	B_d
GPT (Virial)	73.2	27.8	24.6	63.6	19.5	22.7	40.5
GPT	63.9	25.2	21.1	62.6	19.5	19.4	36.1
aGPT ($R_a = 1.8$)	63.5	25.5	20.6	62.7	19.5	19.0	35.9
aGPT ($R_a = 3.4$)	63.3	25.3	21.0	61.6	18.9	19.0	35.9
DFT [224]	61	26	20	63	18	-	-
Exp.[206]	63.4	25.9	21.7	66.6	18.4	18.7	36.9

assumptions made in the aGPT formalism. With reference to our calculated aGPT elastic moduli in Table 3.1, a smaller cut-off radius $R_a = 1.8R_{\mathrm{WS}}$ better reproduces the volume-conserving GPT elastic moduli. Also note from Table 3.1 that the bulk modulus discrepancy is removed, with both the GPT and aGPT values of the dynamic bulk modulus B_d in good agreement with the static value $B_s = 35.8$ GPa.

3.3 Results

3.3.1 Vacancy Formation Energy

A vacancy is the primary test case for the aGPT, since it is the simplest defect for which there is considerable local volume change. As a consequence, a large amount of the energy required to create a vacancy is not captured by the GPT and other methods based on second-order pseudopotential perturbation theory. The vacancy formation energy is usually defined as the energy required to remove one atom to infinity and replace it at the surface. The vacancy formation energy E^{1f} can be written without

Table 3.2: Vacancy formation energies calculated for hcp Mg. The vacancy formation energy $E^{1f}$was calculated using both the GPT and the aGPT for two values of the averaging sphere radius at the GPT equilibrium atomic volume $\Omega =$ 156.8 a.u. and $c/a = 1.62$. The DFT values [225] were calculated at the zero temperature lattice parameters (excluding zero point phonons).

[eV]	v_2^{1f}	E_{vol}^{1f}	Δv_2^{1f}	E_{rlx}^{1f}	E^{1f}	Ω^{1f}
GPT	0.44	0.00	-	-0.01	0.43	0.71
aGPT ($R_a = 1.8$)	0.44	0.47	-0.19	-0.01	0.71	0.65
aGPT ($R_a = 3.4$)	0.44	0.50	-0.23	-0.01	0.70	0.59
DFT[225]	-	-	-	-0.01	0.74	0.69
Exp.	-	-	-	-	0.79 ± 0.03 [215]	-

approximation as [13]

$$E^{\mathbf{1f}} = \lim_{N_a \to \infty} \left[E_{\text{tot}}\left(N_a, 1\right) - \left(\frac{N_a - 1}{N_a} \right) E_{\text{tot}}\left(N_a, 0\right) \right] \tag{3.75}$$

where N_a is the number of sites and E_{tot} is a function of both the number of atoms and number of vacancies. The term in the brackets can be evaluated at finite N and then extrapolated into the thermodynamic limit $N \to \infty$. Provided that the atomic positions are relaxed and we are using the bulk equilibrium lattice parameters, it is unnecessary to relax the lattice parameters for the vacancy cell. We can see this by expanding the bulk and vacancy total energies about the volume at zero pressure. The largest correction to the vacancy formation energy as a result of this expansion is given by $-P\Omega^{1f}$ where Ω^{1f} is the misfit or vacancy formation volume [13].

We have calculated the relaxed vacancy formation energy in hcp Mg at the experimentally observed atomic volume $\Omega = 156.8$ a.u. and $c/a = 1.62$. In our calculations, the atomic volume is kept constant which means that the removal of an atom gives rise to a contraction of the lattice. The vacancy formation energy is calculated at multiple values of N and extrapolated to the thermodynamic limit. In addition, we

also calculate the misfit volume Ω^{1f} using the following formula [100]

$$\Omega^{1f}/\Omega_0 = -B_d^{-1}\frac{\partial E^{1f}}{\partial \Omega} \tag{3.76}$$

where B_d is the bulk modulus as calculated in Section 3.2.2. These results are given in Table 3.2 and compared to GPT and experimental vacancy formation energies. The vacancy formation energy was calculated for $N_a \in \{54, 128, 250, 432\}$ and then extrapolated to infinity. The extrapolated vacancy formation energy is around 1% less than the vacancy formation energy for $N_a = 432$. The divacancy binding energy was also calculated for hcp Mg using the following formula

$$E^{2b}_{i\text{NN}} = 2E^{1f} - E^{2f}_{i\text{NN}} \tag{3.77}$$

where $E^{2f}_{i\text{NN}}$ is the divacancy formation energy for a vacancy at the origin and a vacancy in the i^{th} neighbour shell. The divacancy formation energy was calculated using an analogous expression to Eq.(3.75). The ordering of the first and second nearest neighbours is dependent on the c/a ratio in hcp crystals. In Mg, the c/a ratio is less than the ideal value which means that the first nearest neighbour lies at a distance less than the lattice parameter a. We make a nearest neighbour definition along the same lines as Uesugi *et al* [225] where we distinguish between neighbour shells that are degenerate at the ideal c/a ratio. The divacancy binding energy compiled in Table 3.3, converges more slowly with N_a than the vacancy formation energy. In addition, the divacancy binding energy converges more slowly for the aGPT than it does for the GPT. As such, the divacancy binding energy was calculated for larger values of $N_a \in \{250, 432, 686, 1024\}$. Both the aGPT and the GPT are under bound over the first two neighbour shells relative to DFT. We note however, that the divacancy binding energy is the difference between two quantities with unknown error bars. Therefore, the underbinding of the divacancy with the aGPT is likely a consequence

Table 3.3: Relaxed divacancy binding energies calculated for hcp Mg with the equilibrium GPT values for Ω and c/a. We have calculated $E^{2b}_{i\mathrm{NN}}$ using the GPT and the aGPT for two values of the averaging sphere radius. The DFT values [225] were calculated at the zero temperature lattice parameters (excluding zero point phonons).

[eV]	$E^{2b}_{1\mathrm{NN}}$	$E^{2b}_{2\mathrm{NN}}$	$E^{2b}_{3\mathrm{NN}}$	$E^{2b}_{4\mathrm{NN}}$	$E^{2b}_{5\mathrm{NN}}$
GPT	$+0.02$	$+0.02$	-0.01	$+0.00$	$+0.00$
aGPT ($R_a = 1.8$)	$+0.01$	$+0.01$	-0.05	-0.03	-0.02
aGPT ($R_a = 3.4$)	$+0.00$	$+0.01$	-0.02	-0.01	-0.01
DFT[225]	$+0.06$	$+0.07$	-0.01	$+0.01$	$+0.01$

of the failure to perfectly cancel the errors in the vacancy and divacancy formation energies.

3.3.2 Stacking Fault Energies

Information about the plastic behaviour of a metal can be inferred from a calculation of the stacking fault energies and the profile of the γ-line. In particular, the stacking fault energy controls the dissociation width of dislocations into partial dislocations. This in turn controls the ability of a dislocation to cross-slip and limits easy-glide. The γ-line is defined in the following manner. An infinite crystal is partitioned into two subcrystals with their interface being some crystallographic plane. One half of the crystal is displaced relative to the other along some crystallographic direction parallel to the interface until the crystal has been translated by an integer multiple of the lattice vectors. The γ-line is the relative energy change during this process, normalised by the area of the crystallographic plane.

Practical computations pose several challenges for this procedure. All of the approaches begin by choosing a supercell whose lattice vectors $\{\mathbf{a}_1, \mathbf{a}_2\}$ define the crystallographic plane over which the slip occurs. For instance, in the basal plane of the hcp structure these can be represented as the Cartesian vectors $\mathbf{a}_1 = [1, 0, 0]$ and

$\mathbf{a}_2 = [-1/2, \sqrt{3}, 0]$. The supercell is extended n times in the $\mathbf{a}_3$ direction such that there are n unit cells. The definition of $\mathbf{a}_3$ is not unique and it need not be perpendicular to the crystallographic plane. In fact, the only requirement on $\mathbf{a}_3$ is that it connects to an atom which is out of the crystallographic plane. There are a number of ways to create the stacking fault. One such method is the so-called 'slab' method [226] whereby the stacking fault is created by moving atoms relative to each other at the approximate centre of the supercell. With periodic boundary conditions, the 'slab' method creates an additional stacking fault at the boundary of the supercell with the periodic images. Another method, which we employ, creates the fault by tilting the out-of-plane lattice vector $\mathbf{a}_3 \rightarrow \mathbf{a}_3 + \alpha\mathbf{t}$ where $\mathbf{t}$ is some integer combination of the in-plane lattice vectors and α is a real number in the interval $[0, 1]$. The 'tilt' method creates only one stacking fault per supercell whereas the 'slab' method creates two. Thus, with the tilt method there is faster convergence with the number of unit cells n.

If a crystal has a stacking fault, the atoms will relax in order to minimize the interatomic forces that were created by the fault. Using the original Vítek description of the γ-line [226], only out-of-plane relaxations are allowed. If such restrictions were not in place then the atoms would relax to either the equilibrium positions or the stable stacking fault up to some strain due to the finite supercell. In certain crystallographic planes and for certain elements, notably the Pyramidal II plane for Mg [224], both the stable stacking fault energy and stacking fault vector calculated using the Vítek method are not very close to fully relaxed values. Along these planes if the entire γ-line is desired then it is necessary to remove the restrictions on in-plane relaxations away from the fault itself [227] or using a nudged elastic band method. The aGPT γ-line was calculated using the Vítek method for hcp Mg along 4 directions in 4 crystallographic planes Fig.(3.6) for both the GPT and aGPT. In general, we find

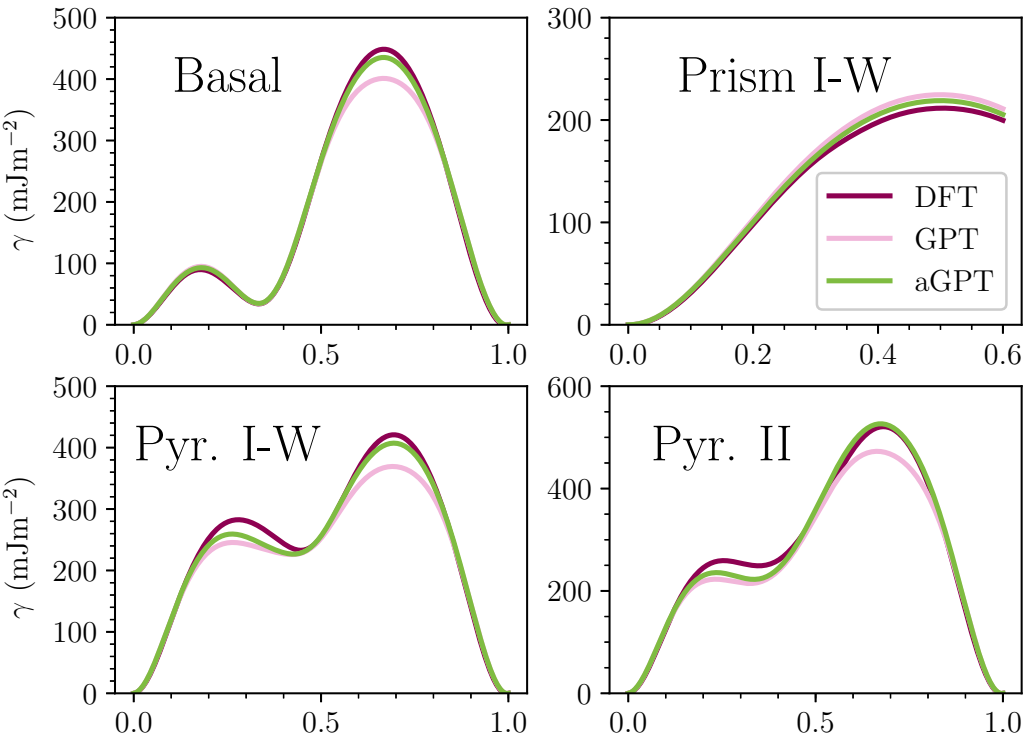

Fig. 3.6: The γ-line calculated for hcp Mg using the GPT (pink), aGPT (green) and compared to the DFT results (red) of Yin *et al* [224]. For comparison, the GPT and aGPT was calculated using the DFT zero temperature lattice parameters. The crystal was tilted along the $[1\bar{1}00]$, $1/3[\bar{1}2\bar{1}0]$, $1/2[\bar{1}102]$ and $1/3[\bar{2}113]$ in the Basal, Prism I, Pyramidal I and II crystallographic planes respectively. The aGPT and GPT are in agreement for the stable stacking fault energy. The aGPT increases the value of the unstable stacking fault relative to the GPT.

that there is agreement between the GPT and aGPT at the stable stacking fault. However, for the unstable stacking fault the aGPT improves upon the GPT relative to the DFT results of Yin *et al* [224].

3.4 Conclusions

We have demonstrated that it is possible to include local volume effects by modifying the GPT so that it now depends on a spatially-averaged local electron density. In particular, we have developed the aGPT formalism to the extent that it is now possible

to do molecular statics and dynamics. To this end, we calculated the vacancy formation energy in hcp Mg at the equilibrium lattice parameters. The aGPT relaxed vacancy formation energy significantly improves upon the relaxed GPT vacancy formation energy relative to the experimentally observed value. In addition, the aGPT provides improved stacking fault energies for hcp Mg.

The computational cost in time of the aGPT is greater than that of the GPT. This is a result of the additional neighbour loop in the calculation of the forces. Provided that the neighbour table maker is linear scaling $\mathcal{O}(N)$, for instance using a linked list, both the GPT and aGPT are $\mathcal{O}(N)$. Relative to empirical potentials, the major computational cost is due the long range cut-off in both the GPT and aGPT. This can be demonstrated by considering a short ranged empirical pair potential whose neighbour cut-off is roughly 1/3 that of the GPT (i.e. it runs over the first handful of neighbour shells), we would expect the GPT to be approximately $3^3 = 27$ times slower. Furthermore, we expect the aGPT to be $27N_c$ slower than the GPT where N_c is the number of atoms in a linked-list block.

Bulk properties such as phonon dispersion and elastic constants were also calculated as fundamental tests of the aGPT. The inclusion of the spatially-averaged local electron density modifies the bulk phonon dispersion. This is a result of the additional derivatives of the electron density that appear in the expression for the force constant matrix. The elastic constants are also modified although the volume-conserving elastic constants should be the same as for the GPT. It is only the assumptions and approximations in the aGPT that make them differ. Thus, we can use the volume conserving elastic constants to find an optimum value for the averaging sphere radius R_a which is the lone free parameter in the aGPT. This constraint would appear to favour near-neighbor values of R_a, for instance $R_a = 1.8R_{\mathrm{WS}}$.

The aGPT can be used to accurately calculate self-diffusion and defect-defect inter-

actions in elemental metals. However, further work needs to be done on extending the aGPT to alloys in order to study solute diffusion or solute-defect interactions. We plan to use the aGPT to further study vacancies and, in particular, the high-temperature deviation from Arrhenius behavior [228]. All of the results presented in this paper were calculated using our in-house Fortran codes. There is a planned future project to incorporate the aGPT into LAMMPS [229].

Chapter 4

Stability of the BCC Structure in the Mg-Ca Alloy System

"...if metallurgists of this country do not learn about the electron theories they may discover too late, that the industry in other countries has benefitted from knowledge of modern theories and is developing alloys"

Geoffrey V. Raynor FRS

Magnesium (Mg) is the lightest structural metal, with a density 78% lower than steel and 37% lower than aluminium (Al) [5]. It is seen by the automotive industry as a potential replacement for Al due to its potential to reduce vehicle mass and increase efficiency. Whilst there are applications for Mg, these have typically been confined to components which can be cast. On the other hand, wrought Mg has rarely been used due to its poor formability [230–232] which arises due to highly anisotropic deformation and a strong basal texture in the microstructure. There have been attempts to

solve both of these issues through alloying. In particular, rare earth metals have been found to soften the basal texture [233–235] and improve the formability. An alternative approach, is to bypass the plastic anisotropy altogether by stabilising a crystal structure which is fundamentally more isotropic like bcc. This has been achieved in the past through alloying with lithium (Li) which has a thermodynamically stable bcc phase at roughly 30% Li.

In this chapter, we will explore the possibility of stabilising the bcc phase with small amounts of Ca. For this purpose, we have created new Mg-Ca alloy GPT potentials which are discussed in Section 4.2. In the next section, we will briefly discuss the problem of the plastic anisotropy in hcp Mg. Finally, the results of this chapter will be detailed in Section 4.4.

4.1 The Plastic Anisotropy in Mg

4.1.1 The von Mises-Taylor Criterion

We need to introduce the relevant dislocation theory concepts before discussing the plastic anisotropy directly. The primary deformation mode for a metal is via slip in close-packed directions [111]. Slip can be viewed as the sliding of one plane of atoms over another and generally occurs through the motion of dislocations. Contrast this to the collective sliding of atomic layers which is energetically unfavourable. A dislocation is an extended line defect characterised by two quantities: the Burgers vector and line sense. The Burgers vector is a measure of the lattice distortion due to the presence of a dislocation and is a topological quantity that is conserved during the dislocation motion [236]. The glide plane is the plane which contains both the Burgers vector and the dislocation line, and is the plane in which a dislocation can move without the need for assistance from point defects.

The Burgers vector and the dislocation glide plane can be associated with the slip direction and slip plane. We define the slip system as the family of symmetrically equivalent slip planes and associated slip directions. In the following, we will assume for generality that the crystal is made up of many differently oriented grains. In other words, that the crystal is a *polycrystal*. For a crystal to exhibit generalised polycrystalline ductility it requires at least five independent slip systems [237, 238]. If five independent slip systems are not available then the crystal may deform via twinning. Imagine that we can decompose the crystal into infinitesimal volume elements and that the strain on such a volume element is homogenous. The total plastic strain on the crystal can be written as a sum of these infinitesimal homogenous strains

$$\eta_{ij}^{\text{tot}} = \sum_{k} \eta_{ij}^{(k)}. \tag{4.1}$$

The volume must be conserved during the slip which places a constraint on the total strain. The volume change under an arbitrary strain can be written as

$$\Delta V = \det\left(\delta_{\alpha\beta} + \eta_{\alpha\beta}\right) \approx 1 + \sum_{\alpha} \eta_{\alpha\alpha} + \cdots \tag{4.2}$$

where the additional terms are of higher order in the strain. For there to be no volume change during slip, we require that the trace of the strain tensor vanishes i.e.

$$\eta_{11}^{\text{tot}} + \eta_{22}^{\text{tot}} + \eta_{33}^{\text{tot}} = 0. \tag{4.3}$$

Therefore, Eq.(4.1) contains only five independent total strain components and thus only five independent slip systems are required to achieve an arbitrary plastic strain. Given the assumptions of the von Mises-Taylor model, only five independent slip systems can exist in a polycrystal [111]. In a real crystal, more than five slip systems may exist due to inhomogeneities in the plastic strain near dislocation cores.

4.1.2 Slip Systems and the Critically Resolved Shear Stress

Not all slip planes possess 5 independent slip systems. Whilst a crystal structure may possess 5 independent slip systems, it may be the case that slip is not energetically favourable along one or more of these slip systems. For a metal to be ductile, we require five independent slip systems to be active. In the hcp crystal structure, which Mg assumes at ambient temperatures and pressures, there are 5 independent slip systems. However, it also true that basal and/or prismatic $\langle a \rangle$-type slip is predominant in hcp metals. The basal plane contains 3 slip systems as there are 3 possible slip directions, corresponding to rotations of $\langle 11\bar{2}0 \rangle$, and only 2 of these slip systems are independent. If prismatic $\langle a \rangle$-type slip is activated too, there are a further 2 independent slip systems. This gives a combined total of 4 independent slip planes, out of a possible 9 slip systems. Furthermore, if slip is possible on any plane for which $\langle 11\bar{2}0 \rangle$ is a zone-axis, there remains only 4 independent slip systems. This is a direct result of the inability of $\langle a \rangle$-type slip to produce a normal component of strain in the $\langle c \rangle$ direction.

In order to satisfy the von Mises-Taylor criterion, $\langle c+a \rangle$-type pyramidal slip needs to be activated. The pyramidal plane has the requisite 5 independent slip systems, including both $\langle a \rangle$- and $\langle c + a \rangle$-type slip, which can be chosen in 6 ways. Despite pyramidal slip being able to support a general deformation alone, it is energetically unfavourable. This can be attributed to the large Burgers vector $\mathbf{b}$ since the energy of a dislocation $E_{\text{dis}} \propto b^2$ and the interplanar spacing is narrow. The inability of $\langle a \rangle$-type slip to support a general deformation is responsible for the prevalence of twinning in hcp metals. In Mg, the twinning systems are not associated with large deformations [239], so they do not contribute significantly to a general deformation.

The hcp crystal structure can support a general deformation. Whether a particular metal is ductile depends on the energetics too. An important notion in this discussion

is the critically resolved shear stress (CRSS). The CRSS is the component of the shear stress resolved in the direction of the slip that is required to initiate slip. In Mg single crystals [5], the CRSS for pyramidal $\langle c+a \rangle$-type slip is 67 times larger than the CRSS for basal slip. Similarly, the CRSS for prismatic $\langle a \rangle$-type slip is 46 times larger. This is known as the plastic anisotropy and is common to all hcp metals. In recent years, there has been a lot of theoretical work towards understanding the important pyramidal $\langle c+a \rangle$ dislocation in elemental Mg [6–8].

The situation in the bcc crystal structure is very different. There are two important types of slip system: slip in the $\langle 111 \rangle$ direction and the glide plane normal to $\{110\}$, and slip in the $\langle 111 \rangle$ direction and the glide plane normal to $\{211\}$. The first slip system gives 384 different ways of choosing 5 independent slip systems whilst the second gives 792 ways. As a result, the bcc crystal structure does not suffer from a plastic anisotropy. It is true however that bcc metals are prone to brittle fracture at low temperature. This is due to a typically large Peierls stress, which is the stress required to move the entire dislocation one lattice vector along the glide direction [240–242]. At elevated temperatures, thermal fluctuations are able to move segments of the initially straight dislocation into the next Peierls valley. The resultant kinks are far more mobile than the original dislocation. This process is known as kink-pair nucleation and is an important factor in considering the ductility of bcc metals. In the following sections, we will not consider kink-pair nucleation, only the stability of the crystal structure.

4.2 GPT Potentials for the Mg-Ca Alloy System

4.2.1 Methods for Random Substitutional Alloys

Realistic simulations of random substitutional alloys require a large number of atoms in the supercell and a statistically significant number of configurations to sample. The calculation of properties should in principle be averaged over configurations. For an A-B binary substitutional alloy, the total number of configurations N_c is given by

$$N_c = \frac{N!}{N_A!N_B!}, \tag{4.4}$$

where N is the total number of atoms, N_A is the total number of A atoms and N_B is the total number of B atoms. Not all of these configurations will give the same total energy and so they are not all equally likely. Clearly for large N, the total number of configurations is an extremely large number needs to be sampled statistically. Since N_c is of the same order as Avogadro's number, we typically apply periodic boundary conditions to a finite supercell. This induces spurious short range order into the calculation and some of these supercells will be symmetrically equivalent due to the restoration of lattice translational symmetry. For instance, in the simplest case where N_A or $N_B = 1$, each configuration is symmetrically equivalent. This scenario is exactly that of a single vacancy in a finite periodic supercell. In the general case, we may decompose the A or B atomic configuration into figures $f = (k, m)$ which are graphs that connect atoms within the supercell. Each figure has k vertices and neighbour distance m [243]. This decomposition allows for a simple comparison between two configurations; if all the figures match then the configuration is symmetrically equivalent.

There are several approaches to random substitutional alloys which bypass the need to average over configurations by building the configurational average directly

into the electronic structure. One such approach is the conceptually-simple *virtual crystal approximation* (VCA)

$$W_{\mathrm{VCA}}\left(\mathbf{r},\mathbf{r}'\right) = c_A W_A\left(\mathbf{r},\mathbf{r}'\right) + c_B W_B\left(\mathbf{r},\mathbf{r}'\right) \tag{4.5}$$

where $c_B = N_B/N$ and $c_A = N_A/N$ are the concentrations of A and B respectively. Due to the normalisation of probability, we will work with single concentration variable $x \equiv c_B = 1 - c_A$. The VCA is nothing more than a concentration averaged pseudopotential and allows one to calculate random substitutional alloys without the need for large supercells. Thus, only a primitive cell is necessary for calculations of elastic constants, equations of state and lattice parameters. Unfortunately, the VCA only provides qualitative agreement with experiment for a number of properties including lattice parameters [244–247].

Similar to the VCA, but physically more justifiable, is the coherent potential approximation (CPA) which is based on multiple scattering theory [248–251]. The goal of the CPA is to obtain a self-energy Σ^{CPA}. The self-energy is a complex and energy-dependent periodic potential that captures the features of disorder in the alloy. The self-energy can be written, without approximation, in terms of the single-site scattering matrices $\{t_i\}$. The CPA imposes the condition that

$$\langle t_i \rangle \equiv (1-x)\, t_i^A + x t_i^B = 0 \tag{4.6}$$

where t_i^α is the α-component of the single-site scattering matrix on the site i. This directly leads to an integral equation for the CPA self-energy Σ_{CPA}. The CPA has been used to calculate total energies and pressures with some success [252, 253]. The CPA formalism becomes extremely complex when the effect of disorder is off-diagonal in the VCA eigenbasis. There are more obvious limitations to the CPA, particularly in the calculation of defects where the local atomic configuration is important. The

CPA is not designed to capture this kind of inhomogeneity and a real-space supercell method is required.

The averaging over configurations may be eliminated by carefully selecting a representative sample that best replicates a truly random alloy. A randomly populated supercell approximating a disordered A-B substitutional alloy may contain spurious ordering due to periodic boundary conditions. Firstly, we map the problem of a random A-B substitutional alloy onto a classical spin-1/2 Ising model. We define Π_f as the product of all 'spins' which comprise the figure. For example, if $k = 2$ and the figure is a graph which connects two A atoms then $\Pi_f = 1$. Alternatively, if the figure connects an A atom with a B atom then $\Pi_f = -1$. In this sense, Π_f is the correlation between atoms which comprise the figure. The average of these correlation functions can then be used as a measure of the ordering within the alloy. For $k = 2$, these averaged correlation functions are related to Cowley's short range order parameters [254]. The average correlation function $\bar{\Pi}_f$ for a figure $f(k, m)$ is given by

$$\bar{\Pi}_f(\mathcal{S}) = \frac{1}{ND_f} \sum_i \Pi_f(i, \mathcal{S}). \tag{4.7}$$

where the sum is over the sites in the supercell, $\mathcal{S}$ is the crystal structure, D_f is the number of figures per site and Π_f is the spin-spin correlation function. For a perfectly random alloy $\mathcal{S} = \mathcal{R}$ with concentration x, there is an exact result for the averaged correlation functions [255, 256]

$$\bar{\Pi}_{k,m}(\mathcal{R}) = \langle \bar{\Pi}_{k,m} \rangle_{\mathcal{R}} = (2x - 1)^k. \tag{4.8}$$

We search for supercells which best match this exact result for a handful of figures. These supercells are called special quasi-random structures (SQS) [255, 256]. For a

given physical property P, the error in the expectation value may be written

$$\langle P \rangle - P(\mathcal{S}) = \sum_{k,m}{}' D_{k,m} \left[(2x-1)^k - \bar{\Pi}_{k,m}(\mathcal{S}) \right] p_{k,m} \tag{4.9}$$

where the checked sum refers to the omission of $k = 0, 1$ and $p_{k,m}$ is the contribution to P of the figure with k vertices over a neighbour distance m. The physical property P depends primarily on the neighbours within a radius L where L is the characteristic length scale. For neighbour distances greater than L, we expect the contribution to the expectation value to fall off exponentially with increasing neighbour distance [257]. Therefore, by matching the correlation functions of the SQS according to Eq.(4.8), we expect that configurational properties will be close to the true configurational average. The SQS formalism is used throughout the remainder of this chapter.

4.2.2 The Binary Alloy GPT Applied to Mg-Ca

In the previous subsection, we have stressed the importance of real-space methods as applied to alloys and showed the considerable reduction in complexity granted by an SQS representation. As the GPT is primarily a linear-scaling real-space method, it is ideally suited to the calculation of the properties of random alloys. The GPT was extended to A-B binary compounds and alloys, where A is a simple metal and B is a transition metal, in a series of papers by Moriarty and Widom [258, 259] based on the earlier ideas of Hafner [97]. It was then extended to ternary compounds and alloys in a subsequent paper [260]. Our starting point for discussion of the alloy GPT is the full transition metal GPT. The transition metal GPT, which goes well beyond Chapter 2, contains an expansion of the electron density and total energy in terms of a weak *sp* pseudopotential, *sp*-*d* hybridisation and *d*-*d* tight binding matrix elements. In real space, the derived interatomic potentials become well-defined functionals of these matrix elements. This leaves us with the central result of the GPT; a rigorous

many body expansion of the total energy [99]

$$E_{\text{tot}}\left(\{\mathbf{R}\},\Omega\right) = NE_{\text{vol}}\left(\Omega\right) + \frac{1}{2}\sum_{ij}{}' v_2\left(ij,\Omega\right) + \frac{1}{3!}\sum_{ijk}{}' v_3\left(ijk,\Omega\right) + \frac{1}{4!}\sum_{ijkl}{}' v_4\left(ijkl,\Omega\right) + \cdots \tag{4.10}$$

where the indices are shorthand for the interatomic separations. As a result of the dependence on relative ion separation and volume, all of the potentials are transferable to any ion configuration. For A-B metallic compounds and alloys, both the volume term E_{vol} and the multi-ion terms will become concentration dependent. The volume term E_{vol} simply becomes

$$E_{\text{vol}}\left(\Omega\right) \rightarrow E_{\text{vol}}\left(\Omega, x\right). \tag{4.11}$$

As $x \rightarrow 0$ we must recover the simple metal volume term for A and, correspondingly, as $x \rightarrow 1$ we recover the transition metal volume term for B. The interatomic potentials v_2 will become species dependent, as well as concentration- and volume-dependent. For an A-B binary alloy or intermetallic compound, there are three independent two-ion potentials

$$v_2 \rightarrow v_2^{AA}, v_2^{AB}, v_2^{BB}, \tag{4.12}$$

four independent three-ion potentials

$$v_3 \rightarrow v_3^{AAA}, v_3^{AAB}, v_3^{ABB}, v_3^{BBB}, \tag{4.13}$$

and five independent four-ion potentials

$$v_4 \rightarrow v_4^{AAAA}, v_4^{AAAB}, v_4^{AABB}, v_4^{ABBB}, v_4^{BBBB}. \tag{4.14}$$

Additional self-consistent electron-density constraints must now be satisfied. This links the *sp*-valences Z_A and Z_B with the *d*-band occupations Z_d^A and Z_d^B as functions of both volume and concentration. In the case where A is a simple metal and B is a transition metal, both Z_A and Z_d^A are fixed whilst Z_B and Z_d^B are variable. In our specific case, the Mg-Ca alloy system where $A = \text{Mg}$ and $B = \text{Ca}$, Mg is a simple metal for all the atomic volumes of interest $\Omega^{\text{Mg}} \in [92.9, 197.5]$ a.u.. On the other hand, Ca is an empty *d*-band metal at its observed equilibrium atomic volume $\Omega_0^{\text{Ca}} = 290.0$ a.u. [116, 136]. The GPT description for empty *d*-band metals includes *sp*-*d* hybridisation, which is important for structural stability and phonon spectra despite these states lying above the Fermi level. For low concentrations of Ca $x \leq 0.25$, the Ca atoms are effectively at high pressure and there is some *s*-*d* transfer. We proceed by including a finite overlap potential into the description, as we would for filled *d*-band metals such as Zn [10]. Our goal will be to find analytic expressions for 4 terms: E_{vol}, v_2^{AA}, v_2^{AB} and v_2^{BB}.

Extending the GPT to binary intermetallic compounds and alloys requires a re-definition of the effective valences and atomic volumes to ensure electron density continuity. The zeroth-order *sp* valence density of the system is Z/Ω where Z is the concentration-weighted average effective *sp* valence occupation

$$Z = c_A Z_A + c_B Z_B = (1 - x)\, Z_A + x Z_B, \tag{4.15}$$

where Z_A and Z_B are the respective *sp* valences of the A and B components. We can

also define effective individual atomic volumes Ω_A and Ω_B with

$$\Omega = c_A\Omega_A + c_B\Omega_B = (1-x)\,\Omega_A + x\Omega_B. \tag{4.16}$$

To ensure electron density continuity we require

$$Z/\Omega = Z_A/\Omega_A = Z_B/\Omega_B. \tag{4.17}$$

These parameter tuples (Z_A, Ω_A) and (Z_B, Ω_B) define zeroth-order pseudoatoms [181] for the A and B components. These pseudoatoms may have been expanded or contracted from their elemental sizes. If both A and B are simple metals, then the *sp* valence occupations, Z_A and Z_B, are fixed. In this case, the above equations are sufficient to calculate the effective atomic volumes. However, if A is a simple metal and B is a transition metal, there will be some *sp*-*d* transfer as Z_B and Z_d^B are not fixed quantities. Further equilibrium constraints are needed to be calculate these quantities. These conditions link Z_B and Z_d^B through the Fermi level ε_F and the $l = 2$ scattering phase shift δ_2 associated with the B pseudoatom [10]

$$Z_d^B = \frac{10}{\pi}\delta_2\left(\varepsilon_F\right), \tag{4.18}$$

$$\varepsilon_F = \frac{\hbar^2}{2m}\left(\frac{3\pi^2 Z}{\Omega}\right)^{2/3}. \tag{4.19}$$

We also have the following constraint that the total number electrons is fixed

$$Z_B + Z_d^B = Z_a^B - Z_c^B, \tag{4.20}$$

where Z_a^B is the atomic number of the B atom and Z_c^B is the number of inner-core electrons. The Fermi energy ε_F and the phase shift δ_2 are highly-dependent on the in-

termetallic environment, and will be shifted away from their bulk elemental values. For given values of Ω, x and Z_A, the seven equations introduced in this subsection can be used to determine the unknown parameters. Due to their inherent non-linearity, these parameters must be iterated numerically. There are some necessary modifications to the pseudoatom formalism to be made. The primary concern is to guarantee that the now concentration-dependent minimum of the valence-band V_0' are in agreement between A and B. To determine V_0', we first define a mean pseudoatom plane-wave matrix element with respect to concentration,

$$\langle \mathbf{k}|w_{\mathrm{pa}}|\mathbf{k}\rangle = c_A\langle \mathbf{k}|w_{\mathrm{pa}}^A|\mathbf{k}\rangle + c_B\langle \mathbf{k}|w_{\mathrm{pa}}^B|\mathbf{k}\rangle \tag{4.21}$$

where the A- and B-component atomic pseudopotentials are given by

$$\langle \mathbf{k}|w_{\mathrm{pa}}^\alpha|\mathbf{k}\rangle = \langle \mathbf{k}|v_{\mathrm{pa}}^\alpha|\mathbf{k}\rangle - V_0' + \sum_c \left(\varepsilon_{\mathbf{k}} - E_c^{\mathrm{vol},\alpha}\right)\langle \mathbf{k}|\phi_c^\alpha\rangle\langle\phi_c^\alpha\rangle|\mathbf{k}\rangle \tag{4.22}$$

with $\alpha = A$ or B. Note that Eq.(4.21) is reminiscent of the VCA introduced in Eq.(4.5). The quantity ϕ_c^α is an α-component core state, while $E_c^{\mathrm{vol},\alpha}$ is the volume component of the corresponding core energy

$$E_c^{\mathrm{vol},\alpha} = E_c^{\mathrm{pa},\alpha} - \langle\phi_c^\alpha|\delta V_{\mathrm{unif}}|\phi_c^\alpha\rangle - V_0' \tag{4.23}$$

where $\delta V_{\mathrm{unif}} = v_{\mathrm{unif}} - V_{\mathrm{unif}}$ is the small structure-independent difference between the Coulomb potential v_{unif} due to a sphere containing charge density n_{unif} and the total uniform electron gas potential V_{unif}

$$\delta V_{\mathrm{unif}}(r) = \begin{cases} 0 & r \le R_{\mathrm{WS}} \\ Ze^2\left[1/r - \left(3 - r^2/R_{\mathrm{WS}}^2\right)/\left(2R_{\mathrm{WS}}\right)\right] & r > R_{\mathrm{WS}} \end{cases} \tag{4.24}$$

The other term, $E_c^{\mathrm{pa},\alpha}$, is the core eigenvalue of the α-component pseudoatom

$$\left(T + v_{\mathrm{pa}}^{\alpha}\right)|\phi_c\rangle = E_c^{\mathrm{pa},\alpha}|\phi_c\rangle \tag{4.25}$$

where the α-pseudoatom potential $v_{\mathrm{pa}}^{\alpha}(r) = v_{\mathrm{unif}}^{\alpha}(r) + v_{\mathrm{ion}}^{\alpha}(r)$. At $\mathbf{k} = 0$, we require

$$\langle 0|w_{\mathrm{pa}}|0\rangle = 0 \tag{4.26}$$

which places the zero of energy at the bottom of the valence bands in the full intermetallic system. If we explicitly remove the V_0' dependence from the pseudoatom matrix element, then,

$$\langle 0|w_{\mathrm{pa}}^{\alpha}|0\rangle_0 = \langle 0|w_{\mathrm{pa}}^{\alpha}|0\rangle + V_0'\left(1 - \langle 0|p_c^{\alpha}|0\rangle\right), \tag{4.27}$$

with p_c^{α} is the α-component inner-core projection operator. This leaves us with the following expression for V_0'

$$V_0' = \frac{c_A\langle 0|w_{\mathrm{pa}}^{A}|0\rangle_0 + c_B\langle 0|w_{\mathrm{pa}}^{B}|0\rangle_0}{1 - c_A\langle 0|p_c^{A}|0\rangle - c_B\langle 0|p_c^{B}|0\rangle}. \tag{4.28}$$

The simple metal A pseudoatom depends on the transition metal B pseudoatom indirectly through the atomic volume Ω_A, and does not otherwise depend on V_0'. However, the transition metal B pseudoatom depends on the simple metal A pseudoatom through both its atomic volume Ω_B and effective valence Z_B, which depend directly on V_0'. The one-ion integrated density of d-states can be written [99]

$$\mathcal{D}_d(E) = -\frac{2}{\pi}\mathrm{Im}\sum_d \log\left[E - E_d^{\mathrm{vol},B} - \Gamma_{dd}^{\mathrm{vol},B}(E)\right]. \tag{4.29}$$

where $\Gamma_{dd}^{\mathrm{vol},B}$ is the volume component of the d-state self-energy [99] and $E_d^{\mathrm{vol},B}$ is

defined in an analogous way to Eq.(4.23)

$$E_d^{\mathrm{vol},B} = E_d^{\mathrm{pa},B} - \langle \phi_d^B | \delta V_{\mathrm{unif}} | \phi_d^B \rangle - V_0'. \tag{4.30}$$

Therefore, the effective d-state occupation for the B pseudoatom can be written as

$$Z_d^B = -\frac{2}{\pi} \mathrm{Im} \sum_d \log \left[\varepsilon_F - E_d^{\mathrm{vol}} - \Gamma_{dd}^{\mathrm{vol}} \left(\varepsilon_F \right) \right]. \tag{4.31}$$

We will broadly detail the steps used to calculate the pseudoatom parameters in the intermetallic GPT self-consistently. For a given atomic volume Ω and concentration x, we have:

(i) We choose a trial Ω_A and calculate the A pseudoatom which determines values for $\langle 0 | w_{\mathrm{pa}}^A | 0 \rangle_0$ and $\langle 0 | p_c^A | 0 \rangle$ entering Eq.(4.28) for V_0'.

(ii) Next, we calculate Ω_B from Eq.(4.16) and infer Z_B from the electron density continuity constraint i.e. $Z/\Omega = Z_B/\Omega_B$. This gives us values for Z_B, Z_d^B, ε_F and V_0'.

(iii) Finally, we check whether $Z_A/\Omega_A = Z_B/\Omega_B$ is satisfied. If not, we repeat (i) and (ii) until it is satisfied to some tolerance. We use 10^{-4} in our calculations.

The real-space total energy for an A-B alloy, with mean atomic volume Ω and concentration x, can be written as

$$E_{\mathrm{tot}} \left(\{ \mathbf{R} \}, \Omega \right) = N E_{\mathrm{vol}} \left(\Omega, x \right) + \frac{1}{2} \sum_{\alpha\beta} {\sum_{ij}}' v_2^{\alpha\beta} \left(R_{ij}^{(\alpha\beta)}, \Omega, x \right) + \cdots \tag{4.32}$$

where the sum is over the species labels $\alpha, \beta = A, B$. We also have $v_2^{AB} = v_2^{BA}$ by symmetry and the three- and four-ion contributions are generalized in a similar way. The interatomic separation $R_{ij}^{(\alpha\beta)}$ becomes implicitly species dependent too. We will

attempt to evaluate the volume term $E_{\rm vol}$ and $v_2^{\alpha\beta}$ along the same lines as Chapter 2. The volume term $E_{\rm vol}$ is most readily expressed as a sum of contributions up to quadratic order in the concentration variables c_A and c_B

$$\begin{aligned} E_{\rm vol} &= c_A E_1^A + c_B E_1^B + c_A^2 E_2^{AA} + c_A c_B E_2^{AB} + c_B^2 E_2^{BB} + \delta E_{\rm vol} \\ &= (1-x)\, E_1^A + x E_1^B + (1-x)^2\, E_2^{AA} + (1-x)\, x E_2^{AB} + x^2 E_2^{BB} + \delta E_{\rm vol}. \end{aligned} \quad (4.33)$$

We make the following definitions for the various contributions to the volume term $E_{\rm vol}$ and $v_2^{\alpha\beta}$. The reciprocal space diagonal element of the pseudopotential can be written as

$$w_{\rm pa}^{\alpha}\left(\mathbf{k}\right) \equiv \langle \mathbf{k} | w_{\rm pa}^{\alpha} | \mathbf{k} \rangle \quad (4.34)$$

for $\alpha = A$ and B. We are also able to write the reciprocal space diagonal element of the inner-core projection operator as

$$p_c^{\alpha}\left(\mathbf{k}\right) \equiv \langle \mathbf{k} | p_c^{\alpha} | \mathbf{k} \rangle. \quad (4.35)$$

We will ignore the complications of self-consistent electron screening. We may immediately write down E_1^A and E_2^{AA} since we have come across them previously in Chapter 2. Firstly, E_1^A is given by

$$\begin{aligned} E_1^A = E_{\rm fe}^A + \frac{2\Omega}{\left(2\pi\right)^3} \int {\rm d}\mathbf{k}\ f_{\mathbf{k}} w_{\rm pa}^A\left(\mathbf{k}\right) - E_{\rm bind}^{{\rm atom},A}\left(Z_A\right) + E_{\rm oh}^A \\ + \left(Z_A^* e\right)^2 \left[\frac{9}{10} \frac{1}{R_{\rm WS}^A} - \frac{1}{\pi} \int_0^{\infty} {\rm d}q\ F_N^{AA}\left(q, \Omega, x\right) \right] \end{aligned} \quad (4.36)$$

where $E_{\rm oh}^A$ is the self-energy of the orthogonalisation-hole correction in Eq.(2.171), F_N^{AA}

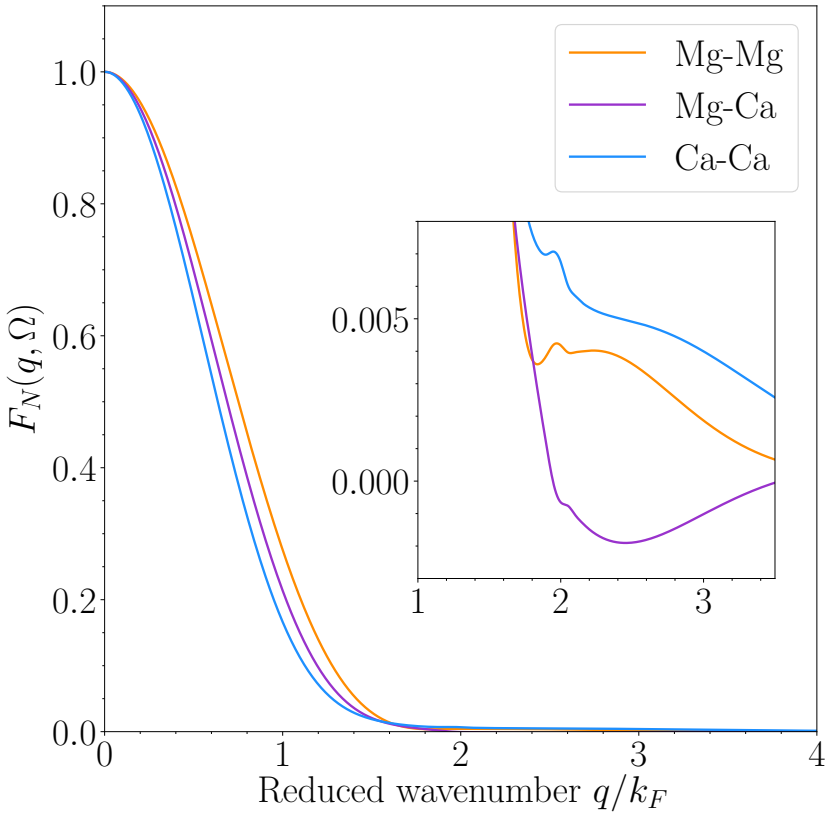

Fig. 4.1: The normalized energy-wavenumber characteristic for Mg-Ca including all hybridization terms in the low solubility limit $x \to 0$. The inset is the same graph zoomed in on the logarithmic singularity at $q = 2k_F$.

is the normalised energy-wavenumber characteristic (see Fig.(4.1) for Mg-Ca) and E_{fe}^{α} is the zeroth-order α-component of the free-electron energy (i.e. Eq.(2.111))

$$E_{\text{fe}}^{\alpha} = \frac{3}{5} Z_{\alpha} \varepsilon_F + Z_{\alpha} \varepsilon_{\text{xc}} - \frac{3}{5} \left(Z_{\alpha} e\right)^2 / R_{\text{WS}}^{A} + Z V_0' \tag{4.37}$$

where ε_{xc} is the exchange-correlation energy of the free-electron gas and R_{WS}^{α} is the Wigner-Seitz radius corresponding to atomic volume Ω_{α}. The second-order term E_2^{AA} is given by

$$E_2^{AA} = \frac{2\Omega}{(2\pi)^3} \int \mathrm{d}\mathbf{k}\ f_{\mathbf{k}} p_c^{A}\left(\mathbf{k}\right) w_{\text{pa}}^{A}\left(\mathbf{k}\right) + \left(Z_A^{*} e\right)^2 \frac{\pi}{\Omega} \frac{\partial^2 F_N^{AA}\left(0, \Omega, x\right)}{\partial q^2}. \tag{4.38}$$

To account for *sp-d* hybridisation, we define a hybridisation form factor [99]

$$h_{nm}^{B}\left(\mathbf{k},\mathbf{q}\right)=-\frac{1}{\pi}\mathrm{Im}\int_{0}^{\varepsilon_{F}}\mathrm{d}E\ \frac{\left[\sum_{d}v_{\mathbf{k}+\mathbf{q}d}'\left(E\right)v_{d\mathbf{k}}'\left(E\right)\right]}{\left(E-E_{r}^{B}\right)^{n}\left(E-\varepsilon_{\mathbf{k}}\right)^{m}} \tag{4.39}$$

where n and m are integers, and E_r^B is the complex energy-dependent d-state resonance position

$$E_{r}^{B}=E_{d}^{\mathrm{vol},B}+\Gamma_{dd}^{\mathrm{vol},B}\left(E\right). \tag{4.40}$$

The matrix elements $v'_{\mathbf{k}+\mathbf{q}d}$ and $v'_{d\mathbf{k}}$ can be written in terms of the overlap matrix $S_{\mathbf{k}d}^{B}=\langle\mathbf{k}|\phi_{d}^{B}\rangle$ and the volume-part of the d-state hybridisation potential Δ_{vol}, first introduced by Harrison [131],

$$v_{\mathbf{k}d}=-\left(E-E_{d}^{\mathrm{vol},B}\right)S_{\mathbf{k}d}^{B}-\langle\mathbf{k}|\Delta_{\mathrm{vol}}|\phi_{d}^{B}\rangle \tag{4.41}$$

The term at linear order in the concentration variable for the B-pseudoatom E_1^B can be written analogously to E_1^A

$$\begin{aligned}E_{1}^{B}=E_{\mathrm{fe}}^{B}+E_{\mathrm{vol}}^{d}+\frac{2\Omega}{\left(2\pi\right)^{3}}\int\mathrm{d}\mathbf{k}\ f_{\mathbf{k}}w_{\mathrm{pa}}^{B}\left(\mathbf{k}\right)-E_{\mathrm{bind}}^{\mathrm{atom},B}\left(Z_{B}\right)+E_{\mathrm{prep}}+E_{\mathrm{oh}}^{B}\\+\left(Z_{B}^{*}e\right)^{2}\left[\frac{9}{10}\frac{1}{R_{\mathrm{WS}}^{2}}-\frac{1}{\pi}\int_{0}^{\infty}\mathrm{d}q\ F_{N}^{BB}\left(q,\Omega,x\right)\right]+\frac{1}{\pi}\mathrm{Im}\sum_{d}\int_{0}^{\varepsilon_{F}}\mathrm{d}E\ \frac{\left[\Gamma_{dd}^{\mathrm{vol},B}\left(E\right)\right]^{2}}{\left(E-E_{r}^{B}\right)^{2}}.\end{aligned} \tag{4.42}$$

where E_{vol}^{d} is the transition metal d-state contribution

$$E_{\mathrm{vol}}^{d}=Z_{d}^{B}\left(\varepsilon_{F}-E_{d}^{\mathrm{vol},B}\right)-\frac{10}{\pi}\int_{0}^{\varepsilon_{F}}\mathrm{d}E\ \delta_{2}\left(E\right), \tag{4.43}$$

The quantity $E_{\mathrm{bind}}^{\mathrm{atom},\alpha}$ is the free-atom binding energy of the α-component. This is

precisely the free-atom binding energy of the Z_α s and p valence electrons. In the simple metal A, this is the same as the quantity introduced in Eq.(2.52). However, for the transition metal B-component, this quantity is not quite the same as the binding energy of the free-atom as there will be a different sp-valence occupation in the intermetallic environment i.e. $Z_B \neq Z_B^{\text{fa}}$. There is an energy associated with forcing the free-atom to assume this particular electron configuration. This energy is the so-called preparation energy E_{prep} and can be calculated within DFT [99]. The second-order terms in the concentration can also be written down. Firstly, for E_2^{AB} we have

$$\begin{aligned} E_2^{AB} = & \frac{2\Omega}{(2\pi)^3} \int \mathrm{d}\mathbf{k}\ f_{\mathbf{k}} \left[p_c^A(\mathbf{k})\, w_{\text{pa}}^B(\mathbf{k}) + w_{\text{pa}}^A(\mathbf{k})\, p_c^B(\mathbf{k}) \right] \\ & + \frac{2\Omega}{(2\pi)^3} \int \mathrm{d}\mathbf{k}\ f_{\mathbf{k}} \left[w_{\text{pa}}^A(\mathbf{k})\, h_{12}^B(\mathbf{k},0) + p_c^A(\mathbf{k})\, h_{11}^B(\mathbf{k},0) \right] \\ & + \left(Z_A^* Z_B^* e^2 \right) \frac{2\pi}{\Omega} \frac{\partial^2 F_N^{AB}(0,\Omega,x)}{\partial q^2}, \end{aligned} \tag{4.44}$$

and for E_2^{BB} we have,

$$\begin{aligned} E_2^{BB} = & \frac{2\Omega}{(2\pi)^3} \int \mathrm{d}\mathbf{k}\ f_{\mathbf{k}} p_c^B(\mathbf{k})\, w_{\text{pa}}^B(\mathbf{k}) \\ & + \frac{2\Omega}{(2\pi)^3} \int \mathrm{d}\mathbf{k}\ f_{\mathbf{k}} \left[w_{\text{pa}}^B(\mathbf{k})\, h_{12}^B(\mathbf{k},0) + p_c^B(\mathbf{k})\, h_{11}^B(\mathbf{k},0) + \frac{1}{2} h_{22}^B(\mathbf{k},0) \right] \\ & + \left(Z_B^* e \right)^2 \frac{\pi}{\Omega} \frac{\partial^2 F_N^{BB}(0,\Omega,x)}{\partial q^2}. \end{aligned} \tag{4.45}$$

The final correction in Eq.(4.33) is due to the change in Fermi energy [99] and is given

by

$$\delta E_{\mathrm{vol}} = -\frac{1}{2} w_{\mathrm{pa}}\left(\mathbf{k}_F\right) \delta Z_{\mathrm{band}}, \tag{4.46}$$

where

$$\delta Z_{\mathrm{band}} = w_{\mathrm{pa}}\left(\mathbf{k}_F\right) \frac{c_B \rho_0\left(\varepsilon_F\right) \rho_d\left(\varepsilon_F\right)}{\rho_0\left(\varepsilon_F\right) + c_B \rho_d\left(\varepsilon_F\right)}, \tag{4.47}$$

with ρ_0 and ρ_d are the free-electron and d-state density of states at the Fermi level respectively. The simple metal AA pair potential has precisely the same form as Eq.(2.134)

$$v_2^{AA}\left(r, \Omega, x\right) = \frac{\left(Z_A^* e\right)^2}{r}\left[1 - \frac{2}{\pi}\int_0^\infty \mathrm{d}q \; F_N^{AA}\left(q, \Omega, x\right) \frac{\sin\left(qr\right)}{q}\right]. \tag{4.48}$$

The normalised energy-wavenumber characteristic F_N^{AA} (see Fig.(4.1) for Mg-Ca) is also written in precisely the same way as in Eq.(2.133)

$$F_N^{AA}\left(q, \Omega, x\right) = -\frac{q^2 \Omega}{2\pi\left(Z_A^* e\right)^2} F_{ss}^{AA}\left(q, \Omega, x\right) \tag{4.49}$$

where F_{ss} is the energy-wavenumber characteristic due to the itinerant s and p valence electrons. In general, we have

$$\begin{aligned} F_{ss}^{\alpha\beta}\left(q, \Omega, x\right) = & \frac{2\Omega}{\left(2\pi\right)^3}\int \mathrm{d}\mathbf{k} \; f_{\mathbf{k}} \frac{w^\alpha\left(\mathbf{k}, \mathbf{q}\right) w^\beta\left(\mathbf{k}, \mathbf{q}\right)}{\varepsilon_{\mathbf{k}} - \varepsilon_{\mathbf{k}+\mathbf{q}}} \\ & - \frac{2\pi e^2 \Omega}{q^2}\left(\left(1 - G\left(q\right)\right) n_{\mathrm{scr}}^\alpha\left(q\right) n_{\mathrm{scr}}^\beta\left(q\right) + G\left(q\right) n_{\mathrm{oh}}^\alpha\left(q\right) n_{\mathrm{oh}}^\beta\left(q\right)\right). \end{aligned} \tag{4.50}$$

The simple-metal screening density for A is once again the same as for the elemental

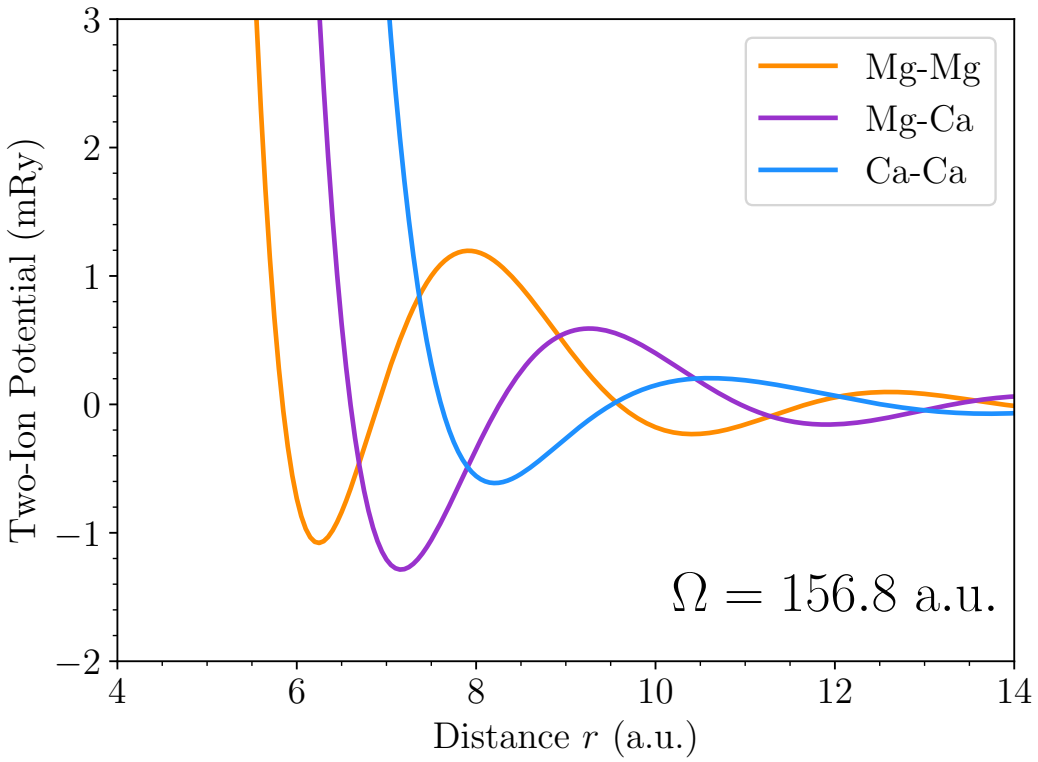

Fig. 4.2: Pair potentials v_2 for the Mg-Ca alloy system in the low solubility limit $x \to 0$ at the observed equilibrium volume for hcp Mg ($\Omega_0 = 156.8$ a.u.^{3}).

case in Eq.(2.100)

$$n^A_{\mathrm{scr}}(q) = \frac{4}{(2\pi)^3} \int \mathrm{d}\mathbf{k}\; f_{\mathbf{k}} \frac{w^A(\mathbf{k},\mathbf{q})}{\varepsilon_{\mathbf{k}} - \varepsilon_{\mathbf{k}+\mathbf{q}}} \tag{4.51}$$

whilst the B-component screening density gets an *sp-d* hybridisation correction

$$n^B_{\mathrm{scr}}(q) = \frac{4}{(2\pi)^3} \int \mathrm{d}\mathbf{k}\; f_{\mathbf{k}} \frac{w^B(\mathbf{k},\mathbf{q})}{\varepsilon_{\mathbf{k}} - \varepsilon_{\mathbf{k}+\mathbf{q}}} + \frac{4}{(2\pi)^3} \int \mathrm{d}\mathbf{k}\; f_{\mathbf{k}} \frac{h^B_{11}(\mathbf{k},\mathbf{q})}{\varepsilon_{\mathbf{k}} - \varepsilon_{\mathbf{k}+\mathbf{q}}}. \tag{4.52}$$

We have also defined the pseudopotential form factor $w^\alpha(\mathbf{k},\mathbf{q})$ for the α-component as

$$w^{\alpha}\left(\mathbf{k},\mathbf{q}\right)=\langle\mathbf{k}+\mathbf{q}|w^{\alpha}|\mathbf{k}\rangle=\langle\mathbf{k}+\mathbf{q}|v^{\alpha}|\mathbf{k}\rangle+\sum_{c}\left(\varepsilon_{\mathbf{k}}-E_{c}^{\mathrm{vol},\alpha}\right)\langle\mathbf{k}+\mathbf{q}|\phi_{c}^{\alpha}\rangle\langle\phi_{c}^{\alpha}|\mathbf{k}\rangle. \tag{4.53}$$

The quantities v^{α} are the self-consistently screened A- and B-component atomic potentials which depend on the screening densities n_{scr}^{A} and n_{scr}^{B} through a generalised Poisson equation. The orthogonalisation-hole density n_{oh}^{α} of the α-component contains a contribution from the inner-core projection operator p_{c}^{α}. This contribution is given by

$$n_{\mathrm{oh}}^{c,\alpha}\left(\mathbf{r}\right)=\frac{2\Omega}{\left(2\pi\right)^{3}}\int\mathrm{d}\mathbf{k}\;f_{\mathbf{k}}\left[\langle\mathbf{r}|p_{c}^{\alpha}|\mathbf{k}\rangle\langle\mathbf{k}|p_{c}^{\alpha}|\mathbf{r}\rangle-\langle\mathbf{r}|p_{c}^{\alpha}|\mathbf{k}\rangle\langle\mathbf{k}|\mathbf{r}\rangle-\langle\mathbf{r}|\mathbf{k}\rangle\langle\mathbf{k}|p_{c}^{A}|\mathbf{r}\rangle\right]. \tag{4.54}$$

For the simple-metal A-component, the full orthogonalisation-hole density is equal to the inner-core component i.e. $n_{\mathrm{oh}}^{A}=n_{\mathrm{oh}}^{c,A}$. On the other hand, the transition-metal B-component gains an additional *sp*-*d* hybridisation contribution from $v'_{\mathbf{k}d}$

$$\begin{aligned}n_{\mathrm{oh}}^{B}\left(\mathbf{r}\right)=n_{\mathrm{oh}}^{c,B}\left(\mathbf{r}\right)-\frac{2}{\pi}\mathrm{Im}\sum_{d\mathbf{k}}\int_{0}^{\varepsilon_{F}}\mathrm{d}E\;\Bigg[&-\frac{\langle\mathbf{k}|\phi_{d}^{B}\rangle v'_{d\mathbf{k}}v'_{\mathbf{k}d}\langle\phi_{d}^{B}|\mathbf{r}\rangle}{\left(E-E_{r}^{B}\right)\left(E-\varepsilon_{\mathbf{k}}\right)^{2}}\\&+\frac{\langle\mathbf{r}|\phi_{d}^{B}\rangle v'_{d\mathbf{k}}\left(\langle\mathbf{k}|\mathbf{r}\rangle-S_{\mathbf{k}d}\langle\phi_{d}^{B}|\mathbf{r}\rangle\right)+\mathrm{c.c.}}{\left(E-E_{r}^{B}\right)\left(E-\varepsilon_{\mathbf{k}}\right)}\Bigg]+\frac{\delta Z_{\mathrm{band}}}{Z_{d}}n_{d}\left(\mathbf{r}\right).\end{aligned} \tag{4.55}$$

where $S_{\mathbf{k}d}$ is the plane-wave d-state overlap matrix element. The effective valence Z_{α}^{*} due to the orthogonalisation-hole density is given by

$$Z_{\alpha}^{*}=Z_{\alpha}-\int\mathrm{d}\mathbf{r}\;n_{\mathrm{oh}}^{\alpha}\left(\mathbf{r}\right). \tag{4.56}$$

The A-B pair potential has the form

$$v_2^{AB}(r,\Omega,x) = \frac{Z_A^* Z_B^* e^2}{r}\left[1 - \frac{2}{\pi}\int_0^\infty \mathrm{d}q\ F_N^{AB}(q,\Omega,x)\,\frac{\sin(qr)}{q}\right] \tag{4.57}$$

where F_N^{AB} is given by

$$F_N^{AB}(q,\Omega,x) = -\frac{q^2\Omega}{2\pi Z_A^* Z_B^* e^2}\left[F_{ss}^{AB}(q,\Omega,x) + F_{sd}^{AB}(q,\Omega,x)\right] \tag{4.58}$$

with F_{ss}^{AB} being given by Eq.(4.50) for $\alpha = A$ and $\beta = B$. We have the energy-wavenumber characteristic for the *sp*-*d* hybridisation

$$F_{sd}^{AB} = \frac{2\Omega}{(2\pi)^3}\int \mathrm{d}\mathbf{k}\ \frac{w^A(\mathbf{k},\mathbf{q})\,h_{11}^B(\mathbf{k},\mathbf{q})}{\varepsilon_{\mathbf{k}} - \varepsilon_{\mathbf{k}+\mathbf{q}}}. \tag{4.59}$$

Finally, the BB or transition-metal pair potential has the form

$$v_2^{BB}(r,\Omega,x) = \frac{(Z_B^* e)^2}{r}\left[1 - \frac{2}{\pi}\int_0^\infty \mathrm{d}q\ F_N^{BB}(q,\Omega,x)\,\frac{\sin(qr)}{q}\right] + v_{\mathrm{ol}}^{BB}(r,\Omega,x)\,, \tag{4.60}$$

with the BB energy-wavenumber characteristic given by (see Fig.(4.1) for Mg-Ca)

$$F_N^{BB}(q,\Omega,x) = -\frac{q^2\Omega}{2\pi(Z_B^* e)^2}\left[F_{ss}^{BB}(q,\Omega,x) + 2F_{sd}^{BB}(q,\Omega,x) + F_{dd}^{BB}(q,\Omega,x)\right]. \tag{4.61}$$

The *dd* contribution to the energy-wavenumber characteristic is given by

$$F_{dd}^{BB}(q,\Omega,x) = \frac{2\Omega}{(2\pi)^3}\int \mathrm{d}\mathbf{k}\ \frac{h_{21}^B(\mathbf{k},\mathbf{q})}{\varepsilon_{\mathbf{k}} - \varepsilon_{\mathbf{k}+\mathbf{q}}}. \tag{4.62}$$

The full overlap potential v_{ol} is given by Moriarty [99]. In our calculation, for $x \leq 0.25$, Ca is effectively under high pressure with the effective Ca pseudoatom volume being

$\Omega_0^{\mathrm{Ca}} = 127.5$ a.u. in the low solubility limit at Mg's observed equilibrium volume. There is a small amount of s-d transfer at this effective pseudoatom volume with $Z_d^{\mathrm{Ca}} = 0.37$. As x increases and under constraint of zero pressure, the effective Ca volume relaxes and the system approaches the empty d-band metal behaviour of elemental Ca. Empty d-band metals pose an additional challenge for the GPT as the d-states required for the hybridisation function will be unbound as they lie above the Fermi level. As such, a localisation potential v_{loc} is introduced into the pseudoatom calculation [10]. Filled d-band metals such as Zn pose similar difficulties, as the d-states are too deeply bound and inappropriate to add into the valence without modification. Despite there being partial occupation of the initially empty d-band, we proceed under the assumption of good physical convergence at the pairwise level, albeit with a now finite overlap potential. As a result, we won't explicitly write the transition metal v_3 and v_4 multi-ion potentials.

The potentials are dependent on the concentration x. This occurs in two ways: firstly through the explicit appearance of x in the formulae previously listed in this chapter and secondly through the implicit concentration dependence of the equilibrium volume. We note that despite this, the low solubility limit $x \to 0$ is adequate for concentrations up to $x = 0.25$ which is testament to the transferability of the GPT (see Fig.(4.3)).

4.3 Stability

Stability is the property of a crystal structure to remain invariant under some shift in the ionic positions away from equilibrium. There are multiple classes of stability, distinguished by the magnitude of displacements that can made before returning to their equilibrium positions. If a crystal structure is thermodynamically stable, then it is tolerant to all fluctuations in ion positions that occur at thermal equilibrium. In other

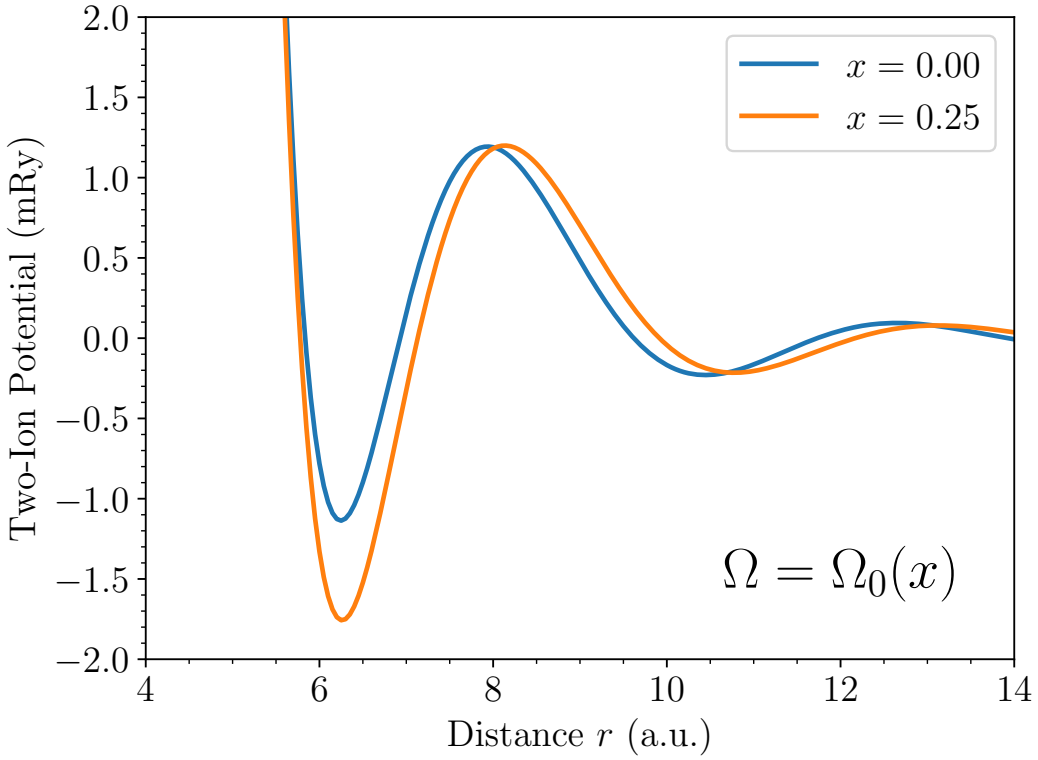

Fig. 4.3: The Mg-Mg GPT alloy potential for $x = 0$ and $x = 0.25$ at their respective calculated equilibrium volumes: $\Omega^{\mathrm{Mg}}_{x=0} = 159.5$ and $\Omega^{\mathrm{Mg}}_{x=0.25} = 182.7$.

words, a thermodynamically stable crystal structure is that which the metal adopts provided that the metal has been allowed to fully equilibrate. In order to determine whether a particular crystal structure is thermodynamically stable, we would have to minimize the relevant thermodynamic potential, say the Gibbs free energy G if the natural variables are temperature T and pressure P, over the entire space of crystal structures. For instance, an arbitrary expansion of the Gibbs free energy G

$$G = G_0 + \delta G \tag{4.63}$$

in terms of ionic displacements leads to $G \geq G_0$ if the crystal structure is thermodynamically stable. At ambient pressure and temperature, Mg assumes the hcp phase. At high pressure (~ 50 GPa), Mg undergoes a phase transition to the bcc structure as

a result of the lowering and partial filling of the initially empty $3d$ band under compression [9]. This is discussed in the next subsection. The bcc phase just below the transition pressure P^* is not thermodynamically stable but it is stable to small virtual displacements of its ions from equilibrium. In this sense, the bcc phase is mechanically stable [204]. We usually take the view that a crystal structure is mechanically stable if $\delta G \geq 0$ for displacements at quadratic order. Furthermore, there are some crystals, including bcc Ti [261], which are mechanically unstable at low temperatures but become stable at higher temperatures. This is because higher order corrections, corresponding to the phonon-phonon interaction, renormalise δG from negative to positive.

4.3.1 Thermodynamic Stability in Mg

One of the early successes of the GPT applied to Mg was the prediction of the high pressure structural phase transition from hcp $\rightarrow$ bcc at 50 GPa [9, 139, 262] which was subsequently discovered experimentally [263]. The explanation for this transition is lowering and subsequent *sp-d* hybridisation of the $3d$ band that lies above the Fermi level. The *P-T* phase diagram of Mg including the melt line and anharmonic corrections to the solid was calculated with the GPT [139, 262]. The hcp-bcc phase boundary was recalculated using DFT including electronic entropy through the Fermi-Dirac distribution [264]. A comprehensive measurement of the *P-T* phase diagram was performed by Stinton *et al* [265] using diamond-anvil cell experiments. They found that the phase boundary was significantly steeper than had been predicted theoretically and confirmed the existence of the double hcp phase (a phase which is broadly speaking a mixture of fcc and hcp stacking), at pressures between 10-20 GPa and temperatures between 1250-1500 K.

We have repeated the calculation of the hcp-bcc phase boundary using DFT, specifically the plane-wave plus muffin-tin orbital method of Kotani and van Schilfgaarde

[266]. This is method is based on the FP-LMTO method of van Schilfgaarde and co-workers [220]. Additional plane-waves are added into the basis to improve the completeness of the basis set. If too many plane waves are added into the basis, the Hamiltonian becomes singular. The plane waves which cause basis set overcompleteness are eliminated through diagonalisation of the overlap matrix and removing the subspace corresponding to eigenvalues less than some tolerance (in our case 10^{-7}). We calculated the total energy and phonon spectrum over a wide range of volumes with the PBEsol exchange-correlation functional [170]. We first fit a Birch-Murnaghan equation of state to the internal energy of the electrons [267, 268]. We capture the volume dependence of the quasiharmonic free energy by using the free energy for the quasiharmonic Einstein approximation where all phonons oscillate with the same frequency i.e. $\omega_{\mathbf{q}\sigma} \equiv \omega_E$

$$F_{\mathrm{qh},E}\left(\Omega, T\right) = \frac{3}{2} k_{\mathcal{B}} \Theta_E\left(\Omega, T\right) + \frac{3}{\beta} \log\left(1 - e^{-\Theta_E(\Omega,T)/T}\right) \tag{4.64}$$

where $k_{\mathcal{B}}$ is Boltzmann's constant and $\Theta_E = \hbar\omega_E / k_{\mathcal{B}}$ is Einstein's temperature. The logarithm of the Einstein temperature can be expanded as a low-order polynomial in the volume with temperature-dependent coefficients

$$\log \Theta_E\left(\Omega, T\right) = \sum_i c_i\left(T\right) \Omega^i. \tag{4.65}$$

The Gibbs free energy can then be calculated at each pressure P by minimising

$$G\left(P, T\right) = \min_{\Omega} \left[E_{\mathrm{tot}}\left(\{\mathbf{R}\}, \Omega\right) + F_{\mathrm{qh},E}\left(\Omega, T\right) + P\Omega\right]. \tag{4.66}$$

For each pressure P, we then find the temperature T^* such that $G^{\mathrm{bcc}} = G^{\mathrm{hcp}}$. The resulting bcc-hcp phase boundary is shown in Fig.(4.4). Our results are in line with those calculated previously both quantitatively and qualitatively. The calculated phase

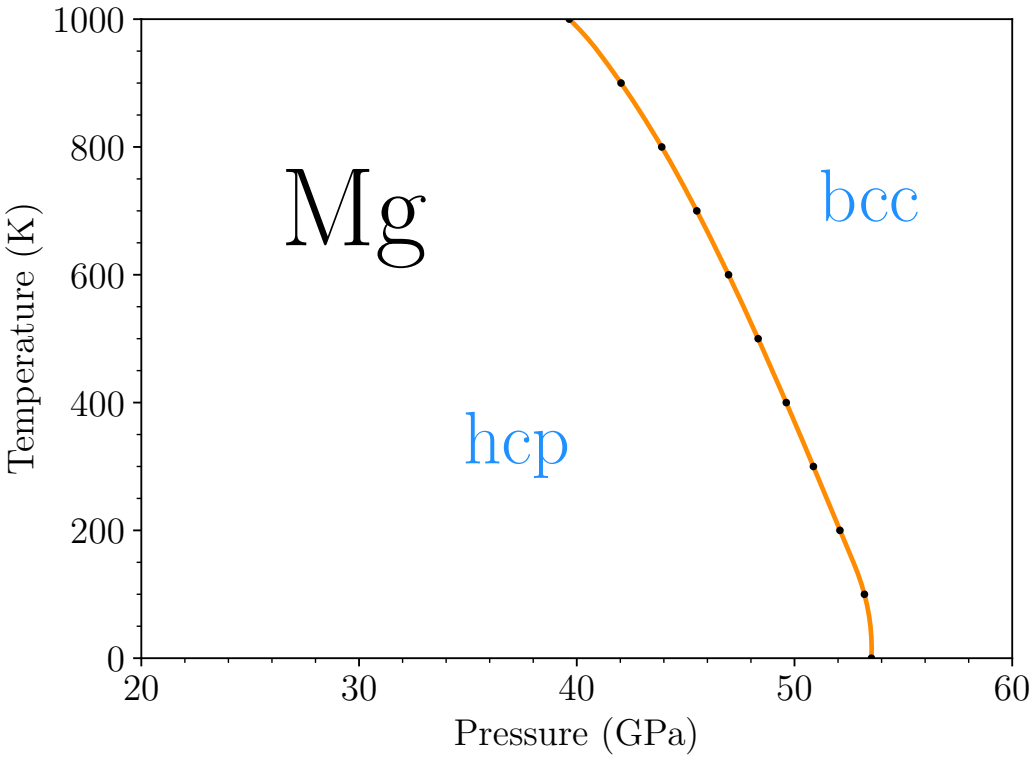

Fig. 4.4: The hcp-bcc phase boundary for elemental Mg calculated using DFT with a plane-wave plus muffin-tin orbital basis set [266].

still underestimates the gradient in Stinton *et al* [265]. The additional steepness in the gradient may arise from a non-negligible electron-phonon coupling, the removal of errors associated witht the less accurate treatment of exchange and correlation, or a quantum-mechanical treatment of the anharmonicity.

4.3.2 Conditions for Mechanical Stability

There are two related methods for testing whether a crystal structure is mechanically stable. Both can be derived by expanding the thermodynamic potential in a Taylor series. For now, we shall take this to be the internal energy U where $U = E_{\text{tot}}$ in the previous chapters. We expand the internal energy U about its equilibrium

configuration to second order in terms of virtual displacements

$$U\left(\{\mathbf{R}\}\right) = U\left(\{\mathbf{R}^0\}\right) + \frac{1}{2}\sum_{ij\alpha\beta}\frac{\partial^2 U}{\partial R_{i\alpha}\partial R_{j\beta}}u_{i\alpha}u_{j\beta} \tag{4.67}$$

where $\{\mathbf{R}^0\}$ are the equilibrium ion positions, the second order partial derivative term is the force-constant matrix and $u_{i\alpha}$ is the displacement vector

$$u_{i\alpha} = R_{i\alpha} - R^0_{i\alpha}. \tag{4.68}$$

The linear term in Eq.(4.67) vanishes identically by the broader mechanical equilibrium condition which requires for there to be no nett force or torque on the crystal. The truncation of Eq.(4.67) at quadratic order is the basis for the harmonic or quasi-harmonic approximation. The requirement for mechanical stability is that the force-constant matrix be positive definite for any small virtual displacement. Recall that a matrix is positive definite if its eigenspectrum is positive. We remember that Eq.(4.67) constitutes the potential part of the quasi-harmonic lattice dynamics Hamiltonian whose kinetic part is given by

$$K = \frac{1}{2}\sum_{i\alpha} M_i \dot{u}^2_{i\alpha}. \tag{4.69}$$

The Hamiltonian is diagonalised by constructing a dynamical matrix D which is the mass-reduced Fourier transform of the force-constant matrix. The eigenvalues of D are the square frequencies of oscillation of the lattice normal modes. Therefore, for mechanical stability, we require the frequencies to be real

$$\omega^2_{\mathbf{q}\sigma} \geq 0, \quad \forall \mathbf{q}, \sigma \tag{4.70}$$

where σ is the branch number. Once we have solved for the eigenfrequencies and

eigenmodes, we can write the displacement vector in terms of them

$$u_{i\alpha}(t) = \left(\frac{\hbar}{2NM_i}\right)^{1/2} \sum_{\mathbf{q}\sigma} \omega_{\mathbf{q}\sigma}^{-1/2} \left[a_{\mathbf{q}\sigma} e^{-i\omega_{\mathbf{q}\sigma}t} + a_{\mathbf{q}\sigma}^{\dagger} e^{i\omega_{\mathbf{q}\sigma}t}\right] e^{i\mathbf{q}\cdot\mathbf{R}_i} d_{i\alpha,\mathbf{q}\sigma} \tag{4.71}$$

where $\{a_{\mathbf{q}\sigma}\}$ and $\{a_{\mathbf{q}\sigma}^{\dagger}\}$ are the phonon creation and annihilation operators respectively, and $\{d_{i\alpha,\mathbf{q}\sigma}\}$ are the normal mode vectors. If one of the eigenfrequencies has a non-zero imaginary part, the displacement blows up exponentially fast.

4.3.3 Wallace Tensor & Stability Criteria

Another condition for mechanical stability applies for homogenous deformations only. Let $\mathbf{X}$ describe an initial configuration and $\mathbf{x}$ describe a final configuration. These two configurations are related by a linear transformation α_{ij}

$$x_i = \sum_j \alpha_{ij} X_j \tag{4.72}$$

with $\alpha_{ij} = (\partial x_i / \partial X_j)$. The displacement in the strain from $\mathbf{X}$ to $\mathbf{x}$ is the vector $\mathbf{u} = \mathbf{x} - \mathbf{X}$. Therefore, the displacement gradients are simply $u_{ij} = (\partial u_i / \partial X_j)$ and clearly

$$\alpha_{ij} = \delta_{ij} + u_{ij} \tag{4.73}$$

where δ is the Kronecker delta. We can calculate the square of the distance between $\mathbf{x}$ and $\mathbf{X}$

$$\sum_i x_i^2 = \sum_{ijk} \alpha_{ij}\alpha_{ik} X_j X_k = \sum_i X_i^2 + 2\sum_{ij} \eta_{ij} X_i X_j \tag{4.74}$$

where the Lagrangian strain parameters η_{ij} are given by

$$\eta_{ij} = \frac{1}{2}\left(u_{ij} + u_{ji} + \sum_k u_{ki}u_{kj}\right). \tag{4.75}$$

We can see that the Lagrangian strain is symmetric $\eta_{ij} = \eta_{ji}$ and also that

$$\eta_{ij} = \frac{1}{2}\left(\sum_k \alpha_{ki}\alpha_{kj} - \delta_{ij}\right). \tag{4.76}$$

The final configuration of the crystal may be completely specified in terms of the initial configuration and either the transformation coefficients α_{ij} or displacement gradients u_{ij}. Importantly, it cannot be specified in terms of the Lagrangian strains alone as they contain no information with regard to rotations. This makes the discussion more subtle than in the inhomogeneous case. We note that the ratio of volume change between configurations is given by the Jacobian

$$V(\mathbf{x})/V(\mathbf{X}) = \det[\alpha_{ij}]. \tag{4.77}$$

The internal energy U is a function of final configuration $\mathbf{x}$ and the entropy S, and both U and the system of applied stresses should possess translational and rotational invariance. The system has an arbitrarily chosen origin so that translational invariance is automatically guaranteed. The rotational invariance implies that U in the final configuration $\mathbf{x}$ depends on the initial configuration $\mathbf{X}$ only through the Lagrangian strains η_{ij}

$$U(\mathbf{x}, S) = U(\mathbf{X}, \eta_{ij}, S) = U(\mathbf{X}, S) + V\sum_{ij}\sigma_{ij}\eta_{ij} + \frac{1}{2}V\sum_{ijkl}C^S_{ijkl}\eta_{ij}\eta_{kl} + \cdots \tag{4.78}$$

where V is the volume of the initial configuration, σ_{ij} is the 2$^{\text{nd}}$ Piola-Kirchoff stress

tensor [112, 269]

$$\sigma_{ij} = \frac{1}{V}\left(\frac{\partial U}{\partial \eta_{ij}}\right)\Bigg|_{S,\eta=0} \tag{4.79}$$

and the adiabatic elastic moduli tensor C is given by

$$C^{S}_{ijkl} = \frac{1}{V}\left(\frac{\partial^2 U}{\partial \eta_{ij}\partial \eta_{kl}}\right)\Bigg|_{S,\eta=0}. \tag{4.80}$$

Consider the case in Eq.(4.78) when the stress tensor $\sigma_{ij} = 0$, then we have a situation similar to before. The crystal structure is stable to virtual strains at zero stress if

$$C_{ijkl}\delta\eta_{ij}\delta\eta_{kl} \geq 0. \tag{4.81}$$

We typically reshape the elastic moduli tensor's indices according to the Voigt prescription which also removes the redundancy due to symmetry. In Voigt notation, this condition is simply that the eigenvalues of the elastic moduli tensor are positive. Given that the structure of the elastic moduli tensor is fixed by crystal symmetry, this leads to a set of Born stability criteria for each crystal structure [205]. The general case is more subtle, and requires a more careful treatment of the relationship between stress and strain [204]. We consider two configurations $\mathbf{X}$ and $\bar{\mathbf{X}}$ which can be related by symmetric strains from $\bar{\mathbf{X}}$ to $\mathbf{X}$. The transformation from $\bar{\mathbf{X}}$ to $\mathbf{X}$ is given by

$$a_{ij} = a_{ji} = \frac{\partial X_i}{\partial \bar{X}_j}. \tag{4.82}$$

The corresponding Lagrangian strain parameters n_{ij} are given by an equation analogous to Eq.(4.76)

$$n_{ij} = \frac{1}{2}\left(\sum_k a_{ki}a_{kj} - \delta_{ij}\right). \tag{4.83}$$

This can be inverted leaving us with a power series in the Lagrangian strains n_{ij}

$$a_{ij} = \delta_{ij} + n_{ij} - \frac{1}{2}\sum_k n_{ki} n_{kj} + \cdots \tag{4.84}$$

which can be readily verified. The ratio of volume change during this transformation is given by

$$\frac{V}{\bar{V}} = \det\left[a_{ij}\right] = 1 + \sum_i n_{ii} + \cdots \tag{4.85}$$

which for infinitesimal strains can be truncated at the trace. If the Lagrangian strains from $\bar{\mathbf{X}}$ to the final configuration $\mathbf{x}$ are given by $\bar{\eta}_{ij}$ and those from $\mathbf{X}$ to $\mathbf{x}$ are given by η_{ij}, then we can write

$$\bar{\eta}_{ij} + \frac{1}{2}\delta_{ij} = \frac{1}{2}\sum_k \frac{\partial x_k}{\partial \bar{X}_i}\frac{\partial x_k}{\partial \bar{X}_j}, \tag{4.86}$$

$$= \frac{1}{2}\sum_k \sum_{rs} \frac{\partial x_k}{\partial X_r}\frac{\partial X_r}{\partial \bar{X}_i}\frac{\partial x_k}{\partial X_s}\frac{\partial X_s}{\partial \bar{X}_j}, \tag{4.87}$$

$$= \sum_{rs}\left(\eta_{rs} + \frac{1}{2}\delta_{rs}\right) a_{ri} a_{sj}. \tag{4.88}$$

This gives us the result for the derivative,

$$\frac{\partial \bar{\eta}_{ij}}{\partial \eta_{rs}} = a_{ri} a_{sj} \tag{4.89}$$

and if we carry out the transformation $\bar{\mathbf{X}}$ to $\mathbf{X}$ adiabatically then we can calculate the stress tensor evaluated at $\mathbf{X}$ as

$$\sigma_{ij} = \frac{1}{V}\left(\frac{\partial U}{\partial \eta_{ij}}\right) = \frac{1}{\bar{V}}\left(\frac{\bar{V}}{V}\right)\sum_{kl}\left(\frac{\partial U}{\partial \bar{\eta}_{kl}}\right)\left(\frac{\partial \bar{\eta}_{kl}}{\partial \eta_{ij}}\right). \tag{4.90}$$

Using the internal energy expansion in Eq.(4.78) and Eq.(4.89), we have

$$\sigma_{ij} = \left(\frac{\bar{V}}{V}\right) \sum_{kl} a_{ik} a_{jl} \left[\bar{\sigma}_{kl} + \sum_{mn} \bar{C}^{S}_{klmn} n_{mn} + \cdots \right] \tag{4.91}$$

where n_{ij} appears as a result of the evaluation at $\mathbf{X}$. Inserting the expression for the transformation matrices into the above yields

$$\sigma_{ij} = \bar{\sigma}_{ij} + \sum_{kl} n_{kl} \left[-\bar{\sigma}_{ij}\delta_{kl} + \bar{\sigma}_{il}\delta_{jk} + \bar{\sigma}_{jk}\delta_{il} + \bar{C}^{S}_{ijkl} \right]. \tag{4.92}$$

Returning to the original notation, we write

$$\sigma_{ij}\left(\mathbf{x}, S\right) = \sigma_{ij}\left(\mathbf{X}, S\right) + B^{S}_{ijkl}\eta_{kl} + \cdots \tag{4.93}$$

where we have defined the adiabatic Wallace tensor B^{S}_{ijkl}

$$B^{S}_{ijkl} = \frac{1}{2}\left(\sigma_{il}\delta_{jk} + \sigma_{jl}\delta_{ik} + \sigma_{ik}\delta_{jl} + \sigma_{jk}\delta_{il} - 2\sigma_{ij}\delta_{kl}\right) + C^{S}_{ijkl}. \tag{4.94}$$

The extra terms appear as a result of the symmetry present in the dummy variables k and l in Eq.(4.91). The Wallace tensor can be thought of as the generalisation of the elastic constants at finite stress. It is important to note that the Wallace tensor does not generally possess full Voigt symmetry. The change in internal energy for an initially stress configuration is thus

$$\frac{1}{V}\delta U \approx \sum_{ij} \sigma_{ij}\delta\eta_{ij} + \sum_{ijkl} \lambda^{S}_{ijkl}\delta\eta_{ij}\delta\eta_{kl} \tag{4.95}$$

where $\lambda^{S}_{ijkl} = \frac{1}{2}(B^{S}_{ijkl} + B^{S}_{klij})$ is the symmetrised Wallace tensor with the Voigt symmetry reimposed

$$\lambda_{ijkl} = \lambda_{jikl} = \lambda_{ijlk} = \lambda_{klij}. \tag{4.96}$$

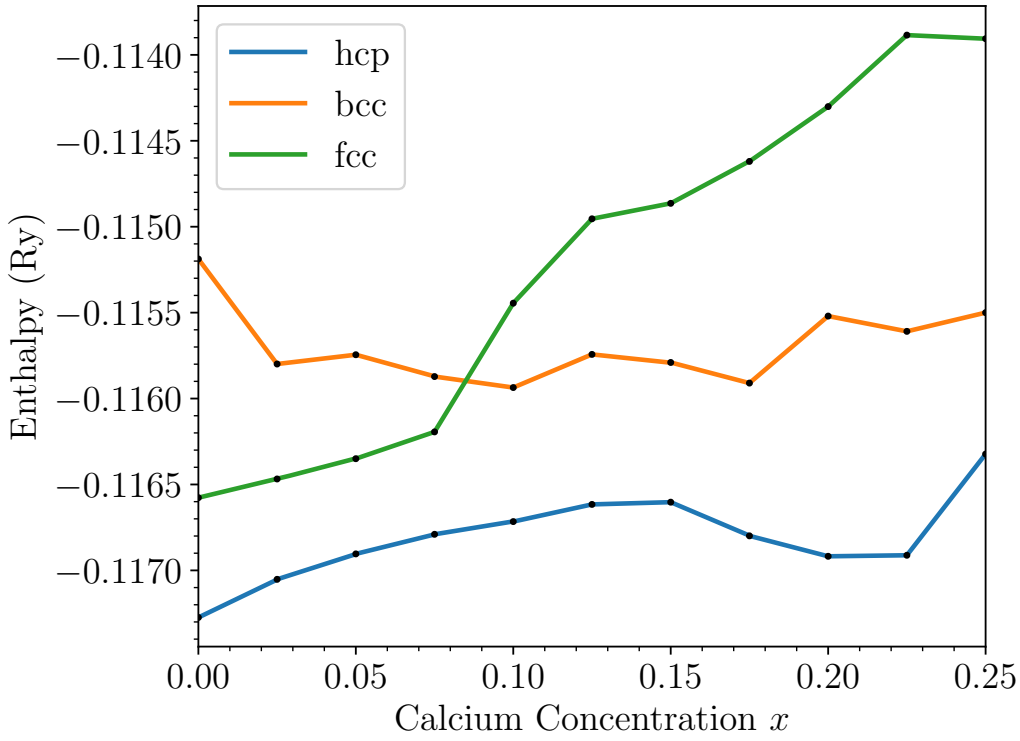

Fig. 4.5: The cohesive energies were calculated as an average over many representative SQSs in the Mg-Ca alloy system. The bcc structure becomes relatively more stable as the Ca concentration is increased.

The first term in the internal energy expansion in Eq.(4.95) is equal to the applied stress due to the mechanical equilibrium condition. The second term provides the condition for mechanical stability which is that the symmetrised Wallace tensor is positive definite. Therefore, the crystal structure is stable under homogenous deformation if the eigenvalues of the symmetrised Wallace tensor are all positive.

4.4 Practical Considerations & Results

4.4.1 Thermodynamic Stability and Solubility

At zero pressure and ambient temperatures, Mg forms in the hcp crystal structure as previously stated. We have calculated the enthalpy H_{tot} as a function of concentration for representative SQSs in each of the common metallic crystal structures. The correlation functions were matched out to range $R_a = 1.8a$ for the pairs and $R_a = 1.4a$ for the triplets. The enthalpy per atom was calculated using the GPT Mg-Ca alloy potentials introduced in Section 4.2.2 and plotted in Fig.(4.5). The volume was relaxed until the magnitude of the internal pressure $|P^{(\text{int})}|$ was less than 0.1 MPa and the forces were relaxed with the FIRE algorithm [148] such that the root mean square force was less than 10^{-6} Ry a.u.$^{-1}$. We see in Fig.(4.5) that the fcc structure is more favourable than bcc at low Ca concentrations. As we increase the Ca concentration to $x = 0.1$, the bcc structure is more favourable than fcc. The enthalpy difference between bcc and hcp at this point is 0.78 mRy. The phonon contribution to the free energy was also considered. The phonon density of states (DOS) was calculated for hcp and bcc at their respective calculated equilibrium volumes with the tetrahedron method [270]

$$g\left(\omega, \Omega\right) = \sum_{\mathbf{q}\sigma} \delta\left(\omega - \omega_{\mathbf{q}\sigma}\left(\Omega\right)\right). \tag{4.97}$$

The full quasi-harmonic contribution to the free energy can be written in terms of the phonon DOS

$$F_{\text{qh}}\left(\Omega, T\right) = \int \mathrm{d}\omega \; g\left(\omega, \Omega\right) \left[\frac{1}{2}\hbar\omega + \frac{1}{\beta}\log\left(1 - e^{-\beta\hbar\omega}\right)\right] \tag{4.98}$$

where β is the inverse temperature. The difference between the quasiharmonic free

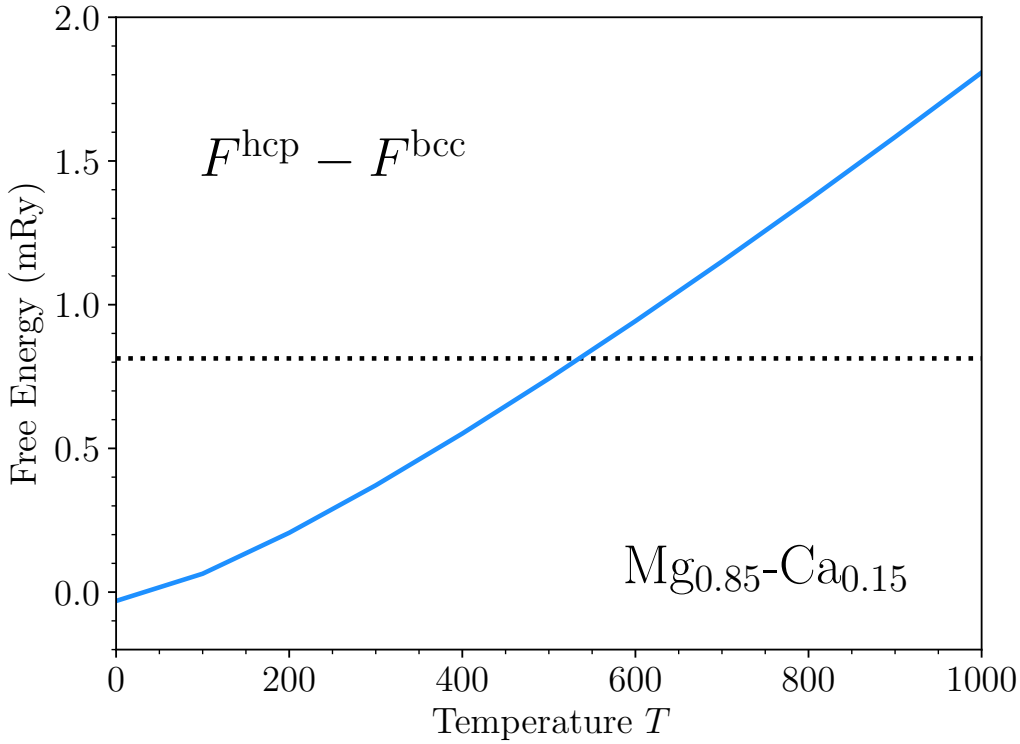

Fig. 4.6: The phonon contribution to the quasiharmonic free energy difference (blue) between the hcp and bcc structures for the Mg-Ca alloy system with $x = 0.15$. The dotted line represents the electronic enthalpy difference between the hcp and bcc structures. The intersection of these lines gives the temperature at which the bcc structure is thermodynamically preferable to hcp.

energies calculated for an SQS with $x = 0.16$ is plotted in Fig.(4.6). The intersection of the dotted line represents the temperature at which the bcc phase becomes thermodynamically preferable to the hcp phase under the assumption that

$$G\left(0,T\right) \approx H_{\mathrm{tot}}\left(\{\mathbf{R}\},\Omega\right) + F_{\mathrm{qh}}\left(\Omega,T\right) - TS_{\mathrm{conf}} \tag{4.99}$$

where G is the Gibbs free energy and S_{conf} is the ideal configurational entropy

$$S_{\mathrm{conf}} = -k_{\mathcal{B}}\left[x\log x + (1-x)\log\left(1-x\right)\right]. \tag{4.100}$$

In principle, there are additional contributions from electronic entropy, electron-phonon coupling and phonon anharmonicity which also shift the zero of pressure. These contributions are expected to be small at ambient temperatures. Recently, there has been an extension of the GPT to include an electronic entropy contribution [271, 272]. Furthermore, the GPT is well suited to the calculation of anharmonic corrections since radial derivatives are easily derived analytically to arbitrary order. The explicit electron-phonon contribution is more challenging and it is not clear how this could be done using the GPT formalism.

Returning to zero temperature, the heat of formation ΔH determines whether the solute, in this case Ca, is soluble. It is the energy required to keep the alloy from separating and can be written as

$$\Delta H = H_{\text{tot}} - xE_{\text{tot}}^{\text{Ca}} - (1-x)\, E_{\text{tot}}^{\text{Mg}}. \tag{4.101}$$

A negative heat of formation indicates that the solute is soluble. The results for Mg-Ca are shown in Fig.(4.7) where $H_{\text{tot}}^{\text{Ca}} = -0.1389$ Ry is taken from GPT calculations in the fcc phase of elemental Ca. In Fig.(4.7), we see that Ca is not soluble in any of the three metallic crystal structures that we have looked at. However, the bcc heat of formation is negative if the total enthalpy at $x = 0$ is taken in the bcc phase. This means that the largest contribution to Ca's insolubility in the bcc phase is from the thermodynamic instability at $x = 0$. In the next subsection, we will explore the metastability of the bcc phase.

4.4.2 Mechanical Stability

We have investigated the mechanical stability of Mg-Ca alloy system in the bcc phase as a function of Ca concentration using the conditions outlined in the previous subsection. Since the bcc phase is a cubic phase and we are primarily concerned with the

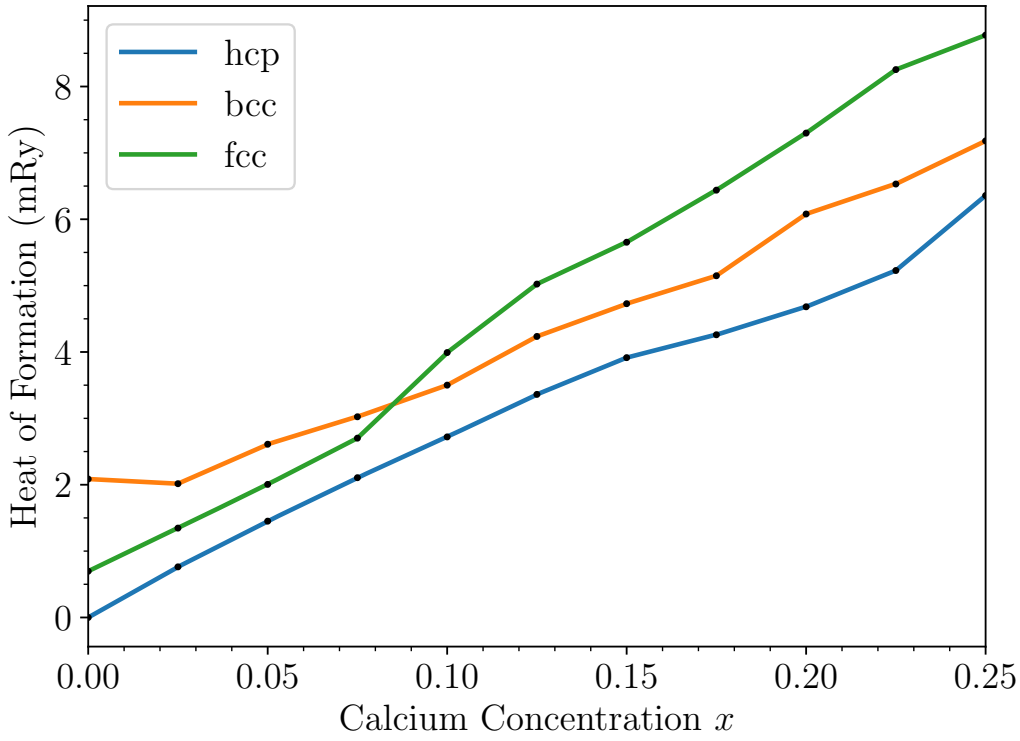

Fig. 4.7: The heat of formation is calculated for representative SQSs in the three common metallic crystal structures. Whilst Ca is not soluble in any of the three structures, the bcc structure has a negative heat of formation relative to the bcc Mg cohesive energy.

stability of these alloys at zero pressure, the eigenvalues of the Wallace tensor reduce to the Born criteria for cubic crystals

$$C_{11} - C_{12} \geq 0, \quad C_{44} \geq 0, \quad C_{11} + 2C_{12} \geq 0 \tag{4.102}$$

where we have used Voigt notation. We notice that first condition is that the shear modulus C' is positive. Similarly, the final condition is equivalent to one specifying that the bulk modulus B_d is positive. The configurational degrees of freedom are treated using the special quasi-random structure (SQS) procedure [255, 256] whereby a finite periodic supercell is constructed with cluster correlation functions that best

Table 4.1: In cubic crystals, the Born stability criteria require the shear moduli $\bar{C}'$ and $\bar{C}_{44}$, and the bulk modulus $\bar{B}_d$ to be positive. These combinations of averaged elastic constants were calculated for the Mg-Ca alloy systems in the bcc phase following a force and volume relaxation of an SQS at different concentrations of Ca. The relaxed (zero pressure) atomic volumes Ω are listed too.

x	Ω [a.u.^{3}]	$\bar{C}'$ [GPa]	$\bar{C}_{44}$ [GPa]	$\bar{B}_d$ [GPa]
0.00	159.25	-1.2	31.9	32.4
0.05	165.66	12.5	17.7	31.4
0.10	170.00	5.8	16.3	31.2
0.15	174.16	4.1	10.3	30.5

match those of the truly random alloy. This was done for 1000 atom supercells at different concentrations of Ca up to 25% using the ATAT framework [273]. The correlation functions were matched out to range $R_a = 2a$ for the pairs and $R_a = 1.6a$ for the triplets and quadruplets. Both the volume and forces were relaxed using the Mg-Ca GPT alloy interatomic potentials of Section 4.2. The forces were relaxed using the FIRE minimisation scheme [148] until the root mean square total force was less than 10^{-6} Ry a.u.$^{-1}$. Similarly, the volume was relaxed until the magnitude of the internal pressure $|P^{(\mathrm{int})}|$ was less than 0.1 MPa. The elastic constants were calculated numerically using a first-order central difference scheme for the variation in stress tensor with strain

$$C_{ijkl} = \left(\frac{\partial \sigma_{ij}}{\partial \eta_{kl}} \right) \Bigg|_{\eta=0} \tag{4.103}$$

where the GPT stress tensor σ_{ij} can be written in terms of radial and volume derivatives of the volume term E_{vol} and pair potential v_2 is given by

$$\sigma_{\mu\nu} = \left[\frac{\partial E_{\text{vol}}}{\partial \Omega} + \frac{1}{2N}\sum_{\alpha,\beta=A,B}\sum_{ij}{}' \frac{\partial v_2^{\alpha\beta}}{\partial \Omega}\left(R_{ij},\Omega\right)\right]\delta_{\mu\nu} + \frac{1}{2V}\sum_{\alpha,\beta=A,B}\sum_{ij}{}' \frac{\partial v_2^{\alpha\beta}}{\partial R_{ij}}\left(R_{ij},\Omega\right)\frac{R_{ij\mu}R_{ij\nu}}{R_{ij}}. \quad (4.104)$$

Following the relaxation of the atomic co-ordinates, the SQSs may have deviated somewhat from the initial cubic symmetry resulting in an elastic moduli tensor which does not have cubic symmetry. Before applying the Born stability criteria, we first average the elastic moduli tensor over the point group operations [274, 275]. In a cubic crystal, this corresponds to the simple arithmetic averages over the crystallographic directions [100], [010] and [001]

$$\bar{C}_{11} = \frac{C_{11}+C_{22}+C_{33}}{3}, \quad \bar{C}_{12} = \frac{C_{12}+C_{13}+C_{23}}{3}, \quad \bar{C}_{44} = \frac{C_{44}+C_{55}+C_{66}}{3}. \quad (4.105)$$

The results of the Born stability criteria with these averaged cubic elastic constants for these SQSs at different concentrations of Ca are listed in Table 4.1. We have also calculated the phonon density of states $g(\omega)$ in the quasi-harmonic approximation in Eq.(4.97). The harmonic phonon frequencies can be calculated by diagonalising the dynamical matrix D which is given by

$$D_{\mu\nu}\left(\kappa\kappa';\mathbf{q}\right) = \frac{1}{\sqrt{M_\kappa M_{\kappa'}}}\sum_{l'} A_{\mu\nu}\left(\kappa 0;\kappa' l'\right) e^{i\mathbf{q}\cdot\mathbf{R}(l')}, \quad (4.106)$$

where $A_{\mu\nu}$ is GPT force constant matrix given by the binary alloy generalisation of Eq.(3.8). The quasi-harmonic density of states is calculated by turning Eq.(4.97) into the form given by the tetrahedron method [270] for the same zero-pressure Mg-Ca SQSs in Table 4.1. In Fig.(4.8), the density of states for zero pressure elemental Mg

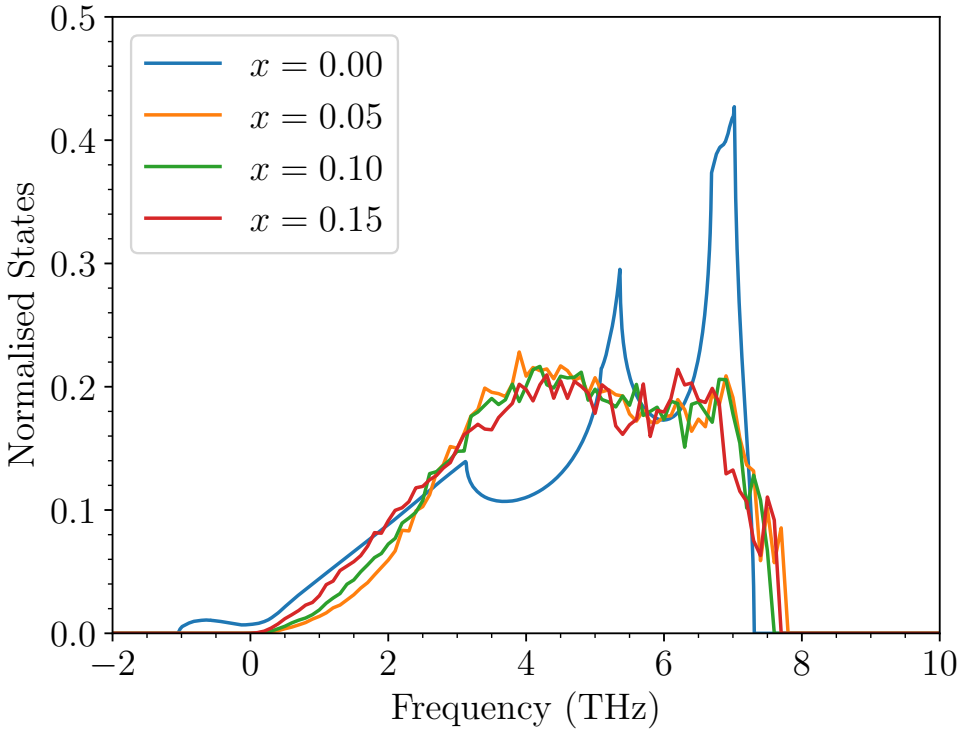

Fig. 4.8: Phonon density of states $g(\omega)$ for the Mg_{1-x}-Ca_x alloy system in the bcc crystal structure. The density of states was calculated using a dense **q**-point subdivision of $101 \times 101 \times 101$ whereas the **q**-point subdivisions for the 1000 atom SQSs were $16 \times 16 \times 16$.

exhibits imaginary frequencies (denoted as negative in the diagram) corresponding to the mechanical instability. With small amounts of Ca ($x \in [0.05, 0.15]$), the phonon density of states no longer exhibit imaginary frequencies. This is in agreement with the elastic stability criteria in Table 4.1.

4.5 Conclusions

In this chapter, we have derived novel Mg-Ca alloy interatomic potentials and applied them to random substitutional Mg-Ca alloys. These interatomic potentials utilised the GPT alloy theory and are transferable to any ion configuration, ordered or disordered, for a particular concentration x. We have used these potentials to understand and

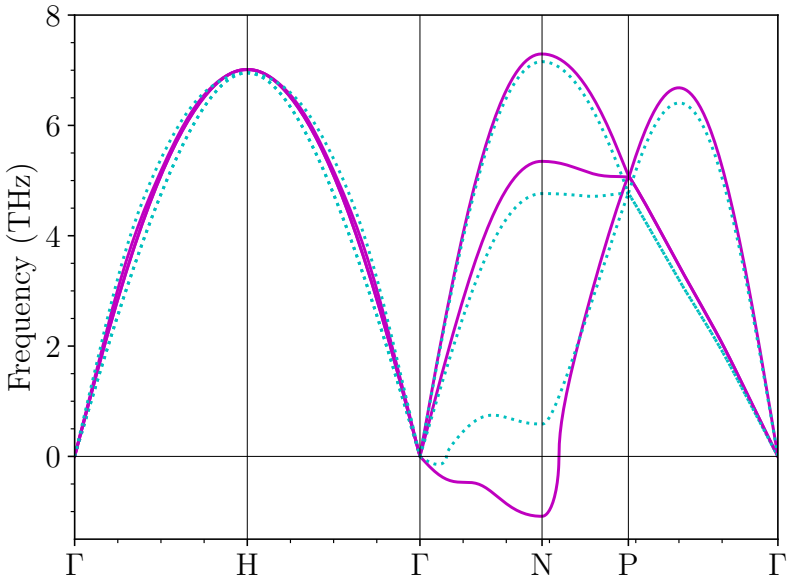

Fig. 4.9: Phonon bandstructure for bcc Mg at $\Omega = 156.8$ a.u. in the harmonic approximation (magenta) and with anharmonic quartic corrections (blue dashed). Whilst there is significant bandstructure renormalisation, we have neglected cubic anharmonicity which may contribute negatively to the frequencies.

predict bcc metastability in the Mg-rich region of the phase diagram. These findings are significant for a number of reasons. Firstly, elemental Mg suffers from a plastic anisotropy which leaves it prone to brittle fracture since 5 slip planes are not guaranteed to be active under an arbitrary deformation. The bcc structure naturally has the 5 requisite slip systems for all its common dislocations. Secondly, we have found that metastability occurs at very small concentrations of Mg i.e. $x = 0.05$. At this concentration, the heat of formation for the bcc structure whilst positive is dominated by the structural energy difference. This leads us to believe that such an alloy may be producible in laboratory perhaps at high pressure in a diamond anvil cell.

4.5.1 Future Work

We finish with a discussion of possible future research directions. The expansion of the thermodynamic potential in terms of virtual crystal displacements was central to the derivation of the conditions for mechanical stability. The expansion in Eq.(4.67) was terminated at second order in the displacements. The presence of imaginary eigenfrequencies was interpreted to mean that the crystal was mechanically unstable. Higher order contributions may work to renormalise the quasi-harmonic phonon frequencies. These contributions may be large enough to stabilise the crystal structure as in bcc Ti [261]. For a strongly anharmonic crystal, such as those which are mechanically unstable at the harmonic level, we can expect the phonon-phonon coupling to be large. This requires a nonperturbative approach to anharmonicity such as the *self consistent phonon approximation* [204, 276, 277]. We assume the existence of an effective quasi-harmonic Hamiltonian and use a cumulant expansion of the free energy together with the Gibbs-Bogoliubov bound to derive a set of equations for the renormalised frequencies which can be self-consistently iterated. Alternatively, we can view it in the context of many-body perturbation theory and the calculation of a self-energy to infinite order. Preliminary calculations in Fig.(4.9) show that there are significant positive contributions to the original harmonic frequencies in bcc Mg at 300 K at the equilibrium volume. These calculations were performed with ALAMODE and they neglect cubic anharmonic terms [219, 276, 277]. Thus, at present, we cannot make any statements with regards to mechanical stability. Further work is necessary to connect with previous results in this chapter.

The nucleation of kinks and pairs is central to the ductility of bcc metals as previously discussed. Firstly, the Peierls barrier would need to be calculated as that would dictate whether the kink-pair nucleation mechanism is necessary for slip. However, the quantity itself is not well defined in an alloy as the dislocations are not straight.

Methods based on the Labusch statistical theory exist for low concentration alloys [278–280]. Central to these methods is the calculation of the solute-defect interaction energies. These calculations place an individual solute atom in an otherwise pure metal at each site in some neighbourhood of the dislocation. In our particular case, this is confused by the fact that Ca is required to be present as it stabilises the structure. One possible solution would be to retain the Ca outside a neighbourhood of the dislocation and calculate the solute-defect interaction energy in the same manner as before.

Chapter 5

Conclusions

"In the long run, we are all dead."

John Maynard Keynes

The purpose of this thesis was to develop QBIPs and extend the GPT formalism for use in Mg and its alloys. The GPT in its modern density functional formulation is the closest method there is to a $\mathcal{O}(N)$ implementation of KS-DFT suitable for metals at low temperature. Previous work with the GPT demonstrated its predictive and explanatory power in bulk elemental simple metals [9, 96]. In Chapter 3, we addressed the central problem with the GPT applied to simple metals i.e. that it cannot describe free surfaces or defects with a large associated free volume. By allowing the GPT total energy to depend on a theoretically-motivated representation of the average local electron density, we found a considerable correction to the fully-relaxed vacancy formation energy. In Chapter 4, we derived Mg-Ca interatomic potentials using the alloy GPT formalism. Ca is of interest to metallurgists in Mg because it is seen as a potential replacement for rare-earth metals in Mg. In our case, we used these potentials to investigate the thermodynamic and mechanical stability of the bcc phase for small concentrations of Ca. We found that at just 5% Ca, the bcc structure was mechanically stable.

The Adaptive Generalised Pseudopotential Theory

In Chapter 3, we introduced the aGPT as a method for including local variations in the electron density into the GPT. We derived forces and the atomic stress tensor and applied them to a range of bulk properties including phonon dispersion, elastic constants and stacking fault energies. We found good agreement with experiment and KS-DFT values for the relaxed vacancy formation energies. We also used the volume conserving elastic constants to determine the optimal values of the distribution function for the averaging of the pseudoatom density. This selected out a smaller averaging sphere radius of $R_a = 1.8R_{\mathrm{WS}}$.

There was some disagreement, ~ 50 meV, with KS-DFT for divacancy binding energies where one vacancy was in the first or second neighbour shell of the other vacancy. There are a couple of things that can be said about this discrepancy. Firstly, the scale of the divacancy binding energy is small and could well be within the unknown DFT and aGPT error bars. Assuming that the error bars are small and non-overlapping, then the problem is with the averaging distribution function. Whilst other distribution functions have been trialled without success, it is still an area that can be explored. An ideal distribution would produce a more localised background electron density function.

Future work should centre on applying the aGPT to free surfaces such as cleaved surfaces, voids and cracks. Previous work by Moriarty and Phillips [147], found good agreement with unrelaxed experimental surface formation energies using the aGPT. It is expected that this would also be the case for relaxed surfaces including those with surface reconstructions. Combined with KS-DFT calculations for comparison, these surface calculations would form a precision test of the form of the averaging distribution function.

The results were produced with our own in-house Fortran codes without much in

the way of code optimisation. Even so, these codes have been used by our research group to study basal kinks in hcp Mg with 1.5 million atoms with the GPT. The computational scaling of the aGPT remains linear with a prefactor $27N_c$ times larger than the GPT where N_c is the size of a linked-list cell block [41, 112]. This increase in scaling is approximately analogous to the difference between MEAM and EAM. Both of these empirical potentials, alongside the GPT/MGPT, have been efficiently implemented within LAMMPS [229]. Building an efficient implementation of the aGPT within LAMMPS remains an open project. A good test application once completed, would be self-diffusion using molecular dynamics [281].

We have thought about applying the aGPT to alloys (using a similar formalism to Chapter 4), but there are a couple of unresolved problems. Firstly, if the B atom were a non-simple metal, we may expect some s-d transfer in the alloy. The B atom valence occupation Z_B would become configuration dependent. In principle, this would require a self-consistency cycle for Z_B and Z_d^B. We could make the approximation that the B atom valence occupation is static, however we would still run into the second problem. In the elemental aGPT, we avoided an explicit calculation of the on-site density $\bar{n}_a$ by using the bulk-constraining equation which doesn't apply in the alloy. It is unclear how to calculate $\bar{n}_a$ in the alloy without resorting to an integration.

Stability of the BCC Structure in the Mg-Ca Alloy System

We derived Mg-Ca interatomic potentials using the GPT alloy formalism. We then used these potentials to determine whether the bcc structure was mechanically stabilised for small Ca concentrations up to $x = 0.25$. Using two mechanical stability criteria, the Born stability criteria and the absence of imaginary frequencies in the phonon spectrum, we have determined that the bcc structure was stabilised at $x = 0.05$. The solubility of Ca in Mg was also investigated. We found that the heat of

formation was generally positive for the common metallic crystal structures. However, the enthalpy for bcc had a negative gradient with respect to concentration at small amounts of Ca. These results are important for a number of reasons. Firstly, the bcc structure is free of the plastic anisotropy that plagues hcp metals. This is because the lowest energy dislocations in bcc possess the requisite 5 independent slip systems. The metastability occurs at very low concentrations of Ca, which leads us to believe that it should be possible to produce the alloy experimentally.

Whilst the bcc structure possesses the requisite number of slip systems, bcc metals are often not ductile at low temperatures. This is due to presence of a large Peierls stress. Before a bcc alloy is declared generally ductile, the Peierls stress would need to be calculated. If the Peierls stress is indeed large, then slip must occur via a kink-pair nucleation mechanism; a thermally activated process. Unfortunately dislocation calculations are challenging in alloys, as the simplifying assumption of a straight dislocation is not applicable. This can usually treated with the Labusch statistical theory [278–280]. In our particular case this is extremely challenging due to the bcc structure being unstable in elemental Mg.

It is also worth investigating the temperature dependence of the mechanical stability of the crystal structure. This is done by introducing anharmonicity into the phonon spectra. The higher order derivatives in the expansion of the potential in terms of virtual displacements renormalise the quasi-harmonic frequencies. The GPT is an ideal electronic structure method for such a calculation, since fourth-order derivatives are easy to calculate and are known analytically. At finite temperature, the amount of Ca required to stabilise the structure may be smaller.

References

[1] N. Morley and D. Eatherley, *Material Security: Ensuring resource availability for the UK economy*. Department of Business Enterprise and Regulatory Reform, 2008.

[2] E. Orowan, "Zur kristallplastizität. i," *Zeitschrift für Physik*, vol. 89, pp. 605–613, sep 1934.

[3] M. Polanyi, "Über eine art gitterstörung, die einen kristall plastisch machen könnte," *Zeitschrift für Physik*, vol. 89, pp. 660–664, sep 1934.

[4] G. I. Taylor, "The mechanism of plastic deformation of crystals. part i. theoretical," *Proceedings of the Royal Society A: Mathematical, Physical and Engineering Sciences*, vol. 145, pp. 362–387, jul 1934.

[5] D. Griffiths, "Explaining texture weakening and improved formability in magnesium rare earth alloys," *Materials Science and Technology*, vol. 31, pp. 10–24, aug 2014.

[6] Z. Wu and W. A. Curtin, "The origins of high hardening and low ductility in magnesium," *Nature*, vol. 526, pp. 62–67, sep 2015.

[7] Z. Wu and W. A. Curtin, "Mechanism and energetics of c adislocation cross-slip in hcp metals," *Proceedings of the National Academy of Sciences*, vol. 113, pp. 11137–11142, sep 2016.

[8] Z. Wu, R. Ahmad, B. Yin, S. Sandlöbes, and W. A. Curtin, "Mechanistic origin and prediction of enhanced ductility in magnesium alloys," *Science*, vol. 359, pp. 447–452, jan 2018.

[9] J. A. Moriarty and A. K. McMahan, "High-pressure structural phase transitions in Na, Mg, and Al," *Physical Review Letters*, vol. 48, pp. 809–812, mar 1982.

[10] J. A. Moriarty, *Theory and Application of Quantum-Based Interatomic Potentials in Metals and Alloys*. OUP Oxford, To be published.

[11] W. A. Harrison, *Electronic Structure and the Properties of Solids*. Dover Publications, Inc., New York, 1989.

[12] D. G. Pettifor, *Bonding and Structure of Molecules and Solids*. Clarendon Press, 1995.

[13] M. W. Finnis, *Interatomic forces in condensed matter*, vol. 1. OUP Oxford, 2003.

[14] R. M. Martin, *Electronic Structure: Basic Theory and Practical Methods*. Cambridge University Press, 2004.

[15] L. I. Schiff, *Quantum Mechanics*. McGraw-Hill Book Company, Inc., 1955.

[16] S. Weinberg, *Lectures on Quantum Mechanics*. Cambridge University Press, 2015.

[17] J. J. Sakurai and J. Napolitano, *Modern Quantum Mechanics*. Cambridge University Press, sep 2017.

[18] N. H. March and G. G. N. Angilella, *Exactly Solvable Models in Many-Body Theory*. World Scientific, apr 2016.

[19] A. Szabo and N. S. Ostlund, *Modern Quantum Chemistry: Introduction to Advanced Electronic Structure Theory (Dover Books on Chemistry)*. Dover Publications, 1996.

[20] R. M. Martin, L. Reining, and D. M. Ceperley, *Interacting Electrons*. Cambridge University Press, 2016.

[21] K. G. Wilson, "The renormalization group: Critical phenomena and the kondo problem," *Reviews of Modern Physics*, vol. 47, pp. 773–840, oct 1975.

[22] S. R. White, "Density matrix formulation for quantum renormalization groups," *Physical Review Letters*, vol. 69, pp. 2863–2866, nov 1992.

[23] S. R. White, "Density-matrix algorithms for quantum renormalization groups," *Physical Review B*, vol. 48, pp. 10345–10356, oct 1993.

[24] G. Vidal, "Efficient simulation of one-dimensional quantum many-body systems," *Physical Review Letters*, vol. 93, jul 2004.

[25] S. Yan, D. A. Huse, and S. R. White, "Spin-liquid ground state of the s = 1/2 kagome heisenberg antiferromagnet," *Science*, vol. 332, pp. 1173–1176, apr 2011.

[26] S. R. White and R. L. Martin, "Ab initio quantum chemistry using the density matrix renormalization group," *The Journal of Chemical Physics*, vol. 110, pp. 4127–4130, mar 1999.

[27] W. M. C. Foulkes, L. Mitas, R. J. Needs, and G. Rajagopal, "Quantum monte carlo simulations of solids," *Reviews of Modern Physics*, vol. 73, pp. 33–83, jan 2001.

[28] R. Grimm and R. Storer, "Monte-carlo solution of schrödinger's equation," *Journal of Computational Physics*, vol. 7, pp. 134–156, feb 1971.

[29] J. B. Anderson, "A random-walk simulation of the schrödinger equation: H_3^+," *The Journal of Chemical Physics*, vol. 63, pp. 1499–1503, aug 1975.

[30] J. B. Anderson, "Quantum chemistry by random walk. H ^{2}P, H_3^+ D_{3h} $^1A_1'$, H_2 $^3\Sigma_u^+$, H_4 $^1\Sigma_g^+$, Be ^{1}S, journal = The Journal of Chemical Physics," vol. 65, pp. 4121–4127, nov 1976.

[31] W. L. McMillan, "Ground state of liquid He^4," *Physical Review*, vol. 138, pp. A442–A451, apr 1965.

[32] D. M. Ceperley and B. J. Alder, "Ground state of the electron gas by a stochastic method," *Physical Review Letters*, vol. 45, pp. 566–569, aug 1980.

[33] X.-P. Li, D. M. Ceperley, and R. M. Martin, "Cohesive energy of silicon by the green's-function monte carlo method," *Physical Review B*, vol. 44, pp. 10929–10932, nov 1991.

[34] G. Rajagopal, R. J. Needs, A. James, S. D. Kenny, and W. M. C. Foulkes, "Variational and diffusion quantum monte carlo calculations at nonzero wave vectors: Theory and application to diamond-structure germanium," *Physical Review B*, vol. 51, pp. 10591–10600, apr 1995.

[35] D. Ceperley and B. Alder, "The calculation of the properties of metallic hydrogen using monte carlo," *Physica BC*, vol. 108, pp. 875–876, aug 1981.

[36] D. M. Ceperley and B. J. Alder, "Ground state of solid hydrogen at high pressures," *Physical Review B*, vol. 36, pp. 2092–2106, aug 1987.

[37] V. Natoli, R. M. Martin, and D. M. Ceperley, "Crystal structure of atomic hydrogen," *Physical Review Letters*, vol. 70, pp. 1952–1955, mar 1993.

[38] V. Natoli, R. M. Martin, and D. Ceperley, "Crystal structure of molecular hydrogen at high pressure," *Physical Review Letters*, vol. 74, pp. 1601–1604, feb 1995.

[39] S. Azadi, B. Monserrat, W. M. C. Foulkes, and R. J. Needs, "Dissociation of high-pressure solid molecular hydrogen: A quantum monte carlo and anharmonic vibrational study," *Physical Review Letters*, vol. 112, apr 2014.

[40] B. J. Alder, D. M. Ceperley, and E. L. Pollock, "Computer simulation of phase transitions in classical and quantum systems," *International Journal of Quantum Chemistry*, vol. 22, pp. 49–61, mar 1982.

[41] M. E. Tuckerman, *Statistical Mechanics: Theory and Molecular Simulation (Oxford Graduate Texts)*. Oxford University Press, 2010.

[42] D. R. Hartree, "The wave mechanics of an atom with a non-coulomb central field. part i. theory and methods," *Mathematical Proceedings of the Cambridge Philosophical Society*, vol. 24, p. 89, jan 1928.

[43] D. R. Hartree, "The wave mechanics of an atom with a non-coulomb central field. part II. some results and discussion," *Mathematical Proceedings of the Cambridge Philosophical Society*, vol. 24, p. 111, jan 1928.

[44] V. Fock, "Näherungsmethode zur lösung des quantenmechanischen mehrkörperproblems," *Zeitschrift für Physik*, vol. 61, pp. 126–148, jan 1930.

[45] N. Ashcroft, "Electron-ion pseudopotentials in metals," *Physics Letters*, vol. 23, pp. 48–50, oct 1966.

[46] P. Hohenberg and W. Kohn, "Inhomogeneous electron gas," *Physical Review*, vol. 136, pp. B864–B871, nov 1964.

[47] W. Kohn and L. J. Sham, "Self-consistent equations including exchange and correlation effects," *Physical Review*, vol. 140, pp. A1133–A1138, nov 1965.

[48] R. O. Jones and O. Gunnarsson, "The density functional formalism, its applications and prospects," *Reviews of Modern Physics*, vol. 61, pp. 689–746, jul 1989.

[49] R. G. Parr and W. Yang, *Density-Functional Theory of Atoms and Molecules*. Oxford University Press, 1989.

[50] R. Jones, "Density functional theory: Its origins, rise to prominence, and future," *Reviews of Modern Physics*, vol. 87, pp. 897–923, aug 2015.

[51] L. F. Mattheiss, "Electronic structure of the 3d transition-metal monoxides. i. energy-band results," *Physical Review B*, vol. 5, pp. 290–306, jan 1972.

[52] L. F. Mattheiss, "Electronic structure of the 3d transition-metal monoxides. II. interpretation," *Physical Review B*, vol. 5, pp. 306–315, jan 1972.

[53] K. T. Moore and G. van der Laan, "Nature of the 5f states in actinide metals," *Reviews of Modern Physics*, vol. 81, pp. 235–298, feb 2009.

[54] L. Hedin, "New method for calculating the one-particle green's function with application to the electron-gas problem," *Physical Review*, vol. 139, pp. A796–A823, aug 1965.

[55] F. Aryasetiawan and O. Gunnarsson, "The *gw* method," *Reports on Progress in Physics*, vol. 61, pp. 237–312, mar 1998.

[56] W. G. Aulbur, L. Jönsson, and J. W. Wilkins, "Quasiparticle calculations in solids," in *Solid State Physics*, pp. 1–218, Elsevier, 2000.

[57] A. Georges, G. Kotliar, W. Krauth, and M. J. Rozenberg, "Dynamical mean-field theory of strongly correlated fermion systems and the limit of infinite dimensions," *Reviews of Modern Physics*, vol. 68, pp. 13–125, jan 1996.

[58] V. I. Anisimov, A. I. Poteryaev, M. A. Korotin, A. O. Anokhin, and G. Kotliar, "First-principles calculations of the electronic structure and spectra of strongly correlated systems: dynamical mean-field theory," *Journal of Physics: Condensed Matter*, vol. 9, pp. 7359–7367, sep 1997.

[59] B. Holm, "Total energies from *gw* calculations," *Physical Review Letters*, vol. 83, pp. 788–791, jul 1999.

[60] I. Leonov, V. I. Anisimov, and D. Vollhardt, "First-principles calculation of atomic forces and structural distortions in strongly correlated materials," *Physical Review Letters*, vol. 112, apr 2014.

[61] K. Haule and G. L. Pascut, "Forces for structural optimizations in correlated materials within a DFTembedded DMFT functional approach," *Physical Review B*, vol. 94, nov 2016.

[62] B. Ramberger, T. Schäfer, and G. Kresse, "Analytic interatomic forces in the random phase approximation," *Physical Review Letters*, vol. 118, mar 2017.

[63] A. D. Becke, "Density-functional exchange-energy approximation with correct asymptotic behavior," *Physical Review A*, vol. 38, pp. 3098–3100, sep 1988.

[64] J. P. Perdew and K. Burke, "Comparison shopping for a gradient-corrected density functional," *International Journal of Quantum Chemistry*, vol. 57, pp. 309–319, feb 1996.

[65] J. P. Perdew, K. Burke, and M. Ernzerhof, "Generalized gradient approximation made simple," *Physical Review Letters*, vol. 77, pp. 3865–3868, oct 1996.

[66] S. K. Ghosh and R. G. Parr, "Phase-space approach to the exchange-energy functional of density-functional theory," *Physical Review A*, vol. 34, pp. 785–791, aug 1986.

[67] A. D. Becke and M. R. Roussel, "Exchange holes in inhomogeneous systems: A coordinate-space model," *Physical Review A*, vol. 39, pp. 3761–3767, apr 1989.

[68] J. Tao, J. P. Perdew, V. N. Staroverov, and G. E. Scuseria, "Climbing the density functional ladder: Nonempirical meta–generalized gradient approximation designed for molecules and solids," *Physical Review Letters*, vol. 91, sep 2003.

[69] A. Görling, "Exact treatment of exchange in kohn-sham band-structure schemes," *Physical Review B*, vol. 53, pp. 7024–7029, mar 1996.

[70] M. Städele, J. A. Majewski, P. Vogl, and A. Görling, "Exact kohn-sham exchange potential in semiconductors," *Physical Review Letters*, vol. 79, pp. 2089–2092, sep 1997.

[71] M. Städele, M. Moukara, J. A. Majewski, P. Vogl, and A. Görling, "Exact exchange kohn-sham formalism applied to semiconductors," *Physical Review B*, vol. 59, pp. 10031–10043, apr 1999.

[72] A. D. Becke, "A new mixing of hartree–fock and local density-functional theories," *The Journal of Chemical Physics*, vol. 98, pp. 1372–1377, jan 1993.

[73] A. D. Becke, "Density-functional thermochemistry. III. the role of exact exchange," *The Journal of Chemical Physics*, vol. 98, pp. 5648–5652, apr 1993.

[74] J. P. Perdew, M. Ernzerhof, and K. Burke, "Rationale for mixing exact exchange with density functional approximations," *The Journal of Chemical Physics*, vol. 105, pp. 9982–9985, dec 1996.

[75] O. K. Andersen, "Linear methods in band theory," *Physical Review B*, vol. 12, pp. 3060–3083, oct 1975.

[76] J. Korringa, "On the calculation of the energy of a bloch wave in a metal," *Physica*, vol. 13, pp. 392–400, aug 1947.

[77] W. Kohn and N. Rostoker, "Solution of the schrödinger equation in periodic lattices with an application to metallic lithium," *Physical Review*, vol. 94, pp. 1111–1120, jun 1954.

[78] J. C. Slater, "Wave functions in a periodic potential," *Physical Review*, vol. 51, pp. 846–851, may 1937.

[79] J. C. Slater, "An augmented plane wave method for the periodic potential problem," *Physical Review*, vol. 92, pp. 603–608, nov 1953.

[80] P. E. Blöchl, "Projector augmented-wave method," *Physical Review B*, vol. 50, pp. 17953–17979, dec 1994.

[81] J. Ihm, A. Zunger, and M. L. Cohen, "Momentum-space formalism for the total energy of solids," *Journal of Physics C: Solid State Physics*, vol. 12, pp. 4409–4422, nov 1979.

[82] M. T. Yin and M. L. Cohen, "Theory of *ab initio* pseudopotential calculations," *Physical Review B*, vol. 25, pp. 7403–7412, jun 1982.

[83] D. M. Wood and A. Zunger, "A new method for diagonalising large matrices," *Journal of Physics A: Mathematical and General*, vol. 18, pp. 1343–1359, jun 1985.

[84] W. M. C. Foulkes and R. Haydock, "Tight-binding models and density-functional theory," *Physical Review B*, vol. 39, pp. 12520–12536, jun 1989.

[85] L. Lin, M. Chen, C. Yang, and L. He, "Accelerating atomic orbital-based electronic structure calculation via pole expansion and selected inversion," *Journal of Physics: Condensed Matter*, vol. 25, p. 295501, jun 2013.

[86] L. Lin, A. García, G. Huhs, and C. Yang, "SIESTA-PEXSI: massively parallel method for efficient and accurateab initiomaterials simulation without matrix diagonalization," *Journal of Physics: Condensed Matter*, vol. 26, p. 305503, jul 2014.

[87] S. Goedecker, "Linear scaling electronic structure methods," *Reviews of Modern Physics*, vol. 71, pp. 1085–1123, jul 1999.

[88] W. Kohn, "Density functional and density matrix method scaling linearly with the number of atoms," *Physical Review Letters*, vol. 76, pp. 3168–3171, apr 1996.

[89] E. Prodan and W. Kohn, "Nearsightedness of electronic matter," *Proceedings of the National Academy of Sciences*, vol. 102, pp. 11635–11638, aug 2005.

[90] A. L. Fetter and J. D. Walecka, eds., *Quantum Theory of Many-Particle Systems*. Dover Publications Inc., may 2003.

[91] L. Hung and E. A. Carter, "Accurate simulations of metals at the mesoscale: Explicit treatment of 1 million atoms with quantum mechanics," *Chemical Physics Letters*, vol. 475, pp. 163–170, jun 2009.

[92] H. Zhuang, M. Chen, and E. A. Carter, "Elastic and thermodynamic properties of complex mg-al intermetallic compounds via orbital-free density functional theory," *Physical Review Applied*, vol. 5, jun 2016.

[93] W. A. Harrison, "Pseudopotentials in the theory of metals," *P. W. A. Benjamin Inc., New York*, 1966.

[94] J. Ziman, "The calculation of bloch functions," in *Solid State Physics*, pp. 1–101, Elsevier, 1971.

[95] L. Dagens, M. Rasolt, and R. Taylor, "Charge densities and interionic potentials in simple metals: Nonlinear effects. II," *Physical Review B*, vol. 11, pp. 2726–2734, apr 1975.

[96] A. K. McMahan and J. A. Moriarty, "Structural phase stability in third-period simple metals," *Physical Review B*, vol. 27, pp. 3235–3251, mar 1983.

[97] J. Hafner, *From Hamiltonians to Phase Diagrams*. Springer Berlin Heidelberg, 1987.

[98] J. A. Moriarty, "First-principles interatomic potentials in transition metals," *Physical Review Letters*, vol. 55, pp. 1502–1505, sep 1985.

[99] J. A. Moriarty, "Density-functional formulation of the generalized pseudopotential theory. III. transition-metal interatomic potentials," *Phys. Rev. B*, vol. 38, pp. 3199–3231, aug 1988.

[100] J. A. Moriarty, "Analytic representation of multi-ion interatomic potentials in transition metals," *Physical Review B*, vol. 42, pp. 1609–1628, jul 1990.

[101] J. A. Moriarty, "Angular forces and melting in bcc transition metals: A case study of molybdenum," *Physical Review B*, vol. 49, pp. 12431–12445, may 1994.

[102] J. A. Moriarty, J. F. Belak, R. E. Rudd, P. Söderlind, F. H. Streitz, and L. H. Yang, "Quantum-based atomistic simulation of materials properties in transition metals," *Journal of Physics: Condensed Matter*, vol. 14, pp. 2825–2857, mar 2002.

[103] J. A. Moriarty, L. X. Benedict, J. N. Glosli, R. Q. Hood, D. A. Orlikowski, M. V. Patel, P. Söderlind, F. H. Streitz, M. Tang, and L. H. Yang, "Robust quantum-based interatomic potentials for multiscale modeling in transition metals," *Journal of Materials Research*, vol. 21, pp. 563–573, mar 2006.

[104] D. Pettifor, "New many-body potential for the bond order," *Physical Review Letters*, vol. 63, pp. 2480–2483, nov 1989.

[105] M. Aoki, "Rapidly convergent bond order expansion for atomistic simulations," *Physical Review Letters*, vol. 71, pp. 3842–3845, dec 1993.

[106] A. P. Horsfield, A. M. Bratkovsky, M. Fearn, D. G. Pettifor, and M. Aoki, "Bond-order potentials: Theory and implementation," *Physical Review B*, vol. 53, pp. 12694–12712, may 1996.

[107] M. Mrovec, D. Nguyen-Manh, D. G. Pettifor, and V. Vitek, "Bond-order potential for molybdenum: Application to dislocation behavior," *Physical Review B*, vol. 69, mar 2004.

[108] M. Mrovec, R. Gröger, A. G. Bailey, D. Nguyen-Manh, C. Elsässer, and V. Vitek, "Bond-order potential for simulations of extended defects in tungsten," *Physical Review B*, vol. 75, mar 2007.

[109] M. Mrovec, D. Nguyen-Manh, C. Elsässer, and P. Gumbsch, "Magnetic bond-order potential for iron," *Physical Review Letters*, vol. 106, jun 2011.

[110] F. H. Streitz, J. N. Glosli, and M. V. Patel, "Beyond finite-size scaling in solidification simulations," *Physical Review Letters*, vol. 96, jun 2006.

[111] P. M. Anderson, J. P. Hirth, and J. Lothe, *Theory of Dislocations*. Cambridge University Press, 2017.

[112] E. B. Tadmor and R. E. Miller, *Modeling Materials*. Cambridge University Press, 2009.

[113] R. Car and M. Parrinello, "Unified approach for molecular dynamics and density-functional theory," *Physical Review Letters*, vol. 55, pp. 2471–2474, nov 1985.

[114] J. Ziman, "The method of neutral pseudo-atoms in the theory of metals," *Advances in Physics*, vol. 13, pp. 89–138, jan 1964.

[115] J. A. Moriarty, "Density-functional formulation of the generalized pseudopotential theory," *Phys. Rev. B*, vol. 16, pp. 2537–2555, sep 1977.

[116] J. A. Moriarty, "Density-functional formulation of the generalized pseudopotential theory. II," *Phys. Rev. B*, vol. 26, pp. 1754–1780, aug 1982.

[117] J. E. Lennard-Jones, "On the determination of molecular fields. II. from the equation of state of a gas," *Proceedings of the Royal Society A: Mathematical, Physical and Engineering Sciences*, vol. 106, pp. 463–477, oct 1924.

[118] P. M. Morse, "Diatomic molecules according to the wave mechanics. II. vibrational levels," *Physical Review*, vol. 34, pp. 57–64, jul 1929.

[119] M. S. Daw and M. I. Baskes, "Embedded-atom method: Derivation and application to impurities, surfaces, and other defects in metals," *Physical Review B*, vol. 29, pp. 6443–6453, jun 1984.

[120] F. H. Stillinger and T. A. Weber, "Computer simulation of local order in condensed phases of silicon," *Physical Review B*, vol. 31, pp. 5262–5271, apr 1985.

[121] J. Tersoff, "New empirical approach for the structure and energy of covalent systems," *Physical Review B*, vol. 37, pp. 6991–7000, apr 1988.

[122] M. I. Baskes, "Modified embedded-atom potentials for cubic materials and impurities," *Physical Review B*, vol. 46, pp. 2727–2742, aug 1992.

[123] P. C. Gehlen, J. R. Beeler, and R. I. Jaffee, eds., *Interatomic Potentials and Simulation of Lattice Defects*. Springer US, 1972.

[124] I. M. Torrens, ed., *Interatomic Potentials*. Academic Press, New York, 1972.

[125] R. A. Johnson, "Empirical potentials and their use in the calculation of energies of point defects in metals," *Journal of Physics F: Metal Physics*, vol. 3, pp. 295–321, feb 1973.

[126] J. K. Lee, ed., *Interatomic Potentials and Crystal Defects*. Metallurgical Society of AIME, New York, 1981.

[127] N. W. Ashcroft and N. D. Mermin, *Solid State Physics*. Cengage Learning, 1976.

[128] A. E. Carlsson, C. D. Gelatt, and H. Ehrenreich, "An *ab initio* pair potential applied to metals," *Philosophical Magazine A*, vol. 41, pp. 241–250, feb 1980.

[129] R. A. Johnson, "Interstitials and vacancies in α-iron," *Physical Review*, vol. 134, pp. A1329–A1336, jun 1964.

[130] M. Rasolt and R. Taylor, "Charge densities and interionic potentials in simple metals: Nonlinear effects. i," *Physical Review B*, vol. 11, pp. 2717–2725, apr 1975.

[131] W. A. Harrison, "Transition-metal pseudopotentials," *Physical Review*, vol. 181, pp. 1036–1053, may 1969.

[132] K. W. Jacobsen, J. K. Norskov, and M. J. Puska, "Interatomic interactions in the effective-medium theory," *Physical Review B*, vol. 35, pp. 7423–7442, may 1987.

[133] M. W. Finnis and J. E. Sinclair, "A simple empirical n-body potential for transition metals," *Philosophical Magazine A*, vol. 50, pp. 45–55, jul 1984.

[134] W. Kohn, "Image of the fermi surface in the vibration spectrum of a metal," *Physical Review Letters*, vol. 2, pp. 393–394, may 1959.

[135] E. J. Woll and W. Kohn, "Images of the fermi surface in phonon spectra of metals," *Physical Review*, vol. 126, pp. 1693–1697, jun 1962.

[136] J. A. Moriarty, "Localized d states for pseudopotential calculations: Application to the alkaline-earth metals," *Physical Review B*, vol. 6, pp. 4445–4458, dec 1972.

[137] F. Ercolessi and J. B. Adams, "Interatomic potentials from first-principles calculations: The force-matching method," *Europhysics Letters (EPL)*, vol. 26, pp. 583–588, jun 1994.

[138] X.-Y. Liu, J. B. Adams, F. Ercolessi, and J. A. Moriarty, "EAM potential for magnesium from quantum mechanical forces," *Modelling and Simulation in Materials Science and Engineering*, vol. 4, pp. 293–303, may 1996.

[139] J. A. Moriarty and J. D. Althoff, "First-principles temperature-pressure phase diagram of magnesium," *Physical Review B*, vol. 51, pp. 5609–5616, mar 1995.

[140] T. Hastie, R. Tibshirani, and J. Friedman, *The Elements of Statistical Learning*. Springer New York, 2009.

[141] J. Behler, "Perspective: Machine learning potentials for atomistic simulations," *The Journal of Chemical Physics*, vol. 145, p. 170901, nov 2016.

[142] A. P. Bartók, M. C. Payne, R. Kondor, and G. Csányi, "Gaussian approximation potentials: The accuracy of quantum mechanics, without the electrons," *Physical Review Letters*, vol. 104, apr 2010.

[143] W. J. Szlachta, A. P. Bartók, and G. Csányi, "Accuracy and transferability of gaussian approximation potential models for tungsten," *Physical Review B*, vol. 90, sep 2014.

[144] A. P. Bartók, J. Kermode, N. Bernstein, and G. Csányi, "Machine learning a general-purpose interatomic potential for silicon," *Physical Review X*, vol. 8, dec 2018.

[145] D. Dragoni, T. D. Daff, G. Csányi, and N. Marzari, "Achieving DFT accuracy with a machine-learning interatomic potential: Thermomechanics and defects in bcc ferromagnetic iron," *Physical Review Materials*, vol. 2, jan 2018.

[146] A. P. Bartók, R. Kondor, and G. Csányi, "On representing chemical environments," *Physical Review B*, vol. 87, may 2013.

[147] J. A. Moriarty and R. Phillips, "First-principles interatomic potentials for transition-metal surfaces," *Physical Review Letters*, vol. 66, pp. 3036–3039, jun 1991.

[148] E. Bitzek, P. Koskinen, F. Gähler, M. Moseler, and P. Gumbsch, "Structural relaxation made simple," *Physical Review Letters*, vol. 97, oct 2006.

[149] G. Bussi, D. Donadio, and M. Parrinello, "Canonical sampling through velocity rescaling," *The Journal of Chemical Physics*, vol. 126, p. 014101, Jan. 2007.

[150] G. Bussi and M. Parrinello, "Accurate sampling using langevin dynamics," *Physical Review E*, vol. 75, May 2007.

[151] G. Bussi, T. Zykova-Timan, and M. Parrinello, "Isothermal-isobaric molecular dynamics using stochastic velocity rescaling," *The Journal of Chemical Physics*, vol. 130, p. 074101, Feb. 2009.

[152] M. Born and R. Oppenheimer, "Zur quantentheorie der molekeln," *Annalen der Physik*, vol. 389, no. 20, pp. 457–484, 1927.

[153] W. H. Zurek, "Decoherence, einselection, and the quantum origins of the classical," *Reviews of Modern Physics*, vol. 75, pp. 715–775, may 2003.

[154] D. Frenkel and B. Smit, *Understanding Molecular Simulation: From Algorithms to Applications (Computational Science Series, Vol 1)*. Academic Press, 2001.

[155] W. Pauli, "Über den einfluß der geschwindigkeitsabhängigkeit der elektronenmasse auf den zeemaneffekt," *Zeitschrift für Physik*, vol. 31, pp. 373–385, feb 1925.

[156] W. Pauli, "The connection between spin and statistics," *Physical Review*, vol. 58, pp. 716–722, oct 1940.

[157] J. C. Slater, "The theory of complex spectra," *Physical Review*, vol. 34, pp. 1293–1322, nov 1929.

[158] D. L. Strout and G. E. Scuseria, "A quantitative study of the scaling properties of the hartree–fock method," *The Journal of Chemical Physics*, vol. 102, pp. 8448–8452, jun 1995.

[159] J. Bardeen, "Theory of the work function. II. the surface double layer," *Physical Review*, vol. 49, pp. 653–663, may 1936.

[160] D. Pines and P. Nozières, *Theory Of Quantum Liquids: Normal Fermi Liquids (Advanced Books Classics)*. W. A. Benjamin, Inc, 1966.

[161] M. van Schilfgaarde, T. Kotani, and S. Faleev, "Quasiparticle self-consistent GW theory," *Physical Review Letters*, vol. 96, jun 2006.

[162] L. H. Thomas, "The calculation of atomic fields," *Mathematical Proceedings of the Cambridge Philosophical Society*, vol. 23, p. 542, jan 1927.

[163] E. Fermi, "Statistical method to determine some properties of atoms," *Rend. Accad. Naz. Lincei*, vol. 6, no. 602-607, p. 5, 1927.

[164] P. A. M. Dirac, "Note on exchange phenomena in the thomas atom," *Mathematical Proceedings of the Cambridge Philosophical Society*, vol. 26, p. 376, jul 1930.

[165] O. Gunnarsson and B. I. Lundqvist, "Exchange and correlation in atoms, molecules, and solids by the spin-density-functional formalism," *Physical Review B*, vol. 13, pp. 4274–4298, may 1976.

[166] J. P. Perdew and A. Zunger, "Self-interaction correction to density-functional approximations for many-electron systems," *Physical Review B*, vol. 23, pp. 5048–5079, may 1981.

[167] S. H. Vosko, L. Wilk, and M. Nusair, "Accurate spin-dependent electron liquid correlation energies for local spin density calculations: a critical analysis," *Canadian Journal of Physics*, vol. 58, pp. 1200–1211, aug 1980.

[168] J. P. Perdew and Y. Wang, "Accurate and simple analytic representation of the electron-gas correlation energy," *Physical Review B*, vol. 45, pp. 13244–13249, jun 1992.

[169] L. Hedin and B. I. Lundqvist, "Explicit local exchange-correlation potentials," *Journal of Physics C: Solid State Physics*, vol. 4, pp. 2064–2083, oct 1971.

[170] J. P. Perdew, A. Ruzsinszky, G. I. Csonka, O. A. Vydrov, G. E. Scuseria, L. A. Constantin, X. Zhou, and K. Burke, "Restoring the density-gradient expansion for exchange in solids and surfaces," *Physical Review Letters*, vol. 100, apr 2008.

[171] J. Hubbard, "The description of collective motions in terms of many-body perturbation theory. II. the correlation energy of a free-electron gas," *Proceedings of the Royal Society of London. Series A. Mathematical and Physical Sciences*, vol. 243, pp. 336–352, jan 1958.

[172] R. W. Shaw, "Exchange and correlation in the theory of simple metals," *Journal of Physics C: Solid State Physics*, vol. 3, pp. 1140–1158, may 1970.

[173] B. Farid, V. Heine, G. E. Engel, and I. J. Robertson, "Extremal properties of the harris-foulkes functional and an improved screening calculation for the electron gas," *Physical Review B*, vol. 48, pp. 11602–11621, oct 1993.

[174] J. C. Kimball, "Short-range correlations and electron-gas response functions," *Physical Review A*, vol. 7, pp. 1648–1652, may 1973.

[175] R. Taylor, "A simple, useful analytical form of the static electron gas dielectric function," *Journal of Physics F: Metal Physics*, vol. 8, pp. 1699–1702, aug 1978.

[176] D. J. W. Geldart and R. Taylor, "Wave-number dependence of the static screening function of an interacting electron gas. II. higher-order exchange and correlation effects," *Canadian Journal of Physics*, vol. 48, pp. 167–181, jan 1970.

[177] S. Ichimaru and K. Utsumi, "Analytic expression for the dielectric screening function of strongly coupled electron liquids at metallic and lower densities," *Physical Review B*, vol. 24, pp. 7385–7388, dec 1981.

[178] W. A. Harrison, "Electronic structure and the properties of metals. i. formulation," *Physical Review*, vol. 129, pp. 2503–2511, mar 1963.

[179] W. A. Harrison, "Electronic structure and the properties of metals. II. application to zinc," *Physical Review*, vol. 129, pp. 2512–2524, mar 1963.

[180] W. A. Harrison, "Theory of sodium, magnesium, and aluminum," *Physical Review*, vol. 136, pp. A1107–A1119, nov 1964.

[181] J. A. Moriarty, "Zero-order pseudoatoms and the generalized pseudopotential theory," *Physical Review B*, vol. 10, pp. 3075–3091, oct 1974.

[182] J. C. Phillips and L. Kleinman, "New method for calculating wave functions in crystals and molecules," *Physical Review*, vol. 116, pp. 287–294, oct 1959.

[183] E. Antončík, "A new formulation of the method of nearly free electrons," *Czechoslovak Journal of Physics*, vol. 4, pp. 439–451, nov 1954.

[184] E. Antončík, "Approximate formulation of the orthogonalized plane-wave method," *Journal of Physics and Chemistry of Solids*, vol. 10, pp. 314–320, aug 1959.

[185] B. J. Austin, V. Heine, and L. J. Sham, "General theory of pseudopotentials," *Physical Review*, vol. 127, pp. 276–282, jul 1962.

[186] V. Heine and I. Abarenkov, "A new method for the electronic structure of metals," *Philosophical Magazine*, vol. 9, pp. 451–465, mar 1964.

[187] D. R. Hamann, M. Schlüter, and C. Chiang, "Norm-conserving pseudopotentials," *Physical Review Letters*, vol. 43, pp. 1494–1497, nov 1979.

[188] D. Vanderbilt, "Soft self-consistent pseudopotentials in a generalized eigenvalue formalism," *Physical Review B*, vol. 41, pp. 7892–7895, apr 1990.

[189] V. Heine and D. Weaire, "Pseudopotential theory of cohesion and structure," in *Solid State Physics*, pp. 249–463, Elsevier, 1970.

[190] M. W. Finnis, "The energy and elastic constants of simple metals in terms of pairwise interactions," *Journal of Physics F: Metal Physics*, vol. 4, pp. 1645–1656, oct 1974.

[191] C. Herring and A. G. Hill, "The theoretical constitution of metallic beryllium," *Physical Review*, vol. 58, pp. 132–162, jul 1940.

[192] P. P. Ewald, "Die berechnung optischer und elektrostatischer gitterpotentiale," *Annalen der Physik*, vol. 369, no. 3, pp. 253–287, 1921.

[193] H. Kornfeld, "Die berechnung elektrostatischer potentiale und der energie von dipol- und quadrupolgittern," *Zeitschrift für Physik*, vol. 22, pp. 27–43, dec 1924.

[194] K. Fuchs and R. H. Fowler, "A quantum mechanical investigation of the cohesive forces of metallic copper," *Proceedings of the Royal Society of London. Series A - Mathematical and Physical Sciences*, vol. 151, pp. 585–602, oct 1935.

[195] D. Pettifor and M. Ward, "An analytic pair potential for simple metals," *Solid State Communications*, vol. 49, pp. 291–294, jan 1984.

[196] J. R. Chelikowsky, "Cohesive energies of simple metals as determined from atomic kinetic energies," *Physical Review Letters*, vol. 47, pp. 387–390, aug 1981.

[197] A. B. Walker and R. Taylor, "Density-dependent potentials for simple metals," *Journal of Physics: Condensed Matter*, vol. 2, pp. 9481–9499, dec 1990.

[198] M. W. C. Dharma-wardana and G. C. Aers, "Determination of the pair potential and the ion-electron pseudopotential for aluminum from experimental structure-factor data for liquid aluminum," *Physical Review B*, vol. 28, pp. 1701–1710, aug 1983.

[199] R. Pick and G. Sarma, "Orthogonalized plane wave method and total energy of a metal," *Physical Review*, vol. 135, pp. A1363–A1371, aug 1964.

[200] R. W. Shaw and W. A. Harrison, "Reformulation of the screened heine-abarenkov model potential," *Physical Review*, vol. 163, pp. 604–611, nov 1967.

[201] F. Bloch, "Über die quantenmechanik der elektronen in kristallgittern," *Zeitschrift für Physik*, vol. 52, pp. 555–600, jul 1929.

[202] L. H. Yang, P. Söderlind, and J. A. Moriarty, "Accurate atomistic simulation of (a/2) 111 screw dislocations and other defects in bcc tantalum," *Philosophical Magazine A*, vol. 81, pp. 1355–1385, may 2001.

[203] L. H. Yang, M. Tang, and J. A. Moriarty, "Dislocations and plasticity in bcc transition metals at high pressure," in *Dislocations in Solids*, pp. 1–46, Elsevier, 2010.

[204] D. C. Wallace, *Thermodynamics of Crystals*. Courier Corporation, 1998.

[205] M. Born and K. Huang, *Dynamical theory of crystal lattices*. Clarendon press, 1954.

[206] L. J. Slutsky and C. W. Garland, "Elastic constants of magnesium from 4.2°k to 300°k," *Physical Review*, vol. 107, pp. 972–976, aug 1957.

[207] A. M. Rosenfeld and M. J. Stott, "Density-dependent pair potentials and the compressibility problem," *J. Phys. F: Met. Phys.*, vol. 17, pp. 605–627, mar 1987.

[208] D. C. Wallace, "Pseudopotential calculation of the elastic constants of simple metals," *Physical Review*, vol. 182, pp. 778–782, jun 1969.

[209] E. Brovman and Y. Kagan, "Long-wave phonons in metals," *Soviet Journal of Experimental and Theoretical Physics*, vol. 30, no. 4, pp. 721–727, 1970.

[210] J. A. Moriarty, "Pseudo green's functions and the pseudopotential theory of *d*-band metals," *Physical Review B*, vol. 5, pp. 2066–2081, mar 1972.

[211] P. Lloyd and C. A. Sholl, "A structural expansion of the cohesive energy of simple metals in an effective hamiltonian approximation," *Journal of Physics C: Solid State Physics*, vol. 1, pp. 1620–1632, dec 1968.

[212] E. Brovman, Y. Kagan, and A. Kholas, "An analysis of the static and dynamic properties of metals and in particular of magnesium (the role of many-ion interaction)," *Soviet Journal of Experimental and Theoretical Physics*, vol. 34, pp. 394–402, 1972.

[213] M. Hasegawa, "Third-order perturbation theory and structures of liquid metals: sodium and potassium," *Journal of Physics F: Metal Physics*, vol. 6, pp. 649–675, may 1976.

[214] W. A. Harrison, "Multi-ion interactions and structures in simple metals," *Physical Review B*, vol. 7, pp. 2408–2415, mar 1973.

[215] P. Tzanetakis, J. Hillairet, and G. Revel, "The formation energy of vacancies in aluminium and magnesium," *physica status solidi (b)*, vol. 75, pp. 433–439, jun 1976.

[216] H. Hellmann, *Einführung in die Quantenchemie*. Leipzig: Franz Deuticke, 1937.

[217] R. P. Feynman, "Forces in molecules," *Physical Review*, vol. 56, pp. 340–343, aug 1939.

[218] C. M. Bertoni, V. Bortolani, C. Calandra, and F. Nizzoli, "Three-body forces in the lattice dynamics of beryllium," *Physical Review Letters*, vol. 31, pp. 1466–1469, dec 1973.

[219] T. Tadano, Y. Gohda, and S. Tsuneyuki, "Anharmonic force constants extracted from first-principles molecular dynamics: applications to heat transfer simulations," *Journal of Physics: Condensed Matter*, vol. 26, p. 225402, may 2014.

[220] M. Methfessel, M. van Schilfgaarde, and R. A. Casali, "A full-potential LMTO method based on smooth hankel functions," in *Electronic Structure and Physical Properies of Solids*, pp. 114–147, Springer Berlin Heidelberg, 1999.

[221] M. Methfessel and A. T. Paxton, "High-precision sampling for brillouin-zone integration in metals," *Physical Review B*, vol. 40, pp. 3616–3621, aug 1989.

[222] M. Parrinello and A. Rahman, "Crystal structure and pair potentials: A molecular-dynamics study," *Physical Review Letters*, vol. 45, pp. 1196–1199, oct 1980.

[223] M. Parrinello and A. Rahman, "Polymorphic transitions in single crystals: A new molecular dynamics method," *Journal of Applied Physics*, vol. 52, pp. 7182–7190, dec 1981.

[224] B. Yin, Z. Wu, and W. Curtin, "Comprehensive first-principles study of stable stacking faults in hcp metals," *Acta Materialia*, vol. 123, pp. 223–234, jan 2017.

[225] T. Uesugi, M. Kohyama, and K. Higashi, "*Ab initio* study on divacancy binding energies in aluminum and magnesium," *Physical Review B*, vol. 68, nov 2003.

[226] V. Vítek, "Intrinsic stacking faults in body-centred cubic crystals," *Philosophical Magazine*, vol. 18, pp. 773–786, oct 1968.

[227] J. R. Morris, J. Scharff, K. M. Ho, D. E. Turner, Y. Y. Ye, and M. H. Yoo, "Prediction of a {1122} hcp stacking fault using a modified generalized stacking-fault calculation," *Philosophical Magazine A*, vol. 76, pp. 1065–1077, nov 1997.

[228] A. Glensk, B. Grabowski, T. Hickel, and J. Neugebauer, "Breakdown of the arrhenius law in describing vacancy formation energies: The importance of local anharmonicity revealed by *ab-initio* thermodynamics," *Physical Review X*, vol. 4, feb 2014.

[229] S. Plimpton, "Fast parallel algorithms for short-range molecular dynamics," *Journal of Computational Physics*, vol. 117, pp. 1–19, mar 1995.

[230] S. R. Agnew, "Wrought magnesium: A 21st century outlook," *JOM*, vol. 56, pp. 20–21, may 2004.

[231] C. Bettles and M. R. Barnett, *Advances in Wrought Magnesium Alloys*, vol. 1. Woodhead Publishing Ltd., 2012.

[232] I. J. Polmear, D. S. John, J.-F. Nie, and M. Qian, "Light alloys: Metallurgy of the light metals," 2017.

[233] J. Bohlen, M. R. Nürnberg, J. W. Senn, D. Letzig, and S. R. Agnew, "The texture and anisotropy of magnesium–zinc–rare earth alloy sheets," *Acta Materialia*, vol. 55, pp. 2101–2112, apr 2007.

[234] N. Stanford, D. Atwell, A. Beer, C. Davies, and M. Barnett, "Effect of microalloying with rare-earth elements on the texture of extruded magnesium-based alloys," *Scripta Materialia*, vol. 59, pp. 772–775, oct 2008.

[235] T. Al-Samman and X. Li, "Sheet texture modification in magnesium-based alloys by selective rare earth alloying," *Materials Science and Engineering: A*, vol. 528, pp. 3809–3822, apr 2011.

[236] N. D. Mermin, "The topological theory of defects in ordered media," *Reviews of Modern Physics*, vol. 51, pp. 591–648, jul 1979.

[237] R. von Mises, "Mechanik der plastischen formänderung von kristallen," *ZAMM - Zeitschrift für Angewandte Mathematik und Mechanik*, vol. 8, no. 3, pp. 161–185, 1928.

[238] G. I. Taylor, "Plastic strain in metals," *Journal of the Institute of Metals*, vol. 62, pp. 307–324, 1938.

[239] J. W. Christian, *The Theory of Transformations in Metals and Alloys*. Pergamon Press Ltd., 1975.

[240] R. Peierls, "The size of a dislocation," *Proceedings of the Physical Society*, vol. 52, pp. 34–37, jan 1940.

[241] F. R. N. Nabarro, "Dislocations in a simple cubic lattice," *Proceedings of the Physical Society*, vol. 59, pp. 256–272, mar 1947.

[242] J. D. Eshelby, "Uniformly moving dislocations," *Proceedings of the Physical Society. Section A*, vol. 62, pp. 307–314, may 1949.

[243] R. Kikuchi, "A theory of cooperative phenomena," *Physical Review*, vol. 81, pp. 988–1003, Mar. 1951.

[244] L. Bellaiche and D. Vanderbilt, "Virtual crystal approximation revisited: Application to dielectric and piezoelectric properties of perovskites," *Physical Review B*, vol. 61, pp. 7877–7882, mar 2000.

[245] N. J. Ramer and A. M. Rappe, "Virtual-crystal approximation that works: Locating a compositional phase boundary in $Pb(Zr_{1-x}Ti_x)O_3$," *Physical Review B*, vol. 62, pp. R743–R746, jul 2000.

[246] B. Winkler, C. Pickard, and V. Milman, "Applicability of a quantum mechanical `virtual crystal approximation' to study Al/Si-disorder," *Chemical Physics Letters*, vol. 362, pp. 266–270, aug 2002.

[247] J. Íñiguez, D. Vanderbilt, and L. Bellaiche, "First-principles study of $(BiScO_3)_{1-x} - (PbTiO_3)_x$ piezoelectric alloys," *Physical Review B*, vol. 67, jun 2003.

[248] P. Soven, "Coherent-potential model of substitutional disordered alloys," *Physical Review*, vol. 156, pp. 809–813, apr 1967.

[249] B. Velický, S. Kirkpatrick, and H. Ehrenreich, "Single-site approximations in the electronic theory of simple binary alloys," *Physical Review*, vol. 175, pp. 747–766, nov 1968.

[250] M. Lax, "Multiple scattering of waves," *Reviews of Modern Physics*, vol. 23, pp. 287–310, oct 1951.

[251] J. L. Beeby, "Electronic structure of alloys," *Physical Review*, vol. 135, pp. A130–A143, jul 1964.

[252] D. D. Johnson, D. M. Nicholson, F. J. Pinski, B. L. Györffy, and G. M. Stocks, "Total-energy and pressure calculations for random substitutional alloys," *Physical Review B*, vol. 41, pp. 9701–9716, may 1990.

[253] A. F. Tatarchenko, V. S. Stepanyuk, W. Hergert, P. Rennert, R. Zeller, and P. H. Dederichs, "Total energy and magnetic moments in disordered Fe_x-Cu_{1-x} alloys," *Physical Review B*, vol. 57, pp. 5213–5219, mar 1998.

[254] J. M. Cowley, "Short- and long-range order parameters in disordered solid solutions," *Physical Review*, vol. 120, pp. 1648–1657, dec 1960.

[255] A. Zunger, S.-H. Wei, L. G. Ferreira, and J. E. Bernard, "Special quasirandom structures," *Physical Review Letters*, vol. 65, pp. 353–356, jul 1990.

[256] S.-H. Wei, L. G. Ferreira, J. E. Bernard, and A. Zunger, "Electronic properties of random alloys: Special quasirandom structures," *Physical Review B*, vol. 42, pp. 9622–9649, nov 1990.

[257] W. H. Butler and W. Kohn, "Local theory of disordered systems," *Journal of Research of the National Bureau of Standards*, vol. 74A, pp. 443–447, oct 1969.

[258] J. A. Moriarty and M. Widom, "First-principles interatomic potentials for transition-metal aluminides: Theory and trends across the 3*d* series," *Physical Review B*, vol. 56, pp. 7905–7917, oct 1997.

[259] M. Widom and J. A. Moriarty, "First-principles interatomic potentials for transition-metal aluminides. II. application to Al-Co and Al-Ni phase diagrams," *Physical Review B*, vol. 58, pp. 8967–8979, oct 1998.

[260] M. Widom, I. Al-Lehyani, and J. A. Moriarty, "First-principles interatomic potentials for transition-metal aluminides. III. extension to ternary phase diagrams," *Physical Review B*, vol. 62, pp. 3648–3657, aug 2000.

[261] W. Petry, A. Heiming, J. Trampenau, M. Alba, C. Herzig, H. R. Schober, and G. Vogl, "Phonon dispersion of the bcc phase of group-IV metals. i. bcc titanium," *Physical Review B*, vol. 43, pp. 10933–10947, may 1991.

[262] J. D. Althoff, P. B. Allen, R. M. Wentzcovitch, and J. A. Moriarty, "Phase diagram and thermodynamic properties of solid magnesium in the quasiharmonic approximation," *Physical Review B*, vol. 48, pp. 13253–13260, nov 1993.

[263] H. Olijnyk and W. B. Holzapfel, "High-pressure structural phase transition in mg," *Physical Review B*, vol. 31, pp. 4682–4683, apr 1985.

[264] S. Mehta, G. D. Price, and D. Alfè, "Ab initio thermodynamics and phase diagram of solid magnesium: A comparison of the LDA and GGA," *The Journal of Chemical Physics*, vol. 125, p. 194507, nov 2006.

[265] G. W. Stinton, S. G. MacLeod, H. Cynn, D. Errandonea, W. J. Evans, J. E. Proctor, Y. Meng, and M. I. McMahon, "Equation of state and high-pressure/high-temperature phase diagram of magnesium," *Physical Review B*, vol. 90, oct 2014.

[266] T. Kotani and M. van Schilfgaarde, "Fusion of the LAPW and LMTO methods: The augmented plane wave plus muffin-tin orbital method," *Physical Review B*, vol. 81, mar 2010.

[267] F. D. Murnaghan, "The compressibility of media under extreme pressures," *Proceedings of the National Academy of Sciences*, vol. 30, pp. 244–247, sep 1944.

[268] F. Birch, "Finite elastic strain of cubic crystals," *Physical Review*, vol. 71, pp. 809–824, jun 1947.

[269] C. Teodosiu, *Elastic Models of Crystal Defects*. Springer Berlin Heidelberg, 1982.

[270] P. E. Blöchl, O. Jepsen, and O. K. Andersen, "Improved tetrahedron method for brillouin-zone integrations," *Physical Review B*, vol. 49, pp. 16223–16233, jun 1994.

[271] J. A. Moriarty and J. B. Haskins, "Efficient wide-range calculation of free energies in solids and liquids using reversible-scaling molecular dynamics," *Physical Review B*, vol. 90, aug 2014.

[272] J. B. Haskins and J. A. Moriarty, "Polymorphism and melt in high-pressure tantalum. II. orthorhombic phases," *Physical Review B*, vol. 98, oct 2018.

[273] A. van de Walle, P. Tiwary, M. de Jong, D. Olmsted, M. Asta, A. Dick, D. Shin, Y. Wang, L.-Q. Chen, and Z.-K. Liu, "Efficient stochastic generation of special quasirandom structures," *Calphad*, vol. 42, pp. 13–18, sep 2013.

[274] J. Z. Liu, A. van de Walle, G. Ghosh, and M. Asta, "Structure, energetics, and mechanical stability of Fe-*Cu* bcc alloys from first-principles calculations," *Physical Review B*, vol. 72, oct 2005.

[275] F. Tasnádi, M. Odén, and I. A. Abrikosov, "*Ab initio* elastic tensor of cubic $Ti_{0.5}$-$Al_{0.5}$-N alloys: Dependence of elastic constants on size and shape of the supercell model and their convergence," *Physical Review B*, vol. 85, apr 2012.

[276] T. Tadano and S. Tsuneyuki, "Self-consistent phonon calculations of lattice dynamical properties in cubic $SrTiO_3$ with first-principles anharmonic force constants," *Physical Review B*, vol. 92, aug 2015.

[277] T. Tadano and S. Tsuneyuki, "First-principles lattice dynamics method for strongly anharmonic crystals," *Journal of the Physical Society of Japan*, vol. 87, p. 041015, apr 2018.

[278] R. Labusch, "A statistical theory of solid solution hardening," *physica status solidi (b)*, vol. 41, no. 2, pp. 659–669, 1970.

[279] G. P. M. Leyson, W. A. Curtin, L. G. Hector, and C. F. Woodward, "Quantitative prediction of solute strengthening in aluminium alloys," *Nature Materials*, vol. 9, pp. 750–755, aug 2010.

[280] G. Leyson, L. Hector, and W. Curtin, "First-principles prediction of yield stress for basal slip in mg–al alloys," *Acta Materialia*, vol. 60, pp. 5197–5203, aug 2012.

[281] D. G. Sangiovanni, O. Hellman, B. Alling, and I. A. Abrikosov, "Efficient and accurate determination of lattice-vacancy diffusion coefficients via non equilibrium *ab initio* molecular dynamics," *Physical Review B*, vol. 93, mar 2016.